EPFL

Molecular insights into the electrical double layer of colloidal oxide particles obtained through second harmonic scattering

Présentée le 8 avril 2022

Faculté des sciences et techniques de l'ingénieur
Chaire Julia Jacobi de photomédecine – Laboratoire de biophotonique fondamentale
Programme doctoral en science et génie des matériaux

pour l'obtention du grade de Docteur ès Sciences

par

Marie BISCHOFF

Acceptée sur proposition du jury

Prof. F. Nüesch, président du jury
Prof. S. Roke, Dr A. Marchioro, directrices de thèse
Prof. S. Baldelli, rapporteur
Prof. J. Gibbs, rapporteuse
Prof. P. Bowen, rapporteur

■ École
polytechnique
fédérale
de Lausanne

2022

To my family

Abstract

Photocatalytic applications play an essential role in the search for alternative energy sources with reduced CO_2 emissions and environmental decontamination techniques. Metal oxides are often considered in photocatalytic applications due to their generally favorable photocatalytic properties and their stability when used in aqueous solutions. In the past years more attention has been drawn to nano-sized systems of the same materials, since they exhibit special optical and electrical features compared to their bulk counterparts that can have a positive impact on the photocatalytic performance. In particular, nanoparticles are an interesting system to study in this context, as they can easily be tailored or modified for a particular application. Besides the need to find more suitable photocatalytic materials, it is of fundamental interest to understand on a molecular level the aqueous solid/liquid interface, where the photocatalytic reactions occur, in order to improve the reaction efficiency. Surface charge, ion diffusion and adsorption are all elements that can have a significant impact on reaction rates and, in the case of nanoparticles, colloidal stability. However, not many experimental techniques are able to probe the electrical double layer (EDL) and its peculiar properties, particularly when it comes to colloidal nanoparticles directly dispersed in solution.

In this thesis we apply polarimetric angle-resolved second harmonic scattering (AR-SHS) to study the EDL of colloidal oxide particles in aqueous environments. We first show the applicability of AR-SHS on a well-known insulating oxide, silica (SiO_2). We then investigate titanium dioxide (TiO_2), a metal oxide that has been extensively studied for photocatalytic applications over the last five decades due to its high stability and low cost. The two oxides are further compared. We show that from our nonlinear optical surface specific measurements, we can extract the surface potential of oxide particles with respect to bulk liquid and the surface susceptibility, as a measure of interfacial molecular orientation. This can be achieved without assuming a specific charge distribution in the electrical double layer, and hence without employing a model such as the Gouy-Chapman or the Gouy-Chapman-Stern models. Through electrophoretic mobility measurements, we additionally obtain the zeta potential of the particles in comparison to the surface potential from AR-SHS measurements. Knowing the surface potential, the surface susceptibility and the zeta potential enables us to establish a molecular level picture of the oxide particle/liquid interface as a function of ionic strength and pH.

First, we provide evidence that a condensed layer of hydrated ions is formed at the 300 nm diameter amorphous SiO_2 aqueous interface in high pH conditions and at high NaCl con-

Abstract

centrations (≥ 1 mM). Computation of surface charge density values based on our measured surface potential values and using the Gouy-Chapman and Gouy-Chapman-Stern models are in good agreement.

Next, we study the EDL of 100 nm diameter amorphous TiO_2 particles as a function of NaCl concentration and basic pH. Three different regions as a function of ionic strength can be identified. These three regions allow us to distinguish three phenomena with increasing ionic strength. First, inner-sphere adsorption at the lowest concentrations, then formation of a diffuse layer of counterions and finally, accumulation of hydrated counterions near the interface. While all these phenomena are predicted by common electrostatic models, our data enables us to retrieve the electrostatic structure of aqueous interfaces at each ionic strength without a priori knowledge on the charge distribution, suggesting AR-SHS could be applied to a variety of more complex systems. Similar regions are observed for TiO_2 particles in basic pH and 100 nm diameter SiO_2 particles as a function of NaCl concentration. The TiO_2 surface is found to have a stronger affinity for Na^+ ions than SiO_2.

We further evaluate ion-specific effects at the SiO_2 and amorphous TiO_2 colloidal aqueous interface. The addition of NaCl, RbCl or $CaCl_2$ to the aqueous environment leads to relative differences in surface potential and in the evolution of the interfacial H-bonding network as a function of ionic strength. The relative variations as a function of ionic strength reveal surface- and cation- specific preferences for inner- and outer-sphere adsorption.

Finally we demonstrate that AR-SHS measurements in different pH conditions can be used to determine the pK_as of 100 nm diameter anatase TiO_2 particles. Our data reveals a correlation between the change in orientation of interfacial water molecules and the pK_as of surface TiO_2 groups. This work shows that AR-SHS is a powerful tool to uncover the EDL structure of colloidal oxide particles, thus contributing to a better understanding of interfacial processes important to a variety of (photo-)catalytic applications.

Keywords: aqueous solid/liquid interfaces, oxides, colloids, electrical double layer, surface potential, molecular orientation, ion adsorption, non-linear optics, second harmonic generation, light scattering

Zusammenfassung

Photokatalytische Anwendungen spielen eine wesentliche Rolle bei der Suche nach alternativen Energiequellen mit geringeren CO_2-Emissionen und Techniken zur Dekontaminierung der Umwelt. Metalloxide werden aufgrund ihrer allgemein vorteilhaften photokatalytischen Eigenschaften und ihrer Stabilität bei Verwendung in wässrigen Lösungen häufig für photokatalytische Anwendungen eingesetzt. In den letzten Jahren wurde mehr Aufmerksamkeit auf Systeme derselben Materialien in Nanogröße gelenkt, da sie im Vergleich zu Bulk-Materialien besondere optische und elektrische Eigenschaften aufweisen, die sich positiv auf die photokatalytische Leistung auswirken können. Insbesondere Nanopartikel sind in diesem Zusammenhang ein interessantes System, da sie leicht für eine bestimmte Anwendung maßgeschneidert oder verändert werden können. Neben der Notwendigkeit, geeignetere photokatalytische Materialien zu finden, ist es von grundlegendem Interesse, die wässrige Fest-Flüssig-Grenzfläche, an der die photokatalytischen Reaktionen stattfinden, auf molekularer Ebene zu verstehen, um die Reaktionseffizienz zu verbessern. Oberflächenladung, Ionendiffusion und Adsorption sind Elemente, die einen erheblichen Einfluss auf die Reaktionseffizienz und - im Falle von Nanopartikeln - die kolloidale Stabilität haben können. Es gibt jedoch nur wenige experimentelle Techniken, mit denen die elektrische Doppelschicht (engl. electrical double layer (EDL)) und ihre besonderen Eigenschaften untersucht werden können, insbesondere bei kolloidalen Nanopartikeln, die direkt in einer Lösung dispergiert sind.

In dieser Arbeit wenden wir polarimetrische winkelaufgelöste zweite harmonische Streuung (engl. angle-resolved second harmonic scattering (AR-SHS)) an, um die EDL von kolloidalen Oxidpartikeln in wässriger Umgebung zu untersuchen. Wir zeigen zunächst die Anwendbarkeit von AR-SHS an einem bekannten isolierenden Oxid, Siliziumdioxid (SiO_2). Anschließend untersuchen wir Titandioxid (TiO_2), ein Metalloxid, das aufgrund seiner hohen Stabilität und geringen Kosten in den letzten fünf Jahrzehnten ausgiebig für photokatalytische Anwendungen untersucht wurde. Die beiden Oxide werden darüber hinaus miteinander verglichen. Wir zeigen, dass wir aus unseren optisch nichtlinearen, oberflächenspezifischen Messungen das Oberflächenpotenzial der Oxidpartikel in Bezug auf die Bulk-Flüssigkeit und die Oberflächensuszeptibilität als Maß für die molekulare Orientierung an der Grenzfläche ermitteln können. Dies kann erreicht werden, ohne eine spezifische Ladungsverteilung in der elektrischen Doppelschicht anzunehmen und somit ohne ein Modell wie das Gouy-Chapman- oder das Gouy-Chapman-Stern-Modell zu verwenden. Durch Messungen der elektrophoretischen Mobilität erhalten wir zusätzlich das Zetapotenzial der Partikel im Vergleich zum Oberflächenpotenzial aus AR-SHS-Messungen. Die Kenntnis des Oberflächenpotenzials, der

Abstract

Oberflächensuszeptibilität und des Zetapotenzials ermöglicht es uns, ein Bild der Oxidpartikel-Flüssigkeits-Grenzfläche auf molekularer Ebene in Abhängigkeit von der Ionenstärke und dem pH-Wert zu etablieren.

Zunächst weisen wir nach, dass sich an der wässrigen Grenzfläche von amorphem SiO_2 mit einem Durchmesser von 300 nm bei hohen pH-Werten und bei hohen NaCl-Konzentrationen (≥ 1 mM) eine kondensierte Schicht aus hydratisierten Ionen bildet. Die Berechnung der Oberflächenladungsdichte auf Grundlage unserer gemessenen Oberflächenpotentialwerte und unter Verwendung der Gouy-Chapman- und Gouy-Chapman-Stern-Modelle zeigt eine gute Übereinstimmung.

Als nächstes untersuchen wir die EDL von amorphen TiO_2-Partikeln mit einem Durchmesser von 100 nm in Abhängigkeit von der NaCl-Konzentration und basischen pH-Werten. Es lassen sich drei verschiedene Bereiche in Abhängigkeit von der Ionenstärke identifizieren. Anhand dieser drei Bereiche lassen sich drei Phänomene mit zunehmender Ionenstärke unterscheiden. Zunächst die Adsorption der Ionen unter partiellem oder vollständigem Verlust ihrer Hydratisierung (engl. inner-sphere) bei den niedrigsten Konzentrationen, dann die Bildung einer diffusen Schicht von Gegenionen und schließlich die Akkumulation von hydratisierten Gegenionen in der Nähe der Grenzfläche. Während alle diese Phänomene durch gängige elektrostatische Modelle vorhergesagt werden, ermöglichen uns unsere Daten, die elektrostatische Struktur wässriger Grenzflächen bei der jeweiligen Ionenstärke ohne vorherige Kenntnis der Ladungsverteilung zu ermitteln, was darauf schließen lässt, dass AR-SHS auf eine Vielzahl komplexerer Systeme angewendet werden könnte. Ähnliche Bereiche werden für TiO_2-Partikel in basischen pH-Werten und SiO_2-Partikel mit 100 nm Durchmesser in Abhängigkeit von der NaCl-Konzentration beobachtet. Die TiO_2-Oberfläche weist eine stärkere Affinität für Na^+-Ionen auf als SiO_2.

Des Weiteren werden ionenspezifische Effekte an der kolloidalen wässrigen Grenzfläche von SiO_2 und amorphem TiO_2 untersucht. Die Zugabe von NaCl, RbCl oder $CaCl_2$ in die wässrige Umgebung führt zu relativen Unterschieden im Oberflächenpotenzial und in der Entwicklung des H-Bindungsnetzwerks an der Grenzfläche in Abhängigkeit von der Ionenstärke. Die relativen Abweichungen in Abhängigkeit von der Ionenstärke zeigen oberflächen- und kationenspezifische Präferenzen für die Adsorption von vollständig oder teilweise dehydrierten Ionen (engl. inner-sphere) oder durch eine Wasserschicht von der Oberfläche getrennte Ionen (engl. outer-sphere).

Schließlich zeigen wir, dass AR-SHS-Messungen unter verschiedenen pH-Bedingungen zur Bestimmung der pK_as von Anatase TiO_2-Partikeln mit 100 nm Durchmesser verwendet werden können. Unsere Daten zeigen eine Korrelation zwischen der Änderung der Orientierung der Grenzflächenwassermoleküle und den pK_as der TiO_2-Oberflächengruppen. Diese Arbeit zeigt, dass AR-SHS ein leistungsfähiges Werkzeug ist, um die EDL-Struktur von kolloidalen Oxidpartikeln offenzulegen und so zu einem besseren Verständnis von Grenzflächenprozessen beizutragen, die für eine Vielzahl von (photo-)katalytischen Anwendungen wichtig sind.

Schlüsselwörter: Wässrige Fest-Flüssig-Grenzflächen, Oxide, Kolloide, elektrische Doppelschicht, Oberflächenpotential, molekulare Orientierung, Ionenadsorption, nichtlineare Optik, Erzeugung der zweiten Harmonischen, Lichtstreuung.

Resumé

Les applications photocatalytiques jouent un rôle essentiel dans la recherche de sources d'énergie alternatives avec émission de CO_2 réduite et de techniques de décontamination environnementale. Les oxydes métalliques sont souvent considérés dans les applications photocatalytiques en raison de leurs propriétés photocatalytiques généralement favorables et de leur stabilité lorsqu'ils sont utilisés dans des solutions aqueuses. Ces dernières années, une attention accrue a été portée aux systèmes de taille nanométrique de ces mêmes matériaux, car ils présentent des caractéristiques optiques et électriques particulières par rapport à celles de ces mêmes matériaux à l'échelle micro ou macroscopique, qui peuvent avoir un impact positif sur la performance photocatalytique. En particulier, les nanoparticules sont un système intéressant à étudier dans ce contexte, car elles peuvent facilement être fabriquées sur mesure ou modifiées pour une application particulière. Outre la nécessité de trouver des matériaux photocatalytiques plus adaptés, il est d'un intérêt fondamental de comprendre au niveau moléculaire l'interface aqueuse solide/liquide, où se produisent les réactions photocatalytiques, afin d'améliorer l'efficacité de la réaction. La charge de surface, la diffusion ionique et l'adsorption sont autant d'éléments qui peuvent avoir un impact significatif sur les vitesses de réaction et, dans le cas des nanoparticules, sur la stabilité colloïdale. Cependant, peu de techniques expérimentales sont capables de sonder la double couche électrique (angl. electrical double layer (EDL)) et ses propriétés particulières, notamment lorsqu'il s'agit de nanoparticules colloïdales directement dispersées en solution.

Dans cette thèse, nous appliquons la diffusion polarimétrique résolue en angle de la seconde harmonique (angl. angle-resolved second harmonic scattering (AR-SHS)) pour étudier l'EDL des particules d'oxyde colloïdal en milieu aqueux. Nous montrons d'abord l'applicabilité de l'AR-SHS sur un oxyde isolant bien connu, la silice (SiO_2). Nous étudions ensuite le dioxyde de titane (TiO_2), un oxyde métallique qui a été largement étudié pour des applications photocatalytiques au cours des cinq dernières décennies en raison de sa grande stabilité et de son faible coût. Les deux oxydes sont ensuite comparés. Nous montrons qu'à partir de nos mesures spécifiques de surface par l'optique non-linéaire, nous pouvons extraire le potentiel de surface des particules d'oxyde par rapport au reste de la solution et la susceptibilité de surface, comme mesure de l'orientation moléculaire interfaciale. Ceci peut être réalisé sans supposer une distribution de charge spécifique dans la double couche électrique, et donc sans employer un modèle tel que le modèle de Gouy-Chapman ou le modèle de Gouy-Chapman-Stern. Grâce aux mesures de mobilité électrophorétique, nous obtenons en outre le potentiel zêta des

Abstract

particules par rapport au potentiel de surface issu des mesures AR-SHS. Connaître le potentiel de surface, la susceptibilité de surface et le potentiel zêta nous permet d'établir une image au niveau moléculaire de l'interface particule d'oxyde/liquide en fonction de la force ionique et du pH.

Premièrement, nous apportons la preuve qu'une couche condensée d'ions hydratés se forme à l'interface aqueuse du SiO_2 amorphe de 300 nm de diamètre dans des conditions de pH élevé et à des concentrations élevées de NaCl ($\geq$ 1 mM). Le calcul des valeurs de densité de charge de surface basé sur nos valeurs de potentiel de surface mesurées et utilisant les modèles de Gouy-Chapman et Gouy-Chapman-Stern sont en bon accord.

Ensuite, nous étudions l'EDL des particules de TiO_2 amorphe de 100 nm de diamètre en fonction de la concentration en NaCl et du pH basique. Trois régions différentes en fonction de la force ionique peuvent être identifiées. Ces trois régions nous permettent de distinguer trois phénomènes avec l'augmentation de la force ionique. Tout d'abord, l'adsorption des ions en sphère interne (angl. inner-sphere) aux concentrations les plus faibles, puis la formation d'une couche diffuse de contre-ions et enfin, l'accumulation de contre-ions hydratés près de l'interface. Alors que tous ces phénomènes sont prédits par les modèles électrostatiques courants, nos données nous permettent de retrouver la structure électrostatique des interfaces aqueuses à chaque force ionique sans connaissance à priori de la distribution des charges, ce qui suggère que l'AR-SHS pourrait être appliquée à une variété de systèmes plus complexes. Des régions similaires sont observées pour les particules de TiO_2 en pH basique et les particules de SiO_2 de 100 nm de diamètre en fonction de la concentration en NaCl. On constate que la surface du TiO_2 a une affinité plus forte pour les ions Na^+ que celle du SiO_2.

Nous évaluons également les effets spécifiques des ions à l'interface aqueuse colloïdale du SiO_2 et du TiO_2 amorphe. L'ajout de NaCl, RbCl ou $CaCl_2$ à l'environnement aqueux entraîne des différences relatives du potentiel de surface et de l'évolution du réseau interfacial de liaisons H en fonction de la force ionique. Les variations relatives en fonction de la force ionique révèlent des préférences spécifiques à la surface et aux cations pour l'adsorption en sphère interne (angl. inner-sphere) et externe (angl. outer-sphere).

Enfin, nous démontrons que les mesures AR-SHS dans différentes conditions de pH peuvent être utilisées pour déterminer les pK_as de particules de TiO_2 anatase de 100 nm de diamètre. Nos données révèlent une corrélation entre le changement d'orientation des molécules d'eau interfaciale et les pK_as des groupes de surface du TiO_2. Ce travail montre que l'AR-SHS est un outil puissant pour découvrir la structure EDL des particules d'oxyde colloïdal, contribuant ainsi à une meilleure compréhension des processus interfaciaux importants pour une variété d'applications (photo-)catalytiques.

Mots-clés : interfaces solides/liquides aqueuses, oxydes, colloïdes, double couche électrique, potentiel de surface, orientation moléculaire, adsorption d'ions, optique non linéaire, génération de seconde harmonique, diffusion de la lumière

Contents

Contents

1 Introduction

1.1 Photocatalytic reactions at aqueous interfaces

In a photocatalytic process, a chemical reaction is accelerated through the absorption of light in a catalyst material. Some of those reactions would be difficult, if not impossible, to carry out in the dark. Photocatalytic reactions become increasingly important in our everyday life. For instance, photocatalysis emerged as promising technology in the context of environmental and energy applications for water decontamination, hydrogen production and the treatment of air pollutants. Moreover, some photocatalytic reactions promote favorable self-cleaning effects that are relevant for the production of industrial coatings, paints, textiles and glass with self-cleaning properties. In particular, heterogeneous photocatalysis at aqueous solid/liquid interfaces has proven useful for industrially relevant chemical transformations and became a key element in the present research challenge to find new methods that guarantee a safe and sustainable future energy supply. In this context, increasing attention has been drawn to solar fuels as an alternative to the depleting fossil fuels. Solar fuels represent a clean, CO_2 emission-free way to generate energy with the main advantage that the energy sources can be stored prior to usage, which is not the case for solar power using photovoltaics. Photo(electro)catalysis offers the possibility to produce solar fuels. As an example, in a photoelectrochemical cell (PEC) the principle of artificial photosynthesis is used to split water (H_2O) into O_2 and the chemical fuel H_2. The oxygen evolution reaction (OER) takes place at the anode/electrolyte interface and the hydrogen evolution reaction (HER) at the cathode/electrolyte interface respectively. It is the subject of ongoing research to realise highly efficient, low-cost water-splitting devices. Note that in this thesis we use photocatalysis as a general term to encompass all catalytic processes driven by light, including photoelectrocatalysis.

1.2 Engineering suitable photocatalyst materials - the case of TiO_2

One major goal is to find appropriate materials to increase the photocatalytic efficiency of interfacial chemical reactions to produce solar fuels. Amongst others, metal oxide materials

have emerged as promising candidates due to their suitable electronic properties for water-splitting and their stability in aqueous environments. Another major advantage of metal oxides is that they are naturally abundant and economically competitive in their synthesis. As the functional properties of metal oxides are largely dependent on the crystal structure, composition, doping and intrinsic defect level, their mechanical, electrical, chemical and optical properties can be tailored in the manufacturing process [1–4]. This tunability of metal oxides offers great assets for a variety of photocatalytic applications, thus explaining the ongoing interest in further developing and understanding these materials.

In the context of finding suitable materials for photocatalytic hydrogen production, the transition metal oxide titanium dioxide (TiO_2) is a widely investigated material and model system since it exhibits a generally favorable photocatalytic activity [5]. The first solar water-splitting cell was reported in Nature by Fujishima and Honda in 1972 [6] and used the n-type semiconductor TiO_2 as electrode material. Nevertheless, the overall performance of TiO_2 in the OER reaction is still limited, because the catalytic activity at the surface and the electronic transport are generally poor. Recombination processes of excited charge carriers and kinetic overpotentials cause the OER reaction to be inefficient. Furthermore, TiO_2 is a wide band gap semiconductor (band gap anatase $\sim 3.2\,\text{eV}$ [1, 7, 8]). This reduces the materials absorption capacity of solar light to the UV range. A considerable amount of research work has been done to further improve TiO_2 anodes for water-splitting applications. One approach is to sensitize the surface of the semiconductor material with the help of dye molecules [9–12] or dopants [13–16]. This can improve the charge carrier separation efficiency and the absorption abilities in the visible light range.

Another important aspect to note is that the three different polymorphs of TiO_2 (anatase, rutile and brookite) are known to differ in their photocatalytic performance [1, 8, 17–22]. Despite the slightly lower band gap of rutile (band gap rutile $\sim 3.0\,\text{eV}$ [8, 17]) and thus better absorption properties for solar light, anatase TiO_2 is generally considered to be the most efficient crystal structure for photocatalysis, compared to brookite and rutile [1, 17, 20, 21]. One of the possible reasons for this behavior is the longer lifetime of charge carriers in anatase TiO_2, which could originate from the indirect band gap nature of anatase [17]. In comparison, rutile and brookite appear to be direct band gap semiconductors, which could cause faster recombination of charge carriers [17]. However, several works also pointed to the more favorable photocatalytic properties of brookite compared to anatase and rutile [19, 23, 24]. Which material really shows the highest catalytic performance highly depends on the experimental conditions and is therefore still under debate amongst scientists. In order to improve the photocatalytic activity of TiO_2 materials in the OER, mixed phase materials have been put forward to combine the most favorable properties of each crystal structure [25–27]. A prominent example for mixed phase catalysts are P25 nanoparticles which are a mixture of anatase and rutile TiO_2. Some research groups also report a fraction of amorphous TiO_2 in those particles [28, 29].

1.3 The special properties of nanomaterials

Other than the intrinsic properties of the material, the specific surface structure and morphology of the catalyst plays an important role for its performance in the OER. For example, nanostructuring the surface that is exposed to the electrolyte in an electrochemical cell leads to an extended surface area. This can increase the efficiency of the catalytic reaction by providing more reaction centres at the surface. That is why a strong research interest has emerged around nanomaterials for photocatalytic applications in the last decades. Nanomaterials exhibit a typical size of tens to hundreds of a nanometer (1 nm = 10^{-9}m). Nanosized systems display special properties compared to bulk materials due to their large surface area and thus high surface to volume ratio. The optical and the electrical properties can differ significantly between different types of nano-objects. In particular the size and shape of nanoparticles strongly determines their physical and chemical properties [30–34]. The characteristics of nanoparticles are also greatly related to the synthetic procedure [2–4]. Indeed, for instance the solubility in water or the abilities to absorb or scatter light can exhibit large differences. This flexibility in the properties of nanoparticles enable their taylored design for a specific application. In the case of photocatalytic applications, one main advantage of nanoparticles is that their surfaces are tunable through the use of dopants, ligands or dye molecules offering a great potential to improve the materials efficiency, stability and performance. This makes them a relevant and important system to study in the quest to develop better renewable energy conversion and storage systems, including the ongoing research challenge to find better materials for solar water splitting applications.

1.4 The influence of the aqueous environment

One further noteworthy point regarding the improvement of the overall OER efficiency and other photocatalytic processes is the non-negligible role of the aqueous environment. The composition of the electrolyte can have a major impact on catalytic surface reactions [35–41]. For instance it was observed that the photocatalytic activity is strongly pH dependent [35, 36, 39, 42]. The exact optimum environmental conditions for the OER are material specific. In addition, the ionic strength of the aqueous environment and the type of salt can have an impact on the photocatalytic performance [36]. More specifically, e.g. in the case of waste water treatment, the ionic species present in the solution can have an effect on the photocatalytic degradation of certain pollutants [43, 44]. In particular, surface charge, adsorbed ionic species and diffusion of chemical species to the surface are all factors that can strongly influence reaction rates and in the case of nanoparticles, the colloidal stability. In order to exploit the promising capabilities of metal oxide materials for photocatalytic applications such as solar water splitting or photocatalytic waste water treatment, it is therefore of fundamental interest to understand the solid nanoparticle/liquid interface on a molecular level.

In the following we want to introduce some major properties of the nanoparticle/liquid interface and common models describing the aqueous particle interface. Furthermore we

give an overview of techniques that are used to study the interfacial properties of colloidal systems in aqueous environments on a microscopic level. In this context we discuss how this work contributes to a better understanding of nanoparticle/liquid interfaces.

1.5   The nanoparticle/liquid interface

When a charged particle is in a solution, oppositely charged ions in the solution approach the particle surface. Figure 1.1 illustrates this phenomenon of surface charge screening for the example of a negatively charged oxide particle surface. In this case positively charged
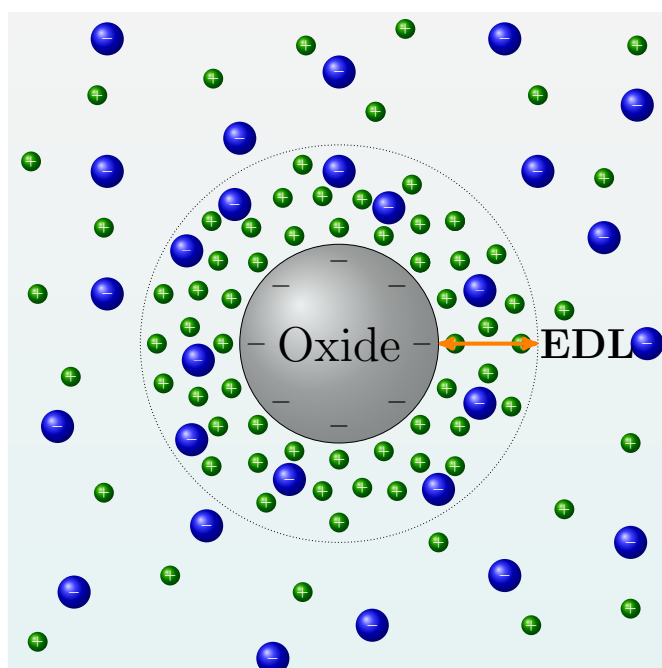
Figure 1.1 – Schematic illustration of the electrical double layer (EDL) of a negatively charged oxide particle in a solution that contains ions. Positively charged counter-cations are displayed in green, negatively charged anions in blue.

counterions accumulate close to the interface. As a result, an electrostatic field E_{DC} is generated between the negatively charged particle surface and the positively charged counterions. The region where E_{DC} is present is called the electrical double layer (EDL). It comprises the charged particle surface and the ionic aqueous environment around the particle, screening the surface charge. A potential $\Delta\Phi_0$ decays from the particle surface into the surrounding liquid until the imaginary boundary of the double layer where an equal distribution of positively and negatively charged ions in the bulk liquid is reached. The ionic atmosphere around the particle in the EDL is composed of water molecules, counterions and co-ions as displayed in Figure 1.1. Yet the exact distribution of charges in the EDL is the subject of current research. A complete microscopic picture of the EDL, especially in the case of colloidal systems, is difficult

to obtain experimentally and therefore remains elusive. Current descriptions rely on the use of simplified electrostatic models for the EDL. In the following we want to give an overview of some of the most commonly used EDL models. A graphic illustration of those EDL models can be found in Figure 1.2 where a negatively charged oxide surface in contact with an aqueous solution that contains ions is displayed. The spherical particle surface is approximated by a flat surface and no anions are shown for simplicity.

1.5.1 Helmholtz double layer

In the so-called Helmholtz double layer (Fig. 1.2 A), the surface charge screening described above is visualized by counterions placed at a fixed distance d from the oppositely charged surface. This distance d is often approximated by the radius of the counterions. Since the situation of a rigid layer of ions at a fixed increment d away from the particle surface resembles a capacitor, the Helmholtz double layer model is also referred to as constant capacitor model. As in the case of a capacitor, the potential decays linearly between the particle surface and the layer of ions. In this picture, the amount of negative and positive charges on each side of the capacitor is equal. The capacitance only depends on the dielectric permittivity ε of the medium and the distance d between the ions and the surface. The Helmholtz double layer model was proposed in the year 1853 by Hermann von Helmholtz [45]. It is a strongly simplified model of the EDL which assumes rigid layers of opposite charges [46]. For instance it does not take into account changes in the surface charge density that can occur due to ion adsorption nor changes in the aqueous environment due to diffusion of ions in solution. Therefore it can not explain all the complex dynamic interactions that can occur in the EDL region. To account for more dynamic interactions another model was put forward which is explained in the next section.

1.5.2 Gouy-Chapman model

Luis Georges Gouy and David Leonard Chapman in 1910 and 1913 independently developed an EDL model that does not speak of a constant capacitance between the charged surface and the counterions in solution [47, 48]. The so called Gouy-Chapman (GC) model (Fig. 1.2 B) additionally considers the effect of electrical fields and thermal motion on the ions [49]. The charge distribution of ions close to a charged surface as a function of distance from that surface can then be described by Boltzmann statistics [46, 49, 50]. In this model the counterions are not seen as rigidly held but form a diffuse layer in the liquid phase close to the charged surface. A distribution of positively and negatively charged mobile ions is considered in the EDL. The interfacial potential decays exponentially between the particle surface and the bulk liquid phase according to the Poisson-Boltzmann equation. An approximate thickness of the EDL is given by the Debye length [51] which is a measure of the penetration depth of the electrostatic field into the solution. In the potential landscape drawn in Figure 1.2 B, C and D, another potential is shown, which is known as the zeta potential (ζ). ζ is the potential at the shear plane (also referred to as slipping plane) of the particle with respect to bulk liquid.

This plane marks the boundary between the hydrated ions and water molecules moving with the particle when an electric field is applied and the rest of the solution. A more detailed explanation of the zeta potential is given in section 2.4.2. The zeta potential is an important and frequently used tool for the characterization of charged interfaces. This is why we show it in Figure 1.2 B, C and D together with the surface potential, even though it is not included in the traditional description of the presented EDL models. In the GC model the ions are considered as point charges thus not experiencing any physical limit to approach the surface [52]. In general the GC model is considered to be a good description of the EDL in the limit of low ion concentrations and small excess charge densities [50].

1.5.3 Gouy-Chapman Stern model

In order to account for the physical limits of ion approach to the surface, Otto Stern modified the Gouy-Chapman model. He proposed in 1924 to combine the concepts of the Helmholtz and the Gouy-Chapman model [53]. In the so-called Gouy-Chapman-Stern (GCS) model (Fig. 1.2 C) an almost immobile Stern and a mobile diffuse layer are considered [51]. Within the Stern layer, the ions are seen as objects with a finite size thus restricting their approach to the charged surface. A part of the ions are therefore accumulating close to the surface at a distance of a few angstroms to a few nanometers. This distance between the surface and the Stern plane is often approximated to the radius of the ions [46]. Inside the Stern layer the potential decays linearly. According to the Gouy-Chapman-Stern model, the remaining ions form a diffuse layer. In this region between the Stern layer and the bulk liquid, where anions and cations are distributed equally, the potential decays exponentially. The overall surface potential Φ_0 is composed of the potential drop in the Stern and in the diffuse layer ($\Delta\phi_{\text{Stern}}^{\text{drop}} + \Delta\phi_{\text{diffuse}}^{\text{drop}}$). In the practical use of the GCS model, the slipping plane is often approximated to the Stern plane for simplicity. The GCS model comes with its own limitations. Like in the GC model, the ions in the diffuse layer of the GCS model are treated as point charges. In addition, the GCS model does not account for all kinds of intermolecular diffuse layer interactions nor the direct adsorption of partially or fully dehydrated ions to the surface. It therefore remains a simplified model of the EDL. Despite these limitations, the GCS model is in general accepted as a good description for highly charged EDLs. For the limit case of very high salt concentrations, the GCS model becomes similar to the Helmholtz double layer model.

1.5.4 Grahame model and other electrical double layer (EDL) descriptions

In 1947, David C. Grahame proposed a modification of the Gouy-Chapman-Stern model in order to take into consideration that ions can not only adsorb at the surface with their intact hydration shells but that they can penetrate the Stern plane to specifically adsorb at the surface [54]. This process implies a full or partial loss of the ion's hydration shell. Such a direct ion adsorption is also termed „inner-sphere"adsorption. Two inner-sphere adsorbed ions are schematically displayed in Figure 1.2 D. Grahame proposed the concept of an Inner-Helmholtz plane which passes through the centres of those specifically adsorbed ions. In this picture,
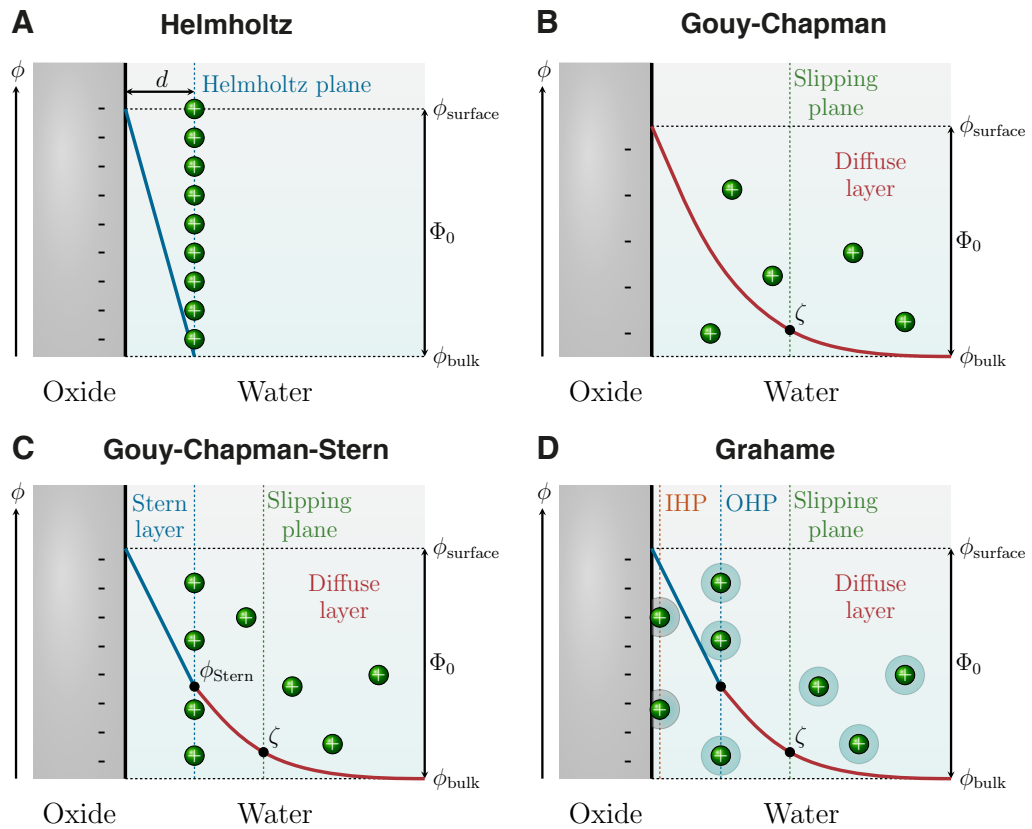
Figure 1.2 – Schematic illustration of the electrical double layer (EDL) in (A) the Helmholtz, (B) the Gouy-Chapman (GC), (C) the Gouy-Chapman-Stern (GCS) and (D) the Grahame model. A negatively charged particle surface in a solution that contains ions is displayed. The particle surface is approximated by a flat surface. Positively charged counter-cations are shown in green. No anions are shown for simplicity. The potential is plotted over the distance from the surface. The ζ potential is the potential at the shear plane, also referred to as slipping plane, of the particle with respect to bulk liquid. The surface potential Φ_0 is the potential difference between the particle surface ($\phi_{surface}$) and bulk liquid (ϕ_{bulk}). ϕ_{Stern} is the potential at the Stern plane. Within the Helmholtz and the Stern layer, a steep linear potential drop is expected, whereas an exponential decay of the potential within the diffuse layer region is expected according to the GC or GCS model. In the illustration of the Grahame model, the ion hydration shells are indicated as darker blue regions around the ions. Through the center of the inner-sphere adsorbed ions at the surface passes the Inner Helmholtz Plane (IHP), and through the center of the outer-sphere adsorbed ions passes the Outer Helmholtz Plane (OHP). The latter is comparable to the Stern plane.

an Outer-Helmholtz plane passes through the centres of ions that undergo solvent-separated adsorption. This Outer-Helmholtz plane is similar to the Stern plane. Solvent-separated adsorption is also referred to as „outer-sphere“adsorption. Like in the Gouy-Chapman-Stern case, a diffuse layer is envisioned starting from the Outer-Helmholtz plane and extending to the bulk liquid where an even distribution of positive and negative charges is reached.

In the past years, many other models describing the EDL properties were put forward [55, 56]. All of them were aiming for a more accurate representation of physical and chemical phenomena occuring in the EDL. As an example, Brockris et al. [55] included the behavior of solvent molecules close to the charged surface into their EDL model. The authors considered the effect of the electrostatic field on the solvent molecular orientation inside the Stern layer. The different orientations of solvent molecules in specific EDL regions, e.g. in the IHP and OHP, can cause variations of the dielectric permittivity inside the EDL [51]. Another, more pragmatic approach is to separate two regions of different permittivity in the EDL confined by the Stern and the diffuse layer region [57, 58].

It appears that the charge distribution and the dynamic molecular interactions in the EDL are difficult to describe in their full complexity by the aforementioned models. In particular, the effect of a change in the interfacial electrostatics on photocatalytic reaction mechanisms remains poorly understood. Therefore it is of high importance to find suitable model systems and experimental techniques to unravel the complex mechanistic details of the EDL.

1.6 SiO_2 as a model system

One model system that is often used in the context of exploring the convoluted structure of the EDL is silica (SiO_2) [41, 59–64]. Because this material is an insulating oxide, with a wide band gap of $\sim 9\,eV$ [65], no absorption of light in the visible range is expected. Compared to semiconductor materials as they are often used for photocatalysis, no light-induced charge transfer reactions from the solid to the liquid phase or vice versa needs to be taken into account. This makes silica a relatively simple oxide material which additionally scores points due to its natural abundance and the advantage of being producible in a relatively controlled manner on a larger scale. As SiO_2 possesses the same potential-determining ions at its surface with regard to the metal oxide TiO_2, it can serve as an excellent comparison to this or other photocatalytic materials. In this regard, a deeper understanding of the SiO_2/aqueous interface can help to deconvolute the complexity of other metal oxide/liquid interfaces.
In catalytic experiments, SiO_2 can be used as a support material for metal- or metal oxide-catalysts [66]. In general reducible oxides are considered to be catalytically active, whereas irreducible oxides are considered to be inert supports. Used as support material for metal- or metal oxide- catalysts, the irreducible oxide material SiO_2 shows a lower metal-support interaction compared to reducible oxides like TiO_2 [67, 68]. This behavior can be strategically used or customized in order to tune the catalytic activity for a specific application.

1.7 Experimental techniques to study the EDL of colloids

It remains difficult to investigate the solid/liquid interface at a molecular level [69, 70]. In the following we want to give an overview of some techniques that are commonly used to access different characteristics of the EDL. First of all, one needs to distinguish between studies

on flat surfaces vs particles. For flat surfaces, there are several well-established techniques to probe the molecular properties of the solid/liquid interface [69]. However here we want to solely focus on techniques that can be used to study the EDL of particles in an aqueous solution since those are the main focus of this thesis. In the case of nanoparticles, probing their liquid interface remains a challenge. Not many experimental techniques are able to access the molecular structure of their EDL or can only probe part of the complex structure of the EDL.

One method that is often employed for nanoparticles measures the electrophoretic mobility. A more detailed description of this technique and how it was used in this thesis can be found in chapter 2.4.2. In electrophoretic mobility measurements, an electric field is applied to the particle suspension, so that the charged particles move to the electrode of opposite charge. The velocity at which they move can be related to the ζ-potential, which was introduced earlier in this chapter. However this technique only provides information about the potential a few nanometers away from the surface [57, 71, 72] and does not provide information about the whole potential landscape around the particles. Yet it is a useful tool to get information on the stability of particles and can serve as a valuable addition to more direct surface charge or surface potential measurements.

To measure directly surface charge densities, a common method is acid-base potentiometric titration [73–78], where an initially acidic colloidal suspension is titrated with a base, or the other way around. In this case the potential-determining ions H^+ or OH^- at the colloidal surface are consumed by the addition of base or acid. The initial surface charge density is related to the net uptake or release of H^+ or OH^-. This uptake or release can be related to the added concentration of the titrant while additionally taking into account the volume of the titrant in a solution that does not contain particles. To determine the surface charge, the specific surface area of the solid, the mass concentration of the solid and the volume of the solution need to be known [73]. In general potentiometric titrations require a high amount of sample (in the order of hundreds of miligrams). Since the surface charge is obtained through the uptake or release of ionic species to or from the surface, this technique is specifically sensitive to acid or base impurities of the sample. It also assumes that the sample is non-porous and that the ions only adsorb at the particle surface. This is why the surface charge as obtained from potentiometric titrations can be regarded as an upper limit for the surface charge but does not represent the exact surface charge of the particles [73, 79–81].

A more direct measure of the electrostatic environment around charged particles in a solution is the surface potential. A common method to study solid/air or solid/vacuum interfacial potentials on planar surfaces is Kelvin probe force microscopy (KPFM), which is a form of contactless atomic force microscopy (AFM) [82–84]. In this case, a conducting metal tip is used to scan the solid material surface and the work function difference between the two is defined as the surface potential. One major advantage of this technique is its high lateral resolution whereas many other techniques usually provide spacially averaged information on interfacial surface properties [84, 85]. However, probing the solid/liquid interface with KPFM comes with major practical challenges [85–87]. Complex diffuse charge dynamics in a broad spectrum of timescales in ionically active aqueous environments complicate the establishment of suitable

KPFM, or more broadly, AFM based techniques [86–90]. For instance, traditional measurement methods that are well established for operation in ambient or vacuum conditions can exhibit limitations for a clean detection of the liquid response [86, 90]. In addition, the detected response can be distorted by electrochemical reactions at the Kelvin probe electrode or bubble formation at the sampling tip [90]. The occurrence of those phenomena is highly dependent on the investigated material and the molarity of the aqueous environment which sets limits for the conditions of a specific experiment [85, 90]. Amongst others, disturbing parasitic currents between the probing tip and the sample electrode originating from the (partially) conducting liquid medium where reported [90]. One can conclude that overall it remains challenging to apply KPFM and AFM based methods for surface potential measurements in aqueous environments [90]. It is particularly difficult to apply KPFM to nanoparticles in a solution. A recent study has shown that KPFM combined with a graphene-capped electrolytic cell can be used to quantitatively study the potential drop across the EDL in aqueous environments in decimolar and molar electrolyte concentrations [85]. In the same work, the authors apply KPFM to alumina nanoparticles attached to a monolayer graphene membrane. It must be noted that in order to study colloids, usually a support material is needed or the spherical particles are attached to the cantilever directly [91–93].

Another method that allows the study of the surface potential of colloidal particles in aqueous environments is X-ray photoelectron spectroscopy (XPS). In a recently developed experiment, particles are investigated in a liquid microjet, which delivers a free-flowing suspension of colloids that is placed in the beam path of a synchrotron radiation source [94–98]. In liquid-microjet XPS, the surface potential is obtained from the binding energy difference between electrons on deeper electronic levels of the material taken at the solution pH of the point of zero charge (PZC) and at a particular salt concentration of the aqueous environment, both divided by the elementary charge. For instance for silica particles one detects photoelectrons from the Si 2p shell. Since the colloidal suspension can not be measured at the point of zero charge directly, the corresponding binding energy is inferred from an extrapolation of measurements performed in different pH conditions and at a constant ionic strength [94]. The authors argue that any uncertainty in the interpolation of the point of zero charge will have a minor influence on their absolute surface potential values given that the surface charge density or surface potential are negligible in the pH window around the PZC [94]. For small-sized particles (< 10 nm) and at high ionic strength, in a regime where a Stern layer is present, this method allows to get valuable insights into the EDL of colloids. However, liquid-jet XPS experiments can be particularly challenging to conduct on nanoparticle suspensions in lower ionic strength conditions due to the low signal-to-noise ratio. Another aspect is that millimolar salt concentrations are needed to reduce photoionization charging effects [99] thus preventing the investigation of colloidal aqueous interfaces at lower salt concentrations. In order to shed light on interfacial processes occuring in the lower ionic strength regime and to complete our understanding of the EDL of colloidal particles over a broad ionic strength range, there is the need for new techniques that are applicable in low salt environments. In particular, setups that can work in ambient conditions and that do not require vacuum conditions or synchrotron facilities are of high interest.

Second-order nonlinear optical techniques are suitable to study processes at surfaces and interfaces of centrosymmetric systems due to the fact that second harmonic generation (SHG) is forbidden in centrosymmetric structures and therefore the signal arises only from the non-centrosymmetric regions at the interface [100–104]. A more complete description of the origin of the second harmonic signal is given in chapter 2.2. Indeed, nonlinear optical techniques such as second harmonic generation (SHG) and sum-frequency generation (SFG) have proved to be particularly applicable for the investigation of both flat and curved solid/liquid interfaces [105–109]. One major advantage of second-order nonlinear optical techniques compared to other methods is that they are relatively low cost and non-invasive. Those methods allow the study of solid materials but also living biological systems in aqueous environments without destroying their structure and functionality [110–112]. In recent years second harmonic scattering techniques have emerged as promising tools for the study of surface potentials and interfacial water order at the colloidal particle/liquid interface [113–116], especially, but not exclusively, in the low ionic strength regime. In the following we want to give a brief historical overview of previous work on second harmonic scattering and its potential to help decipher the EDL structure of particles dispersed in an aqueous solution.

1.8 Previous work on second harmonic scattering from colloids

Nonlinear, second-order scattering was firstly used to obtain information about the surface chemistry of particles in liquids by the Eisenthal group [117]. The same group later applied their second harmonic scattering (SHS) technique to study an interfacial charge-transfer complex (dye sensitization) on TiO_2 particles in an aqueous suspension [118]. Note that the original technique was set up to measure in the forward scattering direction only, therefore not containing any angular information.

With the aim to get deeper insights into the surface properties of various kinds of materials and interfaces, the SHS theory and experimental techniques have been further developed over the years. In 2001, Yang et al. [119] were the first to measure resonant angular-resolved second harmonic scattering (AR-SHS) patterns from polystyrene colloids with surface-adsorbed malachite green in water. The angular dependent scattering holds information on the physical and chemical processes in the medium and the size and shape of the particles [119–124]. In 2010, the development of a non-resonant AR-SHS technique was demonstrated on uncoated polystyrene particles in an aqueous suspension [115]. In this case, the SH signal originates from oriented water molecules at the particle interface [115]. A more detailed definition of resonant vs nonresonant SHG is given in section 2.2.

To theoretically describe nonlinear light scattering several different approximations have been used, such as the Rayleigh-Gans-Debye (RGD) approximation [119, 125–130], the small particle (electrostatic) limit [127, 130–132], and the small index contrast (Wentzel-Kramers-Brillouin (WKB)) limit [127, 133]. As a more exact theoretical model for scattering from spheres, nonlinear Mie-theory (NLM) has been proposed [115, 134, 135]. In 2004, Roke et al. [127] introduced the concept of effective particle susceptibility, making use of symmetry

relations that facilitate the theoretical treatment of nonlinear optical scattering. This approach enables the prediction of the allowed and forbidden polarization combinations (selection rules) considering the surface and bulk symmetries of the scatterers as well as the experimental geometries. In this context, second-order and effective third-order susceptibilities can be distinguished. These quantities describe the local non-linear response of the medium to the incoming electromagnetic fields (second-order) and additionally a static electromagnetic field E_{DC} present in the medium (effective third-order) that is generated between the ions in solution and a charged surface (see chapter 2.3.1 for a more detailed explanation). It has been shown by de Beer et al. [136] that second-order and effective third-order scattering effects, represented by the effective particle susceptibilities, can be separated, due to their specific contribution to the angular radiation patterns.

These theoretical developments laid the foundation to applying second-harmonic nonlinear optical methods for surface potential determination at the colloidal aqueous interface. It was already proposed by Ong et al. in 1992 that SHG can be used to measure the surface potential at planar solid/liquid interfaces [137]. Ong et al. investigated a planar fused silica/water interface in reflection mode and reported absolute values for the surface potential (potential between a charged surface with respect to bulk water) at different pHs. The authors measured the SH field when the static field E_{DC} is zero (at the isoelectric point, when the surface is uncharged) in order to separate the second-order and effective third-order scattering contribution, which then allows for the determination of the surface potential. A first attempt to apply this idea to particles in a solution was undertaken by Yan et al. [138]. The authors measured SHG of polystrene sulfate spheres in the forward scattering direction and extracted the surface potential by fitting their data to the Gouy-Chapman model, approximating the curved surface of their microscopic particles (diameter $\sim 1\,\mu$m) to a planar surface.

As another important contribution to the SHS theory, it was shown by Gonella et al. [113] (Roke group) that the SHG from aqueous interfaces is modulated by interference. This effect is caused by reoriented water molecules affected by the presence of the surface electrostatic field E_{DC}. It is strong for aqueous environments with an ionic strength $< 10^{-3}$ M [113]. Gonella et al. pointed out that a broader range of parameters can be varied measuring SHS from particles compared to SHG from planar surfaces in reflection or transmission mode. In particular the polarization state of light strongly influences the shape of the angle-resolved patterns [113, 139]. The authors highlight that measuring AR-SHS in two independent polarisation combinations allows the determination of absolute values for the surface potential Φ_0 and the remaining nonzero susceptibility element $\chi^{(2)}_{s,2}$ [113, 114]. The latter is a measure of surface molecular orientation. By fitting the AR-SHS patterns with a procedure that takes into account this SHS theory for spherical particles as it is described in Gonella et al. [113], and using the knowledge that second-order and effective third-order scattering effects can be separated [136], the surface potential Φ_0 can be extracted without making assumptions on the exact structure of the EDL [113, 114]. Thus, the charge distribution close to the interface does not need to be known to obtain Φ_0. The fitting procedure is described in more detail in Luetgebaucks et al. [114] and in chapter 2.3.1. These recent developments opened up new ways to study the EDL of colloidal particles in suspension.

1.9 This thesis

The high throughput nonresonant AR-SHS technique developed in the Roke lab [116] has so far been used to investigate oil droplets, liposomes, lipids and other biological samples [113, 114, 140, 141]. In this work we apply AR-SHS for the first time to solid oxide particles in a solution. As a starting point we chose to investigate SiO_2, a material which is often studied as a representative for other oxide/liquid interfaces. The second material of choice investigated in this study is TiO_2, a common model metal oxide for photocatalytic applications. In the case of TiO_2 we probe amorphous but also crystalline particles, such as anatase, which is the most commonly used crystal structure for water-splitting applications as it is considered to have a higher photocatalytic activity than rutile TiO_2 [1, 17, 20, 21, 142]. Colloids of 100 nm to 300 nm diameter size of both materials in aqueous solutions are measured using AR-SHS. Due to the size range of the investigated particles, i. e. nanosized particles, the terms colloid, particle and nanoparticle are often used interchangeably throughout this thesis.

We systematically vary pH and salt concentration to modify the surface charge density and the structure of the EDL. By measuring AR-SHS we extract the surface potential Φ_0 and the surface susceptibility element $\chi_{s,2}^{(2)}$, as two unique parameters. This allows us to get deeper insights into how the EDL properties are changing as a function of pH and ionic strength. The point of zero charge (PZC) of TiO_2 is reported to be in between pH 3.8 and pH 6 [143–145] and depends on the crystalline phase. At this point we expect the surface charge density to change from positive (protonated hydroxy groups) for pH < PZC to negative (deprotonated hydroxy groups) for pH > PZC. In the course of this thesis, we investigate how modifications of the surface charge density or simply of the aqueous environment influence the orientation of the water molecules in the EDL as well as the surface potential. We gain valuable insights into material specific interfacial processes such as ion adsorption, the formation of a condensed layer of charges or diffuse layer formation. We specifically address changes occuring in low ionic strength environments that are difficult to access with other techniques. We further compare our findings with common models that are used to describe the EDL such as the Gouy-Chapman and the Gouy-Chapman Stern model.

In addition we investigate ion-specific effects occuring at the SiO_2 and TiO_2 aqueous interface. We analyze the effect of different salts on the two surfaces, in particular their surface potentials and interfacial water orientation. We uncover how different ion sizes, different ion charge (monovalent vs divalent) and their hydration shells and hydration energies play into the formation of the EDL under a variation of the ionic strength. Since the EDL properties have a major impact on the stability of colloidal systems in general, we expect this work to be of high interest with regard to a broad variety of applications. In particular it contributes to a better understanding of the electrostatic structure of the liquid interface around metal oxide colloids for photocatalytic applications.

This thesis is organized in six chapters as follows:

- **Chapter 2** contains a general introduction to nonlinear optical effects and second harmonic generation. An in-depth description of the polarimetric AR-SHS technique and complementary methods, such as dynamic light scattering and electrophoretic mobility measurements used to study colloidal particles in suspension is provided. The general sample preparation and characterization procedure is explained. More specific experimental details can be found in the Materials and Methods section of each chapter.

- In **Chapter 3** we apply AR-SHS to 300 nm SiO_2 particles in solutions of different NaCl concentrations and in various pH conditions. We extract the surface potential and second-order surface susceptibility and show that a condensed layer of ions is formed in the high pH case and at higher NaCl concentrations (≥ 1 mM). From surface potential values we compute the surface charge densities using the Gouy-Chapman and Gouy-Chapman-Stern models. Molecular dynamics (MD) simulations confirm the experimental trends.

- In **Chapter 4** we study the surface potential and surface susceptibility as obtained from AR-SHS measurements of 100 nm TiO_2 particles in different basic pH and ionic strength conditions. We find three regions of different behavior with increasing NaCl concentration: inner-sphere adsorption, diffuse layer and condensed layer formation. Similar regions of behavior are observed for 100 nm SiO_2 particles. In comparison the TiO_2 interface has a higher affinity for Na^+ ions, which we further confirm with MD simulations.

- In **Chapter 5** we discuss ion-specific effects at the SiO_2 and TiO_2 nanoparticle/aqueous interface. We apply AR-SHS to 100 nm particles in different salts: NaCl, RbCl and $CaCl_2$; and determine the surface potential and second-order surface susceptibility. Relative differences as a function of ionic strength demonstrate cation- and surface-specific preferences for inner- vs outer-sphere adsorption. MD simulations support the experimental conclusions.

- In **Chapter 6** we quantify the pK_as of 100 nm anatase TiO_2 particles by employing AR-SHS measurements at different pH conditions. The surface potential and surface susceptibility together with the zeta potential are used to capture the EDL structure as a function of pH clearly indicating a relationship between the change in orientation of surface water molecules and the pK_as of anatase TiO_2.

- **Chapter 7** contains a summary of the results presented in this thesis and an outlook highlighting opportunities for future work.

2 Theoretical background, methods and experimental details

2.1 Nonlinear optical effects

Nonlinear optical effects arise from the nonlinear polarizability of a material in the presence of an intense electric field. When an electromagnetic wave of sufficiently high power interacts with a medium it can distort the electron clouds of the atoms present in the medium. These induced charge oscillations generate molecular dipole moments $\mathbf{p}$ in the molecule i which can be expressed as

$$\mathbf{p}_i = \beta^{(1)} \cdot \mathbf{E} + \frac{1}{2!} \beta^{(2)} : \mathbf{EE} + \frac{1}{3!} \beta^{(3)} \vdots \mathbf{EEE} + \dots \tag{2.1}$$

where $\beta^{(1)}$, $\beta^{(2)}$ and $\beta^{(3)}$ are the first-, second-, and third-order hyperpolarizability, respectively [146]. While the first-order hyperpolarizability term describes the induced dipole moment that is linearly dependent on the electromagnetic field $\mathbf{E}$, the remaining higher-order terms describe the nonlinear molecular polarization only occuring at higher field strengths. The hyperpolarizabilities are molecule-specific properties that are highly dependent on the molecular symmetry, the bonding characteristics and the electron charge distribution. A molecule's ability to undergo second- and third-order nonlinear optical effects is given by the magnitudes of $\beta^{(2)}$ and $\beta^{(3)}$, respectively. The molecular polarizabilities can be related to the macroscopic polarization $\mathbf{P}$ by

$$\mathbf{P} = N \langle \mathbf{p}_i \rangle \tag{2.2}$$

where $\langle \mathbf{p}_i \rangle$ is the sum of induced molecular dipoles per unit volume and N is the number of molecules. The nonlinear macroscopic polarization of a material arising as a result of an interaction with a strong electromagnetic field is defined as

$$\mathbf{P} = \varepsilon_0 \left[\chi^{(1)} \cdot \mathbf{E} + \chi^{(2)} : \mathbf{EE} + \chi^{(3)} \vdots \mathbf{EEE} + \dots \right]. \tag{2.3}$$

In this expression, ε_0 is the vacuum permittivity and $\chi^{(1)}$ is the linear susceptibility that corresponds to the macroscopic polarization of the medium at low $\mathbf{E}$-field intensity. $\chi^{(2)}$ and $\chi^{(3)}$ are the second- and third-order susceptibility tensors describing the macroscopic nonlinear optical properties of the material as a response to the strong incoming $\mathbf{E}$-field.

2.2 Second harmonic generation (SHG)

In a second harmonic generation (SHG) process, two photons of the same frequency ω interact with a medium and generate a new photon with twice the frequency 2ω. This process can be resonant or nonresonant with the energy levels of the molecules in the medium. In resonant SHG a molecule is excited from the ground state to a molecular state. In this case, the incoming frequency ω or the newly generated sum frequency 2ω is close to a molecular energy state [110, 147, 148]. If a second harmonic generation process is nonresonant, none of the involved frequencies coincides with energy level differences of the molecule and the molecule is excited from the ground state to a virtual state. Figure 2.1 schematically illustrates resonant and nonresonant SHG. As a consequence of the characteristic energy level positions
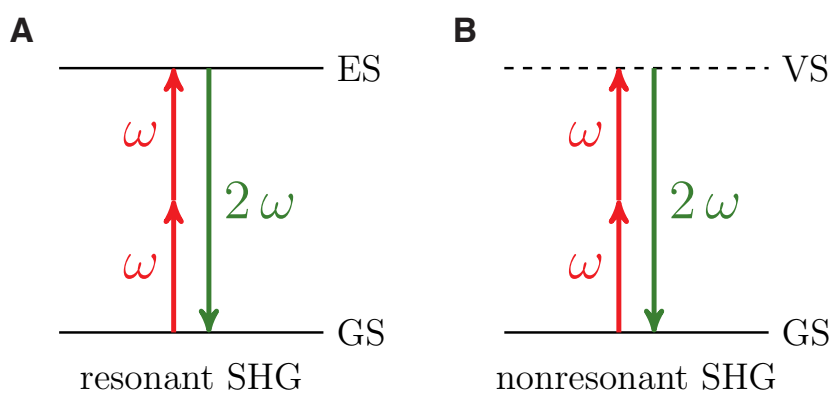
Figure 2.1 – Schematic illustration of resonant and nonresonant SHG. Two photons of frequency ω excite a molecule from the groundstate GS (A) to a molecular energy state ES (resonant SHG) (B) to a virtual state VS (nonresonant SHG) leading to the emission of a second harmonic photon with twice the frequency 2ω

of a specific molecule, a resonant SHG experiment is sensitive to the chemical nature of the sample. It can be used to probe these characteristic energy transitions which represent a molecular fingerprint of the studied material. When the frequency ω or 2ω are in resonance with molecular energy levels the second harmonic signal is enhanced. In contrast, the signal in a nonresonant SHG experiment is less intense since it is not exciting any molecular states. It is possible to carry out SHG experiments in different geometries. SHG can be performed on planar surfaces in reflection mode (Fig. 2.2 A) or in a scattering configuration (Fig. 2.2 B). The latter is particularly suitable to investigate objects with curved surfaces, such as e.g. colloids, since this technique is not bound to planar sample geometries. That is why second harmonic scattering (SHS) is primarily used to study particles or droplets in a solution. It can additionally be employed to investigate bulk liquids.

SHG experiments are known to be particularly surface sensitive, which allows to study interfacial properties that are difficult to access by other techniques. This is possible because the SHG process is forbidden in the bulk of centrosymmetric media due to symmetry selection rules that apply to the second order susceptibility tensor $\chi^{(2)}$. As a consequence, SHG occurs
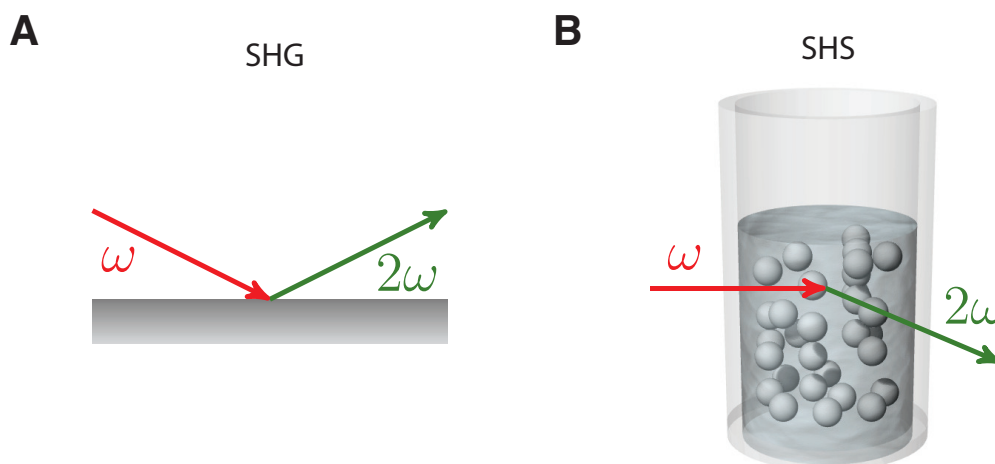
Figure 2.2 – Second harmonic generation (SHG) in (A) reflection mode and (B) scattering configuration, also referred to as second harmonic scattering (SHS).

only in the non-centrosymmetric regions of a probed sample. Considering a material with an isotropic interior in an isotropic medium the SH signal arises only from the interfacial region where the centrosymmetry is broken. This makes SHG a powerful tool to study surfaces and interfaces on a molecular level.
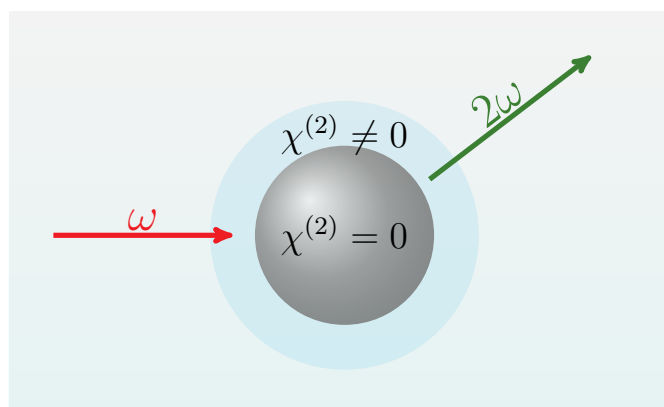
Figure 2.3 – Nonresonant second harmonic scattering (SHS) from a particle with an isotropic interior in water (here considered as an isotropic liquid). $\chi^{(2)}$ is the second order susceptibility, which is equal to zero in an isotropic material due to symmetry rules. As a consequence the scattered SH light arises only from the non-centrosymmetric particle/liquid interfacial region where $\chi^{(2)}$ is non-zero. The incoming electromagnetic wave has a frequency of ω which leads to SHS light with a frequency of 2ω.

The surface sensitivity of SHG is schematically shown in Figure 2.3 for a nonresonant experiment in scattering configuration. In this scenario the SH light is collected from the interfacial region of a particle in water, which is considered here as an isotropic liquid. Given that the sample exhibits inversion symmetry, the second order susceptibility is equal to zero ($\chi^{(2)} = 0$)

in the centrosymmetric particle interior. In this case, and assuming that we are in a nonresonant SHG case, the SH scattered light only arises from the aqueous interfacial region of the particle ($\chi^{(2)} \neq 0$).

2.3 Polarimetric angle-resolved second harmonic scattering (AR-SHS)

In this section we will introduce the polarimetric angle-resolved second harmonic scattering (AR-SHS) technique, which was used throughout this thesis to determine the surface potential Φ_0 and the surface susceptibility $\chi_{s,2}^{(2)}$ as a measure of interfacial water orientation. It is important to note that AR-SHS is a nonresonant SHG experiment in scattering configuration as described in section 2.2. In the following we want to first give a description of the most relevant theoretical basics and assumptions underlying the AR-SHS technique before we explain the experimental details of the AR-SHS setup. We close this section with a brief discussion of the expected measurement uncertainties and the influence of the variation of the fitting parameters used to obtain Φ_0 and $\chi_{s,2}^{(2)}$.

2.3.1 AR-SHS model and theory

In the following, we briefly summarize some of the essential aspects of the AR-SHS model and the nonlinear optics theory relevant for the fitting procedure that is used to extract Φ_0 and $\chi_{s,2}^{(2)}$. A more detailed description can be found elsewhere [113, 114, 127, 136, 149]. In a nonresonant AR-SHS experiment, the fundamental frequency of a high-energy femtosecond laser pulse interacts with an aqueous solution that contains particles. The intense femtosecond laser pulses distort the electron clouds of all non-centrosymmetric molecules, which causes a displacement of charge with a frequency component of 2ω. These induced charge oscillations are, to leading order, the origin of molecular dipole moments. The sum of all second-order induced molecular dipoles results in a macroscopic polarization $\mathbf{P}^{(2)}$. This polarization $\mathbf{P}^{(2)}$ is equal to

$$\mathbf{P}_{2\omega}^{(2)} = \varepsilon_0 \chi^{(2)} : \mathbf{E}(\omega)\mathbf{E}(\omega) \tag{2.4}$$

where ε_0 is the vacuum permittivity, $\chi^{(2)}$ is the second-order susceptibility, which describes the local second harmonic response of the medium, and $\mathbf{E}(\omega)$ is the incoming electromagnetic field for SHS. The generated electromagnetic wave has double the frequency (2ω) of the incoming light with frequency ω. In the electric dipole approximation, the emission of SH light is forbidden in the bulk of centrosymmetric media as they possess inversion symmetry. Considering a spherical particle with an isotropic amorphous interior and water as an isotropic liquid, the SH signal originates specifically from the non-centrosymmetric regions at the interface as it is schematically shown in Figure 2.3. Under nonresonant conditions, the second-order polarization $\mathbf{P}^{(2)}$ depends on the molecular electron density in the interfacial region. Therefore, every non-centrosymmetric molecule in the non-centrosymmetric region around the particle contributes equally to the SH polarization. The SH intensity $I_{2\omega}$ scales

quadratically with the number density of molecules through

$$I_{2\omega} \propto \left| \mathbf{P}_{2\omega}^{(2)} \right|^2 = \left| N \langle \mathbf{p}_{2\omega}^{(2)} \rangle \right|^2, \tag{2.5}$$

where $\langle \mathbf{p}_{2\omega}^{(2)} \rangle$ is the sum of induced molecular second-order dipole moments per unit volume and N is the number of molecules. Because of this relationship, the majority of the SH signal intensity originates from water molecules at the interface, as the number of non-centrosymmetrically distributed surface groups of the particle is much smaller than the number of oriented water molecules at the interface. The SHS signal then arises from the net orientational order of water molecules along the surface normal. Figure 2.4 introduces the different contributions to the SHS signal. Besides the $\chi^{(2)}$ contribution to the SHS intensity that describes the orientational order induced by all (chemical) interactions confined to the particle surface plane (Fig. 2.4 A), the electrostatic field, $\mathbf{E}_{DC}$, generated between the counterions and the charged surface affects the SHS signal. The effective third-order susceptibility tensor, $\chi^{(3)'}$

A $\mathrm{E_{DC}} = 0$ **B** $\mathrm{E_{DC}} \neq 0$
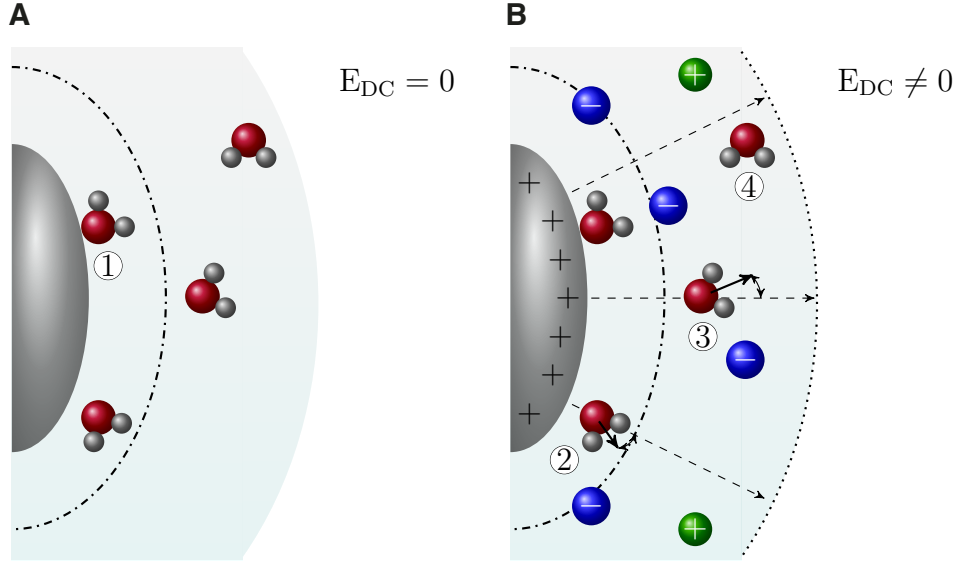
Figure 2.4 – Second-order ($\chi^{(2)}$) and effective third-order ($\chi^{(3)'}$) susceptibility contributions to the SHS signal. (A) Contributions to $\chi^{(2)}$ represented by water molecule number (1): Oriented water molecules that are chemically bound to the surface. This contribution to the SH signal would also exist in the hypothetical case of the absence of an electrostatic field. (B) Contributions to $\chi^{(3)'}$, comprising all processes that lead to the emission of SH light and require interaction with an electrostatic field $\mathbf{E}_{DC}$ forming between a charged particle surface and counterions accumulating close to the particle surface. The non-zero electrostatic field $\mathbf{E}_{DC}$ reorients interfacial water molecules (2) close to the surface and (3) up to the maximum penetration depth of $\mathbf{E}_{DC}$ into the solution (further away from the surface). $\chi^{(3)'}$ also includes a pure third-order effect originating from the isotropic third-order susceptibility of bulk water, represented here by water molecule number (4). Since the third-order contribution of bulk water is expected to be very small (responsible for <1% of SH intensity [114]) this effect can be neglected.

represents all processes that lead to the emission of SH light and require an interaction with $\mathbf{E}_{DC}$. This includes the reorientation of water molecules in the interfacial region up to the maximum penetration depth of $\mathbf{E}_{DC}$ into the solution (main $\chi^{(3)'}$ contributions), as well as a pure third-order interaction that arises from the isotropic third-order susceptibility of bulk water, which is in practice negligible. Figure 2.4 B summarizes the different contributions to $\chi^{(3)'}$. The resulting effective third-order polarization $\mathbf{P}^{(3)'}$ is defined as

$$\mathbf{P}_{2\omega}^{(3)'} \propto \varepsilon_0 \chi^{(3)'} : \mathbf{E}(\omega)\mathbf{E}(\omega)\Phi_0 \tag{2.6}$$

with $\Phi_0 = \int_0^{+\infty} \mathbf{E}_{DC}(z)\mathrm{d}z$ being the surface potential. We then obtain for the total SHS intensity

$$I_{2\omega} = \left| \mathbf{P}_{2\omega}^{(2)} + \mathbf{P}_{2\omega}^{(3)'} \right|^2. \tag{2.7}$$

Thus, within the Rayleigh-Gans-Debye (RGD) approximation, which assumes no reflection nor absorption by the scatterer (explained in more detail in section 2.3.2), the total SHS intensity can be given as

$$I_{2\omega} \propto \left| \Gamma^{(2)}(R, \chi_s^{(2)}, \theta) + \Gamma^{(3)'}(R, \chi^{(3)'}, \theta, \kappa^{-1})\Phi_0 \right|^2 \tag{2.8}$$

where R is the particle radius, θ is the scattering angle, and κ^{-1} is the Debye length (directly correlated to the ionic strength of the solution). The general expression of the Debye length for electrolytes is

$$\kappa^{-1} = \sqrt{(\varepsilon_0 \varepsilon_r k_B T)/(1000 e^2 N_A \sum_i z_i^2 c_i)} \tag{2.9}$$

and takes into account the vacuum and relative permittivity ε_0 and ε_r, respectively, the Boltzmann constant k_B, the temperature T, the elementary charge e, Avogadro's number N_A, the valency z and the ionic concentration c of ions of type i [71]. $\Gamma^{(2)}$ and $\Gamma^{(3)'}$ are, respectively, the effective second- and third-order susceptibilities that are connected to the two SHS contributions $\chi^{(2)}$ and $\chi^{(3)'}$ through multiplication of geometrical form factors F_1, F_2 and F_3 that are specific to the geometry of the scatterer and the geometry of the incoming and outgoing electromagnetic fields [113, 127]. The relationship between the nonzero $\Gamma^{(2)}$ and $\chi^{(2)}$ tensor elements and $\Gamma^{(3)'}$ and $\chi^{(3)'}$ is given in Table 2.1. The geometrical form factors for spheres are shown in Table 2.2 in section 2.3.2. F_1, F_2 and F_3 all depend on the scattering vector $\mathbf{q}$, defined as $\mathbf{q} = \mathbf{k}_0 - (\mathbf{k}_1 + \mathbf{k}_2)$. A schematic illustration of scattering from a spherical particle ($\mathbf{k}_0$) in a general case with two incoming electromagnetic fields $\mathbf{E}_1(\omega)$ and $\mathbf{E}_2(\omega)$ with wavevectors $\mathbf{k}_1$ and $\mathbf{k}_2$ of different angles of incidence is given in Figure 2.5. In this
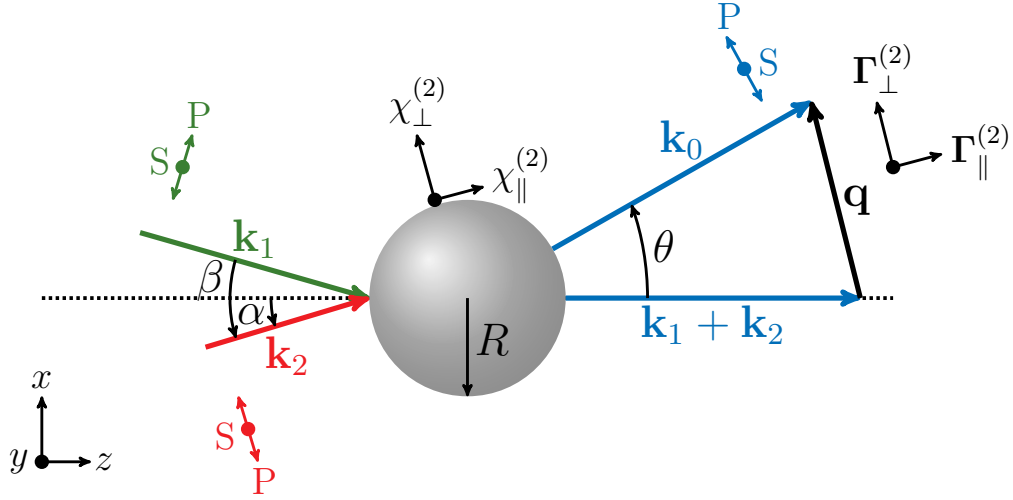
Figure 2.5 – Geometry of a scattering experiment (top view) as schematically illustrated on a spherical particle with radius R, adapted from Ref. [113]. Employing a non-collinear beam geometry, two incoming electromagnetic fields with wavevectors $\mathbf{k}_1$ and $\mathbf{k}_2$ are scattered on the particle, giving rise to an electromagnetic wave with wavevector $\mathbf{k}_0$. The angles α and β describe the angles of incidence of the incoming electromagnetic fields, while the angle θ is the scattering angle defined as the angle between the scattered (detected) light ($\mathbf{k}_0$) and the sum of the incoming wavevectors $\mathbf{k}_1$ and $\mathbf{k}_2$. While the coordinate system of the scattering experiment is defined by the vectors $\mathbf{x}$, $\mathbf{y}$ and $\mathbf{z}$, the coordinate system of the second order susceptibility $\chi^{(2)}$ is given by $\chi^{(2)}_\perp$ and $\chi^{(2)}_\parallel$, where $\perp$ is the direction parallel and $\parallel$ are the directions orthogonal to the radial direction of the particle (using spherical coordinates). $\Gamma^{(2)}_\perp$ and $\Gamma^{(2)}_\parallel$ describe the coordinate system of the effective second order susceptibility $\Gamma^{(2)}$ containing the combined symmetry of the interacting electromagnetic fields and the scatterer. In this case $\perp$ and $\parallel$ are defined with respect to the scattering vector $\mathbf{q}$, where $\perp$ represents the direction parallel to $\mathbf{q}$ and $\parallel$ represents the directions perpendicular to $\mathbf{q}$. The polarization of the incoming and the collected electromagnetic waves can be either P (parallel) or S (perpendicular) with respect to the scattering plane, indicated by the arrows orthogonal to $\mathbf{k}_1$, $\mathbf{k}_2$ and $\mathbf{k}_0$ in the corresponding color.

configuration the amplitude of the scattered electromagnetic field can be expressed as:

$$E_{\text{PPP}} = C\left[\cos\left(\frac{\theta}{2}\right)\cos\left(\frac{\theta}{2}-\alpha\right)\cos\left(\frac{\theta}{2}-\alpha+\beta\right)\Gamma^{(2)}_1 \right.$$

$$\left. + \cos\left(\theta-\alpha+\beta\right)E_{\text{SSP}} + \cos\left(\theta-\alpha\right)E_{\text{SPS}} + \cos\left(\beta\right)E_{\text{PSS}} \right], \qquad (2.10)$$

$$E_{\text{SSP}} = C\left[\cos\left(\frac{\theta}{2}-\alpha\right)\Gamma^{(2)}_2 \right], \qquad (2.11)$$

$$E_{\text{SPS}} = C\left[\cos\left(\frac{\theta}{2}-\alpha+\beta\right)\Gamma^{(2)}_3 \right], \qquad (2.12)$$

$$E_{\text{PSS}} = C\left[\cos\left(\frac{\theta}{2}\right)\Gamma^{(2)}_4 \right], \qquad (2.13)$$

where $C = \frac{k_0^2}{4\pi} \frac{e^{i\mathbf{k}_0\mathbf{r}_0}}{r_0} \mathbf{E}_1(\omega)\mathbf{E}_2(\omega)$. r_0 is the detector position in the far field and i the imaginary number. Note that in a collinear beam geometry, as we employ it in our AR-SHS experiments, the above expressions simplify since the angles α and β are vanishing and $\mathbf{k}_1 = \mathbf{k}_2$ and $\mathbf{E}_1(\omega) = \mathbf{E}_2(\omega)$. Therefore, in the experimental geometry that we use, we obtain nonzero normalized SHS signal in two independent polarization combinations of light: PPP and PSS (for spherical particles with an achiral surface PSS = SSP = SPS). Here the first letter refers to the polarization state of the SH beam and the second and third letter refer to that of the fundamental incoming beam. P polarized light is parallel and S polarized light is perpendicular to the scattering plane. Within the aforementioned RGD approximation, the scattered intensity from a sphere or shell in the two independent polarization combinations normalized by the bulk water signal can analytically be expressed as

$$\frac{I_{\text{PPP}}(\omega)}{I_{\text{SSS}}(\omega)} = \frac{N_p \left(\varepsilon_0 \left[\cos^3(\frac{\theta}{2})\Gamma_1^{(2)} + \cos(\frac{\theta}{2})\left(\Gamma_2^{(2)} + \Gamma_2^{(3)'}\right)(2\cos(\theta) + 1)\right]\right)^2}{\left(\overline{\beta}^{(2)}\right)^2 N_b} \tag{2.14}$$

$$\frac{I_{\text{PSS}}(\omega)}{I_{\text{SSS}}(\omega)} = \frac{N_p \left(\varepsilon_0 \left[\cos(\frac{\theta}{2})\left(\Gamma_2^{(2)} + \Gamma_2^{(3)'}\right)\right]\right)^2}{\left(\overline{\beta}^{(2)}\right)^2 N_b} \tag{2.15}$$

where $\overline{\beta}^{(2)}$ is the averaged second-order hyperpolarizability of water. N_p is the number of colloidal particles per volume and N_b is the number density of bulk water ($3.34 \cdot 10^{28}$ molecules/m^3), so that N_b/N_p is the number of bulk water molecules per particle. Equations 2.14 and 2.15 can alternatively be expressed as a function of the induced second-order dipole moment $\overline{\mu} = \overline{\beta}^{(2)} E(\omega)^2$ as stated in Refs. [150–152]. A summary of all the relevant constants and analytical expressions used can be found in Tables 2.2 and 2.1 in the section 2.3.2 for completeness. Note that the effective third-order susceptibility $\Gamma^{(3)'}$ is directly related to the surface potential Φ_0, and the effective second-order susceptibility $\Gamma^{(2)}$ is related to the orientation of water molecules at the interface given by $\chi^{(2)}$ as described in equation 2.8. By fitting of the measured and normalized AR-SHS patterns in two different polarization combinations according to equations 2.14 and 2.15, absolute values for the surface potential and the orientation of water molecules at the surface can be extracted.

In order to obtain absolute values for the surface potential Φ_0 and the tensor elements of $\chi^{(2)}$ as a measure of surface molecular orientation of water molecules, the relative measured SHS signal needs to be related to absolute quantities. Here we use the fact that the second-order hyperpolarizability $\beta^{(2)}$ and the third-order hyperpolarizability $\beta^{(3)}$ of uncorrelated water are known, so that through normalization by $I_{\text{SSS}}(\omega)$, the measured SHS response can directly be linked to an absolute value of the $\beta^{(2)}$ component of the particle suspension. The second-order hyperpolarizability $\beta^{(2)}$ is connected to the second-order susceptibility $\chi^{(2)}$, which than can be used to determine the orientation of water molecules at the interface. The particle interface of a spherical scatterer can be considered as isotropic in the interfacial plane (tangential coordinates are degenerate). This reduces the 27 possible $\chi^{(2)}$ tensor elements to

only 4 nonzero $\chi^{(2)}$ elements ($\chi_{s,1}^{(2)}$, $\chi_{s,2}^{(2)}$, $\chi_{s,3}^{(2)}$, $\chi_{s,4}^{(2)}$). Considering a lossless medium (appropriate for nonresonant SHG) and Kleinman symmetry, 3 of the 4 remaining elements are degenerate ($\chi_{s,2}^{(2)} = \chi_{s,3}^{(2)} = \chi_{s,4}^{(2)}$). Assuming that the orientational distribution of water molecules at the interface is broad, $\chi_{s,1}^{(2)}$ can be neglected [136, 153]. Knowing $\chi_{s,2}^{(2)}$ is therefore sufficient to describe the molecular ordering at the surface. As a sign convention for $\chi_{s,2}^{(2)}$ we use the following: negative values for water molecules with O atoms pointing toward the surface (dipole moment pointing away from the surface) and positive values for water molecules with H atoms pointing toward the surface (dipole moment pointing in direction of the surface). This sign convention arises from a comparison to values obtained from sum-frequency generation studies [154].

A more detailed description of the vanishing $\chi^{(2)}$ and $\chi^{(3')}$ ($\Gamma^{(2)}$ and $\Gamma^{(3)'}$) elements can be found in table 2.1. The assumptions we use in our AR-SHS model are further explained in section 2.3.2. More information about the measurements and the normalization procedure can be found section 2.3.3.

2.3.2 Relevant constants, analytical expressions and assumptions

The geometrical form factor functions for spheres, as they are shown in Table 2.2 can also be found in Refs. [113, 149]. They depend on the radius of the particles R and the scattering vector $|\mathbf{q}| = q$. The third form factor also depends on the inverse Debye length κ and therefore the ionic strength of the solvent. The constants used to calculate the scattered intensity from spherical particles in equations 2.14 and 2.15 are the dipole moment of water μ_{DC}, and the hyperpolarizability tensor elements of water $\bar{\beta}^{(2)}$ and $\bar{\beta}^{(3)}$. The values of the hyperpolarizability tensor elements were computed from an ab-initio model (using 1064 nm incoming light, Table 4, Model IIIa, of Ref. [155]). Although there are 3 $\beta^{(2)}$ or 6 $\beta^{(3)}$ non-zero hyperpolarizability tensor elements for a single water molecule, a single mean value can be obtained by averaging over many water molecules in an isotropic liquid, here indicated as $\bar{\beta}^{(2)}$ and $\bar{\beta}^{(3)}$. Table 2.1 summarizes some important equalities as well as the surface and effective particle susceptibility elements needed to compute the second harmonic scattering intensity from spherical particles in a solution. The non-zero second- and third-order susceptibility elements, $\chi_{s,1}^{(2)}$, $\chi_{s,2}^{(2)}$ and $\chi_{2}^{(3)'}$ are corrected for changes in the refractive index occurring at the particle/liquid interface following Refs. [130, 131] so that dispersion can be neglected. It was found in previous studies that a linear correction term as proposed by Dadap et al. [130] is sufficient to correct for the changes in the orthogonal coordinate of the electromagnetic field when it crosses the particle/liquid interface [114]. The corrected susceptibility elements $\chi_{s,1}^{(2)''}$, $\chi_{s,2}^{(2)''}$ and $\chi_{2}^{(3)''}$, and are then inserted into the analytical expressions for the non-zero effective particle susceptibility elements $\Gamma_{1}^{(2)}$, $\Gamma_{2}^{(2)}$ and $\Gamma_{2}^{(3)'}$ needed to calculate the scattering intensity in equations 2.14 and 2.15. The effective particle susceptibilities represent the combined symmetry of the incoming electromagnetic fields, the geometry of the scatterers (here: spherical), the interfacial structure and the electrostatic field in the aqueous phase. Note that the scattering intensity equations 2.14 and 2.15 are only valid under the assumption that dispersion from the difference in the refractive indices of the particles (n_p) and the

Table 2.1 – Effective particle susceptibilities, surface susceptibility elements and their equalities used for computing the scattering intensity from spherical particles (Eqs. 2.14 and 2.15). $\perp$ refers to the direction perpendicular to the particle surface and $\parallel$ to the direction parallel to the particle surface. The second- and third-order susceptibility elements are corrected for changes in the refractive index occurring at the particle/liquid interface following Ref. [130, 131] so that dispersion can be neglected.

Second-order surface susceptibilities and their equalities
$\chi_{s,1}^{(2)} = \chi_{s,\perp\perp\perp}^{(2)} - \chi_{s,\parallel\parallel\perp}^{(2)} - \chi_{s,\parallel\perp\parallel}^{(2)} - \chi_{s,\perp\parallel\parallel}^{(2)}, \ \chi_{s,1}^{(2)} \to 0$
$\chi_{s,2}^{(2)} = \chi_{s,\parallel\parallel\perp}^{(2)}, \ \chi_{s,3}^{(2)} = \chi_{s,\parallel\perp\parallel}^{(2)}, \ \chi_{s,4}^{(2)} = \chi_{s,\perp\parallel\parallel}^{(2)}, \ \ \chi_{s,2}^{(2)} = \chi_{s,3}^{(2)} = \chi_{s,4}^{(2)}$
Effective third-order susceptibilities and their equalities
$\chi_1^{(3)'} = \chi_{\perp\perp\perp,\perp}^{(3)'} - \chi_{\parallel\parallel\perp,\perp}^{(3)'} - \chi_{\parallel\perp\parallel,\perp}^{(3)'} - \chi_{\perp\parallel\parallel,\perp}^{(3)'}, \ \ \chi_1^{(3)'} = 0$
$\chi_2^{(3)'} = \frac{N_b}{\varepsilon_0}\left(\bar{\beta}^{(3)} + \frac{\bar{\beta}^{(2)}\mu_{DC}}{3k_B T}\right) = 10.3 \cdot 10^{-22}\,\text{m}^2\text{V}^{-2}, \ \ \chi_2^{(3)'} = \chi_3^{(3)'} = \chi_4^{(3)'}$
Corrected surface- and effective third-order susceptibilities
$\chi_{s,1}^{(2)''} = 27\eta\frac{\left(\chi_{s,1}^{(2)}\eta^2 + 3\chi_{s,2}^{(2)}(\eta^2-1)\right)}{(2+\eta)^3}, \ \ \eta = \left(\frac{n_p}{n_{\text{H}_2\text{O}}}\right)^2$
$\chi_{s,2}^{(2)''} = 27\eta\frac{\chi_{s,2}^{(2)}}{(2+\eta)^3}$
$\chi_2^{(3)''} = 27\eta\frac{\chi_2^{(3)'}}{(2+\eta)^3}$
Effective particle susceptibilities
$\Gamma_1^{(2)} = \left(2F_1(qR) - 5F_2(qR)\right)\chi_{s,1}^{(2)''}$
$\Gamma_2^{(2)} = F_2(qR)\chi_{s,1}^{(2)''} + 2F_1(qR)\chi_{s,2}^{(2)''}$
$\Gamma_2^{(3)'} = 2\chi_2^{(3)''}\Phi_0\left(F_1(qR) + F_3(qR,\kappa R)\right)$

liquid ($n_{\text{H}_2\text{O}}$) can be neglected and that no multiple scattering events occur. Dynamic light scattering experiments and second harmonic scattering experiments as a function of particle concentration were performed (see Figs. 2.8 and 2.9) in order to determine the linearity range ensuring that those assumptions hold. The expressions for the surface and effective particle susceptibilities, presented in Table 2.1, are derived using five commonly used assumptions [103] that are related to the optical properties of isotropic materials and their behavior in nonresonant second harmonic scattering experiments:

Table 2.2 – Constants, geometrical form factor functions and scattering vector used for calculating the scattered intensity from spherical particles (Eqs. 2.14 and 2.15)

Geometrical form factors

$$F_1(qR) = 2\pi R^2 i \left(\frac{\sin(qR)}{(qR)^2} - \frac{\cos(qR)}{qR} \right)$$

$$F_2(qR) = 4\pi R^2 i \left(3\frac{\sin(qR)}{(qR)^4} - 3\frac{\cos(qR)}{(qR)^3} - \frac{\sin(qR)}{(qR)^2} \right)$$

$$F_3(\kappa R, qR) = 2\pi R^2 i \frac{qR\cos(qR) + \kappa R\sin(qR)}{(qR)^2 + (\kappa R)^2}$$

Scattering vector

$$\mathbf{q} \equiv \mathbf{k_0} - 2\mathbf{k_1}, \quad q = \left| \frac{4\pi n_{\mathrm{H_2O}}}{\lambda_{\mathrm{SH}}} \sin\frac{\theta}{2} \right|$$

Constants

$$\mu_{DC} = 8.97 \cdot 10^{-30}\,\mathrm{Cm}$$

$$\bar{\beta}^{(2)} = 3.09 \cdot 10^{-52}\,\mathrm{C^3 m^3 J^{-2}}$$

$$\bar{\beta}^{(3)} = 4.86 \cdot 10^{-62}\,\mathrm{C^4 m^4 J^{-3}}$$

1. The liquids can be considered as spatially isotropic reducing the number of possible $\chi^{(3)'}$ and $\Gamma^{(3)'}$ tensor elements (which are 81 elements considering a lossless medium and that the electric fields are real) to only 4 remaining non-zero elements (Ref. [103] page 53).

2. Applying the assumptions that the material is lossless and that the electric fields are real reduces the amount of possible elements for $\chi^{(2)}$ and $\Gamma^{(2)}$ to 27. As the particle interface can be considered as isotropic in the interfacial plane, meaning that tangential coordinates are interchangeable, the number of non-zero elements reduces to 4 elements for $\chi_s^{(2)}$ and $\Gamma^{(2)}$.

3. Assuming the absence of dispersion due to the probing being off-resonant, three of the four tensor elements of $\chi_s^{(2)}$ ($\Gamma^{(2)}$) and $\chi^{(3)'}$ ($\Gamma^{(3)'}$) are equal to one another ($\chi_{s,2}^{(2)} = \chi_{s,3}^{(2)} = \chi_{s,4}^{(2)}$ and $\chi_2^{(3)'} = \chi_3^{(3)'} = \chi_4^{(3)'}$) so that only two independent tensor elements remain. Those are $\chi_{s,1}^{(2)}$, $\chi_{s,2}^{(2)}$, and $\chi_1^{(3)'}$, $\chi_2^{(3)'}$ respectively. This assumption was verified by confirming that the polarization combinations PSS and SPS (or SSP) generate the same SHS response within experimental uncertainty. Mind that SPS and SSP are the same in SHS as we are using a single incoming frequency $\omega_1 = \omega_2 = \omega$, which makes the last two indices interchangeable.

4. Additionally, the element $\chi_1^{(3)'}$ is equal to zero due to symmetry properties of the third-order susceptibility tensor of an isotropic medium (namely $\chi_1^{(3)'} = \chi_{\perp\perp\perp,\perp}^{(3)'} - \chi_{\|\|\perp,\perp}^{(3)'} - \chi_{\|\perp\|,\perp}^{(3)'} - \chi_{\perp\|\|,\perp}^{(3)'} = 0$) [136, 153]. Thus also $\Gamma_1^{(3)'} = 0$ (Ref. [113])

5. We finally assume that $\chi_{s,1}^{(2)} = 0$, which is the case for a broad orientational distribution of water molecules at the interface. See Ref. [153] for details.

As mentioned in section 2.3.1, our AR-SHS model holds within the so called Rayleigh-Gans-Debye (RGD) approximation. The basic assumption of the RGD theory is that light is not reflected at the nanoparticle/liquid interface, nor attenuated inside the particle. This can be considered true if the following conditions are fullfilled:

$$\left|1 - \frac{n_p}{n_{H_2O}}\right| \ll 1, \tag{2.16}$$

$$\frac{2\pi n_{H_2O}}{\lambda} a \left|1 - \frac{n_p}{n_{H_2O}}\right| \ll 1. \tag{2.17}$$

In these expressions n_p is the refractive index of the particle, n_{H_2O} is the refractive index of the solvent (here water), λ is the wavelength of the light and a is the linear dimension of an arbitrarily shaped particle, which for spherical particles translates into the particle radius R.

2.3.3 AR-SHS setup and measurements

The second harmonic scattering measurements were performed on the same SHS setup previously described in detail in Refs. [114] and [116]. A schematic illustration of the SHS setup used throughout this thesis is shown in Figure 2.6. To measure AR-SHS, a pulsed 190 fs Yb:KGW laser (Pharos-SP system) with a center wavelength of 1028 nm (chapter 3 and 4) or 1032 nm after the replacement of the laser oscillator (chapter 5 and 6), a repetition rate of 200 kHz and an average power of 60 mW (chapter 3) or 80 mW (chapter 4, 5 and 6) was focused into a cylindrical glass sample cell (4.2 mm inner diameter, high precision cylindrical glass cuvettes, LS instruments). The input and output polarization was controlled by a Glan-Taylor polarizer (GT10-B, Thorlabs) and a zero-order half wave plate (WPH05M-1030) and another Glan Taylor polarizer (GT10-A, Thorlabs), respectively. The beam waist was about $w_0 \sim 55\,\mu$m as measured with a beam profiler (Thorlabs BP104-UV); the corresponding Rayleigh length was ~9.23 mm. The scattered SH light ($\lambda = 514$ nm in chapter chapter 3 and 4 or $\lambda = 516$ nm in chapter 5 and 6) was collected, collimated with a planoconvex lens ($f = 5$ cm), polarization analyzed, and filtered (ET525/50, Chroma in chapter 3; ZET514/10x, Chroma in chapter 4; CT516/10bp, Chroma in chapter 5 and 6) before being focused into a gated photomultiplier tube (H7421-40, Hamamatsu). The acceptance angle was set to 3.4° for scattering patterns. Patterns were obtained in steps of 5° from $\theta = -90°$ to $\theta = 90°$ with 0° being the forward direction of the fundamental beam. Data points were acquired using $30 \cdot 1$ s (chapter 3) or $20 \cdot 1.5$ s (chapter 4, 5 and 6)acquisition time with a gate width of 10 ns (chapter 3, 4 and 5) or 5 ns (chapter 6). To correct for incoherent hyper-Rayleigh scattering (HRS) from the solvent phase, both the

SHS response from the sample solution $I(\theta)_{\text{SHS, sample}}$ and the HRS response from a solution of identical ionic strength and pH but without nanoparticles $I(\theta)_{\text{HRS, solution}}$ are collected. The HRS is subtracted from the SHS signal of the sample and the obtained difference is then normalized to the isotropic SSS signal of pure water $I(\theta)_{\text{HRS, water, SSS}}$ to correct for differences in the beam profile on a day-to-day basis:

$$I_{\text{PPP}}^{\text{norm}}(\theta) = \left[\frac{I(\theta)_{\text{SHS, sample, PPP}} - I(\theta)_{\text{HRS, solution, PPP}}}{I(\theta)_{\text{HRS, water, SSS}}} \right] \tag{2.18}$$

Here, the normalized signal of the sample $I^{\text{norm}}(\theta)$ is given for SHS in the PPP polarization combination. The normalization procedure was applied in the same way for SHS measured in the PSS polarization combination. The normalized patterns were then fitted using the AR-SHS model previously derived[113, 114, 116, 140] and described in this thesis in section 2.3.1 in order to extract the surface potential Φ_0 and the second-order surface susceptibility $\chi_{s,2}^{(2)}$. The fitting procedure uses the analytical equations 2.14 and 2.15 and takes into consideration the particle radius R, as it was measured by dynamic light scattering (DLS) (see section 2.4.1 for an explanation of this technique), the ionic strength, as determined from conductivity measurements, the refractive indices of water (1.33) [156] and TiO_2 (2.61) [157] or SiO_2 (1.46) [158], the SH wavelength $\lambda = 514\,\text{nm}$ (or $\lambda = 516\,\text{nm}$ after the oscillator replacement), the temperature T, and the number of particles/mL.
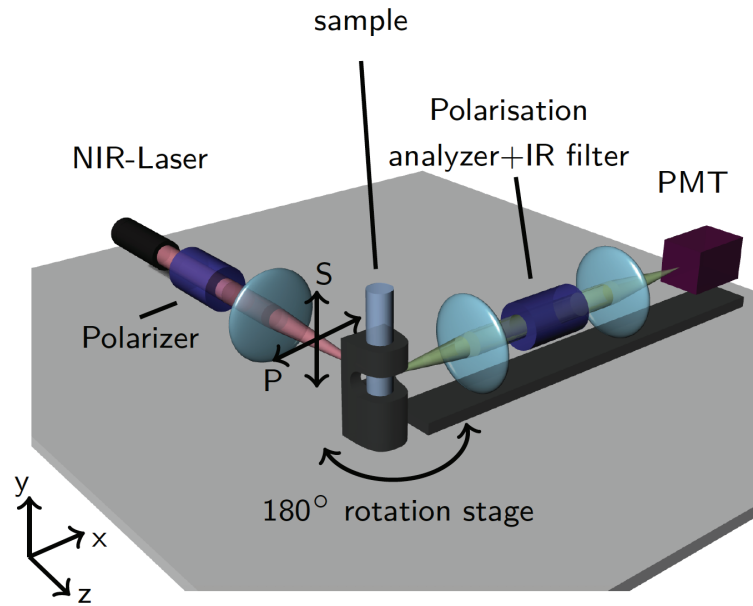
Figure 2.6 – Angle-resolved second harmonic scattering (AR-SHS) setup adapted from Ref. [114]. The polarization in S (perpendicular to the scattering plane) or P (parallel to the scattering plane) can be adjusted for the incoming near-infrared (NIR) beam (red) and the scattered second hamonic (SH) light (green).The SH light is collected as angular patterns over 180° with a photomultiplier tube (PMT) on a rotation stage. Samples are contained in a cylindrical glass cuvette.

2.3.4 Error analysis

We note that the error bars that we report for Φ_0 and $\chi_{s,2}^{(2)}$ throughout this thesis are based on the statistical errors of the measured AR-SHS patterns prior to normalization. A calculation using Gaussian error propagation allows us to obtain the errors of the normalized AR-SHS patterns of the particles dispersed in a solution $\sigma(\theta)_{\text{PPP}}^{\text{norm}}$ (shown here for the example of measurements performed in PPP polarization direction) so that:

$$
\left(\sigma(\theta)_{\text{PPP}}^{\text{norm}}\right)^2 = \left(\frac{\sigma(\theta)_{\text{sample, PPP}}}{I(\theta)_{\text{HRS, water, SSS}}}\right)^2 + \left(\frac{-\sigma(\theta)_{\text{solution, PPP}}}{I(\theta)_{\text{HRS, water, SSS}}}\right)^2
$$
$$
+ \left(\frac{-\left(I(\theta)_{\text{SHS, sample, PPP}} - I(\theta)_{\text{HRS, solution, PPP}}\right) \cdot \sigma(\theta)_{\text{water, SSS}}}{\left(I(\theta)_{\text{HRS, water, SSS}}\right)^2}\right)^2 \tag{2.19}
$$

In this expression $\sigma(\theta)_{\text{sample, PPP}}$ is the statistical error of the original unnormalized AR-SHS patterns obtained for particles in a solution in PPP polarization direction. $\sigma(\theta)_{\text{solution, PPP}}$ is the deviation of the reference solution pattern and $\sigma(\theta)_{\text{water, SSS}}$ is the deviation of a water pattern in SSS polarization direction. $I(\theta)_{\text{sample, PPP}}$ is the SHS response from the sample solution $I(\theta)_{\text{solution, PPP}}$ is the HRS response from a solution of identical ionic strength and pH but without nanoparticles in PPP polarization direction. $I(\theta)_{\text{water, SSS}}$ is the HRS response of water in PPP polarization direction. Equation 2.19 is in the same way applicable for obtaining the errors of the normalized AR-SHS patterns in the PSS polarization direction. The errors on Φ_0 and $\chi_{s,2}^{(2)}$ are numerical errors on the fitting procedure. They are determined by applying the fitting procedure to $I_{\text{PPP}}^{\text{norm}}(\theta) + \sigma(\theta)_{\text{PPP}}^{\text{norm}}$ and $I_{\text{PPP}}^{\text{norm}}(\theta) - \sigma(\theta)_{\text{PPP}}^{\text{norm}}$. The equivalent procedure is applied to AR-SHS patterns in PSS polarization direction.

Other sources of error may contribute to the total error, such as the variations in the experimentally determined parameters (i.e., the particle radius, the number of particles, or the ionic strength). An estimation of the influence of those uncertainties on the surface potential Φ_0 and the surface susceptibility $\chi_{s,2}^{(2)}$ was reported for oil droplets in water in ref [114]. In section 8.3 (Appendix), we examine the effect of a variation of the fitting parameters on the values obtained for Φ_0 and $\chi_{s,2}^{(2)}$. The fitting procedure is applied to the experimental AR-SHS patterns obtained for $\sim 100\,\text{nm}$ amorphous TiO_2 in NaCl solutions of different concentration. The original AR-SHS patterns of $\sim 100\,\text{nm}$ amorphous TiO_2 and the corresponding plots of Φ_0 and $\chi_{s,2}^{(2)}$ as a function of salt concentration are further discussed in Chapter 4. From the variation of the fitting parameters, it can be seen that in most of the cases only the magnitude of both Φ_0 and $\chi_{s,2}^{(2)}$ are affected by a large variation of the investigated parameter, but that the trends observed for the different ions, pH conditions and surfaces studied in this thesis are unaffected.

2.4 Complementary experimental techniques and methodologies

2.4.1 Dynamic light scattering measurements (DLS)

Dynamic light scattering (DLS) is a linear scattering technique that is used in this thesis to determine the hydrodynamic radius of the particles investigated. We used a Malvern Nanosizer ZS in chapter 3, 4 and 5, and a Malvern Zetasizer Ultra in chapter 6 to measure the particle size, which was then used in the SH fitting procedure. The Malvern Zetasizer Ultra system additionally allows us to determine the particle concentration (number of particles/mL) using a multi-angle dynamic light scattering (MADLS) technique. In chapter 6 we used the experimentally determined number of particles obtained through the MADLS method to fit the SHS patterns. Additionally, we used DLS to control that our AR-SHS measurements are performed in a range where the scattering from the particles is linearly dependent on the particle concentration. In the following we want to introduce the main working principles of DLS and MADLS.

When particles are in a solution they undergo Brownian motion, which is a random movement originating from the interaction of solvent molecules with the particles. This movement is dependent on the size of the particle: the larger the particle radius, the slower its motion. Smaller particles are more easily redirected by surrounding solvent molecules and are therefore moving faster. The velocity of the Brownian motion is defined by the so called translational diffusion coefficient D. This property is used in the Stokes-Einstein equation to determine the hydrodynamic diameter d_H which can be expressed as

$$d_H = \frac{k_B T}{3\pi \eta D} \tag{2.20}$$

where k_B is the Boltzmann constant, T is the temperature and η is the viscosity of the solution. Since the viscosity of the liquid is temperature dependent, it is important that the sample is equilibrated at a stable temperature before it is measured. All samples in our studies where equilibrated and measured at room temperature. To obtain the translational diffusion coefficient D of the particles needed to calculate the hydrodynamic diameter, DLS uses an autocorrelation method. A laser with a wavelength of $\lambda = 632.8\,\text{nm}$ is focussed on a sample cell (DTS0012 or DTS1070) that contains particles in a solution. A detector placed at 173° from the angle of incidence of the laser light collects the intensity of the scattered light from the particles. This intensity fluctuates as a function of time due to the Brownian motion of the particles. An autocorrelation of the scattered intensity at various points in time allows us to extract the hydrodynamic size of the particles. The correlation function $G(\tau)$ can be described as

$$G(\tau) = \langle I(t) * I(t+\tau) \rangle \tag{2.21}$$

where t is the time and τ is the sample time of the correlator. For monodispersed particle suspensions $G(\tau)$ can be expressed as

$$G(\tau) = A\left[1 + Be^{-2\Upsilon\tau}\right] \tag{2.22}$$

where A is the baseline and B the intercept of the correlation function. Υ is related to the translational diffusion coefficient D and the scattering vector $q = \frac{4\pi n}{\lambda} \sin(\frac{\theta}{2})$ by

$$\Upsilon = Dq^2. \tag{2.23}$$

In this expression λ is the laser wavelength, θ is the scattering angle and n is the refractive index of the dispersant. For polydispersed particle suspensions $G(\tau)$ can be written as a function of multiple exponential terms.
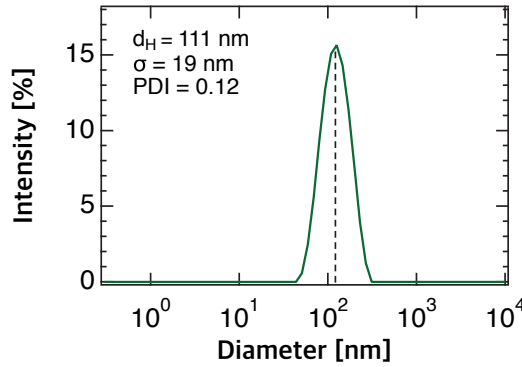
Figure 2.7 – Size distribution of ~100 nm amorphous TiO_2 particles in water as determined by DLS measurements. The intensity percentage is given as a function of particle diameters present in the solution. From this size distribution the hydrodynamic diameter (d_H) of the particles, the standard deviation σ and the polydispersity index (PDI) of the distribution can be determined.

Figure 2.7 shows a typical dynamic light scattering size distribution of a monomodal particle suspension, as it can be obtained by a fitting of the measured autocorrelation function. The polydispersity index (PDI) gives an indication about the broadness of the size distribution and takes into account the standard deviation of the size distribution σ and the mean radius of the particles r, so that

$$PDI = \left(\frac{\sigma}{r}\right)^2. \tag{2.24}$$

In the case of MADLS, the intensity scattered from the sample is collected under three different angles: 173°, 13° and 90°. This allows to obtain a more accurate particle size distribution with improved resolution enabling for the determination of the particle concentration in the solution in the concentration range of 10^8 - 10^{12} particles/mL [159]. The absolute particle concentration distribution $p(d_H)$ (number of particles per volume for a particular size) can be obtained from the intensity-weighted particle size distribution $x(d_H)$ according to

$$p(d_H)\frac{dC_{sca}}{d\Omega}(d_H) = x(d_H)I_p\frac{R_{tol}}{I_{tol}} \tag{2.25}$$

where d_H is the hydrodynamic diameter, $\frac{dC_{sca}}{d\Omega}$ is the differential scattering cross-section of the particles (with respect to the solid angle Ω), I_p is the derived count rate of photons scattered

from the particles, and I_{tol} is the derived photon count rate scattered by toluene as a reference. R_{tol} is the Rayleigh ratio of toluene, which can be found in the literature. The derived count rate is a measure for the actual photon scattering of a specific sample as if the intensity measured in DLS was not attenuated. Mie theory is used to calculate $\frac{dC_{\text{sca}}}{d\Omega}$, which is dependent on size and the refractive index of the particles and the dispersant.
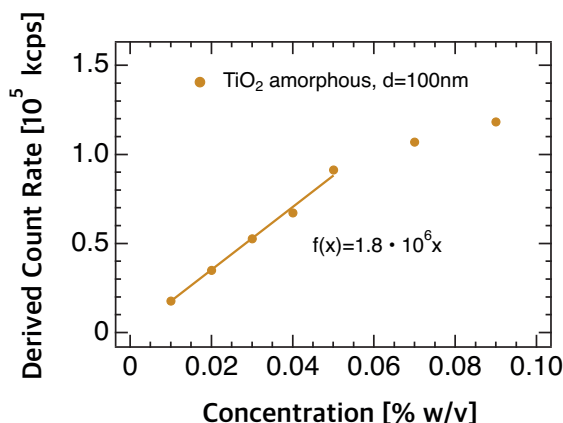
Figure 2.8 – Derived count rate in kilo counts per second (kcps) as a function of particle concentration in weight per volume percent (% w/v) as determined by DLS measurements for ~100 nm amorphous TiO$_2$ particles.

In this thesis, DLS was additionally used to ensure that the AR-SHS measurements are performed in a range where the scattering intensity is linearly dependent on the concentration of particles so that no multiple scattering events occur. Figure 2.8 shows the derived count rate obtained from DLS measurements as a function of particle concentration for amorphous ~100 nm TiO$_2$ particles. It can be seen that the DLS signal scales linearly with concentration from 0.01% w/v to 0.05% w/v. Based on this measurement we chose to perform the AR-SHS of this sample at a concentration of 0.05% w/v to maximize the SHS signal while preventing multiple scattering events. Figure 2.9 shows the AR-SHS patterns of amorphous ~100 nm TiO$_2$ particles measured at different particle concentrations. As in the case of linear light scattering, the SH intensity is increasing linearly with particle concentration in this concentration range. For every sample investigated in this thesis the linear scattering range was determined by a DLS concentration series to find the most suitable concentration for the AR-SHS measurements.

2.4.2 Electrophoretic mobility measurements and ζ-potential

In this thesis we employed electrophoretic mobility measurements to determine the zeta-potential ζ of the SiO$_2$ and TiO$_2$ particles in suspension to control colloid stability. As discussed in detail in chapter 1.5 the zeta-potential ζ is traditionally interpreted as the potential at the shear plane of the particles (see Fig. 1.2) and provides information about the ionic environment of the particles. When charged particles are suspended in an electrolyte solution and an
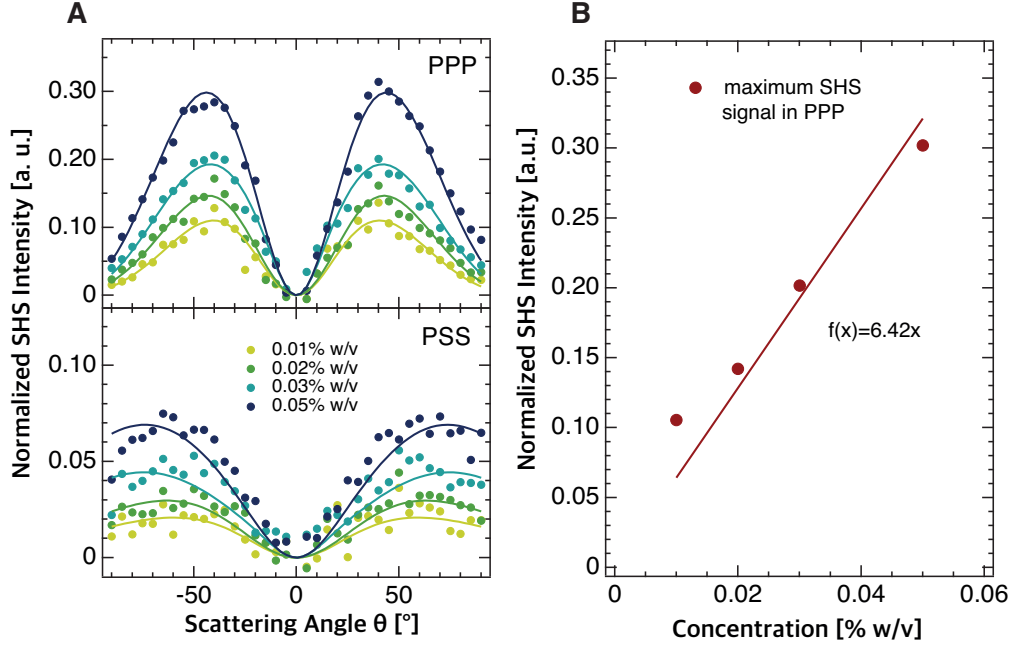
Figure 2.9 – (A) Particle concentration dependence of the AR-SHS scattering patterns in PPP and PSS polarization direction for ~100 nm amorphous TiO_2 particles. (B) Linearity of the increase in SHS signal taken at the maximum of each AR-SHS scattering pattern in the concentration range of 0.01% w/v to 0.05% w/v of ~100 nm amorphous TiO_2 particles.

electric field is applied, the particles are attracted towards the oppositely charged electrode. Depending on the viscosity of the surrounding liquid, its dielectric constant and the strength of the applied electric field, the particle moves with a certain velocity towards the electrode, which is referred to as electrophoretic mobility. The Henry equation relates the electrophoretic mobility v_m and the zeta-potential ζ by

$$v_m = \frac{\varepsilon \zeta f(\kappa R)}{\eta}. \tag{2.26}$$

where $\varepsilon = \varepsilon_r \varepsilon_0$ is the permittivity of the medium (ε_0 is the vacuum permittivity and ε_r is the relative permittivity of water), η is the viscosity of the liquid and $f(\kappa R)$ is the Henry's function. In this function κ is the inverse Debye length and R refers to the radius of the particle. As a consequence, κR describes the ratio of the particle size and the electrical double layer (EDL) thickness.

In the Zetasizer software of the Zetasizer Nano ZS (Malvern Instruments), which we use to measure the electrophoretic mobility, Henry's function is employed to convert v_m to ζ. Two limiting cases can be distinguished for the simplification of Henry's function: Smoluchowski approximation for thin EDLs ($\kappa R \gg 1$) and Hückel approximation for thick EDLs ($\kappa R \ll 1$). While the Smoluchowski approximation is valid for higher ionic strength cases where the Debye length in the electrolyte is reduced (e.g. ~ 10^{-3} M for particle radii of $R = 100$ nm), the Hückel approximation covers lower ionic strength conditions, where the Debye length is
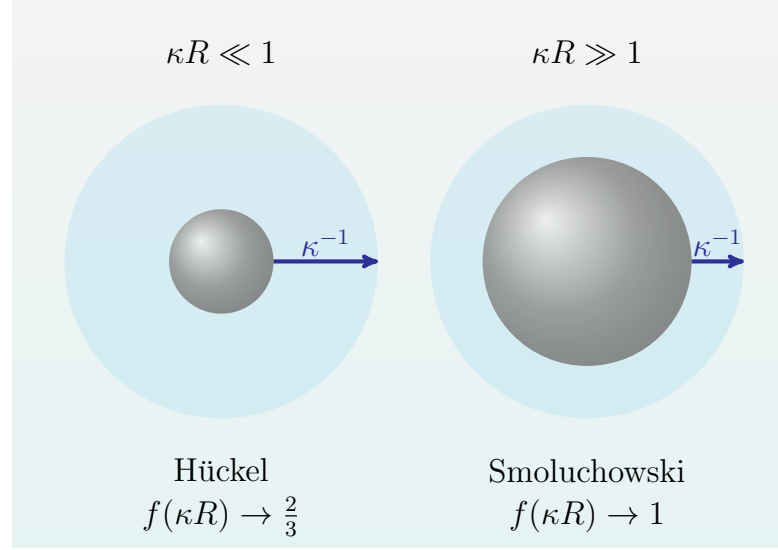
Figure 2.10 – Limiting cases for the simplification of Henry's function: Hückel approximation for small particles and thick EDLs (left) and Smoluchowski approximation for large particles and thin EDLs (right).

increased. The larger the particle radii, the more applicable is the Smoluchowski approximation, where $f(\kappa R) \to 1$, while the smaller the particle radii, the more applicable is the Hückel approximation where $f(\kappa R) \to \frac{2}{3}$. Therefore Henry's equation (2.26) can have two solutions in the Zetasizer software which differ by a factor of 1.5 depending on whether the Hückel or Smoluchowski approximation are used. However, based on the particle size and the ionic strength of the solution investigated, one may find cases where neither the Hückel nor the Smoluchowski approximation fully apply. For those cases we used an approximation derived by Ohshima [160] (further detailed in Ref. [161]) to more precisely convert v_m to ζ. In this approximation the following expression with relative errors less than 1% for $f(\kappa R)$ is used:

$$f(\kappa R) = \frac{2}{3} \left[1 + \frac{1}{2 \left(1 + \frac{2.5}{\kappa R (1 + 2e^{-\kappa R})} \right)^3} \right]. \tag{2.27}$$

Inserting equation 2.27 into equation 2.26 allows to manually convert the measured electrophoretic mobility v_m to the zeta potential ζ using Ohshima's method.

2.5 Sample preparation and characterization

2.5.1 Preparation of colloidal dispersions and reference solutions

The particles investigated in this thesis were received in powder form or already dispersed in solution. A stock solution of the colloidal particles was prepared using ultrapure water (MilliQ, Millipore, Inc., electrical resistance of $18.2 \, \text{M}\Omega \cdot \text{cm}$). The stock solutions were diluted to the

desired concentration of particles and stabilized by addition of NaOH when needed. After sonicating and vortexing the samples, a washing procedure was employed to remove residual ions from the synthetic procedure. The nanoparticles in the diluted stock solutions were collected via centrifugation, the supernatant was removed and the pellet was resuspended in MilliQ water at the same concentration. This washing procedure was repeated upon need to ensure that the initial ionic strength of the particle suspension was as low as possible. The washed particle dilutions were further diluted to the desired particle concentration and the desired amount of salt, base or acid was added. After sonicating and vortexing the prepared particle suspensions, the samples were ready for measurements. In some cases the particles were additionally filtered prior to measurements to remove particle aggregates. Reference solutions were prepared at the same ionic strength or pH of the sample but without particles. The samples were prepared in ambient conditions at room temperature. A more exact description of the sample preparation steps for the particles used in this thesis can be found in the sample preparation section of each chapter.

2.5.2   Sample characterization

In this thesis, the particle size distribution was determined by dynamic light scattering (DLS), and the zeta potential ζ was measured by electrophoretic measurements (Zetasizer Nano ZS or Zetasizer Ultra, Malvern) as described above. The pH of the samples was determined using a pH meter (HI 5522 pH/ISE/EC bench meter and HI 1330 pH electrode, Hanna Instruments) calibrated with the appropriate buffer solutions. In order to control the amount of salt, acid or base added to the samples and the initial ionic strength of the washed particles in water, the conductivity was measured by two different means: first using a conductivity meter (HI 5522 pH/ISE/EC bench meter and HI 76312 conductivity electrode, Hanna Instruments) calibrated with the appropriate buffer solutions and second, using the conductivity obtained from the zeta potential measurements (Zetasizer Nano ZS or Zetasizer Ultra, Malvern). Knowing the conductivity σ, the average ionic strength, represented by the concentration of ions in solution c, was calculated using the equivalent (molar) ionic conductivity Λ_m: [162]

$$c = \frac{\sigma}{\Lambda_m} = \frac{\sigma}{\sum_i \nu_i \lambda_i} \tag{2.28}$$

Here λ_i are the equivalent ionic conductivities of the cations and anions present in the electrolyte that were taken from Ref. [163], and ν_i refers to the number of moles of each ion. In cases where the theoretical salt concentration of the sample is below 0.5 mM, the ionic molar conductivity at infinite dilution Λ^0 can be used for Λ_m, whereas for a theoretical concentration above 0.5 mM, the ionic molar conductivity Λ_m should be calculated according to the Debye-Hückel-Onsager equation. A more detailed description of the sample characterization procedure employed for a particular sample used in this thesis can be found in the sample characterization section of each chapter.

3 Characterization of the SiO$_2$ nanoparticle/aqueous interface

The microscopic description of the interface of colloidal particles in a solution is essential to understand and predict the stability of these systems, as well as their chemical and electrochemical reactivity. However, this description often relies on the use of simplified electrostatic mean field models for the structure of the interface, which give only theoretical estimates of surface potential values and do not provide properties related to the local microscopic structure, such as the orientation of interfacial water molecules. In this chapter we apply polarimetric angle-resolved second harmonic scattering (AR-SHS) to 300 nm diameter SiO$_2$ colloidal suspensions to experimentally determine both surface potential and interfacial water orientation as a function of pH and NaCl concentration. The surface potential values and interfacial water orientation change significantly over the studied pH and salt concentration range, whereas zeta-potential (ζ) values remain constant. By comparing the surface and ζ-potentials, we find a layer of hydrated condensed ions present in the high pH case, and for NaCl concentrations $\geq$ 1 mM. For milder pH ranges (pH < 11), as well as for salt concentrations < 1 mM, no charge condensation layer is observed. These findings are used to compute the surface charge densities using the Gouy-Chapman and Gouy-Chapman-Stern models. Furthermore, by using the AR-SHS data, we are able to determine the preferred water orientation in the layer directly in contact with the silica interface. Molecular dynamics simulations confirm the experimental trends and allow deciphering of the contributions of water layers to the total response.

The results presented in this chapter are adapted from Ref. [150]:

Arianna Marchioro, Marie Bischoff, Cornelis Lütgebaucks, Denys Biriukov, Milan Předota and Sylvie Roke, „Surface Characterization of Colloidal Silica Nanoparticles by Second Harmonic Scattering: Quantifying the Surface Potential and Interfacial Water Order" *J. Phys. Chem. C* 2019, 123, 20393-20404.

The molecular dynamics simulations in this work were performed by Denys Biriukov and Milan Předota (University of South Bohemia, České Budějovice, Czech Republic).

3.1   Motivation

The surface chemistry of silica is key to a large number of applications, both in research and in industrial processes. In the past few decades, colloidal suspensions of SiO$_2$ particles have been extensively used for separation, heterogeneous catalysis, and as major components of ceramics and coatings. Colloidal silica is also widely used in the food, health care and pharmaceutical industries, as well as in the production of microelectronics components [164]. The microscopic characterization of colloidal particle interfaces with liquids is of fundamental interest to understand the stability of these systems and their chemical and electrochemical reactivity. In contact with water or another fluid, a solid surface usually develops a charged layer at its surface that is compensated by a distribution of counterions in the surrounding solution. This so-called „electrical double layer" (EDL) has been first put forth by Helmholtz in the 1850s and since then, many different mean field models have been proposed to describe the structure of a solid/electrolyte interface. In such models, the often complex chemical nature of the interface with its different structures and nonuniformity is reduced to a uniformly charged interface, the aqueous phase is represented by a uniform dielectric, and the ions are represented as point charges. The most frequently used model was originally proposed by Gouy and Chapman. In their model a charged interface is in contact with an aqueous solution in which the counterion distribution decays exponentially along the surface normal. This layer is usually referred to as the diffuse layer (DL). Stern suggested a modification for high charge densities, comprised of the formation of a condensed layer, or Stern layer, of potentially hydrated counterions close to the surface [52, 57, 165]. However, in reality, the structure and chemistry of this electrical double layer is more complex and the electrostatic environment will depend on the local chemical nature of the surface, of the type of ions, their solvation shells and the solvent in the first few atomic dimensions adjacent to the interface [57, 166–170]. As many of the mentioned ingredients are challenging to determine experimentally, the microscopic description of a relatively simple interface such as SiO$_2$/aqueous solution remains elusive.

When considering a colloidal suspension, two parameters are most often reported, as they give an information on the stability of the suspension. These quantities, namely surface charge density and ζ-potential, can be measured with relatively simple experimental techniques. The first quantity is usually determined by potentiometric titrations, [78] assuming that all the charges in the system are confined to an outer smooth surface of the particle, which means such a measurement gives, at best, an upper limit for the surface charge. The second one is obtained by measuring the electrophoretic mobility. The ζ-potential is then calculated from the mobility, assuming a sufficiently thin double layer, and it is defined as the potential at the plane of shear, where the liquid velocity is zero. This plane is likely at some distance outside the particle and includes both the particle plus a 0.3-1 nm thick layer of stationary solvent and ions that can move with the particle in an electric field [71, 72, 171, 172]. However, the ζ-potential only provides an empirical indication of the stability of colloidal suspensions. Direct information on the surface electrostatics is obtained via the surface potential, which in contrast to the ζ-potential, is not a trivial quantity to access experimentally [173]. The

surface potential can be computed from applying the constant capacitor model (CC), the Gouy-Chapman (GC) or the Gouy-Chapman-Stern (GCS) models to titration and ζ-potential data [174] or to nonlinear optics data. Indeed, for planar SiO_2/water interfaces, surface-sensitive techniques such as SHG and sum frequency generation (SFG) have shown to provide insight into the structure of the SiO_2 double layer and water orientation at the interface, [170, 175–182] as well as values for surface potential as developed by Eisenthal and co-workers [137, 183–187]. For colloidal suspensions, the so-called „Eisenthal-chi3 method" can be used to estimate values for surface potential; [138, 176] however, this method is bound to the use of a model such as the CC, GC, or the GCS one, and does not provide a unique solution for the surface potential, as the number of unknowns in the expression exceeds the number of independently available observables. Information about the potential drop in the EDL can be obtained by X-ray photoelectron spectroscopy (XPS) [188]. Brown et al. have shown that surface potential values of colloidal SiO_2 particles can be obtained through XPS of a liquid microjet, [94, 96, 97] using the charge divided energy difference between the binding energy of the Si 2p photoelectrons in the presence of salt and the extrapolated binding energy of the Si 2p photoelectrons at the point of zero charge. However, this measurement requires the use of synchrotron facilities and has some intrinsic limitations due to the relatively low signal-to-noise level. The colloid size needs to be small (ca. 10 nm diameter), and the salt concentration high ($\gtrsim$50 mM).

Our laboratory has recently reported an alternative way to determine the average surface potential of colloidal particles in a solution using polarimetric angle-resolved nonresonant second harmonic scattering (AR-SHS) measurements [113, 114, 136, 140]. AR-SHS does not require any information on the specific structure of the interface, and only assumes exponential decay of the electrostatic potential several nanometers away from the interface. In this all-optical approach taking advantage of nonlinear light scattering theory, the nonresonantly scattered second harmonic (SH) light that is emitted from the particle interface and the EDL contains enough information to determine the surface potential quantitatively. Additionally, because of the symmetry properties of second harmonic experiments, AR-SHS also provides another essential parameter of interfaces: molecular orientation of water molecules at the interface. These two elements together greatly contribute to the microscopic description of colloid/solvent interfaces.

Here, we apply polarimetric AR-SHS to 300 nm diameter SiO_2 colloids suspended in aqueous solution and extract both surface potential and interfacial molecular orientation. Polarimetric AR-SHS experiments are performed as a function of pH and NaCl concentration. The surface potential values, as well as the interfacial water orientation, vary drastically over the studied pH and salt concentration range, in contrast to the ζ-potential values, which do not change much in magnitude. Comparing the surface and ζ-potentials, we find that for high pH cases, as well as for salt concentrations $\geq$ 1 mM, there is a (Stern) layer of condensed charges, forming a capacitor with respect to the surface and causing preferential orientation of interfacial water molecules with their hydrogens facing the particle surface. On the other hand, for pH values below 11, as well as below 1 mM salt concentration, there is no such layer, and the interfacial water is preferentially oriented with the oxygen atom facing the particle surface. These find-

ings are compared to results from molecular dynamics (MD) simulations that consider the orientation of water on a single crystalline quartz surface and agree with the experimental results.

3.2 Materials and Methods

3.2.1 Chemicals

Sodium hydroxide (NaOH, > 99.99% trace metals basis, Sigma-Aldrich) and sodium chloride (NaCl, > 99.999%, Sigma-Aldrich) were used as received. SiO$_2$ colloids (300 nm diameter) were purchased in powder form from Bangs Laboratories, Inc. Colloidal particles were washed as described in section 3.2.2.

3.2.2 Sample preparation

All procedures described hereafter used ultrapure water (Milli Q, Millipore, Inc., electrical resistance of 18.2 M$\Omega \cdot$ cm). First, 50 mg of SiO$_2$ colloidal particles were dispersed in 1 mL of ultrapure water, sonicated for 10 min, and then diluted to 10 mL with ultrapure water and sonicated again for 3 min. The solution was then centrifuged for 10 min at 7800 rpm (5430R, Eppendorf) in order to sediment the colloidal particles. Then 9 mL of the supernatant were removed, and the pellet was resuspended in the same volume of Milli Q water by vortexing, followed by ultrasonication in an ultrasonic bath (35 kHz, 400 W, Bandelin) for 3-5 min. This procedure was repeated twice to ensure proper washing of the SiO$_2$ particles and removal of any additional ions in solution coming from the synthetic procedure. The conductivity of the washed particles was measured as described in section 3.2.3 to ensure that the initial ionic strength of the particle suspension was as low as possible (below 2 μS/cm for a sample in ultrapure water and in equilibrium with atmospheric CO$_2$). Particles were further diluted to 0.1% wt. solutions (corresponding to ca. $3.5 \cdot 10^{10}$ particles/mL). The pH and/or ionic strength of the solution were adjusted using 0.1 or 0.01 M stock solutions of NaOH and NaCl. The sample solutions were used without further filtering and measured on the same day. Corresponding water references at the same pH/ionic strength where prepared for each SiO$_2$ sample. All preparation steps and measurements were performed at room temperature, 23°C.

3.2.3 Sample characterization

The particle size distribution was determined by dynamic light scattering (DLS) and the ζ-potential was measured by electrophoretic measurements (Zetasizer Nano ZS, Malvern). The SiO$_2$ colloids had a mean hydrodynamic diameter of ~300 nm with a narrow distribution (for most samples, polydispersity index (PDI) < 0.1). Average radii and ζ-potentials are tabulated in parts D of Figures 3.1 and 3.2. Values for size and ζ-potential are averages of 3 measurements. pH was measured using a pH-meter (HI 5522 pH/ISE/EC bench meter and HI 1330 pH

electrode, Hanna Instruments) calibrated with the appropriate buffer solutions. Conductivity values were measured to ensure that the proper amount of salt had been added to the sample. Conductivity values were obtained by two different means: using a conductivity meter (HI 5522 pH/ISE/EC bench meter and HI 76312 conductivity electrode, Hanna Instruments) calibrated with the appropriate buffer solutions, as well as from the ζ-potential measurements (Zetasizer Nano ZS, Malvern). Average ionic strengths in solution were calculated using equation 2.28 as described in the sample characterization chapter 2.5.2. Below theoretical concentrations of 0.1 mM, the ionic molar conductivity at infinite dilution was used, whereas for higher theoretical concentrations the ionic molar conductivity, obtained through the Debye-Hückel-Onsager equation, was used. For samples diluted in ultrapure water (no added ionic strength), average conductivity was assumed to be solely due to protons and bicarbonate ions coming from the dissociation of carbonic acid in water, as the volumes of solution were small enough to always be in equilibrium with atmospheric CO_2 (confirmed by pH measurements, pH 5.7). The measured conductivity values were in agreement with the pH of a water solution fully saturated with carbonic acid. This measurement was used in order to determine the value of the ionic strength to be used in the fitting procedure for the sample in ultrapure water.

3.2.4 AR-SHS measurements

Second harmonic scattering measurements were performed on the same AR-SHS setup as described in chapter 2.3.3. In this chapter, the fundamental laser wavelength was $\lambda = 1028$ nm and the average laser power at the sample position was set to 60 mW. Before the SH light was detected at the photomultiplier tube it had to pass an ET525/50, Chroma filter. Data points were acquired using $30 \cdot 1$ s acquisition time with a gate width of 10 ns. The scattering patterns were normalized according to equation 2.18 in chapter 2.3.3. All other measurement parameters where the same as described in chapter 2.3.3.

3.2.5 Molecular dynamics simulations

To support findings obtained by AR-SHS measurements, we also carried out realistic all-atom molecular dynamics simulations. Investigating the water orientation at SiO_2/water interface, we prepared a simulation setup consisting of two SiO_2 slabs (55 Å $\cdot$ 39.82 Å) modeled as quartz surfaces with (101) crystal face that were separated by a ~55 Å thick aqueous NaCl solution. The obtained results are averaged over both identical solid/liquid interfaces present in the system.
The recently developed force field for quartz (101) surfaces [64] allowing simulations over the wide range of pH values (at pH equal to the point of zero charge (~2.5-4) and higher) has been applied and improved to adopt the electronic continuum correction, ECC (also known as model with scaled charges to 75% of their nominal values) [189]. The latter accounts for usually missed solvent polarization effects in nonpolarizable force fields, which can significantly influence interactions of charged species including charged surfaces. A general approach how to apply ECC to the modeling of solid/liquid interfaces has been described previously

for TiO$_2$ systems, [190] while a study dedicated to „ECC-quartz" force field is currently under preparation. Note that the only modifications to the original force field [64] are modified partial charges of surface atoms, while all other parameters remain the same. Compatible ECC models were also used for Na$^+$ and Cl$^-$ ions, [191] while the rigid SPC/E model of water was employed as the solvent [192]. The charge scaling introduced by ECC significantly improves the interactions of multivalent ions (divalent, trivalent, ...) while its effect on monovalent ions is minor. We confirmed that the results presented here with ECC for NaCl are very similar to those we obtained with the original force field for quartz (101) [64]. The number of surface atoms (apart from removed silanol hydrogens to design a surface charge) and water molecules was the same in all simulations, and only the number of Na$^+$ and Cl$^-$ ions was varied to compensate a negative surface charge and yield a specific bulk ionic concentration. All the simulations were 50 ns long after 5 ns equilibration of prepared structures. Other simulations settings were similar to those used in Refs. [64, 190].

To probe the pH and ionic concentration effects on the water orientation at the interface, we performed two sets of simulations. In the first set, we varied a surface charge of quartz (101) surfaces via the deprotonation of selected surface silanols as described previously [64]. The bulk ionic concentration in these simulations was approximately constant (0.1-0.15 M). In the second set, we compared four different ionic concentrations ranging from 0.05 to 0.31 M at the one selected surface charge density (-0.06 C/m^2). While experiments could be performed only up to 1 mM NaCl concentration, computer simulations of a limited sample of 3745 water molecules and dozens of ions face the opposite limitations- already just one ion pair in the bulk region of our box generates a concentration ~0.02 M, and we are therefore restricted to higher bulk concentrations. We were however able to approach the ultimate limit of low bulk concentration of the salt by modeling a system with just the number of Na$^+$ counterions needed to compensate the negative surface charge and no Cl$^-$ in the system. Such a system mimics the effect of added NaOH to pure water, with all the OH$^-$ groups attached to the surface. We admit that this setup is a bit unrealistic, as any Na$^+$ outside of the interfacial region makes the interfacial charge unbalanced, but it represents successfully the salt solution close to infinite dilution.

3.3 Experimental results

Before describing the results, we briefly summarize some of the important aspects of the AR-SHS model; more details can be found in chapter 2.3. In a nonresonant AR-SHS experiment, the fundamental frequency of a laser beam interacts with a liquid dispersion containing particles. In regions where the centrosymmetry of the material is broken - typically at the interface between the particles and the liquid - SH photons at half the wavelength of the fundamental beam will be generated. These photons are then collected as a function of the scattering angle (θ), defined as the angle between the sum of the incoming **k**-vectors of the fundamental beam and the **k**-vector of the scattered SH light. Under nonresonant conditions, the second-order polarization depends on the electron density in the medium, [103] which

implies that the SH response is of the same order of magnitude for every noncentrosymmetric molecule in the sample. However, since the SH intensity scales quadratically with the number density, in most cases the majority of the SH signal intensity is due to water molecules at the interface, as the number of noncentrosymmetrically distributed surface groups is much smaller than the number of noncentrosymmetrically distributed water molecules [183]. In an aqueous solution, the nonresonant SHS signal then arises from the net orientational order of water molecules along the surface normal. Two types of interactions will contribute to this orientational order of water: The orientational order induced by electrostatic field interactions, either at the surface or in the bulk (present in the effective third order particle susceptibility, denoted as $\Gamma^{(3)'}$, and the orientational order induced by all other (chemical) interactions confined to the particle surface plane (represented by the second-order particle surface susceptibility $\Gamma^{(2)}$ that contains the surface susceptibility $\chi^{(2)}$. A third type of effect could be in principle considered, such as a reactant/product gradient along the surface normal; however, such an effect would be mostly noticeable outside of equilibrium conditions and/or during a chemical reaction, which is outside the scope of the present chapter. The scattered intensity of the second harmonic can be expressed as in equation 2.8 in chapter 2.3.1. The scattered intensity for the two independent polarization combinations PPP and PSS (the first letter refers to the polarization state of the SH beam and the second and third letter refer to that of the fundamental beam; P is parallel to the detector plane [114]) is given in equations 2.14 and 2.15 in the same chapter. By definition, $\Gamma^{(3)'}$ is directly related to the surface potential Φ_0, and $\chi^{(2)}$ contains information about interfacial oriented water, limited to the water molecules that experience an orientational change due to chemical interactions with the silica surface [113]. By fitting polarimetric AR-SHS patterns in two different polarization combinations as described by equations 2.14 and 2.15, and knowing the radius of the particle as well as the ionic strength of the solution, unique values for both Φ_0 and $\chi^{(2)}_{s,2}$ can be extracted (see Ref. [114] and chapter 2.3 for more details). Note that all patterns are normalized with respect to the water SSS pattern, which does not influence the value of $\chi^{(2)}_{s,2}$ or Φ_0, as detailed in the chapter 2.3.3. This ensures a comparison to other samples and experiments, and it corrects for any change in the experimental geometry (such as small variations in beam alignment or sample position). We also note that the model assumes an exponential decay in the diffuse layer, [113] which is a common term for all models [193]. For the convention on the sign of $\chi^{(2)}_{s,2}$, we use the following: Negative for water molecules with O atoms pointing toward the surface (dipole moment pointing away from the surface) and positive for water molecules with H atoms toward the surface (dipole moment pointing toward the surface). This sign convention arises from a comparison with imaginary values obtained from SFG studies [154]. Parts A and B of Figure 3.1 show AR-SHS scattering patterns obtained for solutions of 300 nm diameter SiO_2 particles at different pH values. The pH was adjusted through addition of NaOH and no additional salt was added to the solutions. Increasing pH promotes deprotonation of the silanol groups at the surface, leading to a larger negative surface charge density of the SiO_2 particles. The solid lines are fits to equations 2.14 and 2.15, and the values for all experimental parameters used for the fits are summarized in 8.1.1 in the Appendix. The normalized SHS intensity directly relates to the number of oriented water molecules at the interface.
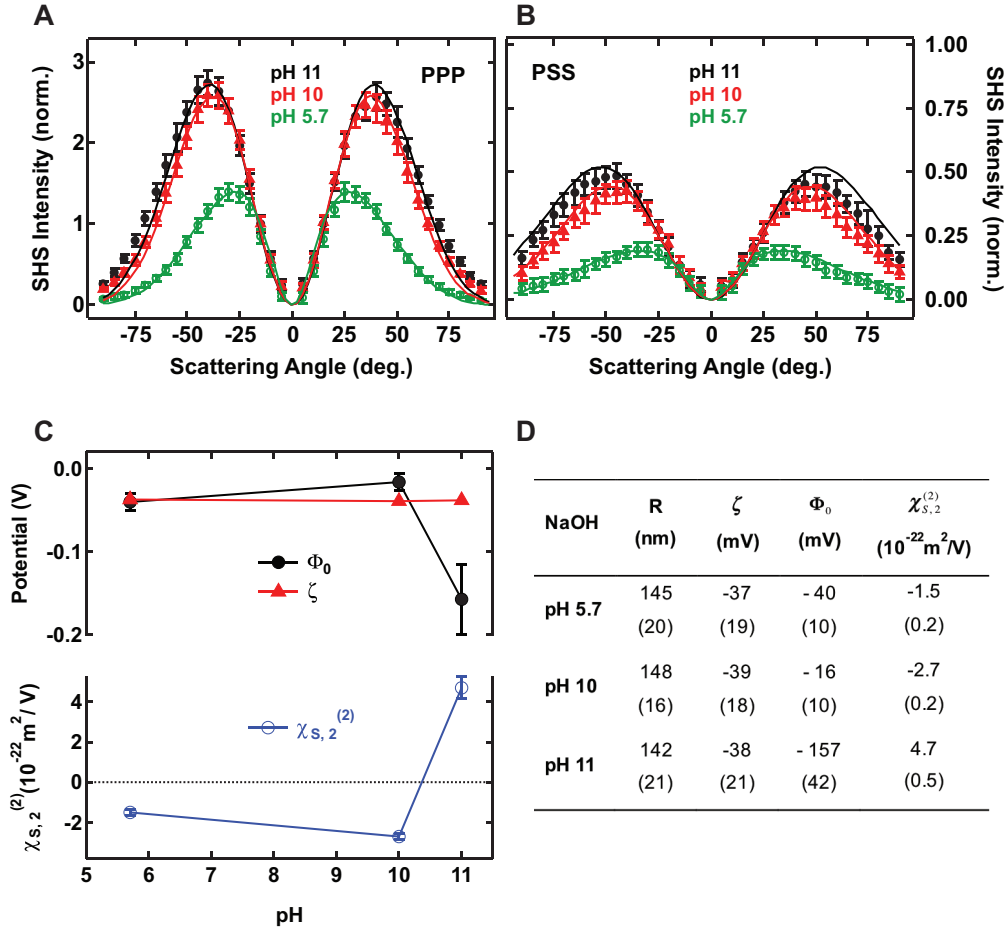
Figure 3.1 – AR-SHS patterns for silica particles in an aqueous solution. SH scattering patterns of 300 nm diameter SiO$_2$ particles as a function of pH in (A) PPP polarization combination and (B) PSS polarization combination. Black plain dots: pH 11. Red plain triangles: pH 10. Green open circles: pH 5.7. pH was adjusted through NaOH addition. The particle density was kept constant for each sample and equal to $3.5 \cdot 10^{10}$ particles/mL. All measurements were performed at $T = 23°C$. All the parameters used for the fits, including ionic concentrations, are summarized in Tables 8.1 and 8.2. Error bars represent the standard deviation from 30 measurements. Solid lines represent the fit to the data points using the AR-SHS model. (C, top) Surface potential Φ_0 and zeta-potential ζ. (C, bottom) Surface susceptibility $\chi_{s,2}^{(2)}$ as a function of pH. The values are extracted from the fit of data of parts A and B, where error bars represent error on the values as estimated from fitting the data ± standard deviation. (D) Table summarizing the radius R, zeta-potential ζ, surface potential Φ_0 and the surface susceptibility $\chi_{s,2}^{(2)}$ for different pH conditions. Numbers in brackets pertain to measurement errors as detailed in section 2.3.4.

Parts A and B of Figure 3.1 show an increasing normalized SHS intensity with increasing pH. The obtained values of both Φ_0 and $\chi_{s,2}^{(2)}$ from the fits of PPP and PSS patterns are plotted in Figure 3.1 C as a function of pH. Figure 3.1 C also shows ζ-potential values measured by electrophoretic light scattering from the same samples. All values are summarized in

Figure 3.1 D for easier comparison. The negative valued ζ-potentials are almost unchanged from pH 5.7 to 11 ($\sim$ -38 mV). For these particles, the isoelectric point ($\zeta = 0$ mV) is reached at pH= 3, as given by electrokinetic measurements. The surface potential has the same sign as the ζ-potential. However, contrarily to the ζ-potential, the obtained surface potential values vary as a function of pH showing two distinct behaviors: one where the ζ- and Φ_0-potentials are very close in magnitude (pH 5.7 and 10) and one where they deviate significantly. This behavior is also shown in the obtained $\chi_{s,2}^{(2)}$ values: pH 11 shows positive values of $\chi_{s,2}^{(2)}$, corresponding to water hydrogen atoms oriented toward the surface, while milder pHs (5.7 and 10) show negative values of $\chi_{s,2}^{(2)}$, corresponding to water hydrogen atoms oriented away from the surface, and oxygen atoms facing the surface.

We also performed similar measurements at constant pH while varying the ionic strength. Parts A and B of Figure 3.2 show SHS scattering patterns for solutions of 300 nm diameter SiO_2 particles at pH 10, where different amounts of NaCl were added. In this case, the surface charge density is mainly expected to be set by the presence of NaOH and to a minor extent by the additional Na^+ ions, which can facilitate the deprotonation of surface silanol groups through electrostatic screening and stabilization of the SiO^- group [95]. On the basis of values of surface charge densities measured for a fixed pH and different NaCl concentrations, [95] this latter effect can be estimated to $\sim$10% of the total deprotonation and will depend on the range of salt concentration and the size of the particles, as well as the nature of the cation [187, 194]. It can be seen that the normalized SHS intensity decreases with increasing salt concentration, indicative of a decrease in the amount of ordered water molecules around the surface of the SiO_2 particles. Figure 3.2 C shows the obtained fit values for the surface potential and the second-order susceptibility element representative of the molecular orientation of interfacial water. The measured ζ-potential values are also plotted. All values are summarized in Figure 3.2 D. For the two lowest salt concentrations both potentials are similar in magnitude. For 1 and 10 mM NaCl, however, the magnitude of the surface potential becomes much higher than the ζ-potential. Another interesting observation is that the sign of $\chi_{s,2}^{(2)}$ changes when salt is added. In the case where no salt is added at a fixed pH of 10, a negative sign of $\chi_{s,2}^{(2)}$ indicates a situation where water molecules are mostly oriented with their hydrogen atoms away from the surface. With the addition of NaCl, and even for the smallest quantity (0.1 mM), the sign of this parameter is inverted and points to a shift in the water orientation, where the hydrogen atoms are oriented toward the surface.

3.4 Simulation results

Computer simulations provide molecular details of the interface and help the experiment in deciphering the contribution of oriented water molecules at a given distance from the surface to the nonlinear optics signal (i.e., $\chi_{s,2}^{(2)}$ or Φ_0). Because a model of $\sim$300 nm diameter colloidal SiO_2 is not available, we utilized our model of the flat (101) quartz surface (see section 3.2.5). The flat geometry is well justified by the large size of the colloidal particles, and the terminations by silanol groups are similar in both cases, [195] though more defects must be
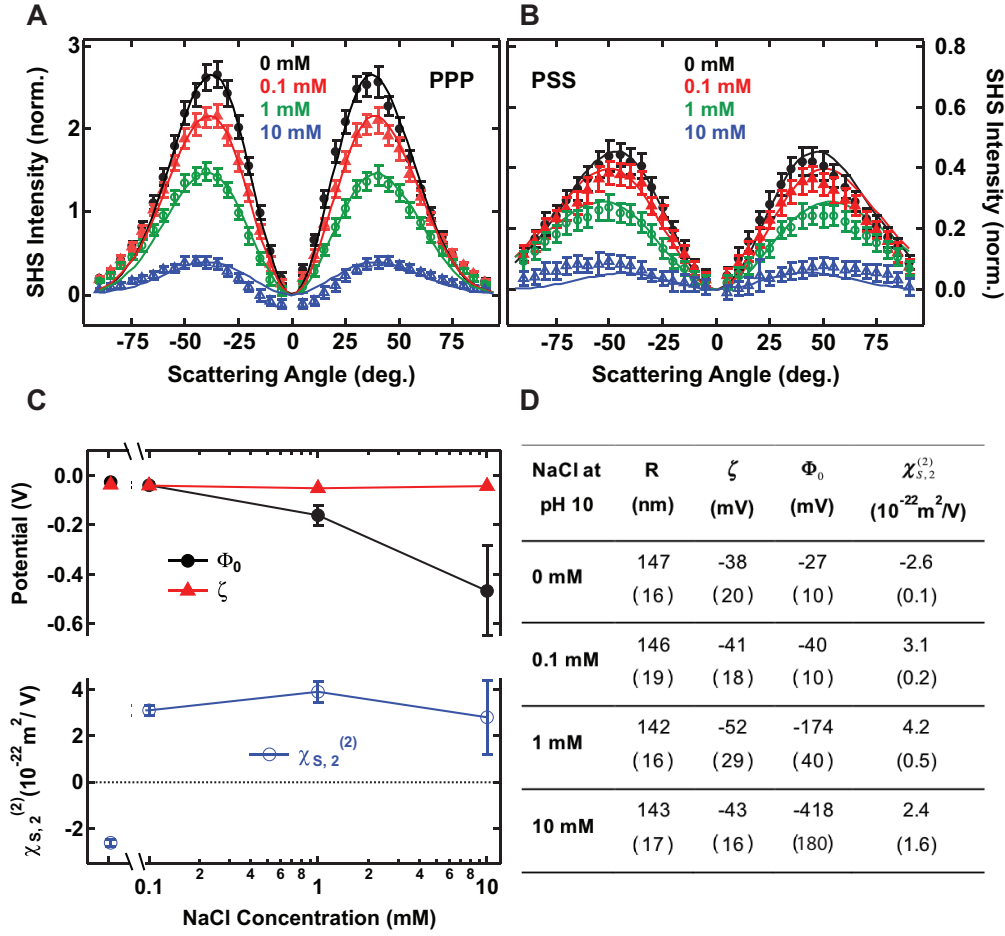
Figure 3.2 – Scattering patterns of 300 nm diameter SiO$_2$ particles in a pH 10 solution as a function of NaCl concentration in (A) PPP polarization combination and (B) PSS polarization combination. Black plain dots: 0 mM NaCl. Red plain triangles: 0. mM NaCl. Green open circles: 1 mM NaCl. Blue open triangles: 10 mM NaCl. pH was adjusted through NaOH addition. The particle density was kept constant for each sample and equal to $3.5 \cdot 10^{10}$ particles/mL. All measurements were performed at $T = 23°C$. All the parameters used for the fits are summarized in Tables 8.1 and 8.3. Error bars represent the standard deviation from 30 measurements. Solid lines represent the fit to the data points using the AR-SHS model. (C,top) Semilog plot of surface potential Φ_0 and zeta-potential ζ. (C, bottom) Surface susceptibility $\chi_{s,2}^{(2)}$ as a function of NaCl concentration for fixed pH = 10. The values are extracted from the fit of data in parts A and B. Error bars represent error on the values as estimated from fitting the data ± standard deviation. (D) Table summarizing the radius R, zeta-potential ζ, surface potential Φ_0, and the surface susceptibility $\chi_{s,2}^{(2)}$ for different salt conditions. Numbers in brackets pertain to measurement errors as detailed in section 2.3.4.

expected for amorphous and spherical particles. The density of silanol groups for perfect (101) quartz (5.8 OH/nm^2 for neutral surface, 5.1 OH/nm^2 for -0.12 C/m^2 negative surface [64]) is close to the value 4.9 OH/nm^2 reported for amorphous silica [196].

The signal of each layer is proportional to the „dipole concentration" given by a product of the number density of water molecules, water dipole orientation (the cosine of the angle between the water dipole vector and z-axis with positive values indicating hydrogens facing the solid surface, i.e. as in the experiment), and the dipole moment of SPC/E water model, which equals 2.35 D (1 D = 3.336 $\times 10^{-30}$ Cm). The running integral of the dipole concentration provides an indicator for the buildup of the total SHS intensity. Indeed, the SHS intensity is by definition given as the square of the absolute value (magnitude) of the summed nonlinear second order and third order polarization (emitted at the second harmonic frequency). We then assume that the sum of the dipoles in a certain volume is proportional to the second order and third order polarization (emitted at the second harmonic frequency), and as such the SHS intensity is proportional to the square of the running integral of the dipole concentration [107]. The interfacial plane at z = 0 corresponds to the average position of surface silicon atoms. MD simulations were carried out for surface charge densities 0, -0.03, -0.06, and -0.12 C/m^2. Using surface titration experiments we can link these simulations to pH ~ 4, 8.5, 9.4, and 10.1, respectively, which allows us to compare simulation and experimental data, though the simulation and experimental conditions cannot be matched exactly due to differences in surface geometry. A simulation of the quartz surface in pure water is also added for comparison.

The results obtained from the molecular dynamics simulations are summarized in Figure 3.3. The left-hand panels (A, B, C) display effects of changing surface charge density, while the right-hand panels (E, F) display effects of changing the ionic strength at fixed surface charge density. Figure 3.3 A shows the axial density profile of water oxygens, i.e., the laterally averaged density of water as a function of distance from the quartz (101) surface. The axial density of water is nearly independent of the surface charge (shown in Figure 3.3 A) and salt concentration (not shown). The positions of the first two clearly evident water layers are z ~ 3.5 Å and z ~ 6 Å, and are invariable. Figure 3.3 B shows the dipole concentration as a function of distance for different surface charge densities. A positive value indicates water molecule with hydrogens facing the surface, while a negative value indicate a reversed molecular orientation with oxygens facing the surface. These features can thus be used to connect to the sign of $\chi_{s,2}^{(2)}$. It can be seen that the curves for low charge density are more negative, while increasing the charge density brings them up to positive values. Figure 3.3 C shows the running integral of the dipole concentration, which reaches a plateau away from the interface, where the average orientation of water molecules is zero (isotropic). This plateau value is an indicator of the total SH intensity and increases with surface charge density. Figure 3.3 E shows the ionic strength dependence of the interfacial dipole orientation for a fixed surface charge density of -0.06 C/m^2, and for the salt concentration range used in the simulations (0.05 to 0.31 M NaCl). The water orientation with hydrogens facing the surface is less pronounced at higher concentrations, leading also to decreasing plateau values of the running integral of the dipole concentration (Fig. 3.3 F) with salt concentration.
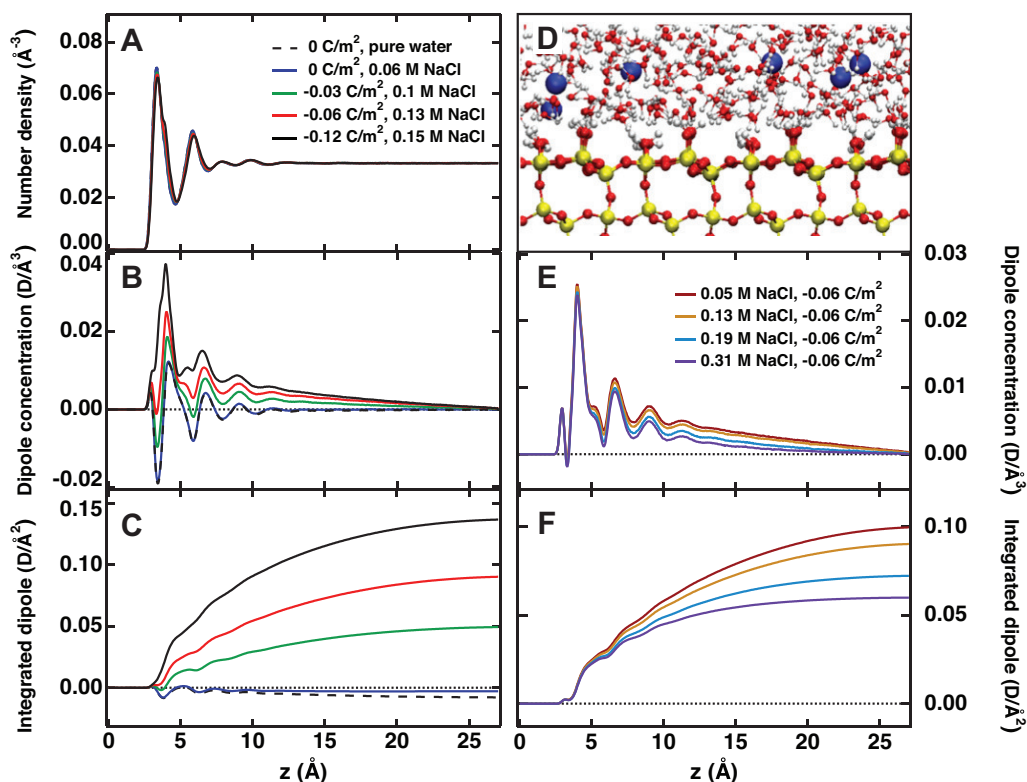
Figure 3.3 – Results obtained from molecular dynamics simulations: (A) Number density of water, (B) dipole concentration, and (C) integrated dipole as a function of distance z from the quartz (101) surface for different surface charge densities at similar bulk ionic concentration. (D) Snapshot of the quartz (101) surface at 0.34 M and -0.12 C/m^2. (E) Dipole concentration and (F) integrated dipole as a function of distance from the quartz (101) surface for different bulk ionic concentrations at the same surface charge density of -0.06 C/m^2.

3.5 Discussion

3.5.1 Surface potential and water orientation in low ionic strength conditions

In mild pH cases (5.7 and 10) and low ionic strength (<1 mM), the values of the surface potential are very close to the ζ-potential values. Negative values of the ζ-potential are found for colloidal SiO$_2$ surfaces [95, 197, 198] as expected from the negative surface charge densities [78, 199, 200]. As mentioned in the introduction, the slip plane where the ζ-potential is measured is considered to be located in the first few water layers away from the surface plane where the surface potential is measured. Therefore, with both values being very similar, it is highly unlikely that there is any buildup of counterions close to or at the surface. This means there is no charge condensation or Stern layer formed. By charge condensation layer, we refer to a packed layer of ions that is at some distance away from the interface, also known as an outer-sphere complex. We note here the specific case of direct counterion adsorption, also referred to as an inner-sphere complex, which would lead to (partial) surface

Table 3.1 – σ_0^{GC} and percentage of deprotonation as a function of pH and salt concentration

NaOH	σ_0^{GC} [mC/m^2]	deprotonation [%]
pH 5.7	-0.35	0.04
pH 10	-0.45	0.06

NaCl conc. at pH=10 [mM]	σ_0^{GC} [mC/m^2]	deprotonation [%]
0	-0.77	0.10
0.1	-1.63	0.21

charge neutralization. This surface charge neutralization effectively decreases the electric field extending in the solution and therefore results in a reduction of the surface potential. However, this effect is expected to be small for small concentrations of counterions in solution. The negative values of $\chi_{s,2}^{(2)}$ are indicative of a net dipole moment pointing away from the surface, with water molecules mainly oriented with their oxygen atom toward the surface. This water orientation in low ionic strength conditions can be rationalized by considering the hydrogen bonding between the silanol groups and the oxygen atom of water. This is illustrated in Figure 3.4 A. Having established that there is no significant accumulation of counterions at the interface, for this particular case, the simplest model that describes the relation between surface charge and surface potential is given by the spherical Gouy-Chapman model. Ohshima derived an approximate analytical solution for the potential distribution around a sphere with arbitrary potential, [193] where the surface charge density is related to the surface potential by

$$\sigma_0^{GC} = \frac{2\varepsilon_r \varepsilon_0 \kappa k_B T}{e} \sinh\left(\frac{ze\Phi_0}{2k_B T}\right) \cdot \left[1 + \frac{1}{\kappa R} \cdot \frac{2}{\cosh^2\left(\frac{ze\Phi_0}{4k_B T}\right)} + \frac{1}{(\kappa R)^2} \cdot \frac{8\ln\left(\cosh\left(\frac{ze\Phi_0}{4k_B T}\right)\right)}{\sinh^2\left(\frac{ze\Phi_0}{2k_B T}\right)}\right]^{\frac{1}{2}} \quad (3.1)$$

where σ_0^{GC} is the surface charge density in the spherical Gouy-Chapman model, R the particle radius, ε_r the relative permittivity of the solvent (water), ε_0 the permittivity of vacuum, κ the Debye parameter, e the elementary electric charge, z the valence of ions, k_B the Boltzmann constant, and T the temperature. Knowing Φ_0, we can compute σ_0^{GC}, and the expected degree of deprotonation. Table 3.1 shows the values for σ_0^{GC} as a function of pH and NaCl concentration, as well as the corresponding percentage of surface deprotonation. Table 3.1 shows that the surface charge densities for the low ionic strength regime range from -0.35 to -1.63 mC/m^2, which correspond approximately to 0.04-0.2% deprotonation, assuming a silanol density of 4.9 OH/nm^2 as reported by Zhuravlev, [196] who showed that this value is a constant for a fully hydroxylated amorphous surface and does not depend on the type of silica. These surface charge densities values are in the range of reported values in the literature for salt free and low salt dispersions [201, 202] and agree with the notion that the majority of the silanol groups remain protonated [203, 204]. Thus, in mild pH conditions and low ionic strength, only a very small fraction of the silanol groups are deprotonated, and the dominant orientation of water dipoles in the first layer away from the surface is due to hydrogen bonding between the protonated silanol groups and the oxygen atoms of water.

3.5.2   Surface potential and water orientation in high ionic strength conditions

In higher pH conditions (pH 11) and with increasing amounts of NaCl ($\geq$1 mM), we observe a much higher magnitude for the surface potential than the ζ-potential. The distance between the slip plane and the surface plane is 1-3 water molecules [72]. The differences $\parallel \Phi_0 - \zeta \parallel$ of 119 mV (pH 11), 122 mV (1 mM NaCl), and 375 mV (10 mM NaCl) means that the electrostatic field in this thin layer must be on the order of 108-109 V/m. This large electrostatic field indicates the presence of a condensed layer of charges [72].

This hypothesis is further supported by the fact that higher values of surface potential are found for both pH 11 and for pH 10 + 1 mM NaCl and above, which correspond to a similar concentration of sodium ions (respectively 1 mM and 1.1 mM Na$^+$). Such a charge condensation layer of positive counterions close to the negative surface influences water orientation. Positive values of $\chi_{s,2}^{(2)}$ here indicate a net dipole moment with the hydrogens pointing toward the surface, thus effectively interpreted as a net flip in the surface water orientation with respect to the low ionic strength situation (Figs. 3.1 C and 3.2 C). This flip in water orientation is illustrated in Figure 3.4 B and arises from the formation of a charge condensation layer composed of hydrated sodium ions. As the hydration shells of the Na$^+$ ions overlap with the surface hydration layer, the Na$^+$ ions disrupt the hydrogen bonding between the silanol groups and the water molecules and a water layer with a net dipole moment facing the surface results.

Having determined experimentally that here we are dealing with a Stern layer, we can compute the charge density on the slip plane, σ_d, assuming that the slip plane and the outer Stern layer coincide, using equation 3.1 and replacing Φ_0 by ζ and σ_0^{GC} by σ_d. Values for σ_d are shown in Table 3.2. Approximating the surface of the particle and the Stern layer as two plates of a spherical capacitor, it is also possible to use the equation describing a spherical capacitor to relate the potential drop in the Stern layer ($\phi_{\text{drop}}^{\text{GCS}} = \Phi_0 - \zeta$) to the surface charge density at the surface, σ_0^{GCS}:

$$\phi_{\text{drop}}^{\text{GCS}} = \frac{\sigma_0^{\text{GCS}} R^2}{\varepsilon_{\text{S/W}} \varepsilon_0} \left(\frac{1}{R} - \frac{1}{R + d_{\text{Stern}}} \right) \tag{3.2}$$

where σ_0^{GCS} is the surface charge density in the presence of a charge condensation layer, R is the radius of the particle, ε_0 is the vacuum permittivity, and d_{Stern} is the thickness of the capacitor. Contrary to the GC case, which assumes the permittivity of bulk water because of the small electric fields generated at the interface, in the GCS case the higher electric fields will orient the water dipoles and therefore change the dielectric constant of the first few layers adjacent to the interface. Therefore, we use here $\varepsilon_{\text{S/W}}$ as the dielectric constant at the silica/water interface ($\varepsilon_{\text{S/W}} = 43$) [205]. Assuming a Stern layer thickness range of $0.3 < d_{\text{Stern}} < 0.9$ nm (between one and three water molecules) one obtains a range of values for σ_0^{GCS}, summarized in Table 3.2.

Table 3.2 shows that the computed surface charge densities range from -50 to -476 mC/m^2 depending on the choice of the Stern layer thickness. These values correspond to deprotonation degrees between 6 and 61%. While the deprotonation value for [NaCl] = 10 mM seems high for $d_{\text{Stern}} = 0.3$ nm (maximum 25% deprotonation is expected at pH 10 and 0.1 M NaCl), [95]
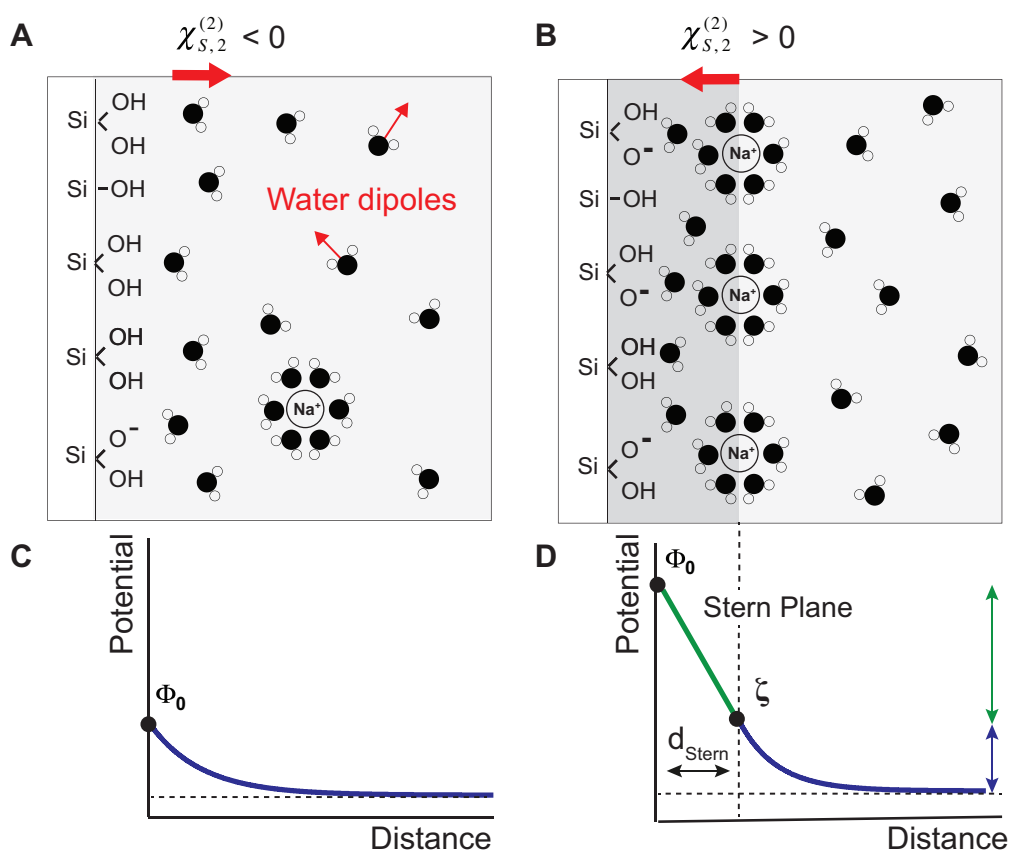
Figure 3.4 – Schematic view of a SiO_2/water interface for (A) Low surface charge density and low Na^+ concentration and (B) High surface charge density and high concentration of Na^+ ions. In both cases the surface keeps a majority of silanol groups protonated and is overall negatively charged. (A) Water molecules are preferably oriented with their oxygen toward the surface. The net water dipole summed over all water molecules is then oriented away from the surface (red arrow). (B) Water molecules are preferably oriented with their hydrogens toward the surface. The net water dipole is oriented toward the surface (red arrow). The potential decay profile is shown in the Gouy-Chapman (C) or Gouy-Chapman-Stern model (D). In the first case, the ionic strength in solution is low and the surface potential decays exponentially with distance. At higher ionic strengths, the GCS approximation is considered, where the potential decay profile integrates two components: a steep decay associated with the strong electric field in the charge condensation layer, known in the model as the Stern layer, and a more gradual one at larger distances from the interface. We approximate here the potential at the Stern plane to be equal to the ζ-potential.

all the other results are comparable to surface charge densities that have been measured by potentiometric titrations for SiO_2 particles in similar conditions, [78, 94, 199, 206] keeping in mind that these values are strongly size-dependent below 30 nm diameter [207, 208]. Interestingly, one can see that surface charge densities in both pH 11 case and the 1 mM NaCl case at pH 10 are very similar, which is a direct result of the similar surface potential values obtained by AR-SHS (Figs. 3.1 C,D and 3.2 C,D). Considering nearly the same concentrations of ions at

Table 3.2 – σ_d, σ_0^{GCS} and percentage of deprotonation as a function of pH and salt concentration

NaOH	σ_d [mC/m^2]	d_{Stern} [nm]	σ_0^{GCS} [mC/m^2]	deprotonation [%]
pH 11	-3.2	0.3	-151	19.2
		0.9	-50.3	6.4

NaCl conc. at pH=10 [mM]	σ_d [mC/m^2]	d_{Stern} [nm]	σ_0^{GCS} [mC/m^2]	deprotonation [%]
1	-5.0	0.3	-155	19.7
		0.9	-51.6	6.6
10	-11.5	0.3	-476	60.6
		0.9	-159	20.2

these two conditions (1 mM Na$^+$, OH$^-$ at pH 11 vs 0.1 mM of Na$^+$, OH$^-$ + 1 mM Na$^+$, Cl$^-$ at pH 10), this indicates that the ionic strength and the interfacial presence of Na$^+$ ions, is here the main element in setting the magnitude of the surface potential.

While both base and salt treatment show a similar increase in the surface potential value, similar surface charge densities for a given value of d_{Stern} and similar orientation of the surface water molecules indicating the presence of a charge condensation layer, the SH intensity change as a function of the ionic strength does show some differences, which has implications on the thickness of this charge condensation layer. In the case of the basic treatment, the surface charge becomes increasingly more negative with increasing NaOH addition. This higher surface charge density is then compensated by screening by the Na$^+$ cations, which additionally participate in orienting the water molecules with their hydrogens facing the surface (Fig. 3.4 B). For a higher surface charge density, we can thus expect a larger number of water molecules to be oriented with their hydrogen facing the surface to counterbalance for the presence of deprotonated silanols. The increase in SH signal intensity as a function of pH (Fig. 3.1 A,B) thus reflects the electric-field induced polarization of the water molecules at the interface as previously described for flat surfaces [137, 209]. In the case of salt addition at fixed pH, we observe a decrease in SH intensity (Fig. 3.2 A,B) that physically corresponds to a decrease in the number of the oriented water molecules. Such a decrease in ordered water is then indicative of more efficient screening of the surface charge by more concentrated salt solution and shrinking of the diffuse layer. This decrease in the amount of ordered water is already visible between 0 mM NaCl at pH 10 and 0.1 mM NaCl at pH 10, while it is not noticeable between pH 10 and 11 when no salt is added. This indicates that the thickness of the charge condensation layer will be dependent on the nature of the added compound (NaOH/NaCl), most likely because of modifications of the surface charge density. Additional information that can be extracted from the AR-SHS plots is the relative variation of the thickness of the charge condensation layer and of the surface charge density. From equation 3.2, a decrease in the thickness would directly result in a decrease of the magnitude of the surface potential. However, since we observe an effective increase in magnitude of surface potential with increasing salt concentration, this implies that, in this range of salt concentrations, the increase in magnitude of surface charge density must be larger than the decrease in the charge conden-

sation thickness. Note that at higher salt concentration (>10 mM), the opposite behavior has been observed: [95] While the surface charge density still increases with increasing salt concentration, the decrease in the thickness of the charge condensation layer overall dominates, thus resulting in a decrease of the surface potential with increasing salt concentration. In our case, due to the limited range of stability of our colloidal suspensions, we could not explore salt concentration ranges above 10 mM. It is also important to note that Brown et al. [95] use particles below 10 nm diameter, and as the surface charge density is strongly size-dependent for particles below 30 nm diameter, [207, 208] we can expect a different relative variation of the surface charge density and the charge condensation layer thickness for different sizes of particles, which could imply a different dependence of the surface potential on the salt concentration. Further measurements are thus needed to test the size dependence of the surface potential at various ionic strengths. Similarly, the surface charge density as well as the pKa of different silanol groups is expected to change depending on the preparation of the surface prior to the experiment, [137, 203, 210] which could be additional factors playing a role in the observed trends for the surface potential. One last observation that can be made on the basis of the AR-SHS results is that the transition between the low ionic strength regime, where $\parallel \Phi_0 \parallel \approx \parallel \zeta \parallel$ and the high ionic strength regime, where $\parallel \Phi_0 \parallel \gg \parallel \zeta \parallel$, occurs for electrolyte concentrations between 10^{-4} and 10^{-3} M, while it is generally considered for flat surfaces (as for example metal electrodes) that the GC model can be used up to electrolyte concentrations of $10^{-3} - 10^{-2}$ M [50, 72, 211].

3.5.3 Comparison of AR-SHS experiment and MD simulation

We turn now to the discussion of the results obtained through simulations. Despite the fact that simulation results for one selected crystal face of quartz surface are used when comparing to experimental data of spherical silica nanoparticles, the trends observed in simulations are in line with experimental findings. The lowest charge densities and salt concentrations studied experimentally are not reachable with the MD simulations (see 3.2.5 for details), but we still can discuss the experimental trends in the presence of only NaOH or for very small salt concentrations with the help of the molecular picture of this model interface. Figure 3.3 A shows that there is interface induced water layering as witnessed by the two peaks at ~3.5 and 6 Å. The orientational first peak in Figure 3.3 B can be easily connected to $\chi_{s,2}^{(2)}$, as by definition $\chi_{s,2}^{(2)}$ contains the orientational order induced by all chemical interactions confined to the particle surface plane. The first peak in Figure 3.3 B for surface charge densities $\sigma = 0$ and -0.03 C/m^2 is negative, in agreement with negative $\chi_{s,2}^{(2)}$ observed experimentally at pH 5.7. The negative signal at low pH is further supported by simulations of neutral quartz surface ($\sigma = 0$ C/m^2), where even the integrated dipole is very slightly negative, both for 0.06 M NaCl solution (represented by only 4 ion pairs in the simulated system) and even more for pure water (which is the limiting case of low salt concentration for neutral surfaces). The first peak for $\sigma = -0.06$ C/m^2 is close to zero and does not predict the negative $\chi_{s,2}^{(2)}$ seen experimentally at pH 10 in absence of salt, but the concentration dependence of the second peak easily explains the positive $\chi_{s,2}^{(2)}$ at larger concentrations. Finally, based on the positive first peak

at $\sigma = -0.12\,\text{C/m}^2$, we predict that at very high pH values, even in the absence of salt, $\chi_{s,2}^{(2)}$ should be positive, in agreement with Figure 3.1 C for pH 11. Figure 3.3 C also agrees with the measured SH intensity shown in Figure 3.1 A,B where increasing pH (and thus more negative surface charge density) leads to an increase in the total SH intensity, indicative of a larger number of overall oriented molecules. Parts E and F of Figure 3.3 capture, as much as possible using our MD setup, the experimental drop in overall SHS intensity with salt concentration (Fig. 3.2 A,B), indicative of more efficient charge screening and less overall oriented water. Figure 3.3 E shows that for higher charge densities (pH) the magnitude and sign of the first peak for a given pH is insensitive to the salt concentration. The second peak ($\sim 6\,\text{Å}$) and the water orientation further out displays however a decreasing magnitude with increasing salt concentration. This behavior is also shown in the curves in Figure 3.3 F, which overlap in the first peak but start to deviate at the second peak and gain less signal at distances of ~6-20 Å for higher salt concentrations. In this high concentration range (>10 mM), the weakening of the orientation with hydrogens facing the solid with increase in concentration also agrees with the drop in susceptibility measured experimentally from 1 to 10 mM (see Fig. 3.2 C,D). These effects were observed for all simulated ionic concentrations and surface charge densities. Simulations indicate Na$^+$ (a strong sorbent) adsorbing as an inner-sphere complex at height ~3.5 Å, i.e., in the location of the first water layer, and also as outer-sphere complex at distances around 5.5 Å, i.e., close to the position of the second water layer (not shown). With increasing pH and salt concentration, the surface attains more negative charge. While less negative surface charge can be easily compensated by a few Na$^+$ ions, at more negative surfaces the compensation of the surface charge is partly hindered by repulsion among numerous adsorbed Na$^+$ ions, leading to formation of the condensed layer further from the surface and more negative surface potential, as deduced from the SHS data.

3.6 Conclusions

Nonlinear light scattering theory can be used to derive expressions for surface potential of colloidal suspensions Φ_0 and interfacial water ordering in terms of the second-order susceptibility $\chi_{s,2}^{(2)}$. This system of two variables can be solved by nonresonant polarimetric AR-SHS measurements in two different polarization combinations. Φ_0 and $\chi_{s,2}^{(2)}$ are obtained from analytical expressions and therefore do not assume any model for the distribution of ions at the interface. In this work, we report AR-SHS patterns for 300 nm diameter SiO$_2$ colloidal suspensions as a function of pH and NaCl concentration, and we support these data by MD simulations of the crystal quartz (101) surface interacting with aqueous solutions. By combining the knowledge of the parameters $\chi_{s,2}^{(2)}$ and Φ_0 with ζ, which is obtained through electrokinetic measurements, we are able to establish a description of the interface that does not rely on a specific model for the charge distribution at the interface. Between pH values close to neutral and 10, as well as at low salt concentration (<1 mM), our data indicate the presence of a diffuse layer where the surface potential is very close to the ζ-potential, and where the most favorable orientation for the interfacial water molecules is the one with the

oxygen atom facing the silanol terminated surface. At higher pH or ionic strength (pH 11 or $\geq$ 1 mM salt), we observe an increase in surface potential, while the ζ-potential changes very little, indicative of the formation of a charge condensation layer. Furthermore, values of $\chi_{s,2}^{(2)}$ indicate that interfacial water adjusts its orientation following counterion adsorption, in this case favoring hydrogen atoms facing the surface. Surface charge densities estimated through the GC or GCS model using the measured surface potential values agree with reported values in the literature. This validates our experimental approach where the surface potential values can be extracted without assuming any model for the structure of the electrical double layer. The experimental trends are nicely supported by molecular simulations, which observe that the orientation of interfacial water increases with pH and decreases with NaCl concentration, in accord with the intensity of the AR-SHS signal. The flipping of the dipolar orientation of water molecules closest the surface from orientations away from the surface (prevailing orientation due to termination of the surface by protonated silanols) at low pH to orientation toward the surface at high pH (induced by negative surface charge and the presence of Na$^+$ counterions), can be directly linked to the trends observed for the pH dependence of the surface susceptibility.

4 Characterization of the amorphous TiO$_2$ nanoparticle/aqueous interface

Colloidal nanoparticles exhibit unique size-dependent properties differing from their bulk counterpart, which can be particularly relevant for catalytic applications. To optimize surface-mediated chemical reactions, the understanding of the microscopic structure of the nanoparticle/liquid interface is of paramount importance. Here we use polarimetric angle-resolved second harmonic scattering (AR-SHS) to determine surface potential values as well as interfacial water orientation of ~100 nm diameter amorphous TiO$_2$ nanoparticles dispersed in aqueous solutions, without any initial assumption on the distribution of interfacial charges. We find three regions of different behavior with increasing NaCl concentration. At very low ionic strengths (0-10 μM), the Na$^+$ ions are preferentially adsorbed at the TiO$_2$ surface as inner-sphere complexes. At low ionic strengths (10-100 μM), a distribution of counterions equivalent to a diffuse layer is observed, while at higher ionic strengths (>100 μM), an additional layer of hydrated condensed ions is formed. We find a similar behavior for TiO$_2$ nanoparticles in solutions of different basic pH. Compared to identically sized SiO$_2$ nanoparticles, the TiO$_2$ interface has a higher affinity for Na$^+$ ions, which we further confirm with molecular dynamics simulations. With its ability to monitor ion adsorption at the surface with micromolar sensitivity and changes in the surface potential, AR-SHS is a powerful tool to investigate interfacial properties in a variety of catalytic and photocatalytic applications.

The results presented in this chapter are adapted from Ref. [151]:

4.1 Motivation

Titanium dioxide (TiO$_2$) is a semiconductor material with high physical and chemical stability, [212, 213] which makes it particularly interesting for use in aqueous environments. Titania has a broad range of applications: It is widely used as white pigment in paints, in food coloring, and in cosmetics and personal care products, such as sunscreen and toothpaste [214–216]. Furthermore, TiO$_2$ is a well-known photocatalyst, used among others in environmental remediation through photocatalytic wastewater treatment, [217–220] as building material for self-cleaning glass, [218, 221, 222] and for energy applications, such as photocatalytic water splitting [6, 223, 224]. The understanding of the surface chemical reactivity of TiO$_2$ is key to develop highly efficient, low-cost, and environmentally friendly photocatalytic devices. Thus, it is of fundamental interest to understand the microscopic structure of this semiconductor-liquid interface and how it is affected by the composition of the surrounding aqueous environment. As colloidal nanoparticles possess a high surface to volume ratio, which is beneficial in order to enhance surface-mediated chemical reactions, they are an attractive and relevant system to study in this context. Colloids in water or another fluid are stable in solution if they develop a charged layer at their surface so that the repulsive forces between the particles are strong enough to prevent aggregation or flocculation (Sterical stabilization is also possible but will not be discussed here as it requires the use of nonionic macromolecules). The surface charge of the particles depends on the pH and ionic strength of the aqueous environment and is compensated by counterions in the surrounding solution [71, 193]. This charged surface together with its counterions is called the „electrical double layer" (EDL). The EDL plays a fundamental role in driving physical and chemical processes at the interface. However, a complete picture of the EDL is still missing. Multiple models describing the EDL have been put forward, which usually simplify the complex structure of the interface by assuming a uniformly charged interface, by reducing the aqueous environment to a uniform dielectric, and by representing ions as point charges. A model frequently referred to is the Gouy-Chapman model in which the counterions are distributed in the fluid surrounding a charged surface in such a way that the potential inside the electrolyte decays exponentially [71, 213]. This charge distribution inside the EDL is called the diffuse layer (DL). As this model fails for high charge densities of counterions near the interface, a modification was proposed by Stern, which involves the formation of a layer of hydrated counterions at the surface, the so-called „Stern layer". This layer of countercharges close to the charged surface is expected to act like a parallel plate capacitor, causing a steep linear potential drop within the Stern layer [52, 57, 71, 72, 213]. Nevertheless, a complete realistic description of the EDL remains challenging, as the electrostatic environment of the interface depends on many factors, such as individual material properties comprising the local chemical nature of the surface, the amount and the type of ions as well as their solvation shells, and the behavior of the solvent, for example the orientation of water molecules at the interface [50, 57, 71, 213, 225–229]. Most of those parameters are difficult to access experimentally, especially without using the assumptions implied by the presented models [50].

The simplest approach to investigate the EDL is to use techniques measuring electrokinetic mobilities. The velocity of a suspension of particles in an applied electric field is measured and can be converted into zeta potential via the Hückel or Smoluchowski equation [57, 71, 72, 230]. In a simplified picture, [172] the zeta potential is the potential at the boundary between the solvent shell of ions and water molecules moving with the particle when an electric field is applied and the rest of the static solution. This boundary is commonly termed the shear plane. However, as the shear plane is presumed to be situated 0.3 to 1 nm away from the charged particle surface, [57, 71, 72] the knowledge of the zeta potential alone does not provide a full picture of the electrostatic environment of the investigated sample. In order to have a more complete picture of the EDL, one can also measure the surface charge density of the particle, which can be obtained by potentiometric titrations [73–77]. Yet this technique requires larger quantities of sample (on the order of hundreds of milligrams) and assumes that ions only adsorb on the surface (i.e., the sample is nonporous [73] therefore providing, at best, an upper limit for the surface charge density.

A more direct indicator of the electrostatic environment around a charged particle in a solution is the surface potential. With current experimental methods, this is a rather complicated parameter to access. Kelvin probe force microscopy (KPFM) can probe surface potentials of semiconductor/air or semiconductor/vacuum interfaces on flat surfaces. In this case, the surface potential is defined as the work function difference of the semiconductor surface and the metal tip probing the surface [82]. However, applying this technique to solid/liquid interfaces brings up practical challenges [86, 87] and is not to date applicable to particles in a solution. So far, a method that has been proved to be suitable for the measurement of surface potential of particles in aqueous environments is X-ray photoelectron spectroscopy (XPS). XPS measurements were done on colloidal SiO_2 particles in a liquid microjet by Brown et al., [94–97] assigning the charge divided binding energy difference between the Si 2p photoelectrons in an environment containing salt and the Si 2p photoelectrons at the point of zero charge to the value of the surface potential. Nevertheless, this method requires small-sized colloidal nanoparticles (~3-20 nm) and high salt concentrations of approximately >10 mM, in addition to synchrotron facilities. First ambient pressure XPS studies on anatase TiO_2 particles in a liquid jet were performed by Makowski et al., [231] examining the role of surface charge in the electronic surface band bending of the semiconductor particles in contact with an electrolyte. Soft X-ray photoelectron spectroscopy measurements with a liquid microjet were also applied to anatase TiO_2 particles in another study by Ali et al. to investigate the interaction between specific surface sites and water molecules in the aqueous environment in different pH conditions [232]. However, to the best of our knowledge no direct surface potential measurements have been performed on TiO_2 particle dispersions until now.

Second-order nonlinear optical techniques are suitable to study processes at surfaces and interfaces of centrosymmetric systems as second harmonic generation (SHG) is forbidden in centrosymmetric and isotropic media and therefore the signal arises only from the noncentrosymmetric regions at the interface [100–103]. Nonlinear second-order scattering was used to obtain information about the interfacial properties of particles in liquids by the Eisenthal group, [117] including TiO_2 particles [118]. A first attempt to measure the surface potential

of particles in a solution was done in the same group [138]. The authors collected SHG of polystyrene sulfate spheres with a wide collection angle in the forward scattering direction and extracted the surface potential by fitting their data to the Gouy-Chapman model. In a more recent work, Yang et al. [119] were the first to measure resonant angular-resolved second harmonic scattering (AR-SHS) patterns from polystyrene colloids with surface-adsorbed malachite green in water. The angular-dependent scattering pattern is strongly polarization-dependent and holds information about the size and shape of the particles [119–121].

We recently showed the universal applicability of polarimetric angle-resolved second harmonic scattering (AR-SHS) in nonresonant conditions to extract values for the surface potential Φ_0 of a particle with respect to bulk liquid, [113, 114, 136, 140, 150] with no a priori theoretical treatment to model the distribution of charges in the electrical double layer. Furthermore, AR-SHS enables one to obtain absolute values for the surface susceptibility $\chi_{s,2}^{(2)}$, which contains information about the orientation of interfacial water molecules. This nonresonant SHS technique has the advantage of being noninvasive and performed at ambient pressure on particles of a broad size range that are directly dispersed in a solution. In this work, we apply AR-SHS to semiconductor particles, showing how the surface potential and surface susceptibility of ~100 nm diameter amorphous TiO$_2$ particles evolve as a function of NaCl and pH. Three different regions can be identified with increasing ionic strength. We compare the results to SiO$_2$ particles of the same size investigated in different ionic strength conditions. Our findings are further supported with molecular information gathered by molecular dynamics (MD) simulations. The knowledge of surface potential and surface susceptibilty, together with the zeta potential and MD simulations, allow us to get a deeper understanding of the microscopic structure of the EDL around colloidal TiO$_2$ and SiO$_2$ in different salt and pH conditions.

4.2 Materials and Methods

4.2.1 Chemicals

Sodium hydroxide, (NaOH, > 99.99% trace metals basis, Sigma-Aldrich) and sodium chloride (NaCl, > 99.999%, abcr GmbH) were used as received. TiO$_2$ colloids (~100 nm diameter) were purchased already dispersed in solution from Corpuscular Microspheres Nanospheres (2.5% w/v). The purity of the sample and the absence of stabilizing surfactants was verified by elemental analysis (1.04% C, 0.31% H, and 0% N). The residual carbon is likely to be due to a small amount of dissolved CO$_2$ or residual impurities from the synthetic process. Furthermore, the elemental analysis results of the stock solution are similar to the ones obtained for a TiO$_2$ sample in powder form with 99.9% purity from a different manufacturer (US Research Nanomaterials, with elemental analysis 1.1% C, 0% H, and 0% N). This confirms that no sizable amount of surfactants is present in the as received particle suspension (before the washing process). SiO$_2$ microspheres of 100 nm diameter were purchased from Polysciences, Inc. (5.9% w/w). The SiO$_2$ and TiO$_2$ particles were washed as described in section 4.2.2.

4.2.2 Sample preparation

All procedures described hereafter used ultrapure water (Milli-Q, Millipore, Inc., electrical resistance of $18.2\,M\Omega \cdot cm$). The 2.5% w/v stock solution of colloidal TiO_2 particles was sonicated in an ultrasonic bath for 30 min (35 kHz, 400 W, Bandelin) and vortexed 2 min prior to usage. The stock was then diluted in water to a 0.5% w/v solution, where the particles were stabilized by addition of NaOH up to a final concentration of $80\,\mu M$. The 0.5% w/v dilution was then further sonicated for 10 min and vortexed 2 min. In order to remove residual ions from the synthetic procedure, nanoparticles were then collected via centrifugation and resuspended in Milli-Q water at the same concentration of 0.5% w/v. The pellet was resuspended by vortexing 5 min and sonicating for 10 min. The conductivity of the washed particles was measured as described in the section 4.2.3 to ensure that the initial ionic strength of the particle suspension was as low as possible. The TiO_2 particles were further diluted to 0.05% w/v solutions (corresponding to approximately $4.3 \cdot 10^{11}$ particles/mL) containing the desired amount of NaOH or NaCl. The pH or ionic strength of the solutions was adjusted using 0.1 mM or 1 mM solutions of NaOH and NaCl. The 0.05% w/v solutions were vortexed 2 min and sonicated 10 min, then filtered using four $0.2\,\mu m$ PES syringe filters (Filtropur Sarstedt) per 10 mL tube to remove particle aggregates. We quantified the percentage of aggregates in the 0.05% w/v dilution by dynamic light scattering experiments and find this number to be very small (0.3% of the total number of particles), indicating that only a small fraction of the sample is lost through the filtering process. After filtering, each sample was sonicated another 10 min and vortexed 2 min. The sample stability over time is dependent on the salt concentration and pH, usually with particles remaining in suspension for several days. However, in order to keep consistent experimental conditions, the TiO_2 suspensions were always prepared and measured on the same day. Corresponding water references at the same pH and ionic strength were prepared for each TiO_2 sample. For SiO_2 particle suspensions and references a similar preparation procedure was employed. The particles were washed twice, but no additional NaOH was added. The SiO_2 stock solution was diluted to a 0.06% w/v solution (corresponding to approximately $2.9 \cdot 10^{11}$ particles/mL) containing the desired amount of NaOH or NaCl. No filtering of the particles was necessary. All preparation steps and measurements were performed at room temperature.

4.2.3 Sample characterization

The particle size distribution was determined by dynamic light scattering (DLS), and the zeta potential was measured by electrophoretic measurements (Zetasizer Nano ZS, Malvern). After the filtering process, the TiO_2 colloids had a mean hydrodynamic diameter of ~120 nm with a uniform size distribution (for most samples, polydispersity index (PDI) ≈ 0.1). The SiO_2 particles had a mean hydrodynamic diameter of ~125 nm with a uniform size distribution (polydispersity index (PDI) < 0.05). Average radii and zeta potentials are given as the average of 3 measurements. The pH of the samples was determined using a pH meter (HI 5522 pH/ISE/EC bench meter and HI 1330 pH electrode, Hanna Instruments) calibrated with the

appropriate buffer solutions. In order to control the amount of salt added to the samples and the initial ionic strength of the washed TiO$_2$ particles in water, the conductivity was measured by two different means: first using a conductivity meter (HI 5522 pH/ISE/EC bench meter and HI 76312 conductivity electrode, Hanna Instruments) calibrated with the appropriate buffer solutions and second, using the conductivity obtained from the zeta potential measurements (Zetasizer Nano ZS, Malvern). The average ionic strength was calculated from the conductivity using equation 2.28 as further detailed in the sample characterization chapter 2.5.2. For all the samples considered here with a salt concentration below 0.5 mM, the ionic molar conductivity at infinite dilution Λ^0 was used for Λ_m. For concentrations above 0.5 mM, the ionic molar conductivity Λ_m as calculated from the Debye-Hückel-Onsager equation was used.

For TiO$_2$ samples diluted in ultrapure water where no salt was added, the average conductivity was assumed to be due to residual Na$^+$ and OH$^-$ ions from the preparation process. The measured conductivity values of washed and filtered samples at pH 7 without additional salt of the same particle batch varied from 9.7 to 11.3 μS/cm (corresponding to an ionic strength of 3.9 $\cdot$ 10^{-5} and 4.6 $\cdot$ 10^{-5} mol/L). This conductivity, attributed to residual Na$^+$ and OH$^-$ ions in solution, was subtracted from the conductivity measured for TiO$_2$ samples where salt was added in order to calculate the pure contribution of Na$^+$ and Cl$^-$ ions to the ionic strength of the solution. The total ionic strength value of the samples used in the fitting procedure includes the ionic strength originating from the Na$^+$ and Cl$^-$ ions, as well as the residual Na$^+$ and OH$^-$ ions.

4.2.4 AR-SHS measurements

The Second harmonic scattering in this chapter measurements were performed on the same AR-SHS setup as described in chapter 2.3.3. Here, the fundamental laser wavelength was λ = 1028 nm and the average laser power at the sample position was set to 80 mW. Before the SH light was detected at the photomultiplier tube it had to pass an ZET514/10x, Chroma filter. Data points were acquired using 20 $\cdot$ 1.5 s acquisition time with a gate width of 10 ns. The scattering patterns were normalized according to equation 2.18 in chapter 2.3.3. All other measurement parameters where the same as described in chapter 2.3.3.

4.2.5 Molecular dynamics simulations

TiO$_2$ was modeled as a negatively charged (-0.104 C/m^2) hydroxylated rutile (110) surface, [190] because dissociative adsorption of water dominates at high pH with estimated 65% $\pm$ 15% first-layer water dissociation in rutile-RbCl solution at pH 12 [233]. At the rutile-deionized water interface, this fraction was estimated as 30% $\pm$ 15%; [233] however, the realistic scenario even for neutral surfaces is that adsorbed cations promote deprotonation of surface groups. A recent STM study found that the dissociative form of water is more stable than associated water molecules [234]. SiO$_2$ was modeled as a negatively charged (-0.12 C/m^2) quartz (101) surface with singly coordinated silanol groups [64].

Water was modeled as rigid SPC/E, [192] whereas parameters for Na$^+$ ions were taken from the

literature [191]. All employed models utilize the electronic continuum correction (ECC) theory, [189] which in a mean-field way incorporates electronic polarization effects into classical, nonpolarizable MD simulations. Other technical details of the simulations are the same or similar to those in section 3.2.5 and 4.2.5 and Refs. [64, 150, 190].

4.3 Results and Discussion

4.3.1 Surface potential and water order in different ionic strength conditions

Part A of Figure 4.1 shows AR-SHS patterns of colloidal ~100 nm diameter amorphous TiO_2 particles in two different polarization combinations (PPP and PSS). The scattering patterns were measured for different concentrations of NaCl ranging from 0 to 300 μM.

Both PPP and PSS AR-SHS patterns show a decrease of the normalized SHS intensity with increasing salt concentration. At a higher ionic strength, more counterions will be situated in proximity of the charged interface of the particle, leading to a reduced penetration of the electrostatic field $\mathbf{E}_{DC}$ in the electrolyte solution. As a consequence, the volume of the overall probed water shell around the particles is reduced, resulting in a lower SHS intensity with increasing ionic strength. The solid lines represent the fit of the corresponding data points using the AR-SHS model described in section 2.3.1. The results of the fits for the surface potential Φ_0 and the surface susceptibility $\chi_{s,2}^{(2)}$ as a function of added NaCl are shown graphically in Figure 4.1 B and are given in Table 4.1. Tables 8.4 and 8.6 (Appendix) summarize all the parameters used for the fitting. Note that the radius obtained through DLS measurements indicated in Table 4.1 is slightly larger than the nominal radius of the particles.

The zeta potential ζ of the TiO_2 samples in different ionic strength conditions is presented in Figure 4.1 B for comparison to the surface potential. The zeta potential is a common measure for the stability of a particle suspension, and in a simplistic view values around ±30 mV are generally indicative of stable suspensions [235]. In reality, colloidal suspension stability limits are material-specific and depend on more complex dispersion interactions [236]. The isoelectric point ($\zeta = 0$) was determined through electrophoretic mobility measurements and is close to pH 4 for the here used colloidal ~100 nm diameter amorphous TiO_2 particles. It can be seen that the zeta potential does not change in magnitude and remains between -24 mV and -30 mV, whereas the surface potential varies from -12 mV to -326 mV in the investigated ionic strength range. For the behavior of the surface potential, three different regions can be identified: (i) 0-10 μM NaCl, where $|\Phi_0| > |\zeta|$, (ii) 10-100 μM NaCl, where $|\Phi_0| \approx |\zeta|$, and (iii) above 100 μM NaCl where $|\Phi_0| \gg |\zeta|$. At the same time, the surface susceptibility shown in the bottom part of Figure 4.1 B changes in sign between 10 and 50 μM NaCl. Negative values of $\chi_{s,2}^{(2)}$ indicate that the net dipole moment of water molecules points away from the surface (oxygens toward the surface), while positive values of $\chi_{s,2}^{(2)}$ indicate that the average orientation of water molecules is with their dipole moment facing the surface (hydrogens toward the surface).

As all the ionic strength measurements were carried out at pH 7, above the isoelectric point of the TiO_2 particles, some surface groups are deprotonated in an amount corresponding to the surface charge density [72, 237]. We estimate the deprotonation to be between 1% and 8% at
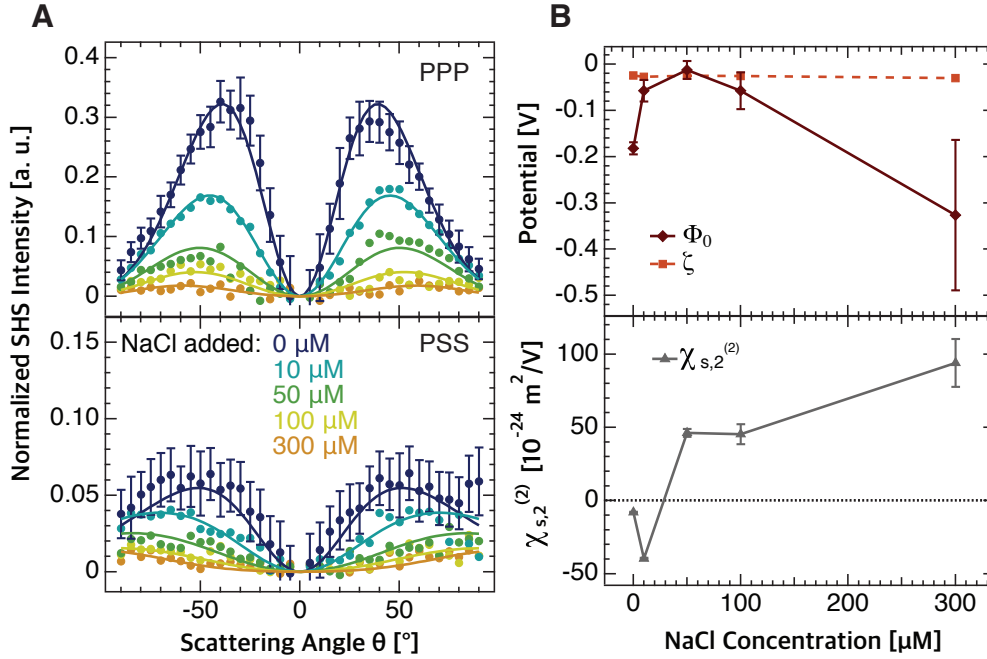
Figure 4.1 – (A) AR-SHS patterns of amorphous ~100 nm diameter TiO$_2$ particles as a function of ionic strength at pH 7 in PPP polarization combination (top) and PSS polarization combination (bottom). Plain data points of different colors represent different salt concentrations of the aqueous environment. The ionic strength was adjusted through NaCl addition. The particle density was kept constant for each sample and equal to $4.3 \cdot 10^{11}$ particles/mL. All measurements were performed at $T = 296.15$ K. Solid lines represent the fits to the corresponding data points using the AR-SHS model. A summary of all the parameters used for the fits can be found in Tables 8.4 and 8.6. (B) Surface potential Φ_0 (dark red diamonds), and surface susceptibility $\chi_{s,2}^{(2)}$ (gray triangles) as a function of ionic strength. Φ_0 and $\chi_{s,2}^{(2)}$ were obtained by fitting the corresponding AR-SHS patterns of ~100 nm diameter amorphous TiO$_2$ particles in suspension in PPP and PSS polarization combination (see panel A). The light red squares represent the zeta potential values ζ, measured for the different ionic strength conditions using electrophoretic mobility measurements.

pH 7 using surface charge density values from the literature (see section 8.2.1 in Appendix). This estimation is only meant as a guidance as very different surface charge density values have been reported by different groups [74–77]. These values can greatly differ depending on the size, [74, 207, 208] the surface roughness, [238] and the crystal phase of the particles, [212] as well as the synthetic procedure. For the less known amorphous phase, no record of surface charge density values could be found so far. Our results show negative values of zeta potentials, as anticipated for a negatively charged surface. In the very low ionic strength range (0-10 μM NaCl), where $|\Phi_0| > |\zeta|$, we observe that the magnitude of the surface potential decreases until a value of the same magnitude of the zeta potential is reached (see Fig. 4.2 A,B). We assign this behavior as arising from positively charged Na$^+$ ions that directly adsorb at the deprotonated Ti-O$^-$ surface groups of the colloids (inner-sphere complex), as illustrated in Figure 4.2 B.

Table 4.1 – Surface potential Φ_0 and surface susceptibility $\chi_{s,2}^{(2)}$ values that were obtained by fitting the AR-SHS patterns of ~100 nm diameter amorphous TiO_2 nanoparticles in aqueous solutions of different NaCl concentrations at pH 7. The radius R was measured by DLS, and the zeta potential ζ was obtained from electrophoretic mobility measurements.

added NaCl [μM]	R [nm]	ζ [mV]	Φ_0 [mV]	$\chi_{s,2}^{(2)}$ [$10^{-24} \frac{m^2}{V}$]
0	59 ± 21	-24 ± 21	-182 ± 13	-8.1 ± 0.4
10	60 ± 19	-27 ± 20	-57 ± 23	-39.6 ± 0.5
50	60 ± 19	-25 ± 17	-12 ± 19	46.1 ± 2.7
100	60 ± 15	-26 ± 20	-57 ± 40	45.3 ± 6.9
300	59 ± 28	-30 ± 22	-326 ± 163	94.1 ± 16.3

Because of the reduction of the effective negative surface charge by the adsorbed counterions, the magnitude of the surface potential will decrease accordingly. Additionally, in this ionic strength region, the surface susceptibility is negative, which indicates that the interfacial water molecules are oriented with their net dipole moment away from the surface (oxygens toward the surface). This behavior can be explained by hydrogen bonding between the oxygen atoms of the water molecules and the hydroxyl surface groups of the TiO_2 particles. Note that we chose a hydroxylated model of the TiO_2 surface as illustrated in Figure 4.2; however our conclusions would remain the same for a nonhydroxylated surface, where the oxygen atom of a water molecule could interact with an undercoordinated Ti surface site. While the surface structure and adsorption of the first monolayer of water has been the object of many debates, [239–241] it is beyond the scope of this study to clarify the exact configuration of the first layer of water molecules at the surface, which is furthermore very dependent on the crystal structure, the presence of surface defects, the sample preparation procedure, and the experimental conditions. Here, the main contribution to the measured surface susceptibility is due to the average dipole of all the water molecules that have a chemical type of interaction with the surface (i.e., not induced by the electric field), with the advantage of easily distinguishing changes in average water orientation as a function of ionic strength, as further detailed hereafter.

In the low ionic strength region (10-100 μM NaCl), the surface potential reaches a minimum in magnitude and is close to zero. This suggests that once all the favorable sites have been occupied by direct adsorption of the counterions, further addition of salt does not affect the surface potential and thus the surface charge density in this concentration range. Our experiment cannot provide insights on the nature of these favorable sites. However, it evidences that only a fraction of the deprotonated hydroxyls is occupied by direct adsorption of Na^+, as complete coverage would result in a neutral particle ($\Phi_0 = 0$), which could not be stable in suspension and would agglomerate. Furthermore, the surface potential remains very close to the zeta potential up to 100 μM NaCl. As the zeta potential is considered to be located a few water layers away from the surface, [57, 71, 72] a value of surface potential close to the zeta potential suggests that there are no mobile counterions accumulated between the shear plane and the surface but that they are rather distributed in solution. In the Gouy-Chapman model, this would be equivalent to a diffuse layer forming around the TiO_2 particles, which
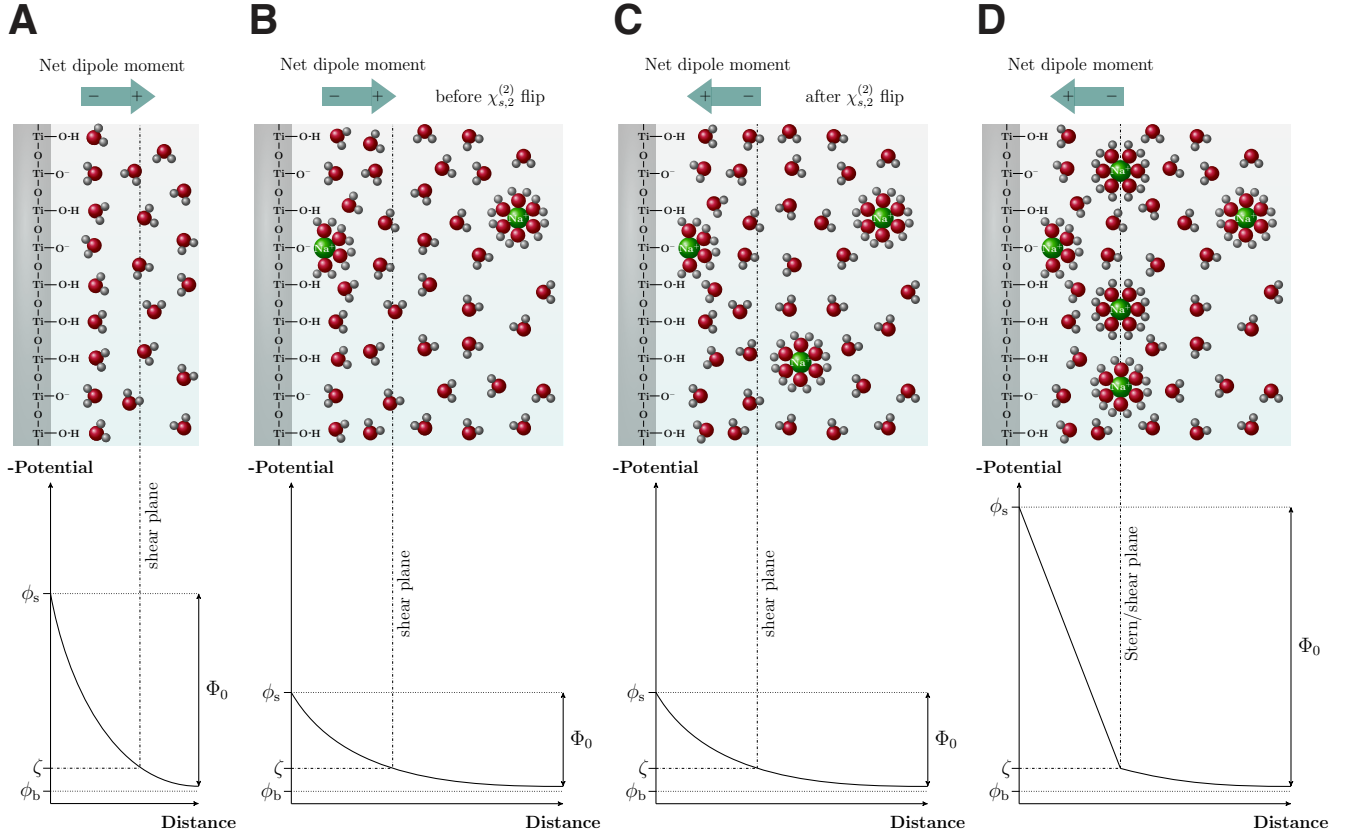
Figure 4.2 – EDL around a TiO$_2$ particle surface and the corresponding surface potential Φ_0 and zeta potential ζ over the distance to the surface (A) with no added salt and under (B) very low ionic strength, (C) low ionic strength and (D) high ionic strength conditions. The particle surface is approximated to a flat surface for clarity, and no anions are displayed. The mean orientation of water molecules in direct proximity of the slightly deprotonated surface is given by the net dipole moment pointing away or toward the surface, reflecting average water orientation with the hydrogens away (A, B) or toward (C, D) the surface. Scheme B displays the direction of the net dipole moment before the sign of the surface susceptibility $\chi_{s,2}^{(2)}$ flips to positive values, while scheme C shows the net dipole moment after the $\chi_{s,2}^{(2)}$ flip. The surface potential Φ_0 is the potential difference between the potential at the surface of the particle ϕ_s and the potential of the bulk solution ϕ_b. Note that this schematic illustration shows the magnitudes of the previously mentioned potentials. ζ is the potential at the shear plane. In this simplistic scheme, the Stern plane is approximated to be equal to the shear plane in the high ionic strength situation where a condensed layer of counterions is formed in panel D.

is illustrated in Figure 4.2 C. At the same time, we observe a change in sign of the surface susceptibility between 10 μM and 50 μM of added NaCl. This reflects a change in orientation of the water molecules situated directly at the interface, as the surface susceptibility describes the orientational order induced by all (chemical) interactions confined to the particle surface plane (see Materials and Methods). The average surface molecular directionality changes from the net dipole moment pointing away from the surface (oxygens toward the surface) to the net dipole moment pointing toward the surface (hydrogens toward the surface). Therefore, it can

be argued that, above a certain threshold, the presence of Na^+ near the interface is responsible for the change in directionality of interfacial water. This phenomenon can be rationalized by the rearrangement of the H-bonding network between the Ti-OH groups and the surface water molecules caused by the Na^+ ions.

In the higher ionic strength region above $100\,\mu$M NaCl, where $|\Phi_0| \gg |\zeta|$, we observe a strong increase in magnitude of the surface potential with salt concentration. This large deviation from the zeta potential suggests the formation of a condensed layer of ions at the interface, which is further supported by the observation of the drastic reduction in the SHS intensity. This charge condensation layer is also predicted by the Gouy-Chapman-Stern model, where the steep potential drop in the very first interfacial layers is approximated to the linear potential drop in a parallel plate capacitor. Taking the distance between the surface and the zeta potential plane to be between 0.3 and 0.9 nm (1-3 water molecules), [57, 71, 72] the electric field can be estimated here to be $\sim 3 \cdot 10^8$ to $1 \cdot 10^9$ V/m for an ionic strength of $300\,\mu$M NaCl. This large value of the electric field in the interfacial region provides additional evidence of the presence of a condensed layer of ions. The latter is schematically illustrated in Figure 4.2 D. Note that in this case the ions cannot be directly adsorbed at the TiO_2 surface. The absence of water molecules between the negatively charged surface and the counterions would lead to charge neutralization and a consequent decrease in surface potential, as already observed for the very low ionic strength case. As such, the ions are present as outer-sphere complexes and likely have one or more layers of water between them and the surface.

The surface susceptibility has a positive sign in this higher ionic strength region. As a consequence, the net dipole moment of the interfacial water is oriented toward the surface with the hydrogen atoms facing the surface. This behavior further confirms the presence of a condensed layer of positively charged ions at the interface. Analogously to the previous case, we expect the net dipole moment to be influenced by the rearrangement of the H-bonding network between the surface hydroxyl groups and the interfacial water molecules, caused by Na^+ ions, as well as by the presence of additional oriented water molecules belonging to the Na^+ hydration shell.

Both the diffuse region and the condensed layer region have been previously experimentally determined by our group for 300 nm diameter SiO_2 particles, [150] exhibiting a similar increase in the surface potential magnitude for NaCl concentrations between 0.1 and 10 mM [150]. However, the direct counterion adsorption was not observed in that case, most likely because the initial ionic strength of the nanoparticles was higher (0.1 mM vs tens of micromolar here). We further speculate that a similar trend in surface potential versus ionic strength would be observed for smaller nanoparticles. In this case, it is reasonable to expect the minimum in the magnitude of the surface potential to be shifted to higher ionic strengths, as surface charge densities have been shown to be size-dependent for TiO_2 particles below 25 nm, with the magnitude of the surface charge density increasing with decreasing size [74]. Interestingly, Brown et al. [95] reported values for surface potential and Stern layer thicknesses for 9 nm SiO_2 particles for higher salt concentrations ($\geq$0.01 M NaCl), showing that surface potential values decrease with increasing salt concentration. This opposite behavior with respect to our observation of increasing surface potential in the 100-300 μM range is related to different

relative variations of the surface charge density and of the condensed layer region thickness and has been discussed in detail in chapter 3 and Ref. [150].

4.3.2 Surface potential and water order in different pH conditions

In order to investigate the influence of different surface charge densities on the molecular water order and the surface potential, similar AR-SHS measurements were performed as a function of pH. The initial TiO$_2$ dispersion in water prior to pH adjustment had a pH = 7, and no additional salt was added. The sample pH was varied by addition of NaOH. Addition of NaOH to the particle suspension results in a more negatively charged surface. In our experiment, the pH range was limited to $7 \leq$ pH ≤ 10.7 because the signal-to-noise ratio of the SHS patterns was too low for pH > 10.7. For $4 <$ pH < 7, where HCl is added to the TiO$_2$ dispersion, but the particle surface remains negatively charged (as the isoelectric point is at pH = 4, and here as first approximation the isoelectric point can be considered equal to the point of zero charge), no SHS patterns could be obtained due to particle aggregation that occurs close to the isoelectric point. The acidic pH range below the isoelectric point, where the surface is positively charged, was not experimentally accessible: With addition of HCl, the particles were unstable between $3 \leq$ pH ≤ 4 and the signal-to-noise ratio of the SHS patterns was too low for pH < 3. The results for the AR-SHS patterns of colloidal ~100 nm diameter amorphous TiO$_2$ at different basic pH are shown in part A of Figure 4.3. It can be seen that the normalized SHS signal decreases with increasing pH for both polarization combinations, as also observed for increasing salt concentrations in Figure 4.1 A, which reflects a smaller number of oriented water molecules. Figure 4.3 B shows the surface potential Φ_0 and the surface susceptibility $\chi_{s,2}^{(2)}$ as a function of the pH of the aqueous environment. A list of the exact values can be found in Table 4.2. A summary of all the parameters used for the fitting is given in Tables 8.4 and 8.7 (Appendix). Despite our limited pH range, the three behaviors found in Figure 4.1 are also seen here: Close to pH 7, the magnitude of the surface potential Φ_0 is larger than the zeta potential. For more basic pH (9.5), the surface potential decreases in magnitude and becomes comparable to the zeta potential. For the highest pH investigated here the surface potential increases again in magnitude. A change of sign in the surface susceptibility is observed between pH 9.5 and pH 10.7, indicative of the reorientation of the net dipole moment of interfacial water molecules from oxygens facing the surface to hydrogens facing the surface.

Between pH 7 and pH 11, the surface charge of the colloids is expected to be increasingly negative due to deprotonation of hydroxyl groups at the surface, while the same counterion (Na$^+$) is expected to interact with the negatively charged groups. As for the neutral pH case, we can estimate the approximate percentage of deprotonation at pH = 9.5 using surface charge density values from the literature (see 8.2.1 in Appendix) and find it to be between 10% and 35%. This indicates that while the surface is approximately three to ten times more charged than at pH = 7, the majority of the surface groups remain protonated. Given the similarities with the results as a function of ionic strength, we assign these findings to the same mechanisms of counterion adsorption (for pH 7 to pH 9.5), the creation of a diffuse
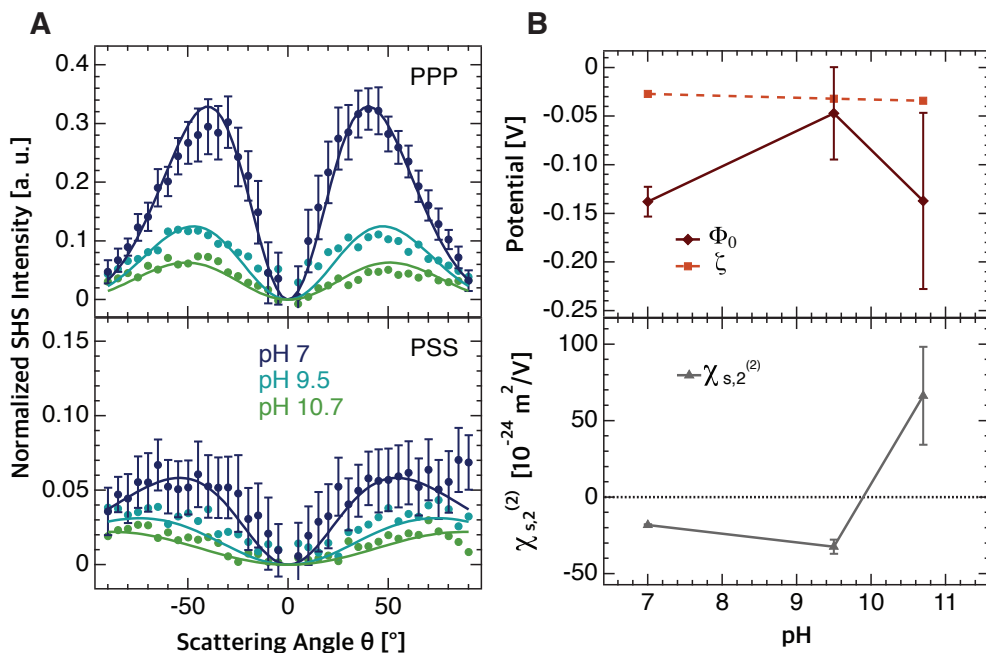
Figure 4.3 – (A) AR-SHS patterns of amorphous ~100 nm diameter TiO_2 particles in solutions of different pH in PPP polarization combination (top) and PSS polarization combination (bottom). Plain data points of different colors represent different pH conditions of the aqueous environment. For pH values above 7, the pH was adjusted through NaOH addition. The particle density was kept constant for each sample and equal to $4.3 \cdot 10^{11}$ particles/mL. All measurements were performed at $T = 296.15$ K. Solid lines represent fits to the corresponding data points using the AR-SHS model. A summary of all the parameters used for the fits can be found in Tables 8.4 and 8.7. (B) Surface potential Φ_0 (dark red diamonds), and surface susceptibility $\chi_{s,2}^{(2)}$ (gray triangles) as a function of pH as they were obtained by fitting the corresponding AR-SHS patterns of 100 nm diameter amorphous TiO_2 particles in suspension in PPP and PSS polarization combination (see panel A). The light red squares represent the zeta potential values ζ that were measured for the different pH conditions of the aqueous environment using electrophoretic mobility measurements.

layer (around pH 9.5), and the creation of a layer of condensed ions (for pH > 9.5) as was discussed in detail above. The change in orientation of the interfacial water molecules from the net dipole moment pointing away from the surface to the net dipole moment pointing toward the surface occurs here between pH 9.5 and pH 10.7. Converting these pH values to the corresponding ionic strength values, we find that the change in sign occurs above 30 μM added NaOH, which is in good agreement with the change in sign observed for the NaCl case (between 10 and 50 μM added NaCl). The fact that the surface potential values are similar and that the change in water orientation occurs in the same ionic strength region in both the salt and pH cases shows that the surface charge densities for a given ionic strength are comparable and do not depend on the use of a salt (NaCl) or a base (NaOH). Note that this is observed in the here investigated range of salt concentration and pH, as well as for the SiO_2 particles

Table 4.2 – Surface potential Φ_0 and surface susceptibility $\chi_{s,2}^{(2)}$ values obtained from fitting the AR-SHS patterns of ~100 nm diameter amorphous TiO$_2$ nanoparticles in aqueous solutions of different pH. The pH was adjusted through NaOH addition. The radius R was measured by DLS, and the zeta potential ζ was obtained from electrophoretic mobility measurements.

pH	R [nm]	ζ [mV]	Φ_0 [mV]	$\chi_{s,2}^{(2)}$ [$10^{-24}\frac{\text{m}^2}{\text{V}}$]
7	63 ± 17	-27 ± 19	-138 ± 15	-18.1 ± 0.5
9.5	63 ± 14	-32 ± 19	-47 ± 48	-32.3 ± 4.6
10.7	59 ± 19	-34 ± 22	-137 ± 91	66.2 ± 31.9

in chapter 3 and Ref. [150]; however it might not be the case for higher salt concentrations (>300 μM) or higher pH values (pH > 10.7). Furthermore, our results suggest that at pH 7, at which the AR-SHS patterns as a function of salt are recorded, the surface charge density is already negative enough to permit the formation of a layer of condensed counterions. Comparison to acidic pH values was not possible due to particle instability close to the isoelectric point and the low signal-to-noise ratio of the SHS patterns below pH 3 as explained above. However, we would expect different surface potential and water orientation behavior as the particle surface is positively charged at pH values below the isoelectric point (as a first approximation, here the isoelectric point can be considered equal to the point of zero charge) and therefore not directly comparable to the NaOH and NaCl case.

4.3.3 Comparison of SiO$_2$ and TiO$_2$ interfacial properties

In order to determine if the evolution of the surface potential and the water orientation with increasing ionic strength and pH is specific to the nature of the investigated surface, we performed AR-SHS on SiO$_2$ particles of the same size (~100 nm diameter). SiO$_2$ was chosen in order to have a comparison with another metal oxide surface bearing the same potential determining ions (H$^+$ and OH$^-$). The SiO$_2$ colloids were found to have a stronger SHS signal than the amorphous TiO$_2$ particles (both relative to neat water, ~10 times higher, see Fig. 4.4, even though the particle density of the two particle suspensions was on the same order of magnitude (2.9 · 10^{11} particles/mL in the case of SiO$_2$ and 4.3 · 10^{11} particles/mL for TiO$_2$). Figure 4.5 A shows the surface potential Φ_0 of 100 nm diameter SiO$_2$ particles in different NaCl concentrations compared to 100 nm diameter amorphous TiO$_2$ particles. Three regions of surface potential behavior can also be distinguished for SiO$_2$ particles. (i) It can be seen that the surface potential of the SiO$_2$ particles decreases in magnitude with increasing salt concentration for low ionic strength (<300 μM). (ii) At 300 μM NaCl concentration, the surface potential value is similar to the zeta potential, which is not shown here for clarity but lies in the range of -32 to -48 mV (See Table 4.3). (iii) For ionic strength >300 μM, the magnitude of the surface potential rises again to values of $|\Phi_0| > |\zeta|$. Compared to TiO$_2$, the increase in magnitude of the surface potential in region (iii) occurs at a higher ionic strength for SiO$_2$. Likewise, the decay in magnitude of the surface potential in region (i) until the surface potential $|\Phi_0| \approx |\zeta|$ in region (ii) spans over a wider ionic strength range for SiO$_2$ compared to TiO$_2$.
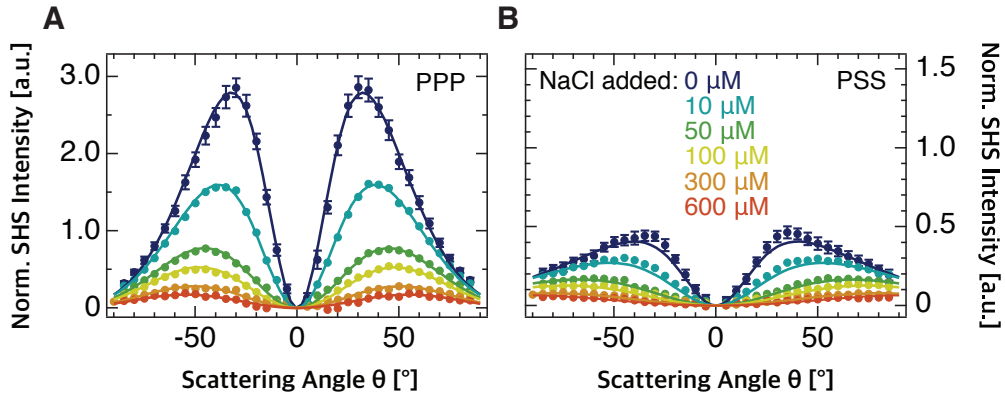
Figure 4.4 – AR-SHS patterns of 100 nm diameter SiO_2 particles as a function of ionic strength in PPP (A) and PSS (B) polarization combination. Plain data points of different colors represent different salt concentrations of the aqueous environment. The ionic strength was adjusted through NaCl addition. The particle density was kept constant for each sample and equal to $2.91 \cdot 10^{11}$ particles/mL. All measurements were performed at $T = 296.15$ K. Solid lines represent the fits to the corresponding data points using the AR-SHS model. A summary of all the parameters used for the fits can be found in Tables 8.5 and 8.8.
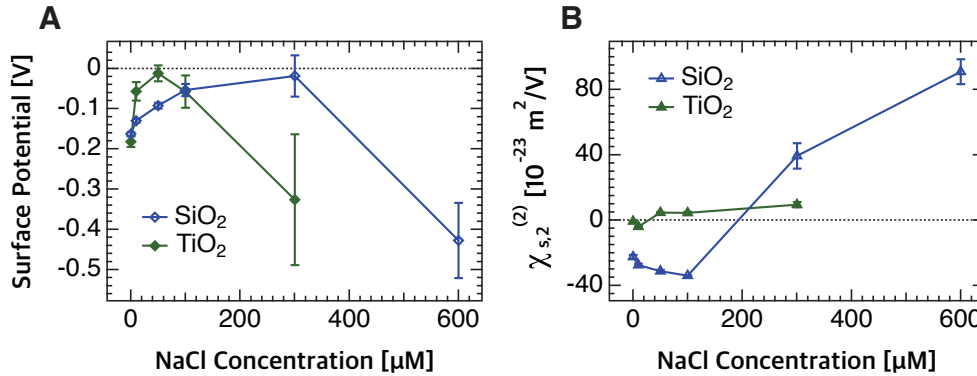
Figure 4.5 – (A) Surface potential Φ_0 and (B) surface susceptibility $\chi_{s,2}^{(2)}$ of ~100 nm diameter SiO_2 particles and ~100 nm diameter amorphous TiO_2 particles as a function of ionic strength at pH 7. The ionic strength was adjusted through NaCl addition. The particle density was kept constant and equal to $2.9 \cdot 10^{11}$ particles/mL for the SiO_2 and equal to $4.3 \cdot 10^{11}$ particles/mL for the TiO_2 samples. All measurements were performed at $T = 296.15$ K and pH=7. Dark blue open diamonds and triangles represent the SiO_2 samples, and dark green diamonds and triangles represent the TiO_2 particles in aqueous environment. A summary of all the parameters used for the fits through which Φ_0 and $\chi_{s,2}^{(2)}$ were extracted can be found in Tables 8.4, 8.5, 8.6 and 8.8.

In Figure 4.5 B, the surface susceptibility $\chi_{s,2}^{(2)}$ of SiO_2 and TiO_2 can be seen. A change in sign of $\chi_{s,2}^{(2)}$ from negative values to positive values happens at NaCl concentration between $100\,\mu$M and $300\,\mu$M. This indicates that the reorientation of the net dipole moment of the water molecules from oxygens facing the surface to hydrogens facing the surface happens

Table 4.3 – Surface potential Φ_0 and surface susceptibility $\chi_{s,2}^{(2)}$ values obtained from fitting the AR-SHS patterns of ~100 nm diameter SiO$_2$ nanoparticles in aqueous solutions of different NaCl concentrations at pH 7. The radius R was measured by DLS, and the zeta potential ζ was obtained from electrophoretic mobility measurements.

added NaCl [μM]	R [nm]	ζ [mV]	Φ_0 [mV]	$\chi_{s,2}^{(2)}$ [$10^{-22} \frac{m^2}{V}$]
0	65 ± 12	-48 ± 31	-163 ± 5	-2.2 ± 0.1
10	64 ± 11	-41 ± 22	-130 ± 5	-2.8 ± 0.08
50	62 ± 7	-36 ± 24	-92 ± 7	-3.2 ± 0.08
100	61 ± 7	-35 ± 23	-54 ± 15	-3.4 ± 0.01
300	60 ± 5	-32 ± 23	-19 ± 50	3.9 ± 0.7
600	58 ± 5	-34 ± 26	-430 ± 90	9.1 ± 0.7

at higher ionic strength for SiO$_2$ than for TiO$_2$. The surface susceptibility of SiO$_2$ is one order of magnitude higher than the surface susceptibility of TiO$_2$, which implies a larger net dipole moment of the interfacial water molecules near the SiO$_2$ surface compared to the water molecules close to the TiO$_2$ surface. This larger net dipole moment translates into a stronger ordering of the interfacial water molecules that contributes to the higher SHS intensity observed in the SiO$_2$ case. Such an effect could be caused by the different molecular surface groups (e.g., bridging or terminal hydroxyls for TiO$_2$ vs different siloxane and silanol groups for SiO$_2$) and their different occurrences, with consequential influence on the interfacial H-bonding network.

The same mechanisms of ion adsorption, formation of a diffuse layer, and creation of a layer of condensed charges, which were discussed in detail for the ionic strength dependency of TiO$_2$ particles and further confirmed in the case of pH variation, can explain the three regions of surface potential and surface susceptibility behavior for the SiO$_2$ particles. Even though the general behavior is similar for both surfaces, the onset of the three regions as a function of ionic strength is clearly different in the case of SiO$_2$ particles. Counterion adsorption is more gradual and requires up to 300 μM to reach a minimum in the surface potential magnitude, indicative of a saturation of all the favorable deprotonated hydroxyls. Analogously to the TiO$_2$, we note here that all the deprotonated hydroxyls cannot be occupied, as this would result in a neutral, unstable particle. It is interesting to see that for both materials the change in sign of $\chi_{s,2}^{(2)}$ occurs just before the minimum in the surface potential magnitude is reached. This result suggests that the hypothesized rearrangement of the H-bonding network at the surface by the counterions is already significant enough before the favorable deprotonated hydroxyls are saturated with Na$^+$ ions. Furthermore, the increase of surface potential magnitudes, which implies the formation of a layer of condensed charges, occurs at ionic strengths above 300 μM in the case of the SiO$_2$ particles, compared to above 100 μM in the case of TiO$_2$ particles. Knowing that the density of OH groups per surface area is similar for both surfaces (4.8 OH/nm^2 for TiO$_2$ [242] and 4.9 OH/nm^2 for SiO$_2$ [196]), this implies that the TiO$_2$ surface has a higher affinity for Na$^+$ ions than SiO$_2$, which has been already observed by our simulations comparing the amount of adsorbed cations at negatively charged (and even neutral) rutile and quartz surfaces [64].

In order to decipher the molecular origin of our experimental results, we performed molecular dynamics (MD) calculations following the same strategy as in section 3.2.5 and Ref. [150]. We adopted our molecular dynamics models of TiO_2 and SiO_2 to investigate and compare the effect of ionic concentration on the orientation of water molecules at these interfaces. TiO_2 was modeled as a negatively charged (-0.104 C/m^2) hydroxylated rutile (110) surface, while as a SiO_2 model, we used a negatively charged (-0.12 C/m^2) quartz (101) surface, as described in section 4.2.5 (Materials and Methods). A similar negative surface charge density, which is constant in a single simulation, was chosen to fairly compare properties above the point of zero charge for both TiO_2 and SiO_2, when a portion of surface hydroxyls is deprotonated, corresponding to neutral or slightly basic pH.

Despite the fact that the behavior of amorphous solids used in our SHS experiments and of crystalline solids used in our simulations may differ, the comparison to the crystalline form still can provide valuable information on the sorption properties of both materials. To probe concentration effects, we prepared a set of three systems for each modeled surface. To mimic extremely low concentrations studied in the experiments (micromolar concentrations) that are not directly accessible in simulations, the number of Na$^+$ ions in the system was set to be equal to the amount of negative surface charges (and there were no anions). However, the number of ions allowed in the vicinity of the negative surface up to 10 Å varied from 0% compensation (i.e., all the counterions were forced to be further away from the surface) to 50% compensation (only half of the ions were allowed in the region up to 10 Å) and 100% compensation (no restriction on the position of ions, that is, a surface charge could be fully compensated). In the latter case, the surface charge could be fully (100%) compensated up to 10 Å. However, due to the equilibrium between the distribution of ions at regions closest to the surface and further away (including the bulk region), in conjunction with the low total number of ions allowed in the simulation, even in this 100% case, part of the surface charge remains uncompensated up to 10 Å. This situation resembles our experimental low ionic concentration conditions when, even in the presence of a sufficient number of cations to compensate the surface charge, the particles remain negatively charged and stable.

The measure that can be compared to the experimental data is the integral of the „dipole concentration", which is a product of the average number density of water molecules and the perpendicular component of the water dipole moment with respect to the surface (with positive values indicating hydrogens facing the surface, that is, as in the experiment). The running integral of the dipole concentration provides an indicator for the buildup of the SHS intensity as a function of distance. The SHS intensity is proportional to the square of this running integral along the z-axis perpendicular to the surface [150]. The plane at z = 0 corresponds to the average position of the last TiO layer. Figure 4.6 shows the running integrals of dipoles as a function of distance for TiO_2 and SiO_2 surfaces. Both surfaces exhibit similar behavior as a function of sodium concentration as observed in region (i) of SHS experiments: addition of ions to the interface, resulting in inner-sphere complexes (or outer-sphere complexes adsorbed at the surface), shifts the signal toward negative values, that is, fewer water molecules are oriented, which is consistent with the effect of adsorbed Na$^+$ compensating a negative surface charge. Moreover, the rate of change in the interfacial region

(up to ~10 Å from the surface) is more drastic for TiO$_2$. At 50% compensation, the integrated dipole value at 10 Å is 0.094 D/Å^2 for TiO$_2$ and 0.130 D/Å^2 for SiO$_2$. At 100% compensation, the integrated dipole value at 10 Å decreases to 0.026 D/Å^2 for TiO$_2$ and to 0.096 D/Å^2 for SiO$_2$. This steeper decrease of the integrated dipole moment with the amount of counterions indicates that the surface charge of TiO$_2$ is more efficiently screened by Na$^+$ counterions. In other words, fewer ions are required at the TiO$_2$ surface to result in similar changes as in the case of SiO$_2$. This observation is also in line with the SHS experiments, where a minimum in
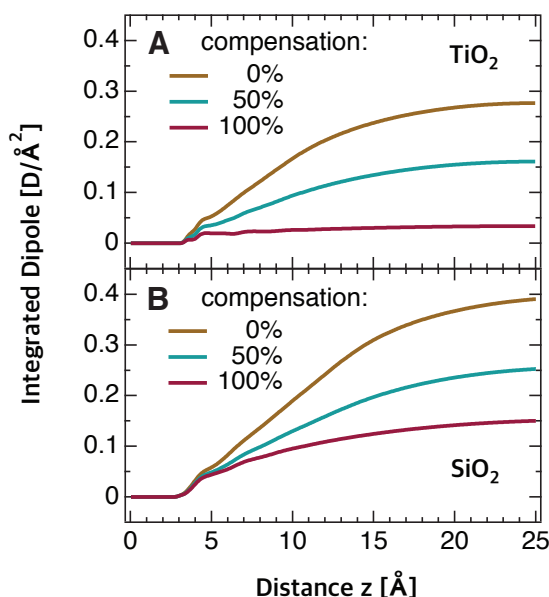
Figure 4.6 – Integrated dipole as a function of distance from negatively charged (A) (110) rutile (-0.104 C/m^2) and (B) (101) quartz (-0.12 C/m^2) surfaces from molecular dynamics simulations. The brown line represents simulations allowing 0% compensation of the surface charge (i.e., all the counterions were forced to be at least 10 Å away from the surface), the turquois line represents 50% compensation (only half of the ions were allowed in the region up to 10 Å from the surface), and the purple line is from simulations allowing 100% compensation (no restriction on the positions of ions).

the surface potential magnitude is reached at lower ionic strengths for TiO$_2$ than for SiO$_2$. Note also the flat profile of the curve allowing 100% compensation of the TiO$_2$ surface, compared to the same curve for SiO$_2$, which is still growing, that is, gaining further contributions to the SHS signal, with increasing distance from the surface. That clearly documents that while in both cases the ions can fully compensate the surface charge (and eventually do so at large distances), for TiO$_2$ nearly all the compensation occurs in the nearest vicinity of the surface, while for SiO$_2$, we observe a wide diffuse layer.

4.4 Conclusions

In summary, nonresonant polarimetric AR-SHS was applied for the first time to semiconductor nanoparticles in aqueous environments. By collection of two different polarization combinations of light from a colloidal suspension, the two analytical expressions from nonlinear optical theory containing Φ_0 and $\chi_{s,2}^{(2)}$ can be solved without assuming any model for the distribution of the ions at the interface. The surface potential and molecular orientation of interfacial water molecules of ~100 nm diameter spherical TiO_2 particles in different NaCl and pH conditions are reported and compared to the results for insulating SiO_2 particles as a function of NaCl concentration. By comparison of the surface potential to the zeta potential, three different regions can be identified for TiO_2: At very low ionic strengths (0-10 μM), Na^+ ions preferentially adsorb as inner-sphere complexes. At low ionic strengths (10-100 μM), we observe the presence of a distribution of counterions equivalent to a diffuse layer in the GC model, while at higher ionic strengths (>100 μM), the presence of an additional layer of condensed charges, similar to a Stern layer in the GCS model, is detected. Changes in interfacial water orientation as a consequence of counterions accumulating in proximity of the charged surface further support this picture and indicate a rearrangement of the water H-bond network caused by the Na^+ ions. This rearrangement occurs already for small amounts of counterions present in solution (below 50 μM added Na^+). Regions of equivalent behavior are observed for TiO_2 particles in varying basic pH conditions. Comparing TiO_2 and SiO_2 particles as a function of NaCl concentration shows that the TiO_2 surface has a higher affinity for Na^+ ions than SiO_2. These findings are in line with data obtained by MD simulations of the rutile and quartz surfaces interacting with aqueous solutions, where the rate of change of the integrated dipole with increasing Na^+ adsorption at the surface is faster for TiO_2 than for SiO_2.

Overall, these results pave the way to a better understanding of processes taking place at the surface of semiconductor nanoparticles dispersed in solution. In particular, they highlight the potential of AR-SHS to monitor ion adsorption at the surface, changes in the surface effective charge, and general interfacial properties in a variety of (photo)catalytic applications.

5 Ion-specific effects at the SiO$_2$ and TiO$_2$ nanoparticle/aqueous interface

Ion-specific effects play a crucial role in controlling the stability of colloidal systems and regulating interfacial processes. Although mechanistic pictures have been developed to explain the electrostatic structure of solid/water colloidal interfaces, ion-specific effects remain poorly understood. Here we quantify the average interfacial water orientation and the electrostatic surface potential around 100 nm SiO$_2$ and TiO$_2$ colloidal particles in the presence of NaCl, RbCl and CaCl$_2$ using polarimetric angle-resolved second harmonic scattering. We show that these two parameters can be used to establish the ion adsorption mechanism in a low ionic strength regime (< 1 mM added salt). The relative differences between salts as a function of the ionic strength demonstrate cation- and surface-specific preferences for inner- vs outer-sphere adsorption. Compared to monovalent Rb$^+$ and Na$^+$, Ca^{2+} is found to be preferentially adsorbed as outer-sphere on SiO$_2$ surfaces, while a dominant inner-sphere adsorption is observed for Ca^{2+} on TiO$_2$. Molecular dynamics simulations performed on crystalline SiO$_2$ and TiO$_2$ surfaces support the experimental conclusions. This work contributes to the understanding of the electrostatic environment around colloidal nanoparticles on a molecular level by providing insight into ion-specific effects with micromolar sensitivity.

The results presented in this chapter are adapted from Ref. [152]:

Marie Bischoff, Denys Biriukov, Milan Předota, and Arianna Marchioro, „Second Harmonic Scattering Reveals Ion-Specific Effects at the SiO$_2$ and TiO$_2$ Nanoparticle/Aqueous Interface" *J. Phys. Chem. C* 2021, 125, 25261-25274.

All the molecular dynamics simulation results in this chapter are the work of Denys Biriukov and Milan Předota (University of South Bohemia, České Budějovice, Czech Republic).

5.1 Motivation

Ion adsorption at solid/liquid interfaces is a key phenomenon in various fields including catalysis, electrochemistry, energy conversion, corrosion, and geochemistry. Classical electrostatic theories, such as the Gouy-Chapman (GC) or the Gouy-Chapman-Stern (GCS) models, can predict to some extent the behavior of ions at interfaces but cannot always account for ion-specific effects. Ion adsorption is even more complex to rationalize for colloids, since the stability of colloidal dispersions is strongly influenced by the pH and ionic composition of the aqueous environment. In particular, the distribution of charges close to the particle/liquid interface, also referred to as the electrical double layer (EDL) region, plays a fundamental role in the electrostatic stabilization of the colloids. Because the surface of colloids in suspension is inherently more challenging to describe than planar surfaces, it is not trivial to establish a complete molecular picture of the EDL and ion adsorption at the particle/liquid interface. Additionally, not all experimental techniques investigating surface properties of colloidal particles can be employed in low salt environments, or are sensitive enough to detect changes with addition of sub-millimolar salt concentrations. For this reason, investigations of the EDL are often carried out with bulk salt concentrations in the millimolar to molar range. Such experimental conditions allow probing materials specificities when a layer of condensed charges (or Stern layer) is already present, but preclude the study of surface processes occurring at salt concentrations where the charged surface sites outnumber the added counterions.

For colloidal SiO$_2$ and TiO$_2$ particles, two widely investigated oxide materials, several studies have reported on the effect of different counterions on surface charge densities using potentiometric titrations [243–253]. The effect of a specific ion on the surface charge density yields information on the ion adsorption mechanism. For example, potentiometric titrations have been used to explain the catalyzing effect of cations on the dissolution rates of mineral oxides. In this context, such measurements have been able to distinguish between partially dehydrated ions directly adsorbed at the surface (inner-sphere ions) and solvent-separated ionic adsorption with the intact hydration shell (outer-sphere ions) [243]. Because the accuracy of such titrations improves with increasing total surface area, the measurements are usually performed on large amounts of particles and high salt concentrations (in the order of mM-M) [73].

Electrophoretic mobility and zeta potential measurements have often been used to investigate specific ion adsorption of colloidal suspensions. A zeta potential study by Franks [254] on SiO$_2$ suspensions under variation of the monovalent alkali cations concentration showed that the least hydrated ions adsorb in greater quantities than well-hydrated ions, with the zeta potential magnitude increasing for larger hydrated radii [254]. A similar behavior in electrophoretic mobility measurements was also reported by Kosmulski [197]. The zeta potential is an integral property of the EDL, resulting from an interplay of interfacial charge distribution and dynamics. It only indirectly probes surface electrostatics, which can be a drawback when trying to access the mechanism of ion adsorption. More recently, X-ray based techniques have allowed direct evaluation of surface potential, another EDL parameter containing information about surface properties. The effect of different ions on the surface potential of SiO$_2$ nanoparticles

was investigated using X-ray photoelectron spectroscopy (XPS) from a liquid microjet [94, 98]. The authors describe an increase in surface potential and Stern layer thickness with growing hydrated-cation radius of the monovalent ions, corroborating the findings of zeta potential studies [197, 254]. Liquid jet XPS experiments can be especially challenging to perform on dilute nanoparticle suspensions, due to the low signal-to-noise level. Furthermore, salt concentrations in the millimolar range are necessary to reduce photoionization charging effects, [99] preventing the analysis of molecular phenomena occurring at lower salt concentrations. Yet another parameter to characterize the EDL is the interfacial water structure, as water structuring effects are expected to occur during ion adsorption. The effect of different ions on the interfacial water structure has been extensively studied on macroscopically flat surfaces both experimentally by vibrational sum-frequency spectroscopy/sum-frequency generation, [62, 63, 106, 175, 177, 255–257], second-harmonic generation [187, 258, 259] and simulations [64, 173, 190, 260–269]. For colloidal particle suspensions, ion effects on the interfacial water structure are difficult to investigate with current experimental and computational techniques. The ability to probe several parameters of the EDL of colloidal particles in a single experiment would significantly enhance our comprehension of the electrostatic environment at the particle/liquid interface.

We recently showed the applicability of polarimetric angle-resolved second harmonic scattering (AR-SHS) to study the electrical double layer properties around large TiO_2 and SiO_2 nanoparticles (100 nm-300 nm diameter) [150, 151]. This technique allows determining both the surface potential of the particles with respect to bulk liquid and the water structure at the particle interface with micromolar sensitivity in a single experiment. In this work, we report the effect of different salts (NaCl, RbCl and $CaCl_2$) on the surface potential and the surface susceptibility (describing average interfacial water orientation) around SiO_2 and TiO_2 colloids of 100 nm diameter in the low ionic strength regime ($\leq 600\,\mu$M added salt). The general mechanism for ion adsorption appears to be independent of the nature of the oxide surface or of the cation. At the lowest ionic strengths, cations partially compensate the negative surface charge by inner-sphere adsorption, while with increasing ionic strength, our experimental data indicate the formation of a condensed layer of hydrated ions (outer-sphere adsorption). However, the relative differences between salts as a function of ionic strength provide valuable information on the adsorption mechanisms on each oxide surface and reveal specific inner- or outer-sphere preferences of the investigated cations. Compared to monovalent Na^+ and Rb^+, outer-sphere adsorption of Ca^{2+} is favored on SiO_2 surfaces. On the other hand, inner-sphere adsorption of Ca^{2+} is favored on TiO_2 surfaces. Molecular dynamics simulations performed on crystalline TiO_2 and SiO_2 surfaces support the experimental conclusions. Overall, our results consistently demonstrate different adsorption abilities of colloidal silica and titania and their ionic selectivity, complementing the understanding of the EDL structure at oxide nanoparticle surfaces on a microscopic level.

5.2 Materials and Methods

5.2.1 Chemicals

Sodium hydroxide, (NaOH, > 99.99% trace metals basis, Sigma-Aldrich), sodium chloride (NaCl, > 99.999%, abcr GmbH), rubidium chloride (RbCl, > 99.95%, Sigma-Aldrich) and calcium chloride (CaCl$_2$, > 99.99%, Sigma-Aldrich) were used as received. SiO$_2$ colloids dispersed in water (~ 100 nm diameter) were purchased from Polysciences, Inc. (5.9% w/w). TiO$_2$ colloids dispersed in water (~ 100 nm diameter) were purchased from Corpuscular Microspheres Nanospheres (2.5% w/v). The TiO$_2$ colloids are core-shell particles composed of a SiO$_2$ core and a TiO$_2$ shell. As the main contribution to the AR-SHS signal is given by water molecules oriented at the TiO$_2$ surface (see section 2.3.1), our experiment only requires the presence of a few atomic layers of TiO$_2$ in contact with the aqueous solution. We further demonstrate in section 8.4 (Appendix) that the AR-SHS data are independent of the thickness of the TiO$_2$ shell.

5.2.2 Sample preparation

All procedures described hereafter used ultrapure water (MilliQ, Millipore, Inc., electrical resistance of 18.2 M$\Omega \cdot$ cm). The stock solutions of colloidal particles were sonicated for 10 min (35 kHz, 400 W, Bandelin) and vortexed for 2 min prior to usage. The stocks were diluted in water to 0.6% w/v (for SiO$_2$) and 0.5% w/v (for TiO$_2$). In the TiO$_2$ case only, the particles were stabilized by addition of NaOH up to a final concentration of 80 μM. The diluted solutions were further sonicated for 10 min and vortexed for 2 min. In order to remove residual ions from the synthetic procedure, nanoparticles were collected via centrifugation and resuspended in MilliQ water at the same concentration. The pellet was resuspended by vortexing for 5 min and sonicating for 10 min. This washing step was repeated twice for SiO$_2$ particles. The conductivity of the washed particles was measured as described in sections 2.5.2 and 5.2.3 to ensure that the initial ionic strength of the particle suspension was as low as possible. The washed SiO$_2$ particles were further diluted to a 0.06% (w/v) solution (corresponding to approximately $2.9 \cdot 10^{11}$ particles/mL) and the washed TiO$_2$ particles were diluted to 0.05% w/v solutions (corresponding to approximately $4.3 \cdot 10^{11}$ particles/mL), where the desired amount of NaCl, RbCl, or CaCl$_2$ was added. The suspensions were further sonicated for 10 min and vortexed for 2 min. In both cases, the ionic strength of the solutions was adjusted using 0.1 mM stock solutions of NaCl, RbCl, or CaCl$_2$. No filtering of the SiO$_2$ particles was necessary, while the 0.05 w/v% TiO$_2$ solutions were filtered using 0.2 μm PES syringe filters (Filtropur Sarstedt) to remove particle aggregates. After filtering, each sample was sonicated for another 10 min and vortexed for 2 min. The sample solutions were measured on the same day they were prepared. Corresponding water references at the same ionic strength were prepared for each SiO$_2$ and TiO$_2$ sample. All preparation steps and measurements were performed at room temperature.

5.2.3   Sample characterization

The particle size distribution was determined by dynamic light scattering (DLS) and the zeta potential was measured by electrophoretic measurements (Zetasizer Nano ZS, Malvern). In the Zetasizer software, electrophoretic mobility is converted to zeta potential using Henry's function $f(\kappa R)$, where κ is the inverse Debye length and R the particle radius. Henry's function is usually simplified to two limiting cases, namely the Smoluchowski approximation ($\kappa R \gg 1$) or the Hückel approximation ($\kappa R \ll 1$) as further detailed in section 2.4.2. Because in our case the Debye length is varying with increasing ionic strength and some of the measurements may be outside those two limiting cases, we used an approximation derived by Ohshima [160] and further detailed in Ref. [161], allowing for a more precise conversion of electrophoretic mobilities to zeta potential. The SiO_2 particles had a mean hydrodynamic diameter of ~ 125 nm with a uniform size distribution (polydispersity index (PDI) < 0.05). After the filtering process, the TiO_2 colloids had a mean hydrodynamic diameter of ~ 120 nm with a uniform size distribution (for most samples, polydispersity index (PDI) ~ 0.1). Average radii and zeta potentials are given as the average of 3 measurements. The pH of the samples was determined using a pH-meter (HI 5522 pH/ISE/EC bench meter and HI 1330 pH electrode, Hanna Instruments) calibrated with the appropriate buffer solutions. This step ensured that all the samples were measured in pH neutral conditions. The conductivity was measured in order to control the initial ionic strength of the washed particle suspensions and the amount of salt added to the samples, as described in section 2.5.2. For TiO_2 samples diluted in ultrapure water where no salt was added, the average conductivity was assumed to be due to residual Na^+ and OH^- ions from the preparation process. The measured conductivity values of washed and filtered samples at pH 7 without additional salt of the same particle batch varied from 9.4 to 10.6 $\mu S/cm$ (corresponding to an ionic strength of $3.8 \cdot 10^{-5}$ to $4.3 \cdot 10^{-5}$ M). This conductivity, attributed to residual Na^+ and OH^- ions in solution, was subtracted from the conductivity measured for TiO_2 samples where salt was added to calculate the pure contribution of Na^+, Rb^+ or Ca^{2+} cations and Cl^- anions to the ionic strength of the solution. The total ionic strength value of the samples used in the fitting procedure includes the ionic strength originating from the respective cations and anions (Na^+, Rb^+, Ca^{2+} and Cl^-), as well as the residual Na^+ and OH^- ions. A summary of those effective ionic strength values is given in section 8.1.3 (Appendix). Note that the graphs presented in the Results and Discussion section 5.3 are plotted vs added ionic strength or added ionic concentration (i.e. without considering the initial offset introduced by NaOH) to illustrate the effect of NaCl, RbCl and $CaCl_2$ only.

5.2.4   AR-SHS measurements

The Second harmonic scattering in this chapter measurements were performed on the same AR-SHS setup as described in chapter 2.3.3. Here, the fundamental laser wavelength was $\lambda = 1032$ nm and the average laser power at the sample position was set to 80 mW. Before the SH light was detected at the photomultiplier tube it had to pass a bandpass filter (CT516/10bp, Chroma). Data points were acquired using $20 \cdot 1.5$ s acquisition time with a gate width of 10 ns.

The scattering patterns were normalized according to equation 2.18 in chapter 2.3.3. All other measurement parameters where the same as described in chapter 2.3.3.

5.2.5 Molecular dynamics simulations

SiO$_2$ and TiO$_2$ were modeled as neutral crystal quartz (101) and rutile (110) surfaces, respectively. The simulated flat surfaces are a good and verified representation of the metal-oxide/water interfaces, [64, 190] particularly considering the large size of the particles used in the experiments. Our MD simulations in Refs. [150, 151] and in chapters 3 and 4 in this thesis successfully employing the same models for the interpretation of SHS data confirm the validity of the selected approach. The simulated surfaces were of lateral sizes 5.5 nm × 3.928 nm and 3.89814 nm × 3.5508 nm, respectively. The system was constructed as a parallel slab with two identical surfaces facing each other, separated by ~ 5 nm of ionic solution. All the results are averaged over the two solid/water interfaces to improve the sampling. On the other hand, comparison of results at each of the two interfaces confirmed the convergence of simulations. The number of NaCl, RbCl, or CaCl$_2$ ions added to the system was set to achieve a similar bulk ionic strength for all solutions, that is, the ratio of bulk ionic concentrations of CaCl$_2$ and NaCl/RbCl was ~ 1:3. This was gained by adding 6/13 Ca^{2+} (SiO$_2$/TiO$_2$) or 18 monovalent ion pairs solvated in ~ 3700/2050 water molecules. Water was modeled as rigid SPC/E, [192] and the parameters for ions were adopted from the literature [190, 191, 270]. The ionic charges were scaled to 75% of their nominal values according to the Electronic continuum model [189]. All simulations were at least 60 ns long. All other simulation details were the same or similar to those in sections 3.2.5 and 4.2.5 and in Refs. [150, 151, 190, 260].

5.3 Results and Discussion

Similarly-sized SiO$_2$ and TiO$_2$ particles were dispersed in water in the presence of different salts and measured with AR-SHS in PPP and PSS polarization direction as described in section 2.3.3. From the AR-SHS patterns (Fig. 5.1), we extract the surface potential Φ_0, together with the second-order surface susceptibility $\chi_{s,2}^{(2)}$ using the fitting procedure explained in sections 2.3.1, 2.3.2 and 2.3.3. The second-order surface susceptibility represents a measure of the orientational order induced by all (chemical) interactions confined to the particle surface plane. More specifically, $\chi_{s,2}^{(2)}$ describes the interfacial water orientation, as further discussed in section 2.3.1. The zeta potential ζ extracted through electrophoretic mobility measurements is reported for comparison. In order to account for the different charge of monovalent and divalent ions, all the concentrations in this work are expressed in ionic strength and not ionic concentration, unless otherwise stated. The graphs of Φ_0 and $\chi_{s,2}^{(2)}$ as a function of ionic concentration are shown in Figure 5.4 (later in the text) for comparison.
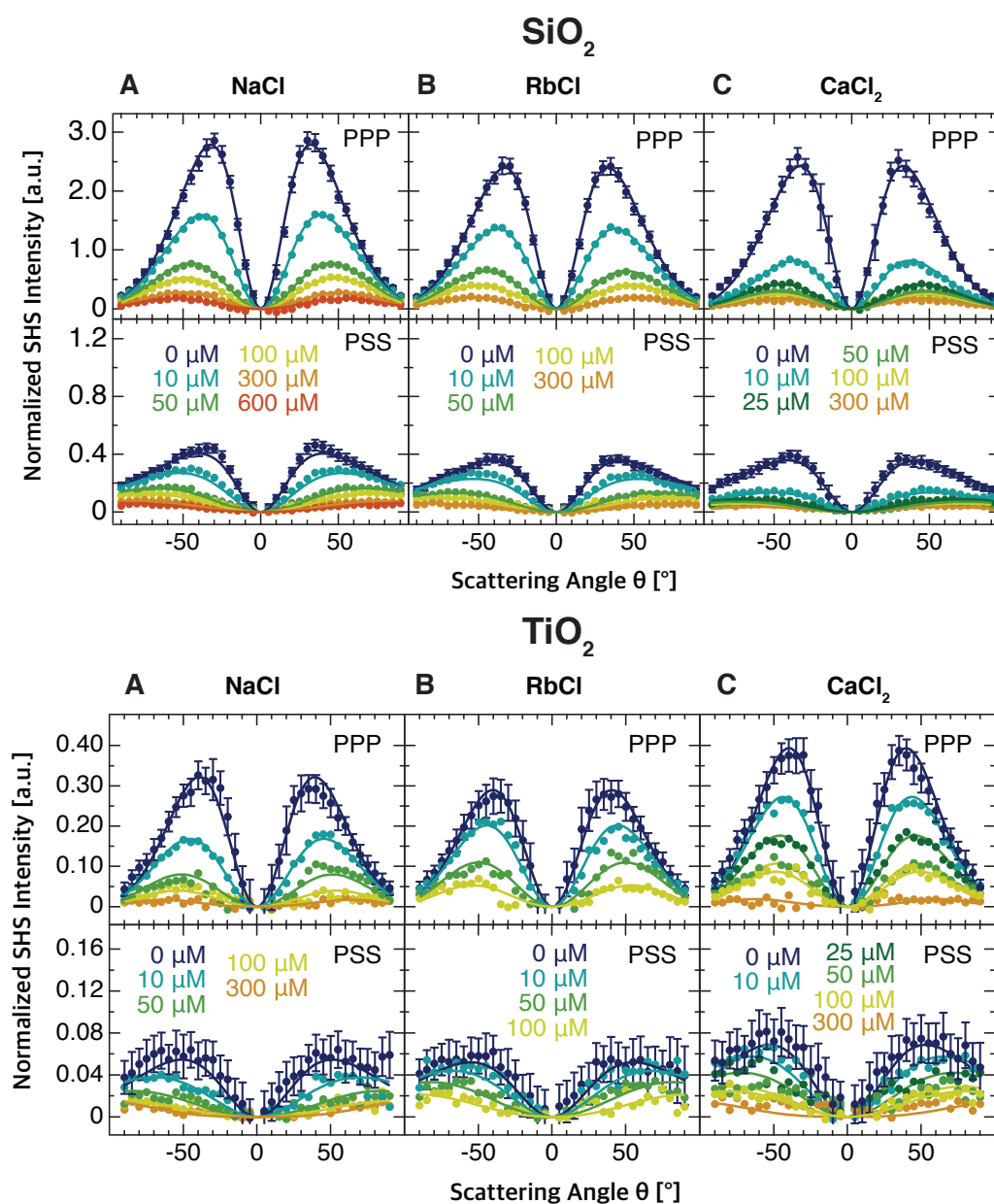
SiO$_2$

TiO$_2$

Figure 5.1 – AR-SHS patterns of ∼ 100 nm diameter SiO$_2$ particles (top) and ∼ 100 nm diameter TiO$_2$ particles (bottom) in suspension in PPP and PSS polarization combination as a function of ionic strength at pH 7. The ionic strength was adjusted through the addition of NaCl (A), RbCl (B) and CaCl2 (C). Plain data points of different colors represent different ionic strength of the aqueous environment. The particle density was kept constant for each sample and equal to $2.9 \cdot 10^{11}$ particles/mL for SiO$_2$ and $4.3 \cdot 10^{11}$ particles/mL for TiO$_2$. All measurements were performed at $T = 296.15$ K. Solid lines represent the fits to the corresponding data points using the AR-SHS model. A summary of all parameters used for the fits can be found in Tables 8.5, 8.4, 8.9 and 8.10.

5.3.1 SiO$_2$ surface potential

Figure 5.2 shows the zeta potential ζ, the surface potential Φ_0 and the surface susceptibility $\chi_{s,2}^{(2)}$ of ~ 100 nm diameter SiO$_2$ particles in water as a function of ionic strength for three different salts, NaCl, RbCl and CaCl$_2$. Figure 5.2 A plots ζ as a function of ionic strength, where ζ is the electrostatic potential at the shear plane of the particle. The shear plane is considered to represent a boundary between the bulk dispersant and the liquid layer (ions and water molecules) strongly associated with the particle. This firmly associated layer moves together with the particle when exposed to an electric field. While only a minor decrease in ζ as a function of ionic strength is noticeable for NaCl and RbCl, a sharper drop in the zeta potential magnitude $|\zeta|$ can be noticed in the case of CaCl$_2$.

In Figure 5.2 B we identify, for all the salts used in this study, three regions showing distinct surface potential trends that we define as region (i), (ii) and (iii). For clarity, these three regions are schematically indicated on Figure 5.2 B for NaCl only. We briefly describe the general surface potential behavior as a function of ionic strength for all the investigated salts in the following section. A more detailed discussion of the dependence of Φ_0 and $\chi_{s,2}^{(2)}$ of TiO$_2$ and SiO$_2$ particles on NaCl concentration and pH can be found in chapters 3, 4 and Refs. [150, 151]. Firstly, at the lowest ionic strengths, a significant decrease in surface potential magnitude (region (i)) can be observed. This region spans from 0 to 100 μM for NaCl, from 0 to 100 μ for RbCl, and from 0 to 25 μ for CaCl$_2$. We assign this decrease to cations being adsorbed at the slightly deprotonated particle surface as inner-sphere complexes [151]. The positively charged cations screen the negative surface charge of the SiO$_2$ particles arising from deprotonated silanol oxygens (we expect a deprotonation of ≤3% at pH 7 for SiO$_2$, see 8.2.2 in Appendix). This surface charge screening causes the effective surface charge density to decrease, leading to a decreased surface potential magnitude $|\Phi_0|$.

With increasing ionic strength, $|\Phi_0|$ reaches its lowest absolute value (region (ii)), with values close to $|\zeta|$ for all three salts (see Fig. 5.2 A). Region (ii) spans from 100 and 300 μM for NaCl, 100 and 200 μM for RbCl, and between 25 μM to 50 μM for CaCl$_2$. Our general surface potential trends are not changed when plotting the surface potential vs ionic concentration (see Fig. 5.4 A)): The minimal surface potential value is reached for lower ionic strengths/concentrations in the following order: Ca^{2+} < Rb$^+$ < Na$^+$. This second region can be interpreted as the formation of a diffuse layer. Once favorable deprotonated surface sites are occupied, the surface potential does not vary substantially within region (ii). Note that not all the surface deprotonated sites are compensated by a surface-adsorbed cation, as this would imply a charge-neutral particle and subsequent colloidal instability, which we do not observe experimentally. As a result, additional cations are more likely to distribute in the solution around the particles to form a diffuse layer, with a part of these cations approaching the surface as outer-sphere complexes [150, 151].

A further increase of the salt concentration leads to a substantial increase in $|\Phi_0|$ (region (iii)) while $|\zeta|$ does not increase significantly. The increase in $|\Phi_0|$ can be observed above 300 μM for NaCl, 200 μM for RbCl, and 50 μM for CaCl$_2$. We propose that this strong increase in $|\Phi_0|$ is caused by outer-sphere ion complexes that gradually form a condensed layer close
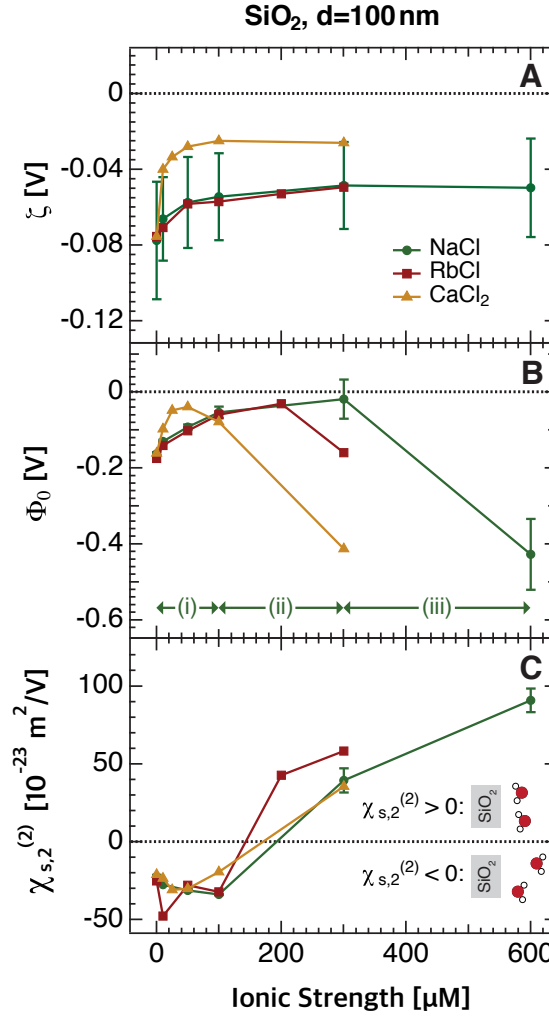
Figure 5.2 – (A) Zeta potential ζ, (B) surface potential Φ_0 and (C) surface susceptibility $\chi_{s,2}^{(2)}$ of SiO$_2$ as a function of ionic strength at pH 7, shown for three different salts (NaCl, RbCl, and CaCl$_2$). $\chi_{s,2}^{(2)}$ represents average interfacial water orientation. Φ_0 and $\chi_{s,2}^{(2)}$ were obtained by fitting the corresponding AR-SHS patterns of ~ 100 nm diameter SiO$_2$ particles in suspension in PPP and PSS polarization combination (see section 2.3 for more details). In (B), the three distinct regions of surface potential behavior, which can be identified for all the three salts used in this study, are displayed for NaCl only (green arrows). The three regions are indicative of different stages of ion adsorption at the surface: (i) inner-sphere adsorption, (ii) diffuse layer formation, and (iii) charge condensation layer formation. For clarity, error bars are shown for NaCl only and are further discussed in sections 2.3.4 and 8.3. All values plotted here are additionally tabulated in Table 5.1.

to the particle surface. This condensed layer generates a strong electric field in between the positively charged cations and the negatively charged particle surface, therefore causing a steep potential drop in the layer similar to the potential behavior in a parallel plate capacitor (a more accurate description could be provided using the spherical capacitor equation, however

Table 5.1 – Particle radius R, zeta potential ζ, surface potential Φ_0, and surface susceptibility $\chi_{s,2}^{(2)}$ of SiO$_2$ as a function of ionic strength at pH 7, shown for three different salts (NaCl, RbCl, and CaCl$_2$). Φ_0 and $\chi_{s,2}^{(2)}$ were obtained by fitting the corresponding AR-SHS patterns of $\sim$ 100 nm diameter SiO$_2$ particles in suspension in PPP and PSS polarization combination (see Figure 5.1). The particle radius R was measured using dynamic light scattering and the zeta potential ζ was obtained from electrophoretic mobility measurements using Ohshima's approximation as described in sections 2.4.2 and 5.2.3. Error bars on Φ_0 and $\chi_{s,2}^{(2)}$ are discussed in sections 2.3.4 and 8.3.

	SiO$_2$				
	added ionic strength [μM]	R [nm]	ζ [mV]	Φ_0 [mV]	$\chi_{s,2}^{(2)}$ [10^{-23} m^{2}V^{-1}]
NaCl	0	65	-78	-163	-22.5
	10	64	-66	-130	-27.6
	50	62	-57	-92	-31.3
	100	61	-54	-54	-33.9
	300	60	-48	-19	39.4
	600	58	-50	-428	90.8
RbCl	0	61	-75	-175	-25.2
	10	62	-71	-141	-47.9
	50	60	-58	-102	-28.0
	100	59	-57	-60	-32.2
	200	59	-53	-31	42.6
	300	58	-49	-160	58.3
CaCl$_2$	0	65	-76	-161	-21.1
	10	60	-40	-98	-23.5
	25	59	-33	-48	-31.0
	50	58	-28	-39	-30.1
	100	59	-25	-78	-19.6
	300	58	-26	-413	35.4

the latter reduces to the parallel plate capacitor equation in the limit where $d_{\text{Stern}} \ll R$):

$$\Delta\phi_{\text{Stern}}^{\text{drop}} = \frac{\sigma d_{\text{Stern}}}{\varepsilon_0 \varepsilon_r} \tag{5.1}$$

where σ is the surface charge density, ε_0 the vacuum permittivity, ε_r is the dielectric constant at the solid/water interface, and d_{Stern} is the spacing of the capacitor. This condensed layer represents an experimental observation of the Stern layer postulated by the GCS theory, [150, 151] where Φ_0 is defined as the sum of the potential drop in the Stern layer $\Delta\phi_{\text{Stern}}^{\text{drop}}$ and of the potential drop between the Stern plane and the bulk solution (usually approximated to ζ). Note that, in this picture, a further increase in ionic concentration (beyond region (iii)) at a fixed surface charge density would lead to a compression of such layer (decrease in d_{Stern}) and a corresponding decrease in $|\Phi_0|$. Our data for region (iii), collected in the micromolar regime, are not indicative of this phenomenon. However, it has been experimentally observed for con-

centrations > 10 mM [95]. This is an important distinction to keep in mind when comparing surface potential values reported in the literature obtained through different methods: The ionic strength range will largely influence the phenomena occurring in the EDL, therefore having a strong effect on the measured surface potential values. It has been suggested previously that SHG measures electrokinetic potentials (ζ) instead of surface potentials [94]. Based on our data, we suggest that the similarities of $|\zeta|$ and $|\Phi_0|$ might only be a consequence of the selected ionic strength range. We observe experimentally in region (ii) that $|\zeta| \approx |\Phi_0|$, while it is not the case in region (i) and (iii). At the same time, reports showing a compression of the Stern layer [95] might, at high ionic strength, probe a situation where $|\zeta|$ is again close to $|\Phi_0|$. We summarized several values reported in the literature for SiO_2 in NaCl electrolyte at neutral pH in Figure 5.3 to allow for further comparison of our AR-SHS results to values of Φ_0 obtained by other methods on both flat and particle surfaces. At low ionic strengths ($10^{-6} - 10^{-4}$ M), our surface potential values are well in agreement with those computed with the Gouy-Chapman model adapted to spherical particles (see Fig. 5.3 and Ref. [150] or chapter 3 of this thesis). Interestingly, recent work on flat surfaces using HD-SHG points to the existence of an additional imaginary term $\chi_X^{(3)}$, with a value 1.5 times that of bulk water, which contributes to the SHG response of charged interfaces [271]. This contribution could produce higher surface potential values at low ionic strengths (blue line in Fig. 5.3) [271]. Given the differences observed at low ionic strength, this new term is unlikely to be significant in the case of spherical, nanosized particles, where any field extending across the SiO_2/water interface and penetrating into the particle will not be screened as it would in their macroscopic counterpart (see Ref. [274] for an explanation). This is further confirmed by our data on different particles sizes (100 nm diameter in this manuscript and 300 nm diameter in chapter 3 and Ref. [150]), where the bulk volume is significantly different and $|\Phi_0|$ does not increase with increasing bulk volume.

At higher ionic strengths ($> 10^{-4}$ M for monovalent ions), our surface potential values are in agreement with those reported for flat surfaces. At even higher ionic strengths ($> 10^{-3}$ M), a range that is generally not accessible with AR-SHS due to the low signal-to-noise ratio, surface potential values have been reported to decrease with increasing ionic strength due to the Stern layer compression, as discussed above.

5.3.2 SiO_2 surface susceptibility

Analysis of the surface potential values as a function of ionic strength in Figure 5.2 B demonstrates that the three separate regions for ion accumulation at the surface previously described [151] are observed for both monovalent and divalent salts. We now address the second parameter obtained through our fitting procedure, namely the surface susceptibility $\chi_{s,2}^{(2)}$, which represents the average water orientation close to the particle surface. Figure 5.2 C shows $\chi_{s,2}^{(2)}$ for SiO_2 particles in the presence of NaCl, RbCl and $CaCl_2$ as a function of ionic strength. For all three salts, $\chi_{s,2}^{(2)}$ has a negative sign for low ionic strength (until 100 μM), indicating an average orientation (net dipole moment) of interfacial water molecules with oxygen atoms towards the surface. The sign convention for $\chi_{s,2}^{(2)}$ is discussed in section 2.3.1, where we attribute the net dipole moment at low ionic strength (oxygens towards the surface) to a majority of water
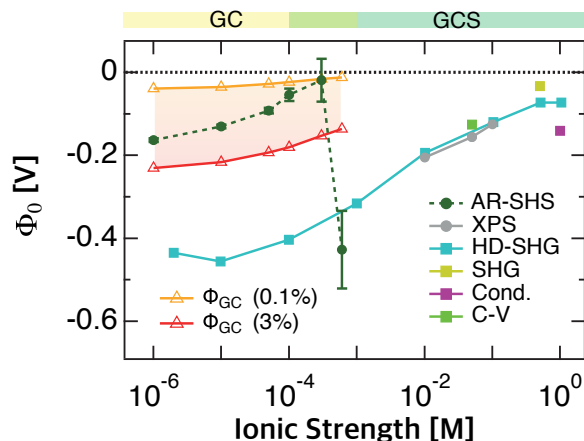
Figure 5.3 – Surface potential (Φ_0) as a function of ionic strength adjusted through the addition of NaCl for the SiO$_2$/water interface in neutral pH conditions. Dark green filled circular markers (dashed line) are Φ_0 values for amorphous ~ 100 nm SiO$_2$ particles as determined from AR-SHS in this study. In comparison, Φ_0 values taken from the literature and obtained through different techniques are shown: XPS (grey), [94, 95] HD-SHG (blue), [271] SHG (yellow), [137] conductance method (purple), [272] C-V measurements (green) [273]. Filled circular markers represent Φ_0 reported for SiO$_2$ particles compared to flat SiO$_2$ surfaces illustrated as filled square markers. The orange and red open triangle markers represent estimates of Φ_0 values obtained using the Gouy-Chapman (GC) model applied to spherical particles and surface charge density values reported in the literature for SiO$_2$ particles in neutral conditions, using the treatment proposed by Ohshima [193]. Φ_0 values shown as red open triangles are calculated with a fixed surface charge density of -0.02153 C/m^2 (Sonnefeld), [206] which corresponds to 3% deprotonation. Φ_0 values plotted as orange open triangles use a fixed surface charge density of 0.0008 C/m^2 (Yamanaka et al.) [201] corresponding to 0.1% deprotonation (see section 8.2.2 in Appendix for more details). The region between the orange and red line therefore represents a range of possible Φ_0 values for spherical particles in neutral conditions using the GC model. Our AR-SHS results fit within the range of predicted values. Colored boxes indicate the typical range of application of the Gouy-Chapman and the Gouy-Chapman-Stern (GCS) models.

molecules being hydrogen-bonded to protonated silanols. This specific net dipole moment at low ionic strength is in line with simulations showing the interfacial water molecules forming ring-like structures with oxygens mainly pointing toward the surface and interacting with surface geminal silanols [275]. With increasing ionic strength, the sign of $\chi_{s,2}^{(2)}$ changes from negative to positive values for all three salts, indicating a change in average water orientation from oxygens facing the surface to hydrogens facing the surface. This specific orientation at higher salt concentration has also been reported by SFG studies on flat SiO$_2$ surfaces [63]. Knowing that by definition $\chi_{s,2}^{(2)}$ does not include water molecules directly ordered by the electric field but only describes the orientational order induced by surface-specific (chemical) interactions confined to the particle surface plane (see section 2.3.1), this flip in $\chi_{s,2}^{(2)}$ can have different origins. For example, oriented water molecules belonging to the ion hydration shells

might contribute to the surface hydration layers, or the presence of ions could cause changes in the interfacial hydrogen bond network. The latter case has recently been observed by SFG [63]. As another option, recent studies have proposed that ions change the structural makeup of the electrical double layer from dominant water-surface interactions to water-water interactions, [276] or intrasurface H-bonding as suggested by theoretical studies [264, 277, 278].
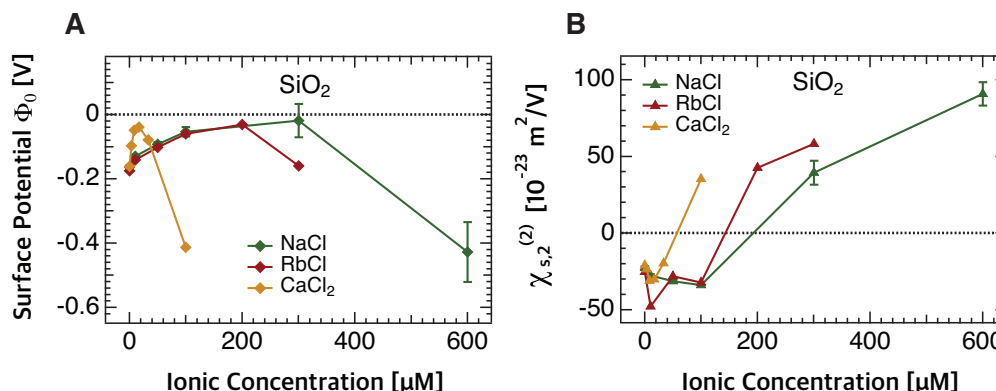

Figure 5.4 – Surface potential Φ_0 (A) and surface susceptibility $\chi_{s,2}^{(2)}$ (B) of SiO_2 as a function of added ionic concentration at pH 7, shown for three different salts (NaCl, RbCl, and $CaCl_2$). Φ_0 and $\chi_{s,2}^{(2)}$ were obtained by fitting the corresponding AR-SHS patterns of ∼ 100 nm diameter SiO_2 particles in suspension in PPP and PSS polarization combination.

We note that, when plotting the surface susceptibility as a function of ionic concentration (see Fig. 5.4 B), a three times lower concentration of Ca^{2+} in the bulk solution is needed to produce the same effect as Na^+ and Rb^+. Knowing the hydration numbers of all three ions (in our MD simulations, those are ∼ 5 water molecules for Na^+, ∼ 8 for Rb^+, and ∼ 6.5 for Ca^{2+}, which is comparable to previously reported data), [279, 280] it appears that a smaller number of Ca^{2+} ions and a corresponding smaller number of water molecules belonging to their hydration shell has a comparable effect to a much larger number of Na^+ and Rb^+ ions and their associated hydration shells. While these rather similar hydration numbers might imply a minor effect of the oriented water molecules in the ion hydration shells on $\chi_{s,2}^{(2)}$, it is plausible to assume that water molecules in the first hydration shell around divalent Ca^{2+} are more restricted by the cation (and even the second hydration shell could be more affected) compared to monovalent ions. As a result, even a lower number of water molecules can induce a noticeable change in the interfacial bond network.

While our data cannot establish unequivocally a mechanism for the change in sign of $\chi_{s,2}^{(2)}$, it does indicate that only the presence of a sufficient amount of positive charges close to the negatively charged surface does lead to a change in the average water orientation from oxygens facing the surface to hydrogens facing the surface. For all three salts, the flip in the average interfacial water orientation from negative to positive $\chi_{s,2}^{(2)}$ values occurs between 100 μM and 300 μM. Figure 5.2 C shows that for SiO_2 particles, the change in water orientation with increasing ionic strength is rather insensitive to the nature of the cation (monovalent or divalent).

5.3.3   Ion-specific effects at the SiO$_2$/water interface

Having established the distribution of charges at the surface with increasing salt concentration, we now turn to ion-specific effects. Looking at Figure 5.2 B, we find that the minimum in the surface potential magnitude is reached at lower ionic strength for CaCl$_2$ (50 μM) with respect to RbCl (200 μM) and NaCl (300 μM). Additionally, for Ca^{2+}, we observe a rapid decrease in $|\zeta|$ (from -46 mV to -25 mV) with only 10,μM added ionic strength, which we do not find in the case of Na$^+$ and Rb$^+$. The difference in the minima of $|\Phi_0|$ for the three different cations indicates that diffuse layer formation (region (ii)) takes over from inner-sphere adsorption (region (i)) at a lower ionic strength for Ca^{2+} ions than for Na$^+$ and Rb$^+$ ions. It also indicates that the build-up of the charge condensation layer starts at a lower ionic strength for Ca^{2+} ions (region (iii)). On the other hand, the inner-sphere adsorption of Na$^+$ and Rb$^+$ ions (region (i)) is similar, whereas the build-up of the charge condensation layer (region (iii)) starts at slightly lower ionic strength for RbCl than for NaCl (200 μM vs 300 μM). Note that, in a high concentration regime ($\sim$ 1 M), several studies have reported that Ca^{2+} is anomalously capable of promoting negative surface charge development at the silica surface by partial deprotonation of the silanols with respect to other alkaline-earth metals [243, 281]. In such high concentration regime, the presence of a Stern layer around the surface is expected, and the potential drop close to the surface can be approximated to the potential drop within the parallel plates of a capacitor as shown earlier in Eq. 5.1. In such conditions, an increase in surface charge density also translates in a corresponding increase in surface potential with increasing ionic strength, which would be similar to our experimental data. However, our conclusions are obtained for a much lower ionic strength range (micromolar salt concentrations) than in any of the aforementioned studies. We therefore believe that region (iii) does not reflect a regime where the high Ca^{2+} concentration induces deprotonation of the silica surface, but rather a regime where the change in surface potential is linked to the progressive transition from a diffuse layer to the formation of the capacitor layer.

We envision two possible hypotheses to explain the ion-specific surface potential trends: a) Ca^{2+} is a better adsorbate for SiO$_2$ surfaces than Na$^+$ and Rb$^+$, therefore saturating all the available surface sites for concentrations as small as 50 μM (preferential inner-sphere behavior). Only with increasing ionic concentration ($> 50\,\mu$M), additional ions introduced in the system contribute as outer-sphere ions, thus increasing the magnitude of the surface potential; or b) Ca^{2+} is not a good adsorbate with respect to Na$^+$ and Rb$^+$, and will not preferentially occupy surface sites. Instead, the majority of the Ca^{2+} ions will approach the surface as outer-sphere ions, therefore contributing to the large increase in surface potential magnitude for ionic strengths $> 50\,\mu$M.

Several ionic properties could influence the inner- vs outer-sphere partitioning. In particular, one could think about the solvation energy (Gibbs free energy of hydration, ΔG_{hyd}). For Ca^{2+}, ΔG_{hyd} is notably higher than for monovalent ions ($\Delta G_{\mathrm{hyd}} = -1505$ kJ/mol for Ca^{2+}, vs -365 and -275 kJ/mol for Na$^+$ and Rb$^+$, respectively), [282] indicating that the water molecules in the hydration shell of the Ca^{2+} ions are more tightly bound than the water molecules in the hydration shell of Na$^+$ and Rb$^+$ ions. As solvation energy also correlates with the residence

time of water molecules in the first cation hydration shell, the same effect is apparent in the higher residence times reported for Ca^{2+} ($\sim 100\,ps$ for Ca^{2+} vs $\sim 10\,ps$ for Na^+) [283]. Ca^{2+} is, therefore, less likely to lose parts of its hydration shell when approaching the negatively charged particle surface. This would point towards a preferential outer-sphere behavior of Ca^{2+} on silica.

In order to distinguish between hypotheses a) and b) using the AR-SHS data, it is informative to look at the water orientation data in Figure 5.2 C. The change in sign of $\chi^{(2)}_{s,2}$ takes place in between an ionic strength of $100\,\mu M$ to $300\,\mu M$ for all the three salts, indicating that the divalent Ca^{2+} ions do not induce a remarkable difference in the interfacial water orientation compared to monovalent Na^+ and Rb^+ ions for similar ionic strengths. On the other hand, the data as a function of ionic concentration shown in Figure 5.4 B indicate that the water orientation flips for a lower amount of Ca^{2+} ions in the bulk solution. These observations would play against hypothesis a): A preferential inner-sphere adsorption of Ca^{2+} is unlikely to promote a change in water orientation at similar ionic strengths (i.e. lower ionic concentrations) than Na^+ and Rb^+. When adsorbing as inner-sphere, positive ions screen existing negative surface sites. Because of this screening, the number of water molecules oriented with hydrogens towards the surface by the negative surface sites will decrease. This phenomenon effectively increases $|\chi^{(2)}_{s,2}|$, resulting in more negative surface susceptibility values, indicating a larger fraction of water molecules oriented with oxygens towards the surface. For Ca^{2+}, we observe such an increase from 0 to $25\,\mu M$ (from -21.1 to -31.0 $cdot 10^{-23}$ m^2V^{-1}, Figure 5.2 C and Table 5.1). Starting from $25\text{-}50\,\mu M$, $|\chi^{(2)}_{s,2}|$ decreases towards positive values. The decrease towards positive values indicates that the fraction of water molecules oriented with oxygens towards the surface decreases in favor of the opposite orientation. The onset of the decrease of $|\chi^{(2)}_{s,2}|$ towards positive values for Na^+ starts at slightly higher ionic strengths ($100\,\mu M$), and for Rb^+, this onset is less clear but takes places between 10 and $100\,\mu M$. Taken together, these findings indicate that past $25\text{-}50\,\mu M$ added ionic strength, additional Ca^{2+} ions will most likely not occupy surface sites, and that Ca^{2+} does not have a preferential inner-sphere adsorption compared to the monovalent ions. When analyzing the data as a function of ionic concentrations (Fig. 5.4), it is even more evident that surface screening by inner-sphere Ca^{2+} ions is not the prevalent mechanism after $8.3\text{-}16.7\,\mu M$ ionic concentration. An additional argument against preferential inner-sphere adsorption of Ca^{2+} can also be found knowing the particularities of the H-bonding network at the surface of hydrated silica. Silica, like other charged surfaces, is known to form ordered water structures at its surface [284–288]. This can also be inferred from the axial number density of water molecules obtained through molecular dynamics simulations displayed in Figure 3.3 A in chapter 3. Simulations predict immobile structures [284] and shorter H-bond distances, [275] with a consequent more robust interfacial H-bond network. Such water structures could hinder ion approach to the surface. This ordered water layer would additionally account for the fact that the nature of the ion has little effect on the net interfacial water orientation.

For all these reasons, a mechanism involving preferential outer-sphere complexes for Ca^{2+} (hypothesis b)) compared to Na^+ and Rb^+ is more likely to explain the similarities in $\chi^{(2)}_{s,2}$ of the three salts. Evidence for a preferential outer-sphere mechanism of Ca^{2+} is also visible in

Table 5.2 – Inner-sphere, outer-sphere and diffuse-layer preference of Na$^+$, Rb$^+$, and Ca^{2+} on SiO$_2$ determined by molecular dynamics simulations of quartz (101). In simulations, the diffuse layer indicates surface cations that are neither inner- nor outer-sphere, but closer to the surface than 15 Å.

	SiO$_2$		
	inner-sphere [%]	outer-sphere [%]	diffuse layer [%]
Na$^+$	20	20	60
Rb$^+$	25	18	57
Ca^{2+}	4	20	76

the AR-SHS patterns as explained in section 8.5 (Appendix). Additionally, the results presented in Figure 5.2 B indicate that, while region (i) is identical for Na$^+$ and Rb$^+$, the formation of a condensed layer (region iii) is favored at lower ionic strength for Rb$^+$ than Na$^+$. Because no substantial difference is observed between the two monovalent ions for the water orientation in Figure 5.2 C, we propose a slightly preferential outer-sphere mechanism for Rb$^+$ compared to Na$^+$ on SiO$_2$ surfaces based on similar arguments as for Ca^{2+}. In this case, when comparing directly the two monovalent ions, the different hydration number (~ 5 for Na$^+$ and ~ 8 for Rb$^+$) and hydrated radii (decreasing from Na$^+$ to Rb$^+$) might influence the approach to the surface and play a role in the propensity to adsorb as outer-sphere ions to form a condensed layer. Finally, similar conclusions can be drawn based on MD simulations, where we used a model of the flat neutral quartz (101) surface. The flat geometry is well justified by the large size of the colloidal particles, and the termination by silanol groups is similar in both the quartz and amorphous cases, [195] though more defects must be expected for amorphous and spherical particles. The model of a neutral surface is justified by the fact that the particles used in the SHS experiment are barely charged at the studied pH (see section 8.2.2 in the Appendix). Moreover, we are mainly interested in the behavior within experimental regions (ii) and (iii) that should correspond to the situation when most charged sites are already occupied/compensated by cations. We analyzed the MD simulations distinguishing the inner-sphere (silanol oxygen replacing one water molecule in the first hydration shell of a cation), outer-sphere (silanol oxygen in the second hydration shell of a cation), and other surface cations, defined as neither inner- nor outer-sphere, but closer to the surface than 15 Å referred here below as diffuse layer). The cation-water cut-offs based on radial distribution functions were set to 3.15/5.4, 3.8/5.9, and 3.15/5.5 Å for inner-/outer-sphere adsorption of Na$^+$, Rb$^+$, and Ca^{2+}, respectively. When comparing the simulations to the experiment, it is important to keep in mind that the AR-SHS experiment might not solely probe the effect of outer-sphere ions as strictly defined in the MD simulation (silanol oxygen in the second hydration shell of a cation), but also more broadly the effect of other solvent-separated surface cations.

Table 5.2 summarizes the adsorption preferences for each studied cation. Our results indicate that overall the cation adsorption at SiO$_2$ is solvent-separated, with Ca^{2+} having the weakest inner-sphere adsorption. This data supports the validity of hypothesis b). Since the concentration range in simulations is higher than in the experiment, we performed additional simulations varying the ionic bulk concentration. Only minor variance in the results was

observed (see Table 8.13 in Appendix), suggesting that this outer-sphere preference is mostly concentration-independent, at least in the concentration range investigated (between 0.09 M and 0.29 M). A small discrepancy is noted between the slight outer-sphere preference of Rb^+ with respect to Na^+ observed in the experiment and the MD data (approximately the same outer-sphere preference for Na^+ and Rb^+, 20% and 18% respectively). As discussed above, this effect could be attributed to the different definition of outer-sphere ions in the experiment and in the simulations.

5.3.4 TiO$_2$ surface potential

Figure 5.5 shows the zeta potential ζ, the surface potential Φ_0 and the surface susceptibility $\chi_{s,2}^{(2)}$ as a function of ionic strength for ~ 100 nm diameter amorphous TiO$_2$ particles when NaCl, RbCl, or CaCl$_2$ is added. As for the SiO$_2$ case, no substantial change in ζ (Fig. 5.5 A) is visible in the case of NaCl and RbCl addition. On the other hand, CaCl$_2$ does have a more noticeable effect on ζ, although only above 50 μM. Similar to the variation of Φ_0 for 100 nm diameter SiO$_2$ as a function of ionic strength shown in Figure 5.2 B, three different regions can also be identified for similarly sized TiO$_2$ particles (Fig. 5.5 B). We find that $|\Phi_0|$ decreases significantly from 0 μM to 10 μM (region(i)) for all three salts. As described hereabove for the SiO$_2$ surface, we assign this effect to inner-sphere ion adsorption at the surface, where the surface charge density of the particles is partly neutralized by the surface-adsorbed positively charged counterions. We expect the deprotonation of the TiO$_2$ particle surface at this pH to be < 8% as further detailed in section 8.2.2 in the Appendix. Region (ii), where Φ_0 is close to ζ, spans from 10 μM to 100 μM added salt and represents the formation of a diffuse layer, with a fraction of the total cations approaching the surface as outer-sphere complexes. We then observe an increase in $|\Phi_0|$ for salt concentrations ranging from 100 μM to 300 μM (region (iii)), whereas $|\zeta|$ does not change significantly. In this region, the cation accumulation close to the surface as outer-sphere complexes starts forming a condensed layer of ions and causes the significant surface potential change by one order of magnitude. Overall, the surface potential trend as a function of ionic strength observed in Figure 5.5 B is similar to the one described in the section above for silica. However interestingly, the variation of surface potential as a function of ionic strength is nearly identical for monovalent and divalent salts. When plotting Φ_0 as a function of ionic concentration (see Fig. 5.6 A), one can see that, due to the divalent nature of the Ca^{2+} ions, a lower concentration of CaCl$_2$ is needed to screen the negative surface charge at the particle surface.

5.3.5 TiO$_2$ surface susceptibility

Figure 5.5 C shows the surface susceptibility $\chi_{s,2}^{(2)}$ in dependence on the ionic strength for the amorphous TiO$_2$ particles in the presence of NaCl, RbCl, and CaCl$_2$. Similar to the results discussed above for the water orientation at the silica surface, we find a comparable change in sign of $\chi_{s,2}^{(2)}$ from negative to positive values occurring in between 10 μM to 50 μM added salt for NaCl and RbCl and in between 100 μM to 300 μM added salt for CaCl$_2$. A negative
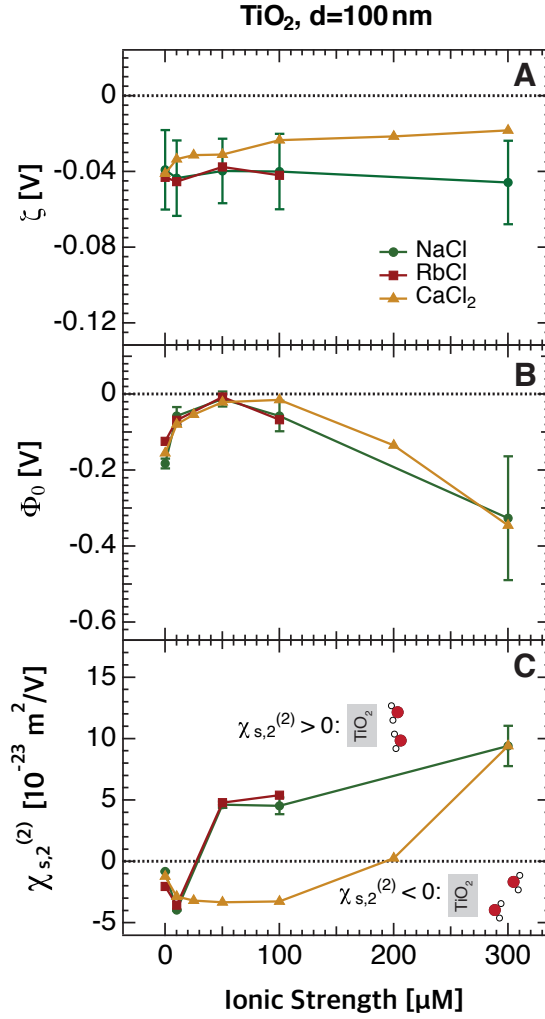
Figure 5.5 – (A) Zeta potential ζ, (B) surface potential Φ_0 and (C) surface susceptibility $\chi_{s,2}^{(2)}$ of TiO$_2$ as a function of ionic strength at pH 7, shown for three different salts (NaCl, RbCl, and CaCl$_2$). $\chi_{s,2}^{(2)}$ represents average interfacial water orientation. Φ_0 and $\chi_{s,2}^{(2)}$ were obtained by fitting the corresponding AR-SHS patterns (shown in Fig. 5.1) of ~ 100 nm diameter TiO$_2$ particles in suspension in PPP and PSS polarization combination (see section 2.3). For clarity, error bars are shown for NaCl only and are further discussed in sections 2.3.4 and 8.3. All values plotted here are additionally tabulated in Table 5.3.

$\chi_{s,2}^{(2)}$ indicates a surplus of interfacial water molecules pointing with the oxygens towards the surface and likely hydrogen-bonding to surface Ti-OH groups. The change to positive $\chi_{s,2}^{(2)}$ again shows the flip of the net dipole moment to hydrogen towards the surface, as discussed above and in Ref. [151] and chapter 4 of this thesis. The flip occurs at higher ionic strengths for Ca^{2+} with respect to Na$^+$ and Rb$^+$, and the same trend is evident in the plot of surface susceptibility vs ionic concentration (see Fig. 5.6 B). Figure 5.5 indicates that, whereas Φ_0 does not seem to depend on the nature of the counterions (monovalent or divalent), $\chi_{s,2}^{(2)}$ is strongly influenced by the respective salt used.

Table 5.3 – Particle radius R, zeta potential ζ, surface potential Φ_0, and surface susceptibility $\chi_{s,2}^{(2)}$ of TiO_2 as a function of ionic strength at pH 7, shown for three different salts (NaCl, RbCl, and CaCl$_2$). Φ_0 and $\chi_{s,2}^{(2)}$ were obtained by fitting the corresponding AR-SHS patterns of ~ 100 nm diameter amorphous TiO_2 particles in suspension in PPP and PSS polarization combination (see Fig. 5.1). The particle radius R was measured using dynamic light scattering and the zeta potential ζ was obtained from electrophoretic mobility measurements using Ohshima's approximation as described in sections 2.4.2 and 5.2.3. Error bars on Φ_0 and $\chi_{s,2}^{(2)}$ are discussed in sections 2.3.4 and 8.3.

<div align="center">TiO$_2$</div>

	added ionic strength [μM]	R [nm]	ζ [mV]	Φ_0 [mV]	$\chi_{s,2}^{(2)}$ [10^{-23} m^{2}V^{-1}]
NaCl	0	59	-39	-182	-0.8
	10	60	-43	-57	-4.0
	50	60	-40	-12	4.6
	100	60	-40	-57	4.5
	300	59	-46	-326	9.4
RbCl	0	62	-43	-124	-2.0
	10	61	-45	-69	-3.6
	50	62	-38	-7	4.8
	100	60	-42	-67	5.4
CaCl$_2$	0	63	-41	-155	-1.2
	10	65	-33	-79	-2.9
	25	63	-31	-53	-3.2
	50	62	-31	-21	-3.3
	100	62	-23	-15	-3.3
	200	59	-21	-135	0.3
	300	59	-18	-346	9.4

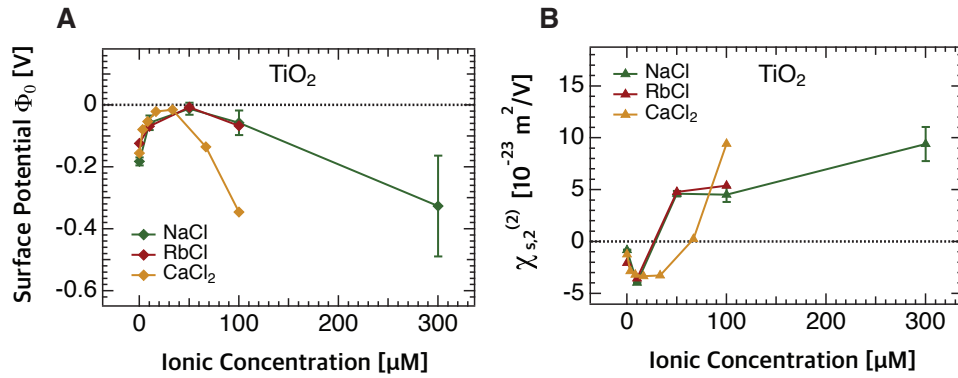Figure 5.6 – Surface potential Φ_0 (A) and surface susceptibility $\chi_{s,2}^{(2)}$ (B) of TiO_2 as a function of added ionic concentration at pH 7, shown for three different salts (NaCl, RbCl, and CaCl$_2$). Φ_0 and $\chi_{s,2}^{(2)}$ were obtained by fitting the corresponding AR-SHS patterns of ~ 100 nm diameter amorphous TiO_2 particles in suspension in PPP and PSS polarization combination.

5.3.6 Ion-specific effects at the TiO$_2$/water interface

For the titania surface, we conclude that for a fixed ionic strength the divalent nature of the Ca^{2+} counterions compared to monovalent Na$^+$ and Rb$^+$ ions does not significantly influence the surface potential trends at the TiO$_2$/liquid interface, even though the Ca^{2+} concentration is then three times lower than the Na$^+$ and Rb$^+$ concentration. These surface potential trends are additionally consistent with the zeta potential results. Between 0 and 50 μM, we find that the decrease in $|\zeta|$ is relatively small in the presence of Ca^{2+} (< 20%) and comparable to the zeta potential trends of Na$^+$ and Rb$^+$. On the other hand, in the case of Ca^{2+} on SiO$_2$ surfaces, a 50% decrease in $|\zeta|$ could be observed with only 10 μM added ionic strength. These results taken together indicate that both monovalent and divalent ions have a similar effect on the electrostatics of TiO$_2$ surfaces.

A mechanism for ion adsorption can be inferred from comparison with the SiO$_2$ case described in Figure 5.2 B. In the case of SiO$_2$, we have established that the increase in $|\Phi_0|$ (region iii) that occurs at lower ionic strength for Ca^{2+} than Na$^+$ and Rb$^+$ is indicative of preferential outer-sphere adsorption. By opposition to the SiO$_2$ results, a situation where the onset of region (iii) is not significantly influenced by the nature of the cation (monovalent or divalent) suggests that outer-sphere adsorption of Ca^{2+} on TiO$_2$ is not the preferential mechanism at the origin of our trends. However, here as well the knowledge of surface potential is not sufficient and it is necessary to examine the average water orientation to get a complete description of the investigated system. Our results show that the surface susceptibility variation as a function of ionic strength is identical for RbCl and NaCl. For both salts the change in sign of $\chi_{s,2}^{(2)}$ takes place in between 10 μM to 50 μM ionic strength, while in the case of CaCl$_2$, this flip in sign can only be observed at higher ionic strength (at around 200 μM), showing a clear effect of the divalent ion with respect to monovalent ions. These observations can be rationalized in a picture where Ca^{2+} ions are preferentially acting as inner-sphere ions at the TiO$_2$ surface, being very effective at dehydrating the TiO$_2$ surface in order to directly adsorb to surface oxygens. In this picture, the Ca^{2+} ions dehydrating the surface contribute to keeping the surface susceptibility negative, as they suppress the contribution of water molecules oriented with their hydrogens towards negatively charged surface sites. Because of this marked inner-sphere preference, the formation of an outer-sphere layer of Ca^{2+} ions only occurs at a higher ionic strength (and a larger ionic concentration) than in the case of Na$^+$ and Rb$^+$. As discussed before, only the presence of a sufficient amount of outer-sphere ions close to the surface can induce a flip in the average water orientation, explaining why in the case of Ca^{2+} on TiO$_2$ a higher ionic strength (and a larger ionic concentration) is necessary to induce a flip in the average water interfacial orientation. These findings are in contrast to the SiO$_2$ surface, where a preferential outer-sphere adsorption of Ca^{2+} compared to Na$^+$ and Rb$^+$ was observed. The different behavior of Ca^{2+} on TiO$_2$ compared to SiO$_2$ is further highlighted by the AR-SHS scattering patterns as a function of ionic strength as detailed in section 8.5 (Appendix). Considering that the solvation energy (ΔG_{hyd}) of Ca^{2+} is larger than for Na$^+$ and Rb$^+$ as discussed above, our results indicate a strong capacity of TiO$_2$ for removing water molecules from the hydration shell of Ca^{2+}. Additionally, TiO$_2$ is also known to form

Table 5.4 – Inner-sphere, outer-sphere and diffuse-layer preference of Na^+, Rb^+, and Ca^{2+} on TiO_2 determined by molecular dynamics simulations of rutile (110). In simulations, the diffuse layer indicates surface cations that are neither inner- nor outer-sphere, but closer to the surface than $15\,Å$.

	TiO_2		
	inner-sphere [%]	outer-sphere [%]	diffuse layer [%]
Na^+	76	7	17
Rb^+	71	7	22
Ca^{2+}	97	0	3

strong interfacial H-bond networks as determined by experiments [289, 290] and predicted by simulations [291–293]. In the case of SiO_2, this surface property could explain the hindered approach of Ca^{2+} as an inner-sphere ion. On the other hand, in the case of TiO_2, the same property underscores the exceptional affinity of its surface for Ca^{2+}.

MD simulations further support the trends observed by AR-SHS. A strong innersphere adsorption preference at the TiO_2 surface (rutile (110)) is observed for Ca^{2+} (97%, see Table 5.4). Almost all Ca^{2+} ions added to the system irreversibly adsorb as inner-sphere within the simulation timescale, highlighting the affinity of TiO_2 even when the surface is neutral as modeled. Moreover, while our AR-SHS experiment draws conclusions on the relative ion-specific adsorption preferences, MD simulations reveal a general inner-sphere preference for all studied cations at the TiO_2 surface (also observed for other bulk ionic concentrations between $0.08\,M$ and $0.36\,M$, see Table 8.14), further emphasizing the affinity of titania surfaces for cations. At the same time, for amorphous particles, we expect less dominating yet prevailing inner-sphere adsorption due to the disruption of geometrically-perfect inner-sphere adsorption sites present all over the modeled flawless surface. The preferred inner-sphere absorption of cations at titania surfaces observed in simulations further helps rationalizing why no noticeable difference between Na^+ and Rb^+ is visible in the AR-SHS measurements: Contrarily to the case of monovalent ions on SiO_2, where the difference in hydration number/hydrated radii might influence the outer-sphere approach, the same property would not have much impact in the case of inner-sphere adsorption, where the ions are partially dehydrated to adsorb at the surface.

5.3.7 Inner- and outer-sphere adsorption at SiO_2/water and TiO_2/water interfaces

Figure 5.7 schematically summarizes the overall ion adsorption mechanism in the case of Ca^{2+} for SiO_2 and TiO_2 surfaces at different ionic strengths. Figure 5.7 A illustrates inner-sphere adsorption occurring in the lowest investigated ionic strength range (region (i)) for both surfaces. This process contributes to a decrease in $|\Phi_0|$. The net dipole moment of water molecules is oriented with oxygens towards the surface (negative $\chi^{(2)}_{s,2}$). On the other hand, at the highest investigated ionic strengths (region (iii)), Ca^{2+} ions adsorb as outer-sphere as illustrated in Figure 5.7 B,C. This process contributes to an increase in $|\Phi_0|$. The net dipole
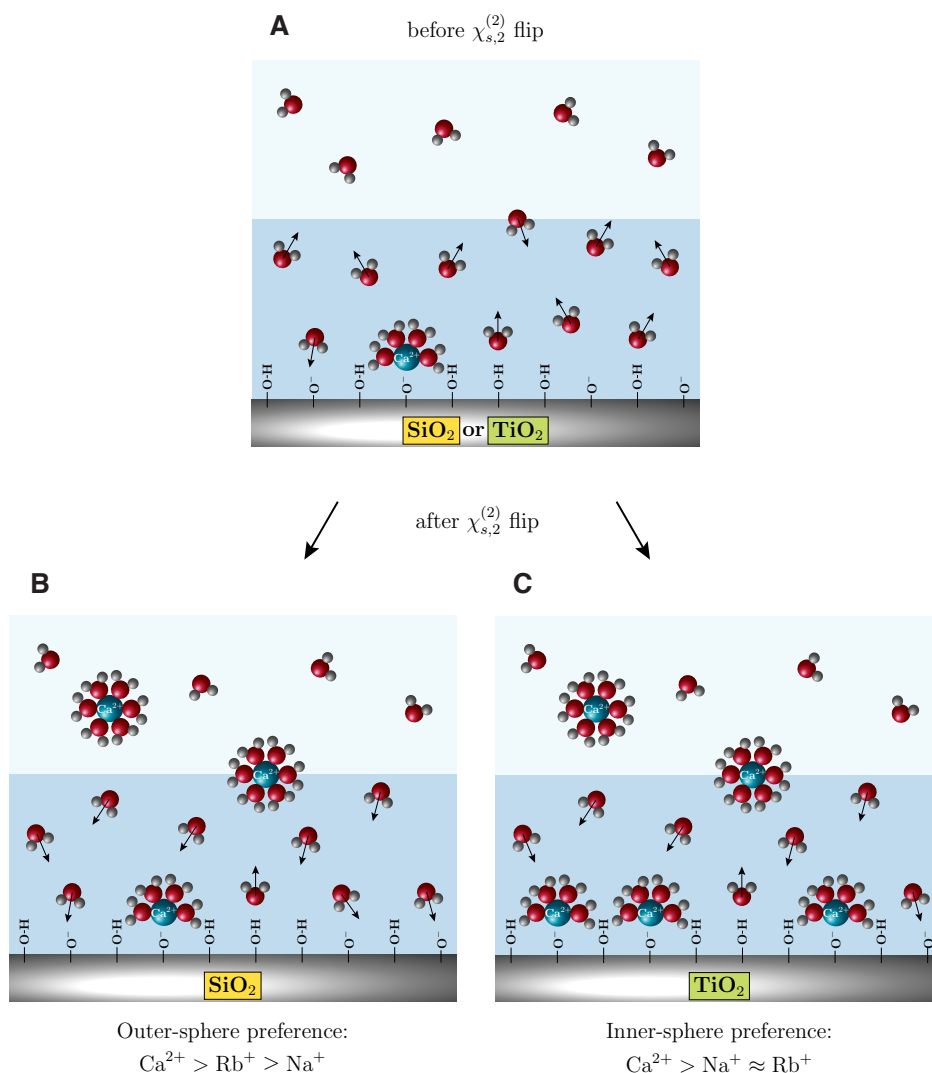
Figure 5.7 – Schematic illustration of the overall ion adsorption process for Ca^{2+}. The hydration shell for Ca^{2+} is simplified and displayed with six water molecules in the first hydration shell. No anions are shown for clarity. (A) In the lowest investigated ionic strength range (region (i)), inner-sphere adsorption occurs for both SiO$_2$ and TiO$_2$ surfaces. This process contributes to a decrease in $|\Phi_0|$. The dark blue region contains molecules that are contributing to $\chi_{s,2}^{(2)}$. The net dipole moment represents the sum of the dipole moments for each individual water molecule (small black arrows) and is oriented with oxygens towards the surface, giving rise to a negative $\chi_{s,2}^{(2)}$. (B,C) At higher ionic strengths (region (iii)), Ca^{2+} ions adsorb as outer-sphere, inducing a flip in the net dipole moment of water molecules (hydrogens towards the surface, or positive $\chi_{s,2}^{(2)}$). The relative differences in Φ_0 and $\chi_{s,2}^{(2)}$ as a function of ionic strength indicate different preferential adsorption mechanisms for Ca^{2+} compared to Na$^+$ and Rb$^+$ ions. For Ca^{2+} on SiO$_2$ (B), preferential outer-sphere adsorption with respect to Na$^+$ and Rb$^+$ ions is observed. For Ca^{2+} on TiO$_2$ (C), preferential inner-sphere adsorption with respect to Na$^+$ and Rb$^+$ ions is observed.

moment of water molecules is oriented with hydrogens towards the surface (positive $\chi_{s,2}^{(2)}$). Only a sufficient amount of outer-sphere ions close to the surface causes a change in interfacial water orientation from a majority of oxygens facing the surface to a majority of hydrogens facing the surface. While inner- and outer-sphere mechanisms are common to both surfaces, the relative differences as a function of ionic strength indicate different preferential adsorption mechanisms for Ca^{2+} compared to Na^+ and Rb^+ ions. For the silica surface in Figure 5.7 B, preferential outer-sphere adsorption with respect to Na^+ and Rb^+ ions is observed (outer-sphere preference for SiO_2: $Ca^{2+} > Rb^+ \geq Na^+$). The outer-sphere preference of Ca^{2+} on SiO_2 is confirmed by MD simulations. On the other hand, our results reveal preferential inner-sphere adsorption of Ca^{2+} with respect to Na^+ and Rb^+ ions for the titania surface in Figure 5.7 C (inner-sphere preference for TiO_2: $Ca^{2+} > Na^+ \approx Rb^+$). A similar order is also determined by MD simulations for crystalline surfaces (quartz (101) and rutile (110)). While there might be differences between the interfacial behavior of different crystal faces investigated with MD vs. the amorphous structures investigated with AR-SHS, we believe the fundamental properties of the ions and the selected oxide surfaces would be dominant irrespective of a specific crystalline structure.

5.4 Conclusions

In this work, we use polarimetric angle-resolved second harmonic scattering (AR-SHS) to investigate the electrical double layer properties of 100 nm diameter SiO_2 and TiO_2 particles in the low ionic strength regime ($\leq 600\,\mu$M added salt) for three different salts, NaCl, RbCl and $CaCl_2$. AR-SHS patterns yield in a single experiment values for the surface potential of colloidal suspensions Φ_0 and for the second-order surface susceptibility $\chi_{s,2}^{(2)}$, which represents interfacial water ordering at the particle surface. The surface potential results as a function of ionic strength show that three different stages for ion adsorption can be observed for both monovalent and divalent salts on both surfaces. The three regions are identified as (i) Inner-sphere adsorption, (ii) Diffuse layer formation and (iii) Build-up of a charge condensation layer (outer-sphere adsorption). This ion adsorption mechanism appears to be general for all cations and surfaces investigated here.

Furthermore, we demonstrate that the relative differences between salts as a function of the ionic strength provide information on the specific adsorption abilities of silica and titania and reveal inner- or outer-sphere preferences of Na^+, Rb^+ and Ca^{2+}. In the case of the SiO_2 surface, the surface potential changes as a function of ionic strength distinctively depend on the nature of the cation, while the surface susceptibility values are hardly affected by the nature of the cation. Combining the knowledge of surface potential values with the surface susceptibility, we were able to demonstrate a preferential outer-sphere adsorption of Ca^{2+} ions on silica surfaces with respect to Na^+ and Rb^+. In the case of the TiO_2 surface, the surface potential changes as a function of ionic strength showed little dependence on the cation, whereas the surface susceptibility data indicate the need for a larger Ca^{2+} ionic strength/concentration to change the average water orientation in the vicinity of the titania surface with respect to

Na$^+$ and Rb$^+$. Here, both parameters together are used to reveal the more favorable inner-sphere adsorption of calcium ions on titania surfaces with respect to the monovalent ions. Molecular dynamics simulations performed on both quartz (101) and rutile (110) surfaces were used to determine the percentage of inner-sphere and outer-sphere adsorption for all three salts, confirming the experimental trends. Simulations additionally indicate a general inner-sphere preference for all studied cations at the TiO$_2$ surface, emphasizing the affinity of titania surfaces for cations.

The present experiments demonstrate the possibility to probe the adsorption abilities of colloidal oxide nanoparticles and their ionic selectivity with micromolar sensitivity. Because our AR-SHS results are obtained for a low concentration regime that is difficult to access with other experimental techniques probing colloidal surface properties, they give a new insight into processes occurring before a charge condensation layer (Stern layer) is established, and processes at the electrical double layer in general. As colloidal nanoparticles are increasingly used in many technological applications, ranging from drug delivery to catalysis, the ability to characterize their electrostatic environment in solution will assist in engineering more efficient materials and devices.

6 Surface acidity at the anatase TiO$_2$ nanoparticle/aqueous interface

Surface acidity is known to play an important role in photocatalytic reactions. However, with common experimental techniques that can access surface charge and surface acidity, it remains difficult to obtain a complete picture of interfacial processes occuring in the electrical double layer region as a function of pH. More refined experimental methods are needed that are able to combine knowledge about surface specific properties and interfacial molecular behavior. In this chapter, we show that polarimetric angle-resolved second harmonic scattering can be used to monitor the surface acidity of 100 nm anatase TiO$_2$ colloidal particles in aqueous environments. We extract the surface potential and surface susceptibility, which can be interpreted as a measure of interfacial water orientation, in solutions of different pH. The change in sign of the surface susceptibility reveals the surface pK$_a$s of anatase TiO$_2$ particles in water. With the ability to probe both surface potential and surface susceptibility, angle-resolved second harmonic scattering can serve as a complementary technique to existing methods to probe surface acidity. This technique offers the possibility to measure dilute colloidal suspensions and provides future opportunities to directly monitor proton transfer reactions in situ.

The anatase TiO$_2$ particles investigated in this chapter were provided by Na Yeon Kim and Ji Bong Joo (Konkuk University, Seoul, Korea).

6.1 Motivation

Photocatalytic reactions are of major importance in the quest to develop efficient, economical and environmentally-friendly energy conversion and storage systems. Furthermore, photocatalysis is a promising tool to promote environmental decontamination processes. Anatase TiO$_2$ is a widely studied semiconductor material that is generally considered to show a high photocatalytic activity [1, 17, 20, 21]. This makes it an interesting candidate for the use as photocatalyst material in a variety of applications. To improve the overall performance of anatase TiO$_2$ photocatalysts it is key to understand the semiconductor/liquid interface on a molecular level. In particular, the evolution of surface acidity is of fundamental interest, since the photocatalytic activity was shown to strongly depend on the photocatalyst surface properties [37, 294, 295] and the composition of the aqueous environment [36]. However, it remains difficult to monitor interfacial properties that determine the efficiency of photocatalytic processes. Therefore it is of paramount importance to find experimental techniques that can provide both information on the interfacial surface properties of the photocatalyst and the aqueous environment in the vicinity of the surface to establish a molecular picture of the photocatalyst/liquid interface.

Amongst surface properties, surface charge density drives electrostatic processes. The semiconductor material TiO$_2$ is an amphoteric oxide, which can act as both donor or acceptor of protons depending on environmental pH conditions. For TiO$_2$, the surface charge density as a function of pH was previously investigated with the help of potentiometric titrations [74–77, 145, 296, 297]. The surface acidity of TiO$_2$ was additionally studied by reflectance-based conduction band edge energy measurements [298] and simulations [299–301]. For a pure crystalline TiO$_2$ phase, the point of zero charge (PZC) equilibrium, where the surface concentration of TiO$^-$ and TiOH$_2^+$ are equal, can be expressed as pH$_{\text{PZC}} = \frac{1}{2}\left(\text{pK}_{a1} + \text{pK}_{a2}\right)$ [296, 297, 300, 302].

In this chapter, we apply AR-SHS to $\sim$100 nm anatase TiO$_2$ particles in different pH conditions. We investigate the surface potential Φ_0 of the particles with respect to bulk liquid and the surface susceptibility $\chi_{s,2}^{(2)}$, as a measure of interfacial water orientation. Both parameters can be determined from AR-SHS measurements. Additionally, we employ electrophoretic mobility measurements to obtain the zeta potential in comparison. We demonstrate that our AR-SHS method provides insights into how the surface acidity evolves as a function of pH in an all-optical, non-invasive experiment that is complementary to potentiometric titration methods. Surface water orientation extracted through AR-SHS measurements is used as a direct probe of the relative concentration of protonated and deprotonated surface species, therefore yielding information on the surface pK$_a$s. We observe that the changes in interfacial water orientation as a function of pH indicate transitions from a majority of one surface species to another. Our AR-SHS data reveal surface pK$_a$s and a point of zero charge (PZC) that are in line with the above-mentioned equation as it was previously reported in the literature. This further underlines the capability of the AR-SHS method to measure surface acidity of colloidal oxide particles in an aqueous solution. With these features, AR-SHS has the potential to probe surface acidity in-situ during photoelectrochemical reactions without the need to apply

electrodes. We expect our research to contribute to a better molecular level understanding of semiconductor/liquid interfaces that are relevant to advance energy and environmental applications for a more sustainable and greener future.

6.2 Materials and Methods

6.2.1 Chemicals

Sodium hydroxide, (NaOH, > 99.99% trace metals basis, Sigma-Aldrich) and hydrochloric acid (HCl, > 99.999% trace metals basis, Sigma-Aldrich) were used as received. Ethyl alcohol (C_2H_5OH, 99.9%, anhydrous), acetonitrile (ACN, CH_3CN 99.9%, special guaranteed grade), and ammonium hydroxide (NH_4OH, 28%) were obtained from Daejung Chemical Company. Titanium (IV) n-butoxide (TBOT, 97%, reagent grade) and hydroxypropyl cellulose (HPC, average M_W ~80000) were obtained from Aldrich. Spherical anatase TiO_2 colloids (~100 nm diameter) were prepared by Na Yeon Kim (Joo group, Konkuk University, Seoul, Korea) via a sol-gel reaction in mixed solvent solution, as previously reported [303]. This synthetic procedure employs TBOT as precursor and ammonium hydroxide is used to control the growth to the desired size. HPC (50 mg) was used as a surfactant and dissolved in a solution of ethanol and acetonitrile (100 mL, volume ratio of 3:1) under vigorous stirring. After completely dissolving the HPC, 1 mL of aqueous ammonia solution was added to the solution. After stirring for 10 min, a solution of TBOT (4 mL) in a mixture of ethanol (12 mL) and acetonitrile (4 mL) was quickly injected into the above solution. The mixture was vigorously stirred for 2 h under ambient conditions and the white precipitate was isolated by centrifugation. The obtained precipitate was washed with ethanol and with deionized (D.I.) water several times and dried under vacuum. The dried amorphous TiO_2 particles were transferred into an alumina boat in a muffle furnace and calcined in air at 500 °C for 3 h. After calcination, the spherical amorphous TiO_2 particles were crystallized into the anatase crystal structure. X-ray diffraction (XRD) was employed to validate the crystallinity of the sample. The purity of the sample was verified by energy dispersive X-ray (EDX) analysis (atomic fraction: 40.6% ± 10% Ti, 59.4% ± 10% O). The TiO_2 particles were dispersed in a solution as described in section 6.2.2.

6.2.2 Sample preparation

All procedures described hereafter used ultrapure water (MilliQ, Millipore, Inc., electrical resistance of 18.2 $M\Omega \cdot cm$). A stock solution of 1% w/v was prepared from the TiO_2 anatase powder. This stock solution of colloidal particles was sonicated for 40 min (35 kHz, 400 W, Bandelin) and vortexed for 2 min prior to usage. The sonication was performed in intervals of 10 min with intermediate cooling times for sonicator and sample. The anatase TiO_2 stock was diluted in water to 0.05% w/v. The diluted solutions were further sonicated for 10 min and vortexed for 2 min. No washing of the particles was needed. The conductivity of the particles was measured as described in section 2.5.2 to ensure that the initial ionic strength of the

particle suspension was as low as possible. Sample solutions of 0.005% w/v (corresponding to approximately $2.5 \cdot 10^{10}$ particles/mL (theoretical value) with $R = 50$ nm) with the desired amount of NaOH or HCl were produced. The suspensions were further sonicated for 10 min and vortexed for 2 min. The pH of the solutions was adjusted using 1 mM and 0.1 mM stock solutions of NaOH and HCl. No filtering of the anatase TiO$_2$ samples was necessary to obtain a monomodal and narrow particle size distribution. The sample solutions were measured on the same day they were prepared. Corresponding water references at the same pH were prepared for each TiO$_2$ sample. In cases where the pH of the sample was close to the pH of ultrapure water (pH 5 to pH 7), water was used as a reference. The glass sample cuvettes for AR-SHS measurements were rinsed 3 times with MilliQ water prior to usage. All preparation steps and measurements were performed at room temperature.

6.2.3 Sample characterization

The particle size distribution was determined by dynamic light scattering (DLS) and additionally measured by transmission electron microscopy (TEM). The anatase TiO$_2$ particles had a mean hydrodynamic diameter of ~ 140 nm with a uniform size distribution (for most samples polydispersity index (PDI) < 0.2). Note that the hydrodynamic diameter is related to the intensity-based particle size distribution directly obtained from DLS. Another possible representation is the number-based particle distribution which can be obtained from the intensity distribution assuming spherical, homogeneous particles whose optical properties are known. The particle diameter obtained from the number analysis of the anatase TiO$_2$ particles is ~ 96 nm and appears smaller than the hydrodynamic diameter. The mean TEM diameter could be determined as $d_{\text{TEM}} = 96$ nm for a selection of thousands of particles assuming a spherical particle shape. Figure 6.1 shows two TEM images of the anatase TiO$_2$ particles with different fields of view (1 μm (A) vs 0.5 μm (B) magnification) as they were used to deduce the TEM diameter. Note that several images of the same kind were utilized to determine the mean TEM diameter d_{TEM}.

While the number-based particle diameter from DLS and the mean TEM diameter are similar in magnitude and more directly comparable since they both rely on a number analysis [304, 305], the hydrodynamic diameter from the DLS intensity distribution naturally displays larger values. Differences between the hydrodynamic diameter and the TEM diameter can be explained by the liquid shell of water molecules and ions that remain closely attached to the particles during Brownian motion, which additionally contribute to the hydrodynamic diameter. Contrarily to amorphous TiO$_2$ particles in chapters 4 and 5, the deviation between the hydrodynamic DLS radius and TEM radius is much larger for anatase TiO$_2$ particles (~ 20 nm radius). This discrepancy could be explained by 1) not perfectly spherical particle shape which may cause anatase TiO$_2$ to appear larger in DLS and 2) different surface roughness of crystalline anatase vs amorphous TiO$_2$ samples, which could additionally influence the hydrodynamic diameter. A TEM image of a single anatase TiO$_2$ particle is shown in Figure 6.1 C to report on the general shape of the particles. Because of this larger deviation between the hydrodynamic DLS radius and the TEM radius, in this chapter the TEM radius was chosen as
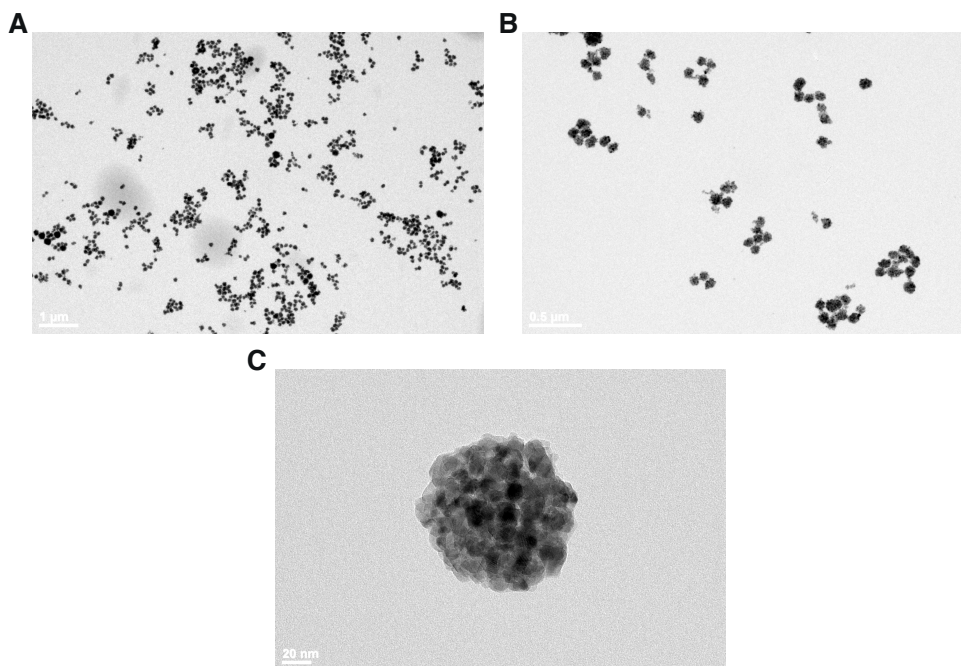
Figure 6.1 – Bright-field TEM images of $\sim 100\,\text{nm}$ diameter anatase TiO$_2$ particles with $1\,\mu$m (A) and $0.5\,\mu$m (B) magnification. The morphology of a single anatase TiO$_2$ particle is shown in (C).

the parameter to be used in the AR-SHS fitting procedure. This can additionally be justified by the good agreement between the TEM and the number-based DLS radius.

The concentration of particles in the solution (particles/mL) was measured for each sample with multiangle dynamic light scattering (MADLS) as explained in chapter 2.4.1 in more detail. The particle concentration is originally obtained as a function of the hydrodynamic diameter. A scaling factor $\left(1/\left(\frac{d_{\text{TEM}}}{d_H}\right)^6\right)$ was applied to the measured particle concentration value in order to account for the smaller TEM radius.

The zeta potential was measured by electrophoretic measurements (Zetasizer Ultra, Malvern). In the Zetasizer software, electrophoretic mobility is converted to zeta potential using Henry's function $f(\kappa R)$, where κ is the inverse Debye length and R the particle radius. Henry's function is usually simplified to two limiting cases, namely the Smoluchowski approximation ($\kappa R \gg 1$) or the Hückel approximation ($\kappa R \ll 1$) as further detailed in section 2.4.2. Because in our case the Debye length is varying as a function of pH and some of the measurements may be outside those two limiting cases, we used an approximation derived by Ohshima [160] and further detailed in Ref. [161], allowing for a more precise conversion of electrophoretic mobilities to zeta potential. The same procedure was already applied in chapter 5.

Average hydrodynamic radii, particle concentrations and zeta potentials are given as the average of 3 measurements. The pH of the samples and reference solutions was determined using a pH-meter (HI 5522 pH/ISE/EC bench meter and HI 1330 pH electrode, Hanna Instruments)

calibrated with the appropriate buffer solutions. For anatase TiO$_2$ samples diluted in ultrapure water without additional acid or base, the pH was ~ 5. The conductivity was measured in order to control the initial ionic strength of the particles dispersed in water and the ionic strength of the samples at different pH, as described in section 2.5.2. For anatase TiO$_2$ samples diluted in ultrapure water where no acid or base was added, the average conductivity was assumed to be due to residual H$^+$ and Cl$^-$ ions from the preparation process. The measured conductivity values of samples in water without additional acid or base was ~ 1.2 μS/cm (corresponding to an ionic strength of $2.9 \cdot 10^{-6}$ M). This conductivity, attributed to residual H$^+$ and Cl$^-$ ions in solution, was subtracted from the conductivity measured for anatase TiO$_2$ samples where acid or base was added to calculate the pure contribution of Na$^+$ and OH$^-$ ions or H$^+$ and Cl$^-$ ions to the ionic strength of the solution. The ionic strength value of the samples used in the fitting procedure only takes into account the ionic strength originating from NaOH and HCl addition.

6.2.4   AR-SHS measurements

In this chapter the second harmonic measurements were performed on the same AR-SHS setup as described in chapter 2.3.3. Here, the fundamental laser wavelength was $\lambda = 1032$ nm and the average laser power at the sample position was set to 80 mW. Before the SH light was detected at the photomultiplier tube it had to pass a bandpass filter (CT516/10bp, Chroma). Data points were acquired using $20 \cdot 1.5$ s acquisition time with a gate width of 5 ns. The scattering patterns were normalized according to equation 2.18 in chapter 2.3.3. All other measurement parameters where the same as described in chapter 2.3.3.

6.3   Results and Discussion

Anatase TiO$_2$ particles were dispersed in solutions of different pH and measured with AR-SHS in PPP and PSS polarization direction as described in sections 6.2.4 and 2.3.3. From the AR-SHS patterns (Fig. 6.2), we determine the surface potential Φ_0 and the second-order surface susceptibility $\chi_{s,2}^{(2)}$ applying the fitting procedure explained in sections 2.3.1, 2.3.2 and 2.3.3. $\chi_{s,2}^{(2)}$ represents a mean to assess the interfacial molecular orientation of water that is chemically bound to the particle surface plane, as further discussed in section 2.3.1. In comparison to the surface potential Φ_0, the zeta potential ζ, obtained from electrophoretic mobility measurements is reported as a function of pH.

Figure 6.3 A shows the Φ_0 and ζ of ~100 nm anatase TiO$_2$ particles in different pH conditions. Both Φ_0 and ζ are of positive magnitude for 4≤pH<6. In this pH range, |Φ_0| and |ζ| generally decrease in magnitude. At pH~6, the surface potential Φ_0 and zeta potential ζ change sign. For 6<pH≤9 Φ_0 and ζ are of negative magnitude. In this pH region, |Φ_0| and |ζ| generally increase in magnitude. The point where ζ is zero, meaning that the particle has zero velocity when exposed to an electric field in electrophoretic measurements, is called the isoelectric

point (IEP). On the other hand, when Φ_0 reaches zero, this is usually referred to as the point of zero charge (PZC). For colloids, no direct measurements can be performed at the IEP or the PZC since the particles become unstable and are likely to form aggregates when the repulsive forces between the particles decrease as a result of the vanashing surface charge. In our case, the IEP occurs at slightly higher pH values (~pH 6.1) than the PZC (~pH 6).
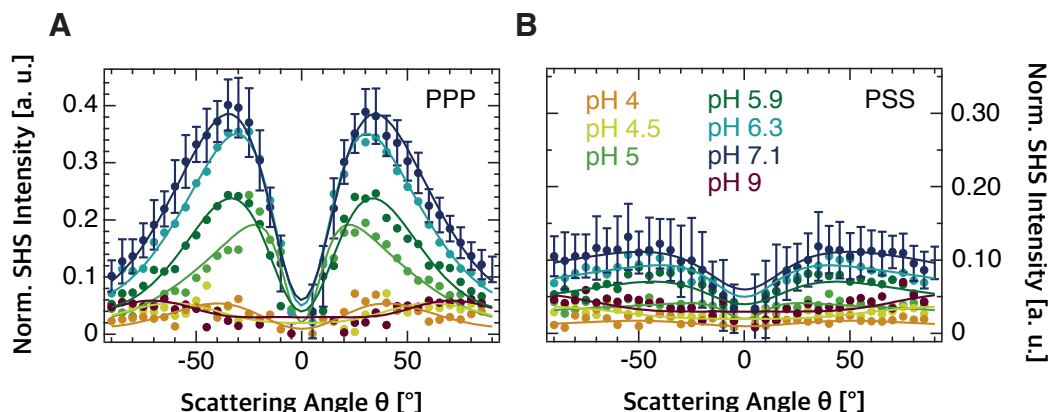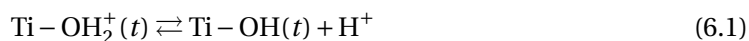

Figure 6.2 – AR-SHS patterns of ∼ 100 nm diameter anatase TiO_2 particles in solutions of different pH conditions in (A) PPP and (B) PSS polarization combination. The pH was adjusted through the addition of HCl and NaOH. Plain data points of different colors represent different pH conditions of the aqueous environment. The particle density was kept constant and was measured by MADLS for each sample. All measurements were performed at $T = 296.15$ K. Solid lines represent the fits to the corresponding data points using the AR-SHS model. A summary of all parameters used for the fits can be found in Tables 8.11 and 8.12.

In Figure 6.3 B, the surface susceptibility $\chi_{s,2}^{(2)}$ is displayed as a function of pH. While the sign of $\chi_{s,2}^{(2)}$ is negative for pH 4 to pH 4.5, it changes to positive values for pH 5 and pH 5.9. For pH 6.3 and pH 7.1 $\chi_{s,2}^{(2)}$ turns again to negative values and flips back to a positive value for pH 9. A further point extracted at pH 10 confirms the positive trends of $\chi_{s,2}^{(2)}$, however the absolute values are unreliable due to the small signal-to-noise ratio and therefore not shown on this graph. In the sign convention that we are using, described in detail in chapter 2.3.1, negative values of $\chi_{s,2}^{(2)}$ represent an average orientation (net dipole moment) of interfacial water molecules pointing with their oxygen toward the surface. Positive values of $\chi_{s,2}^{(2)}$ indicate an average orientation of interfacial water molecules with hydrogens toward the surface.

Before we move to the interpretation of our AR-SHS data, we briefly describe surface reactions that can occur for TiO_2 in acidic or basic environments. Explanations for the surface acidity of TiO_2 have tended to focus on the terminal oxo and hydroxo groups. Taking into consideration only the terminal groups is in most cases sufficient to describe the acid-base properties of TiO_2. The acidity of the bridging oxygens, where $pK_a < 2$ as evidenced by experiments [297, 306] and predicted by simulations [301], is in most cases irrelevant in common experimental

conditions. Considering only the terminal site, one can write the following chemical equilibria:

$$\text{Ti} - \text{OH}_2^+(t) \rightleftharpoons \text{Ti} - \text{OH}(t) + \text{H}^+ \tag{6.1}$$

$$\text{Ti} - \text{OH}(t) \rightleftharpoons \text{Ti} - \text{O}^-(t) + \text{H}^+ \tag{6.2}$$

where (t) indicates the terminal Ti−OH. pK$_a$s reported in the literature for anatase span a wide range and additionally depend on the preparation method, as well as the relative aging of the particles [307]. For reaction (6.1), the deprotonation of the hydroxo group, values of $2 < \text{pK}_{a,1} < 5$ can be expected [296, 307–310]. Reaction (6.2), corresponding to the deprotonation of the oxo group, has pK$_{a,2}$ values ranging from 8 to 9 [296, 307–310]. A theoretical report has suggested that the deprotonation of the bridging Ti−OH$^+$−Ti group could occur at values close to pK$_{a,1}$, while the deprotonation of the hydroxo terminal Ti − OH$_2^+$ would be occurring instead closer to pK$_{a,2}$, but this exceptional case will not be considered here [299].
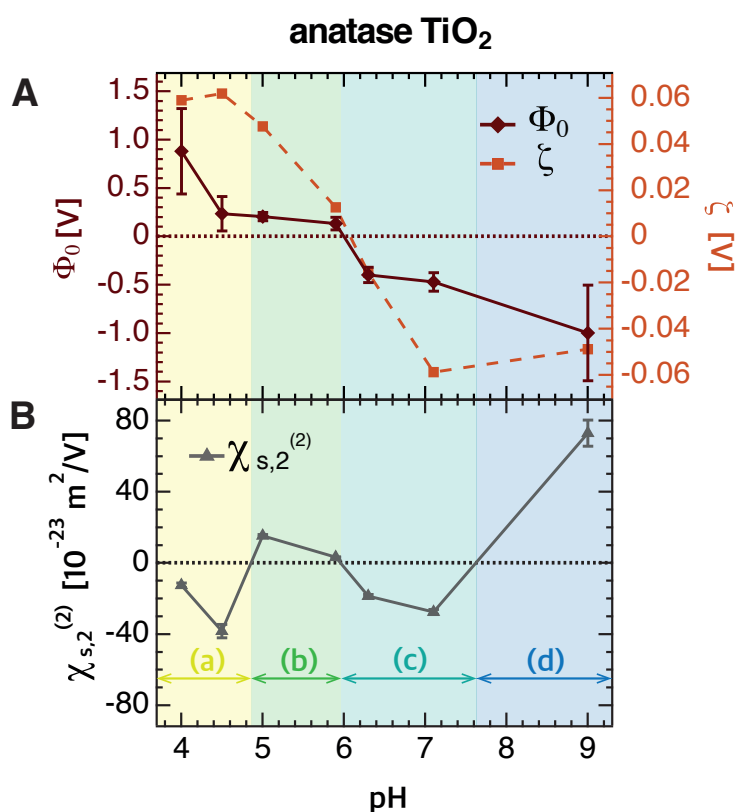

Figure 6.3 – Surface potential Φ_0, zeta potential ζ (A) and surface susceptibility $\chi_{s,2}^{(2)}$ (B) of ∼ 100 nm diameter anatase TiO$_2$ as a function of pH. Φ_0 and $\chi_{s,2}^{(2)}$ were obtained by fitting the corresponding AR-SHS patterns of ∼ 100 nm diameter anatase TiO$_2$ particles in suspension in PPP and PSS polarization combination. The zeta potential ζ was determined through electrophoretic mobility measurements.

For TiO$_2$, the pH at the PZC is usually estimated taking the mean of the pK$_a$s of both groups (pK$_{a,1}$ and pK$_{a,2}$) [296, 297, 300, 302] so that:

$$\mathrm{pH_{PZC}} = \frac{1}{2}\left(\mathrm{pK_{a,1}} + \mathrm{pK_{a,2}}\right). \tag{6.3}$$

The PZC is around pH 5 - pH 6.5 for anatase as reported in the literature [296, 297, 302, 307–309, 311, 312]. A detailed compilation of PZC/IEP values for anatase can be found in the reference textbook by Kosmulski [313]. It can be seen from the data in Figure 6.3 A that the PZC (defined by $\Phi_0 = 0$) and the IEP (defined by $\zeta = 0$) are found close to pH = 6 for our anatase samples, as described above.

Having established the possible surface reactions in acidic/basic environment, we can now link the chemical equilibria above to our AR-SHS data. According to the $\chi_{s,2}^{(2)}$ sign change, four regions can be distinguished as indicated in Figure 6.3 by differently coloured backgrounds. In region (a), which includes the samples at pH 4 and pH 4.5, both ζ and Φ_0 have positive values, indicating a positively charged particle surface. In the same range, $\chi_{s,2}^{(2)}$ is negative with, on average, water molecules pointing with their oxygens toward the surface. The sign of $\chi_{s,2}^{(2)}$ can be related to the majority species at the surface. At pH < pK$_{a,1}$, the majority of the Ti−OH terminal sites are expected to be protonated (Eq. 6.1). In this case, the terminal Ti − OH$_2^+$ can hydrogen-bond with the neighbouring water molecules via their protons, therefore generating a preferential net orientation with oxygen towards the surface as illustrated in Figure 6.4 A. Therefore, the sign of $\chi_{s,2}^{(2)}$ in region (a) reflects a majority of Ti − OH$_2^+$ and Ti−OH species.

Region (b), which is still in the acidic range and includes the samples at pH 5 and pH 5.9, displays positive ζ and Φ_0, as well as positive $\chi_{s,2}^{(2)}$ values. ζ and Φ_0 are lower than in (a), indicating a loss in the average positive charge of the surface. At pH 5.9, the particles are very close to the PZC (and IEP) and the sample only forms a stable colloidal suspension on a timescale of a few hours. The stability of the sample over time was monitored through separate zeta potential measurements. The sign of $\chi_{s,2}^{(2)}$ provides evidence for a flip in the net dipole moment of interfacial water molecules with respect to region (a), where hydrogen atoms are now preferentially facing the surface. This flip in average water orientation can be related to the pH of the solution being higher than pK$_{a,1}$. Crossing of pK$_{a,1}$ generates an excess (more than 50%) of neutral, deprotonated Ti−OH groups according to (Eq. 6.1). The loss of doubly protonated species (Ti − OH$_2^+$) decreases $|\chi_{s,2}^{(2)}|$. At the same time, the presence of possible proton-sharing intermediates as depicted in Figure 6.4 B might generate a positive contribution to $\chi_{s,2}^{(2)}$. Overall, both effects combined could be responsible for the observed turn over in the average water orientation from negative to positive $\chi_{s,2}^{(2)}$. A sketch of the corresponding surface charge vs pH trend is presented in the same figure.

Beyond region (b), at around pH 6, ζ and Φ_0 change from positive to negative values. This indicates that the particles surface becomes on average negatively charged. We define region (c) as containing our samples measured at pH = 6.3 and 7.1, and where $\chi_{s,2}^{(2)}$ values are negative. The switch from positive $\chi_{s,2}^{(2)}$ values (region b) to negative $\chi_{s,2}^{(2)}$ values (region c) provides here as well information on the nature of the surface species interacting with neighbouring interfacial water molecules. Given the sign of the surface charge and the fact that the pH in
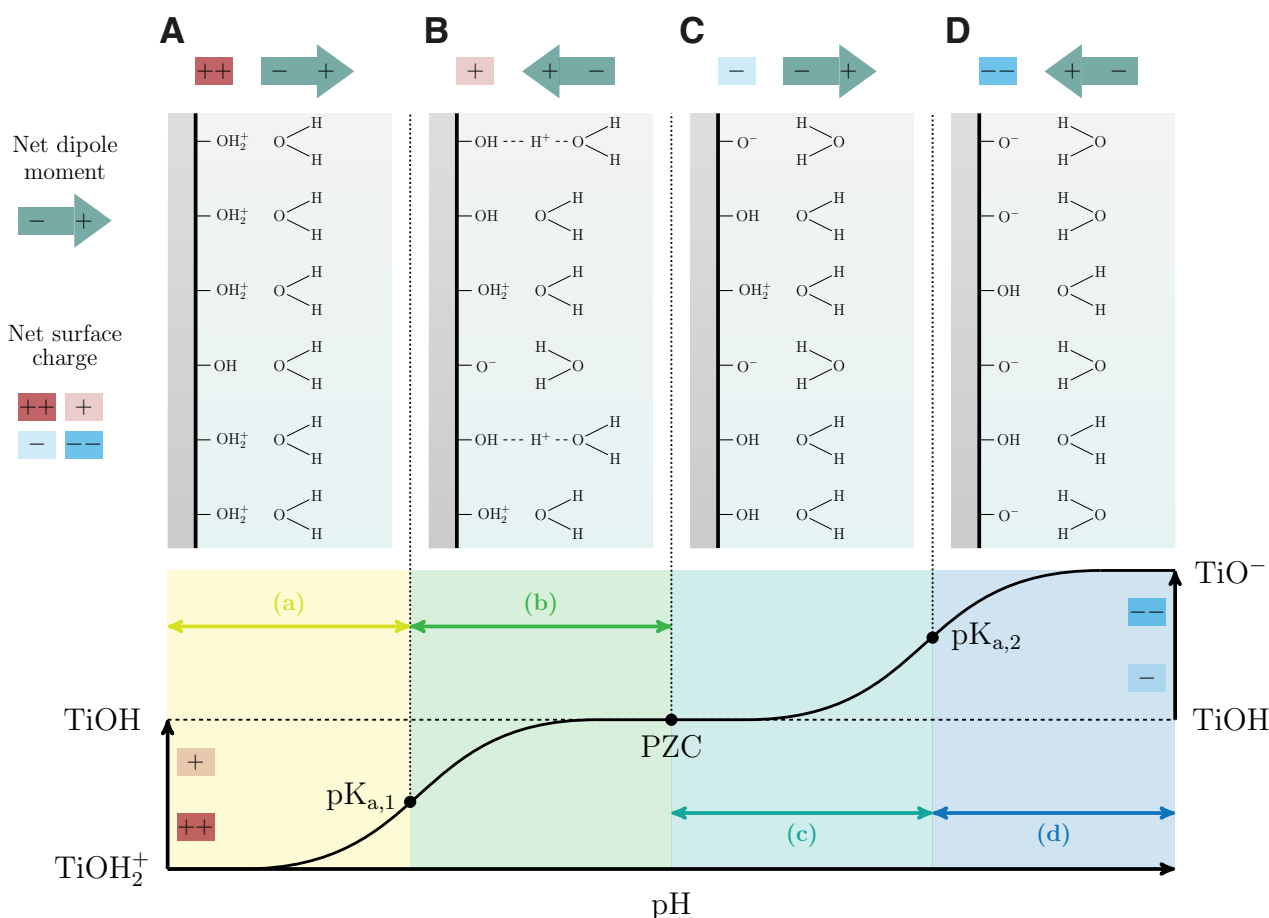
Figure 6.4 – Schematic illustration of the net surface charge and average water orientation, represented by the net dipole moment, at the anatase TiO$_2$/water interface as a function of pH from (A) acidic to (D) basic. Different pH regions, corresponding to the same regions as previously defined in Figure 6.3, are indicated by small letters (a) to (d) and different background colors. A representational, simplified picture of how the terminal groups at the TiO$_2$ surface affect the interfacial water molecules is shown in the top part. In the bottom part, the transition from one predominant terminal surface group species to another as a function of pH is visualized. At the turning points, which correspond to pK$_{a,1}$, the point of zero charge (PZC) and pK$_{a,2}$, the net dipole moment of interfacial water changes orientation.

region (c) is smaller than pK$_{a,2}$ values reported in the literature, we now expect the coexistence of a small fraction of deprotonated species corresponding to the chemical equilibrium (6.2), together with a majority of uncharged Ti−OH species corresponding to equilibrium (6.1). The fact that pH > pK$_{a,1}$ also indicates that only a small fraction of Ti − OH$_2^+$ species are still present, although in a smaller fraction than the deprotonated Ti − O$^-$ species. The sign of $\chi_{s,2}^{(2)}$ is representative of equilibria 6.1 and 6.2, as the majority of water molecules are oriented with oxygens facing the surface to hydrogen-bond with terminal Ti−OH groups. Figure 6.4 C schematically illustrates the average water orientation and surface deprotonation in region (c).

A similar situation has already been discussed in previous chapters for amorphous TiO_2 (see chapters 4 and 5 for more details).

For higher pH values ($\sim$>pH 8), comprising our sample at pH 9, we observe once more a change in sign of $\chi_{s,2}^{(2)}$ back to positive values, while ζ and Φ_0 remain negative. We note that a further point at pH = 10 (not shown here) gives similar trends, but the values of Φ_0 were found to be unrealistically high due to the low signal-to-noise ratio of the experiment. The measured zeta potential at pH = 10 was $\zeta = -52\,mV$, confirming the negative surface charge of the particles. In this region (d), the chemical equilibrium shown in equation (6.2) predicts that more than 50% of the terminal groups are found in a deprotonated state. This is well reflected by the change in sign of $\chi_{s,2}^{(2)}$ to positive values, where the net dipole moment of water switches to hydrogens facing the surface. Figure 6.4 D captures this scenario. A similar change in sign of $\chi_{s,2}^{(2)}$ was also observed for amorphous TiO_2 in chapter 4 as a function of pH, although at higher pH values (between pH 9.5 and pH 10.7). This difference can be explained by the specific surface characteristics of different TiO_2 polymorphs and crystalline vs amorphous samples. As it was discussed by Akratopulu et al. [76], rutile and anatase (or mixtures of both) can show different acid-base behavior. This can be explained by the different specific surface areas of the two polymorphs and the fact that the PZC and the acidity constants are temperature-dependent properties [76, 314]. Temperature can have the opposite effect on rutile vs anatase, thus shifting the corresponding pK_as and PZC positions according to the exact sample composition [76]. Therefore we believe that the differences between the exact flipping points of the average water orientation that we observe are a consequence of the specific surface characteristics of different TiO_2 polymorphs.

Our AR-SHS data unequivocally shows a specific water orientation associated with the majority species present at a given pH. Together with the information on the charge at the slipping plane given by ζ and on the surface charge given by Φ_0, it is possible to experimentally evidence not only the majority surface species, but also the transition points corresponding to the crossing of pK_a points. Taking the first change in sign in $\chi_{s,2}^{(2)}$ (between region a and b) to occur at pH $\sim$4.8, and the third change in sign in $\chi_{s,2}^{(2)}$ (between region c and d) to take place at pH $\sim$7.6, one can calculate the pH at the PZC, where the second change in $\chi_{s,2}^{(2)}$ occurs (between region b and c), to be: $pH_{PZC} = (4.8 + 7.6)/2 = 6.2$ according to equation 6.3. This result is very close to the pH at which the PZC (and IEP) is observed on the curve of surface potential vs pH (Fig. 6.3 A) and is in agreement with literature values discussed above.

For planar surfaces and fused silica in particular, SHG has been already successfully employed to predict surface acidity: pK_a values were reported in 1992 by Ong et al. by analyzing the trend of the SH electric field as a function of pH [137]. Several studies demonstrated the applicability of SHG and SFG to investigate the acid-base behavior at interfaces and to infer surface pK_as [184, 315–317]. More recently, bimodal and trimodal behavior of a planar fused silica surface were observed in the Gibbs group [203, 258, 318]. Estimations of the pK_as of isolated silanol groups using vibrational sum frequency spectroscopy were also reported for planar silica by the Tyrode group [319]. A distribution of pK_a values was extracted from second harmonic microscopy images of a silica glass microcapillary immersed in aqueous solutions as a function of pH by the Roke group [111]. The second harmonic images reported

on the orientational order of interfacial water molecules and were further converted into surface potential maps. Combining the knowledge of surface potential with information on the interfacial water order is key to elucidate the acid-base behavior of planar surfaces in contact with an aqueous solution. In situ structural changes of interfacial water at the planar silica/water interface under the addition of salt in different pH conditions were revealed by the Borguet group in a vibrational SFG study [178]. Recent advances in the determination of surface potential for planar surfaces with SHG and vibrational SFG [320] could further improve our understanding of surface acidity.

In the case of colloidal inorganic suspensions, SHS studies have usually focused on extracting the surface potential [138, 176], however additionally extracting information on interfacial water orientation of scatterers in solutions only became possible with recent developments of the angle-resolved polarimetric SHS technique [113, 114]. Combining information on the surface charge through Φ_0 together with interfacial water orientation given by $\chi_{s,2}^{(2)}$, one can follow the evolution of surface acidity of colloidal suspensions as a function of pH and predict pK$_a$ values. We suggest that AR-SHS can be used as a complementary technique to potentiometric titrations, for example with samples where the excess porosity might lead to an overestimation of surface charge density by acid/base titration, or for samples that cannot be synthesized in the large quantities, as sample masses in the order of milligrams are sufficient for AR-SHS experiments.

6.4 Conclusions

In summary, we report zeta potential (ζ) and surface potential (Φ_0) values for ~ 100 nm diameter anatase nanoparticles dispersed in aqueous solutions as a function of pH. The information given by Φ_0 on the surface charge is combined with knowledge of the interfacial water orientation represented by $\chi_{s,2}^{(2)}$. Both quantities can be extracted as two distinct solutions of a two-equation system by fitting the AR-SHS model functions to our measured AR-SHS patterns. We show that the water orientation changes with pH, and that four separate ranges can be identified as a function of pH. As the change in bulk pH modifies the interface populations of $Ti-OH_2^+$, $Ti-OH$ and $Ti-O^-$ groups, the interfacial water orientation in each of these four different pH ranges can be associated with the majority species at the surface. A flip in water orientation is evidence for a shift between more than 50% protonated surface species to more than 50% deprotonated surface species (or vice-versa). Consequently, this observation allows for direct evaluation of the acid dissociation constant from graphs of $\chi_{s,2}^{(2)}$ vs pH. This work provides new opportunities for future studies of surface acidity of colloidal suspensions in situ. As such, the experimental method presented here could be used to estimate the position of the conduction band as well as to probe proton transfer during electrochemical or photoelectrochemical reactions.

7 Conclusions and Outlook

In this thesis we show the broad applicability of AR-SHS to study oxide particle/liquid interfaces on a molecular level. With nonlinear light scattering theory expressions to determine the surface potential Φ_0 of the particles with respect to bulk liquid and the surface susceptibility $\chi_{s,2}^{(2)}$ can be derived. The latter is a measure for the orientational order of water molecules that are (chemically) attached to the particle surface. An overview of the most important expressions of nonlinear light scattering theory is presented in chapter 2. In the same chapter (chapter 2), the AR-SHS model is introduced, which can be used to obtain Φ_0 and $\chi_{s,2}^{(2)}$ from the measured AR-SHS patterns without assuming a particular distribution of charges at the interface. This allows to obtain unique values for Φ_0 and $\chi_{s,2}^{(2)}$ without the need to apply simplified models describing the interfacial charge distribution (e.g. the Gouy-Chapman or the Gouy-Chapman-Stern model) as they were presented in the introduction (chapter 1) of this thesis. This opens up new possibilities to gain molecular insights into the electrical double layer (EDL) around colloidal oxide particles in suspension.

In chapter 3 we apply AR-SHS to 300 nm diameter SiO_2 particles in a solution as a function of pH and NaCl concentration. Knowing Φ_0 and $\chi_{s,2}^{(2)}$, together with the zeta potential ζ from electrophoretic mobility measurements allows to establish a molecular picture of the silica particle/aqueous interface. For pH values from neutral pH to pH 10 and low salt concentration (<1 mM) we observe a diffuse layer (DL) behavior where Φ_0 and ζ are close in magnitude. In this case the dominant interfacial water orientation is with oxygens toward the silanol terminated surface ($\chi_{s,2}^{(2)}$<0). At higher pH (pH 11) and higher salt concentrations ($\geq$ 1 mM) Φ_0 increases in magnitude while ζ remains close to the values observed for the low ionic strength and lower pH case. We attribute this behavior to the accumulation of hydrated counterions close to the interface. The sign of $\chi_{s,2}^{(2)}$ changes to positive values, indicating that water molecules adjust their orientation to mainly hydrogens facing the surface as a consequence of this condensed layer of ions. Surface charge density values obtained from applying the Gouy-Chapman (GC) or Gouy-Chapman-Stern (GCS) model to our measured Φ_0 values and literature surface charge density values are in good agreement. In addition, our results are supported by MD simulations.

In chapter 4 we investigate for the first time semiconductor particles with AR-SHS. Amorphous titanium dioxide colloids of ~ 100 nm diameter are measured as a function of NaCl concentration and basic pH. We extract Φ_0 and $\chi_{s,2}^{(2)}$ from the AR-SHS patterns and compare those values to the zeta potential ζ. Similarly to chapter 3, we identify the formation of a diffuse layer region at low ionic strength (10-100 μM) and the formation of a condensed layer of charges at higher ionic strengths (>100 μM). A change in sign of $\chi_{s,2}^{(2)}$ from negative to positive values caused by the addition of Na$^+$ ions to the solution supports this picture indicating a rearrangement of the interfacial H-bond network already at low salt concentrations (<50 μM). The most significant finding of chapter 4 is that, besides the diffuse layer and condensed layer region which was already observed for 300 nm diameter SiO$_2$ particles in chapter 3, we can identify a third region where the surface potential magnitude decreases as a function of ionic strength for very low salt concentrations (0-10 μM). We assign this region, referred to as region (i), to the inner-sphere adsorption of ions at the amorphous TiO$_2$ surface. We additionally find a similar behavior for SiO$_2$ particles of the same size at very low NaCl concentrations, showing this is a general effect and not only specific to TiO$_2$. Overall, we can generally distinguish three phenomena with increasing ionic strength. First, inner-sphere adsorption at the lowest concentrations (region (i)), then formation of a diffuse layer of counterions (region (ii)) and finally, accumulation of hydrated counterions near the interface (region (iii)). While common electrostatic models predict all these phenomena, our findings show that we can retrieve the electrostatic structure of aqueous interfaces at a certain ionic strength without a priori knowledge on the charge distribution, implying that AR-SHS could be applied to a variety of more complex systems. Furthermore, a direct comparison between SiO$_2$ and TiO$_2$ shows that the semiconductor TiO$_2$ has a higher affinity to adsorb Na$^+$ ions than SiO$_2$. MD simulations support this conclusion.

In chapter 5 we continue the investigation of ~ 100 nm diameter amorphous TiO$_2$ and SiO$_2$ particles with AR-SHS to study ion-specific effects. We measure colloidal suspensions of $\leq$ 600 μM ionic strength for three different salts, NaCl, RbCl and CaCl$_2$. We generally observe the same three regions (i), (ii) and (ii) for all the surfaces and ions investigated in this chapter. However, relative differences of Φ_0, $\chi_{s,2}^{(2)}$ and ζ as a function of ionic strength reveal specific adsorption preferences of silica and titania for Na$^+$, Rb$^+$ and Ca^{2+} ions. For the silica surface, the surface potential Φ_0 trends as a function of ionic strength strongly depend on the nature of the cation, whereas the surface susceptibility $\chi_{s,2}^{(2)}$ trend is similar for the three ions. Opposite results are observed for the titania surface, where the surface potential trends as a function of ionic strength are similar but the surface susceptibility data show specific relative differences depending on the cations in the solution. We deduce a preferential outer-sphere adsorption of Ca^{2+} ions on silica surfaces with respect to Na$^+$ and Rb$^+$, while Ca^{2+} ions are preferentially inner-sphere adsorbed on the titania surface compared to the monovalent ions. Those trends are confirmed by MD simulations and a general inner-sphere adsorption preference of all the studied cations at the titania surface with respect to silica is suggested.

Having demonstrated that AR-SHS can be used to explore ion-specific effects, we investigate the surface acidity of ~ 100 nm anatase TiO$_2$ with AR-SHS in chapter 6. We report Φ_0, $\chi_{s,2}^{(2)}$ and ζ values as a function of pH and observe several changes in sign of $\chi_{s,2}^{(2)}$, which translates

into changes of interfacial water orientation. According to the $\chi_{s,2}^{(2)}$ behavior four different pH ranges can be identified. Because a change in pH affects the population of surface terminal groups, i.e. Ti-OH$_2^+$, Ti-OH and Ti-O$^-$, the change in water orientation can be related to the majority species at the surface. This allows to probe the transitions between more than 50% protonated to more than 50% deprotonated surface groups (or vice-versa) by simply examining the water orientation as a function of pH. We therefore propose that AR-SHS can be used to investigate the surface acidity of colloidal oxide particle suspensions.

Overall, our results show that AR-SHS can provide valuable molecular level information on the composition of the EDL around nanometer sized oxide particles dispersed in solution. We can obtain unique values for the surface potential and surface susceptibility in a non-invasive manner, which allows to gain direct molecular insights into interfacial processes, such as ion-adsorption or possibly proton transfer reactions. We demonstrate that AR-SHS allows to access molecular information for micromolar salt concentrations, a regime which remained chiefly unexplored until now. Our work highlights the potential of AR-SHS to shed light on a variety of interfacial properties that are relevant to improve the efficiency of (photo)catalytic and (photo)electrochemical reactions. A strong advantage of this technique is that it can provide both knowledge about the surface potential and the interfacial aqueous environment, the role of which in interfacial reactions still remains controversial among scientists [321]. We envision that AR-SHS could be used to monitor proton transfer reactions during (photo)electrochemical reactions in situ, which would contribute to a deeper understanding of this matter. As nanomaterials are increasingly used in a variety of technological applications ranging from drug delivery to catalysis, the capacity to characterize the electrostatic environment of colloidal nanoparticles in suspension will aid in the development of more efficient materials and devices.

In the following we want to reflect on possibilities for future experiments in the context of AR-SHS. Firstly we want to focus on opportunities for experiments that could be realized with the existing AR-SHS setup. Secondly, we propose a modification of the current setup that would allow for time-resolved AR-SHS measurements. Both ideas will be discussed in more detail in the next paragraphs.

As a first follow-up experiment on the two oxide materials that were investigated in this thesis (SiO$_2$ and TiO$_2$), one could think of investigating the effect of a variety of different salts on the nanoparticles. We already reported on the effect of NaCl, RbCl and CaCl$_2$. Possible other candidates for monovalent salts in the family of chlorides would be amongst others potassium chloride (KCl), lithium chloride (LiCl) and caesium chloride (CsCl). In particular the effect of LiCl on TiO$_2$ particles would be interesting to explore given that the small size of the lithium ions can lead to different interactions than for larger alkali metal chlorides. For instance, it has been reported that Li$^+$ ions can penetrate the TiO$_2$ lattice [322–324]. This effect, also referred to as lithium intercalation, has drawn scientific attention in the context of developing more efficient lithium-ion batteries [325–329]. Interesting representatives of divalent salts that could be investigated in comparison to calcium chloride, are magnesium chloride (MgCl$_2$) or zinc chloride (ZnCl$_2$). While MgCl$_2$ is used as a food additive and in pharmaceutical

preparations, $ZnCl_2$, besides being a parental nutrition additive, can be utilized to dissolve passivating oxides e. g. as a flux for soldering. It would be interesting to investigate if the $ZnCl_2$/metal oxide surface reactions underlying this metal surface cleaning mechanism can be observed at oxide surfaces in aqueous environments and possibly how they evolve as a function of temperature. One could also think of the investigation of polyvalent ions, such as ammonium chloride (NH_4Cl), which is equally used as a soldering flux. In this case more complex cation-surface interactions are expected. Another possibility would be to investigate water soluble fluoride, bromide or iodide based salts. The anatase TiO_2 particles used in chapter 6, that are naturally positively charged when dispersed in water, offer the possibility to study the interfacial behavior of negatively charged anions, such as Cl^-, F^-, I^- or Br^- as a function of salt concentration.

As a continuation of the compilation on how the surface potential of silica changes as a function of NaCl over a broad range of concentrations, as it has been shown in figure 5.3 in chapter 5 it would be beneficial to perform another series of AR-SHS measurements on 300 nm silica particles as a function of NaCl. In the NaCl series measured on those particles in chapter 3, the pH has been adjusted to pH 10. In order to explore the pure effect of salt on the particles without adjusting the initial surface charge through the addition of NaOH, as in the case of the NaCl series on 100 nm silica particles in chapters 4 and 5 it would be of high interest to repeat the measurement under the proposed conditions. As the probed shell volume of water molecules is expected to be generally larger for the larger 300 nm silica particles compared to the smaller 100 nm silica particles investigated in chapters 4 and 5 the corresponding better signal-to-noise ratio of the measurements might allow to access information about the surface potential at even higher ionic strength values. The acquisition of a significant number of NaCl concentration points on 300 nm silica particles in an ionic strength range of $0\,\mu M$ to $\sim 50\,mM$, together with the knowledge about the regions (i), (ii), and (iii) described in chapters 4 and 5 would allow to get a more complete picture of the surface potential trends even beyond region (iii). It would be of high interest for the research community to compare those results with Brown et al.'s surface potential values on smaller sized silica particles [94, 95] displayed in figure 5.3 and literature values obtained for flat silica surfaces [137, 271–273].

Another insightful experiment would be to study the effect of particle size on the pH dependence. This could be done by measuring silica or titania particles of different sizes (e.g. 100 nm - 300 nm diameter) with AR-SHS as a function of pH and investigating the impact on the corresponding surface potential and surface susceptibility. As it can already be noticed comparing the AR-SHS patterns of 300 nm silica in chapter 3 (see Fig. 3.1) and of 100 nm amorphous titania in chapter 4 (see Fig. 4.3), the size or material have a different effect on the SH intensity. While the AR-SHS scattering intensity increases as a function of basic pH for 300 nm silica particles, it decreases for 100 nm amorphous titania particles. This trend is also confirmed by the pH series on 100 nm anatase titania particles in chapter 6 (see Fig. 6.2), where the AR-SHS intensity decreases from pH 7.1 to pH 9. A size-dependent experiment would show if the observed differences are subject to the particle size change or if they are material specific. We speculate that this is rather a size effect due to the influence of geometrical form factors on the AR-SHS patterns which were already briefly discussed in section 8.5 of the Appendix.

Certainly it would also be relevant to investigate functionalized or doped TiO_2 particles, as those can show more advantageous properties for specific applications [2, 16, 330, 331]. One could think of investigating the nanoparticle/liquid interface as a function of doping level. AR-SHS could also help to find the most suitable sample synthesis method in order to realize certain bulk or interfacial material properties.

Furthermore, rutile, brookite or mixed-phase TiO_2 colloids could be investigated, provided that they remain stable in solution for the time of the experiment. The same applies to colloids made from other oxide materials. Possible candidates that are widely studied for photocatalytic water splitting applications would be amongst others zinc oxide (ZnO), tungsten oxide (WO_3), hematite (α-Fe_2O_3) and bismuth vanadate ($BiVO_4$) [2]. AR-SHS measurements could assist in establishing a better microscopic picture of interfacial processes occuring at the metal oxide/liquid interface of those materials.

As an additional project, one could study the interfacial properties of excited semiconductor particles. The absorption of UV light by TiO_2 particles generates electron-hole pairs. The charge carriers can further react with chemical species at the interface. Some of the important questions in this context are:

- How are surface potential and surface susceptibility changing under illumination, and what are the timescales for these changes?

- Can we relate surface potential and surface susceptibility changes to structural changes in the EDL during a charge-transfer process at the semiconductor/liquid interface?

- How does the aqueous side of the interface influence interfacial charge transfer and photocatalytic activity?

To answer these questions, we need to photoexcite the TiO_2 particles with UV light and measure the SH surface response of the particles under illumination. With this experiment we could specifically address the change in surface potential and change in molecular orientation of interfacial water molecules under non-equilibrium conditions. Such experimental scheme could additionally be used to access quantities relevant to the semiconductor itself such as the change in band bending under illumination. In the absence of change in the surface charge, a reduction of the maximum band bending under illumination with respect to the maximum band bending under equilibrium condition is expected [332], as further detailed in section 8.7 of the Appendix.

First exploratory measurements on 100 nm diameter anatase TiO_2 particles under illumination where performed extending the AR-SHS setup by adding a continuous UV LED light source as illustrated in Figure 7.1. In comparison to a very concentrated anatase TiO_2 particle suspension, water and amorphous SiO_2 particles of the same size where investigated. Figure 7.2 shows the results of those single angle SHS measurements. The SHS intensity of the particle suspensions or pure water with and without UV illumination is displayed. Whereas no significant difference could be seen for the water reference sample nor the highly concentrated SiO_2 particles in suspension, the 100 nm anatase TiO_2 sample showed a strong difference in second
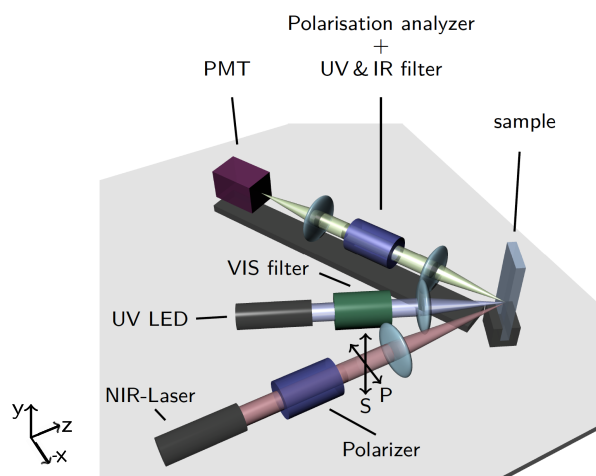
Figure 7.1 – Continuous UV/AR-SHS setup with 365 nm UV LED (blue) for the excitation of the anatase TiO_2 particle sample. The power of the UV beam in the focal spot is ~21.5 mW. With a focal spot area of ~12 mm^2 this translates into a fluence of ~0.17 J/cm^2 per second. The power of the near-infrared (NIR) beam was set to 80 mW. The polarization in S (perpendicular to the scattering plane) or P (parallel to the scattering plane) can be adjusted for the incoming NIR beam (red) and the scattered second hamonic (SH) light (green).The SH light is collected in reflection mode under a 50° angle between the incoming NIR light and the analyzer arm with a photomultiplier tube (PMT) on a rotation stage. Samples are contained in a flat UV-compatible spectrosil cuvette.
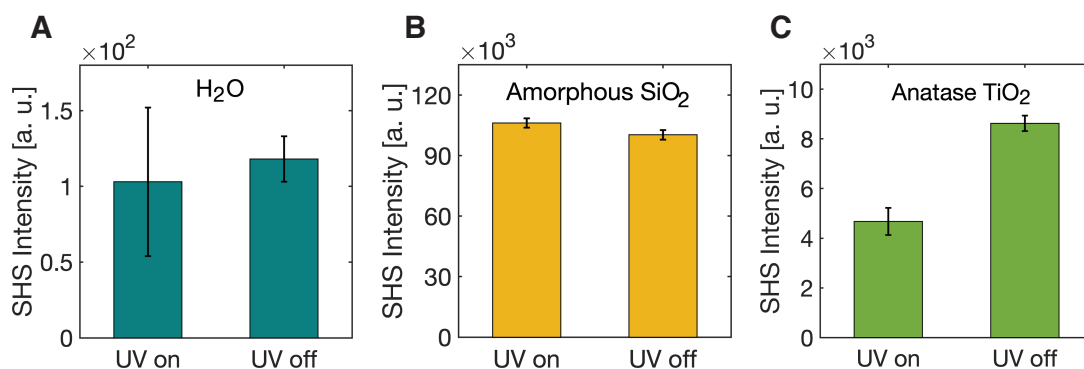

Figure 7.2 – Single-angle second harmonic scattering in reflection mode under UV excitation ($\lambda = 365$ nm) with the continuous UV/AR-SHS setup of (A) pure water, (B) amorphous SiO_2 and (C) anatase TiO_2 particles. While no significant difference in SH intensity for UV illuminated vs non-illuminated samples is seen for pure water and amorphous SiO_2, a clear change can be observed for a highly concentrated anatase TiO_2 sample.

harmonic signal with and without illumination. The strong difference in SH signal under continuous illumination suggests that a change in surface potential or surface susceptibility must occur under illumination. Another possibility is that a change in band bending under non-equilibrium conditions additionally contributes to the SH signal change.

With this surface potential probe available, one could envision time-resolved pump-probe experiments. A UV pump/AR-SHS probe experiment offers the possibility to perform measurements that allow to follow charge transfer dynamics with femtosecond time resolution. This project could help to clarify the above mentioned questions and in this way generally deepen our understanding of photocatalytic reactions at the semiconductor/liquid interface.

8 Appendix

8.1 Fitting parameters

8.1.1 300 nm SiO$_2$ particles in NaCl and different pH conditions (Ch. 3)

Table 8.1 – Parameters used for fitting the normalized second harmonic scattering patterns applying the AR-SHS model. These parameters are common to all sets of ~300 nm SiO$_2$ data presented and fitted.

Second harmonic wavelength λ [nm]	515
Refractive index n$_{H_2O}$ (@ 515 nm)	1.33
Refractive index n$_{SiO_2}$ (@ 515 nm)	1.46
Temperature [°C]	23
Number of particles [particles/mL]	$3.50 \cdot 10^{10}$

Table 8.2 – Parameters used for fitting the normalized second harmonic scattering patterns of ~300 nm SiO$_2$ particles applying the AR-SHS model. The values presented are specifically used for fitting the pH series.

pH	5.7	10	11
Radius [nm]	145	148	142
Ionic strength [mM]	$4.02 \cdot 10^{-3}$	0.1	1

Table 8.3 – Parameters used for fitting the normalized second harmonic scattering patterns of ~300 nm SiO$_2$ particles applying the AR-SHS model. The values presented are specifically used for fitting the NaCl concentration series.

added NaCl, at pH=10 [mM]	0	0.1	1	10
Radius [nm]	147	146	142	143
Ionic strength [mM]	0.1	0.2	1.1	10.1

8.1.2   100 nm SiO$_2$ and amorphous TiO$_2$ particles in NaCl and basic pH (Ch. 4)

Table 8.4 – Parameters used for fitting the normalized second harmonic scattering patterns applying the AR-SHS model. These parameters are common to all sets of amorphous ~100 nm TiO$_2$ data presented and fitted.

Second harmonic wavelength λ [nm]	515
Refractive index n_{H_2O} (@ 515 nm)	1.33
Refractive index n_{TiO_2} (@ 515 nm)	2.61
Temperature [°C]	23
Number of particles [particles/mL]	$4.26 \cdot 10^{11}$

Table 8.5 – Parameters used for fitting the normalized second harmonic scattering patterns applying the AR-SHS model. These parameters are common to all sets of ~100 nm SiO$_2$ data presented and fitted.

Second harmonic wavelength λ [nm]	515
Refractive index n_{H_2O} (@ 515 nm)	1.33
Refractive index n_{SiO_2} (@ 515 nm)	1.46
Temperature [°C]	23
Number of particles [particles/mL]	$2.91 \cdot 10^{11}$

Table 8.6 – Parameters used for fitting the normalized second harmonic scattering patterns of ~100 nm amorphous TiO$_2$ particles applying the AR-SHS model. The ionic strength is determined via conductivity as described in sections 2.5.2 and 4.2.3. The values presented are specifically used for fitting the NaCl concentration series.

added NaCl [μM]	0	10	50	100	300
Radius [nm]	59	60	60	60	59
Ionic strength [μM]	40.4	46.5	91.2	134.7	311. 0

Table 8.7 – Parameters used for fitting the normalized second harmonic scattering patterns of ~100 nm amorphous TiO$_2$ particles applying the AR-SHS model. The ionic strength is determined via conductivity as described in sections 2.5.2 and 4.2.3. The values presented are specifically used for fitting the pH series.

pH	7	9.5	10.7
Radius [nm]	63	63	59
Ionic Strength [μM]	39.1	98.0	569.7

Table 8.8 – Parameters used for fitting the normalized second harmonic scattering patterns of ~100 nm SiO$_2$ particles applying the AR-SHS model. The ionic strength is determined via conductivity as described in sections 2.5.2 and 4.2.3. The values presented are specifically used for fitting the NaCl concentration series.

added NaCl [μM]	0	10	50	100	300	600
Radius [nm]	65	64	62	61	60	58
Ionic strength [μM]	13.0	23.0	57.5	96.6	288. 0	561. 0

8.1.3   100 nm SiO$_2$ and amorphous TiO$_2$ particles in different salts (Ch. 5)

Table 8.9 – Parameters used to fit the normalized second harmonic scattering patterns of ~100 nm SiO$_2$ particles in NaCl, RbCl, and CaCl$_2$ as a function of added ionic strength with the AR-SHS model. The effective ionic strength is determined via conductivity as described in section 2.5.2 and includes the contribution from the added salt as well as the initial ionic strength of the solution of washed particles as further detailed in section 5.2.3.

	Added ionic strength [μM]	0	10	25	50	100	200	300	600
NaCl	Radius [nm]	65	64		62	61		60	58
	Effective ionic strength [μM]	13.0	23.0		57.5	96.6		288.0	561.0
RbCl	Radius [nm]	61	62		60	59	59	58	
	Effective ionic strength [μM]	14.1	16.6		59.2	112.6	198.8	323.3	
CaCl$_2$	Radius [nm]	65	60	59	58	59		58	
	Effective ionic strength [μM]	14.5	18.8	35.3	58.7	112.4		319.2	

Table 8.10 – Parameters used to fit the normalized second harmonic scattering patterns of ~100 nm amorphous TiO$_2$ particles in NaCl, RbCl, and CaCl$_2$ as a function of added ionic strength with the AR-SHS model. The effective ionic strength is determined via conductivity as described in section 2.5.2 and includes the contribution from the added salt as well as the initial ionic strength of the solution of washed particles as further detailed in section 5.2.3.

	Added ionic strength [μM]	0	10	25	50	100	200	300
NaCl	Radius [nm]	59	60		60	60		59
	Effective ionic strength [μM]	40.4	46.5		91.2	134.7		311.0
RbCl	Radius [nm]	62	61		62	60		
	Effective ionic strength [μM]	37.9	45.6		87.3	102.4		
CaCl$_2$	Radius [nm]	63	65	63	62	62	59	59
	Effective ionic strength [μM]	42.7	51.5	68.4	85.7	123.2	240.2	323.0

8.1.4 100 nm anatase TiO$_2$ particles as a function of pH (Ch. 6)

Table 8.11 – Parameters used for fitting the normalized second harmonic scattering patterns applying the AR-SHS model. These parameters are common to all sets of ~100 nm anatase TiO$_2$ data presented and fitted.

Second harmonic wavelength λ [nm]	515
Refractive index n_{H_2O} (@ 515 nm)	1.33
Refractive index n_{TiO_2} (@ 515 nm)	2.58
Temperature [°C]	23

Table 8.12 – Parameters used for fitting the normalized second harmonic scattering patterns of ~100 nm anatase TiO$_2$ particles applying the AR-SHS model. The ionic strength is determined via conductivity as described in sections 2.5.2 and 6.2.3. In cases where the pH was close to neutral the ionic strength parameter was left open converging to the numbers in brackets. The particle radius was obtained through TEM measurements. The radius was kept the same for most pH values except for pH 5.9, where double the radius value was taken to account for particle aggregates. Those could be observed in DLS measurements close to the PZC. MADLS was used to obtain the number of particles in the solution as further explained in sections 2.4.1 and 6.2.3. The values presented are specifically used for fitting the anatase TiO$_2$ pH series.

pH	4	4.5	5	5.9	6.3	7.1	9
R$_{TEM}$ [nm]	48	48	48	96	48	48	48
Ionic strength [μM]	69.6	23.0	(3.3)	(15.4)	(8.6)	(11.4)	41.6
Number of particles [10^{10} particles/mL]	1.8	2.1	3.0	2.3	2.9	2.3	1.6

8.2 Surface charge densities and deprotonation

8.2.1 Amorphous TiO$_2$ particles in different pH conditions (Ch. 4)

From surface charge density values found in the literature [74–77] that were measured by potentiometric titration, we calculated the percentage of deprotonation at pH 7 using an initial density of 4.8 OH/nm^2 as determined for the hydroxylated surface of P25 TiO$_2$ particles (Degussa) taken from Ref. [242]. The radius of the particles was taken as 60 nm, which is close to what was measured in our dynamic light scattering experiments for amorphous TiO$_2$ particles. We obtain a deprotonation of 1% using the reported surface charge densities of -0.00763 C/m^2 for 21 nm diameter P25 TiO$_2$ particles (Degussa) at pH 7.10 by Holmberg et al., [74] and -0.00833 C/m^2 for $\approx$72 nm diameter rutile TiO$_2$ particles (CL/D 528 Tioxide International Limited) at pH 7.13 by Yates [77]. Values up to -0.06417 C/m^2 have been reported by Machesky et al. [75] for $\approx$83 nm diameter rutile TiO$_2$ particles (Tioxide Specialities Ltd.) at pH 7.02, which correspond to deprotonation values of 8%. Similar values were reported by Akratopulu et al. [76] for 30 nm diameter P25 TiO$_2$ particles (Degussa) at pH 6.93 who obtained a surface charge density of -0.05074 C/m^2 which corresponds to a deprotonation of 7%. Calculating the percentage of deprotonation in the same way for pH 9.5 by using the reported surface charge densities of -0.06250 C/m^2 for 21 nm diameter P25 TiO$_2$ particles (Degussa) at pH 9.3 (Holmberg et al.) [74] and -0.07431 C/m^2 for $\approx$72 nm rutile TiO$_2$ particles synthesized at pH 9.6 (Yates) [77] we obtain a deprotonation of 8-10%. Higher deprotonation values, up to 35% are calculated using a surface charge density of -0.27644 C/m^2 reported at pH 9.4 by Akratopulu et al. [76] for 30 nm diameter P25 TiO$_2$ particles. Machesky et al. [75] found similar values for the surface charge density of $\approx$83 nm diameter rutile TiO$_2$ particles at pH 9.63 (-0.22686 C/m^2) translating into 30% deprotonation. Given the fact that the measurements in Holmberg et al., [74] Yates, [77] Machesky et al. [75] and Akratopulo et al. [76] were performed at higher ionic strength of 0.1 M NaNO$_3$, 1 mM KNO$_3$, 0.03 M NaCl and 0.1 M KNO$_3$, respectively, the calculated deprotonation values can be regarded as an upper limit for the real deprotonation that we expect for our amorphous TiO$_2$ particles in the lower ionic strength region.

8.2.2 SiO$_2$ and amorphous TiO$_2$ particles at neutral pH (Ch. 5)

For the SiO$_2$ and TiO$_2$ particles used in chapter 5, the pH of the 0.05% solutions used for the AR-SHS measurements was $\sim$ 7. Using surface charge density values found in the literature that were measured by potentiometric titration, we can estimate the percentage of deprotonation expected for both surfaces at pH 7. As the surface charge densities for both materials have been shown to be strongly size-dependent for particles < 25 nm, [74, 207, 208] all the references listed here have been selected to match the size range of our particles and excluded very small nanoparticles (< 25 nm). For both materials, the density of surface hydroxyl groups was taken from the literature. Zhuravlev [196] showed for amorphous SiO2 that the $-$OH surface density

is a physicochemical constant for a fully hydroxylated surface and does not depend in a significant way on the type of silica.

For TiO_2, we use an initial density of $-OH$ groups of 4.8 OH/nm^2 as determined for the hydroxylated surface of P25 TiO_2 particles (Degussa) taken from Ref. [242]. The radius of the particles is taken as 60 nm, based on our dynamic light scattering experiments for amorphous TiO_2 particles. We obtain a deprotonation value of 1% using the reported surface charge densities of -0.00763 C/m^2 for P25 TiO_2 particles (Degussa) at pH 7.10 by Holmberg et al., [74] or -0.00833 C/m^2 for rutile TiO_2 particles (CL/D 528 Tioxide International Limited) at pH 7.13 by Yates [77]. Values up to -0.06417 C/m^2 have been reported by Machesky et al. [75] for rutile TiO_2 particles (Tioxide Specialities Ltd.) at pH 7.02, corresponding to deprotonation values of 8%. Similar values were reported by Akratopulu et al. [76] for P25 TiO_2 particles (Degussa) at pH 6.93 who obtained a surface charge density of -0.05074 C/m^2, which corresponds to 7% deprotonation.

The percentage of deprotonation is estimated in the same way for SiO_2. Here the initial density of $-OH$ groups at the surface is taken as 4.9 OH/nm^2 [196]. The radius of the silica particles is set to 60 nm based on our dynamic light scattering measurements. Using the reported surface charge density value by Sonnefeld [206] of -0.02153 C/m^2 for hydrophilic fumed silica particles (Aerosil 300, Degussa) at pH 7, we calculate a deprotonation value of 3%. With the surface charge density reported by Bolt [199] of -0.01 C/m^2 for amorphous Silica (Ludox) at pH 7, we obtain 1% deprotonation.

Given the fact that the potentiometric measurements were performed at higher ionic strengths for TiO_2 (0.1 M $NaNO_3$ in Holmberg et al., [74] 1 mM KNO_3 in Yates, [77] 0.03 M NaCl in Machesky et al. [75] and 0.1 M KNO_3 in Akratopulo et al. [76]) as well as for SiO_2 (0.005 M KCl in Sonnefeld [206] and 10^{-3} N NaCl in Bolt [199]), the calculated deprotonation values can be regarded as an upper limit for the real deprotonation that we expect for our amorphous TiO_2 and SiO_2 particles at pH 7 and in the lower ionic strength region. For silica, a more realistic estimation of deprotonation in neutral pH for low ionic strength conditions can be obtained using effective surface charge densities reported by Yamanaka et al. [201]. The authors performed conductivity measurements and conductometric titrations on silica particles (Seahoster KE-P10W, Nippon Shokubai Co.Ltd.) in salt-free conditions and calculated an effective surface charge density value of 0.0008 C/m^2, which corresponds to 0.1% deprotonation. This lower value is in good agreement with the surface charge density values calculated from surface potential measurements that we performed on silica particles (Bangs Laboratories Inc.) in chapter 3 and Ref. [150], where we reported surface deprotonation values of 0.04% (pH 5.7) to 0.06% (pH 10) in salt-free conditions. These results show that most silanol groups are expected to remain protonated in neutral pH and low ionic strength conditions. For TiO_2 particles, we are not aware of surface charge density values reported in salt-free conditions. However, the upper limit for surface deprotonation discussed above also indicates that most Ti-OH groups remain protonated in neutral pH and low ionic strength conditions.

8.3 Variation of fitting parameters

The normalized second harmonic scattering patterns of the particles in suspension investigated in this thesis (SiO_2 or TiO_2) are fitted applying the AR-SHS model to determine the surface potential and surface susceptibility. As a mean to give an estimation of how much an error on the material-dependent and the experimentally derived parameters could influence the AR-SHS fits, in the following section we show how the surface potential Φ_0 and surface susceptibility $\chi_{s,2}^{(2)}$ results change when modifying the fitting parameters, namely the size, the refractive index, the number of particles and the ionic strength. The influence of the fitting parameters on the surface potential and the surface susceptibility is discussed on the data collected for 100 nm diameter amorphous TiO_2 particles as a function of added NaCl (shown in chapter 4 Fig. 4.1 and in chapter 5 Fig. 5.6). Note that the results are plotted here as a function of NaCl concentration and are identical to the ones in chapter 5 displayed as a function of ionic strength since NaCl is a monovalent salt. Only one fitting parameter is varied at a time while the other fitting parameters remain fixed, as stated in Tables 8.4 and 8.6 or 8.10 respectively.

a) Variation of particle radius

Figure 8.1 shows the effect of smaller and larger particle radii on the surface potential and surface susceptibility. We use the normalized second harmonic scattering patterns measured for 100 nm diameter amorphous TiO_2 particles as a function of added NaCl and use the radius (R) measured by dynamic light scattering (DLS) for fitting. We then vary the radius fitting parameter by 10 nm ($R + 10$ nm and $R - 10$ nm). Note that we use the same normalized SHS pattern for the fitting and only change the input fitting parameters.
Figure 8.1 A shows that the surface potential trends remain the same when the particle radius R is varied by 10 nm in the fitting input parameters. The surface potentials at $0\,\mu$M and at
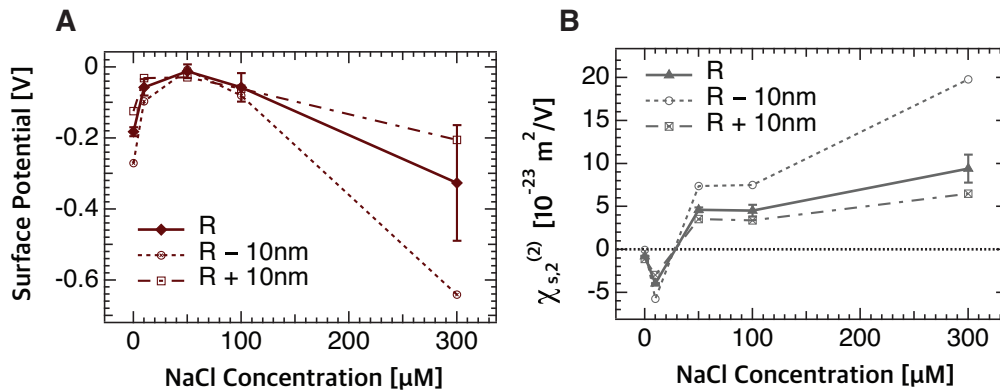

Figure 8.1 – Surface potential Φ_0 (A) and surface susceptibility $\chi_{s,2}^{(2)}$ (B) of TiO_2 as a function of added NaCl concentration. Φ_0 and $\chi_{s,2}^{(2)}$ were obtained by fitting the corresponding AR-SHS pattern of ~ 100 nm diameter TiO_2 particles in suspension in PPP and PSS polarization combination. The graph shows the effect of a variation of the particle size fitting parameter, where R is the radius of the particle as measured by dynamic light scattering (DLS).

$300\,\mu$M show the largest divergence when the size parameter increases or decreases by 10 nm. Although the surface potential values are not identical for different radius values, the same three regions (i, ii and iii) described in the main text (chapters 4 and 5 can be identified. In Figure 8.1 B a similar observation can be made regarding the trends of the surface susceptibility. While the surface susceptibility values change, the overall water orientation behavior remains the same, including the flipping point from negative surface susceptibility values to positive surface susceptibility values (change from average water orientation with oxygens pointing towards the surface to hydrogens pointing towards the surface).

b) Variation of the number of particles

Figure 8.2 shows the surface potential and surface susceptibility as a function of added NaCl concentration when varying the number of particles (NP) fitting input parameter [particles/mL]. Similar to the previously shown variation of size in Figure 8.1, we see in Figure 8.2 that the overall trends of surface potential and surface susceptibility remain the same when fitting with a higher or lower number of particles by one order of magnitude. The same three regions (i, ii, iii) as described in chapters 4 and 5 in the main text can be found (not visible on this y-scale for the largest amount of particles) and the flipping point of the surface susceptibility remains between $10\,\mu$M and $50\,\mu$M added salt when the number of particles is changed in the fitting. Even though the values of the surface potential and surface susceptibility are changed when fitting with different numbers of particles, the overall surface potential and surface susceptibility trends are not impacted by one order of magnitude change in this parameter.
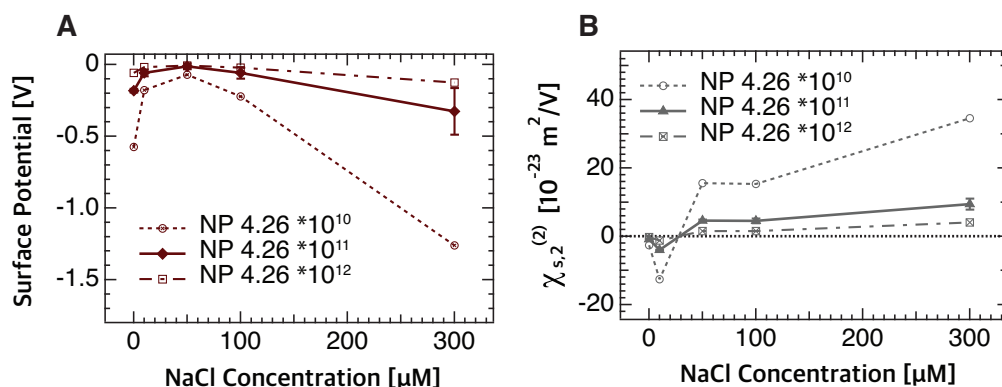

Figure 8.2 – Surface potential Φ_0 (A) and surface susceptibility $\chi_{s,2}^{(2)}$ (B) of TiO_2 as a function of added NaCl concentration. Φ_0 and $\chi_{s,2}^{(2)}$ were obtained by fitting the corresponding AR-SHS pattern of $\sim 100\,$nm diameter TiO_2 particles in suspension in PPP and PSS polarization combination. The graph shows the effect of a variation of the number of particles (NP) fitting parameter [particles/mL].

c) Variation of particle refractive index

In Figure 8.3, the surface potential and surface susceptibility as a function of added NaCl concentration are shown with a variation of the refractive index. Previous reports in the literature have stated a value of 2.61 [157] for the refractive index of amorphous TiO_2 films. We have therefore chosen this value to fit the normalized SHS patterns of the amorphous TiO_2 particles used in chapters 4 and 5 to be comparable between our results. However, for amorphous particles, refractive index values as low as 1.9 have been reported [333]. Additionally, a report on particles composed of an anatase core and an amorphous titania-shell structure has demonstrated tailoring of the shell refractive index from 1.5 to 2.3 [334]. Because of this wide range of refractive indices reported for amorphous TiO_2, we here show the results of the fitting procedure using refractive indices of 1.8 as an intermediate value, and 1.46 as the lower limit (the latter one corresponding to the refractive index of silica). While the surface potential values differ by less than 100 mV, which is for most of the ionic strength points investigated a smaller deviation than the variation induced by the statistical error of our measurements, the surface susceptibility values change by nearly one order of magnitude. Nevertheless, the surface susceptibility trends do not change as the flip in sign occurs between $10\,\mu$M and $50\,\mu$M added NaCl for all the three refractive indices used for the fitting. We can therefore conclude that the choice of the refractive index does mainly influence the values of the surface susceptibility, while the values of the surface potential are barely changed and only to the extent that is in most cases covered by the statistical error of the measurement. Despite these variations, the overall trends of surface potential and surface susceptibility as a function of salt concentration for all three refractive indices remain the same.
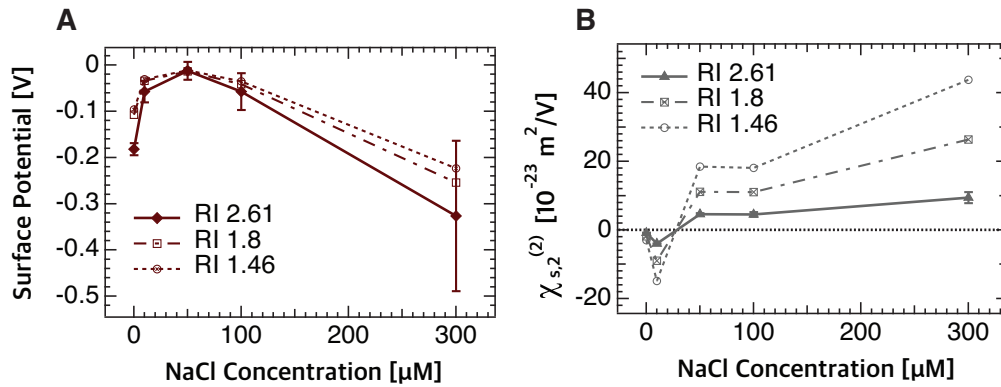

Figure 8.3 – Surface potential Φ_0 (A) and surface susceptibility $\chi_{s,2}^{(2)}$ (B) of TiO_2 as a function of added NaCl concentration. Φ_0 and $\chi_{s,2}^{(2)}$ were obtained by fitting the corresponding AR-SHS pattern of ~ 100 nm diameter TiO_2 particles in suspension in PPP and PSS polarization combination. The graph shows the effect of a variation of the refractive index (RI) fitting parameter.

d) Variation in the ionic strength

Figure 8.4 shows the influence of a decrease or increase of the ionic strength fitting parameter by one order of magnitude on the surface potential and surface susceptibility of ~ 100 nm diameter amorphous TiO_2 particles as a function of added NaCl. In contrast to the change of size, number of particles or refractive index, the change of ionic strength strongly influences the values and trends of the surface potential and surface susceptibility. The surface potential values differ by up to one order of magnitude (from around 200 mV to 2 V) for a higher ionic strength. Regarding the surface susceptibility, the flipping point changes from between 10 μM and 50 μM to between 50 μM and 100 μM for an ionic strength that is one order of magnitude higher. Note that a lower ionic strength by one order of magnitude induces less changes in the surface potential values and does not change the surface susceptibility flipping point.

The hypothetical situation described in Figure 8.4 could only occur if there was an order of magnitude discrepancy between the ionic strength extracted from conductivity measurements (this procedure is further explained in section 2.5.2), used to fit the data, and the real ionic strength in the solution. However, it is important to mention that it is implausible to introduce an error of one order of magnitude on the ionic strength parameter. In our experimental procedure, we measure the conductivity by two different means (conductivity meter and conductivity obtained through zeta potential measurements, see section 2.5.2), which allows for a cross-check. We then convert the value obtained using a conductivity meter into ionic strength to perform our fitting (for more details see 2.5.2). Nevertheless, compared to all the parameters shown above (radius, number of particles, refractive index) the ionic strength is the fitting parameter with the strongest influence on Φ_0 and $\chi_{s,2}^{(2)}$ as it can change the general surface potential and surface susceptibility trends.
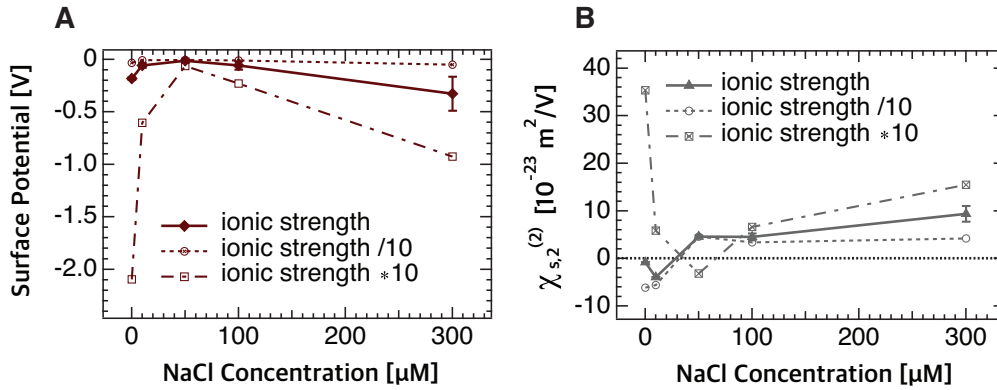

Figure 8.4 – Surface potential Φ_0 (A) and surface susceptibility $\chi_{s,2}^{(2)}$ (B) of TiO_2 as a function of added NaCl concentration. Φ_0 and $\chi_{s,2}^{(2)}$ were obtained by fitting the corresponding AR-SHS pattern of ~ 100 nm diameter TiO_2 particles in suspension in PPP and PSS polarization combination. The graph shows the effect of a variation of the ionic strength fitting parameter.

8.4   Comparison of different TiO$_2$ core-shell thicknesses (Ch. 5)

While the preparation of small-sized (< 20 nm) amorphous TiO$_2$ colloidal suspensions is well established, [335–340] the preparation of aqueous suspensions of uniform and monodispersed amorphous TiO$_2$ particles with a larger diameter (> 100 nm diameter) remains challenging and is the subject of more recent work [341, 342]. Commercially-available amorphous TiO$_2$ aqueous colloidal suspensions are therefore usually found as core-shell particles with a SiO$_2$ core. As the main contribution to the AR-SHS signal is given by water molecules oriented at the TiO$_2$ surface (see section 2.3.1), our experiment only requires the presence of a few atomic layers of TiO$_2$ in contact with the aqueous solution. To support this point, we show below that the AR-SHS data does not depend on the thickness of the TiO$_2$ shell. Therefore, this property allows us to use core-shell particles to study the colloidal amorphous TiO$_2$/aqueous interface, difficult to access otherwise.

The data presented in chapter 5 were obtained on ∼ 100 nm diameter amorphous TiO$_2$ particles from Corpuscular Microspheres Nanospheres (2.5% w/v stock solution in water). Dynamic light scattering characterization data before and after growth of the TiO$_2$ amorphous shell were provided by Corpuscular Microspheres Nanospheres, indicating the growth of a 5-10 nm-thick layer of amorphous TiO$_2$ on a 90-100 nm silica core. In order to verify that the shell thickness of the investigated particles is sufficient to avoid any contributions of the SiO$_2$ core to our signal, we investigated identically-sized particles with a different shell thickness. Aqueous dispersions of 100 nm diameter particles with a 20-30 nm silica core and a 30-40 nm thick amorphous TiO$_2$ shell (custom amorphous TiO$_2$ dispersion, cat. number DNG-GT015) were purchased from Creative Diagnostics. The particles were prepared and washed in the same way as the Corpuscular Microspheres Nanospheres particles (described in section 5.2.2). In the following we show that the surface potential and interfacial water order as a function of NaCl concentration are independent of the thickness of the amorphous TiO$_2$ shell.

Figure 8.5 A shows the surface potential of 100 nm diameter TiO$_2$ amorphous core-shell particles (Creative Diagnostics) with a shell thickness of 30-40 nm compared to identically sized TiO$_2$ amorphous core-shell particles from Corpuscular Microspheres Nanospheres with a shell thickness of 5-10 nm. It can be seen that the surface potential values are similar for the two different core-shell particles from different suppliers. The different core-shell thicknesses of the two particle types investigated do not notably influence the surface potential trends. Therefore, it can be concluded that our SHS surface potential is only influenced by a few atomic layers of TiO$_2$ in contact with the aqueous interface and independent of the nature of the core particle.

Figure 8.5 B shows the surface susceptibility $\chi_{s,2}^{(2)}$ of 100 nm diameter particles with a 30-40 nm amorphous TiO$_2$ shell (Creative Diagnostics) compared to 100 nm diameter particles with a 5-10 nm amorphous TiO$_2$ shell (Corpuscular Microspheres Nanospheres). The values of the surface susceptibility of the two kinds of particles are slightly different (Creative Diagnostics shows about double the surface susceptibility value compared to the Corpuscular Microspheres Nanospheres particles) and the flip in sign of $\chi_{s,2}^{(2)}$ occurs in between 10 μM to 50 μM for the Corpuscular Microspheres Nanospheres particles whereas it occurs in between
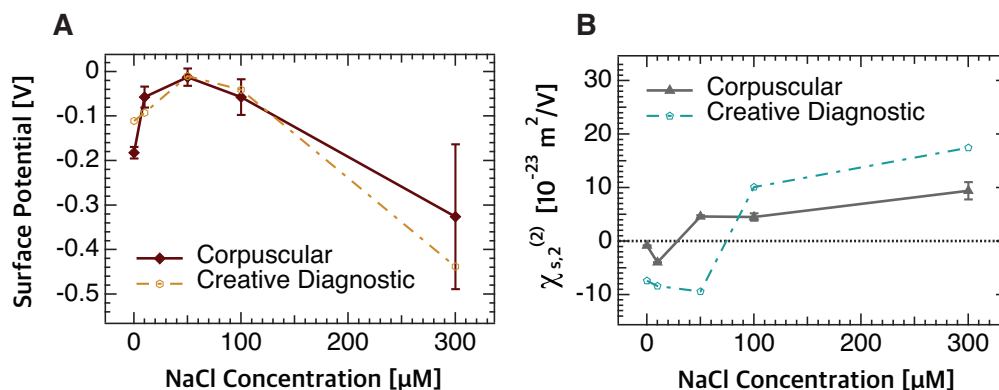
Figure 8.5 – Surface potential Φ_0 (A) and surface susceptibility $\chi_{s,2}^{(2)}$ (B) of $\sim 100\,$nm diameter core-shell TiO_2 particles in suspension as a function of added NaCl concentration. Φ_0 and $\chi_{s,2}^{(2)}$ were obtained by fitting the corresponding AR-SHS pattern in PPP and PSS polarization combination. The graphs show identically sized particles from two different suppliers (Corpuscular Microspheres Nanospheres vs Creative Diagnostic) with different TiO_2 shell thicknesses: 5-10 nm (Corpuscular) vs 30-40 nm (Creative Diagnostic).

50 μM to 100 μM added ionic strength for the particles from Creative Diagnostics. These differences can be explained by the Corpuscular Microspheres Nanospheres particles exhibiting a higher conductivity after the washing process, which translates into a higher intrinsic ionic strength of the particles when no salt is added to the solution. While the Corpuscular Microspheres Nanospheres particles have an ionic strength of $4.0 \cdot 10^{-5}\,$M at 0 μM added salt, the Creative Diagnostics particles have an ionic strength of $2.4 \cdot 10^{-5}\,$M at 0 μM added salt, assuming that the measured conductivity originates from residual NaOH that was used in the synthetic process. Adding the intrinsic ionic strength of the particles to the one due to NaCl incorporation (effective ionic strength), the flip in sign of the surface susceptibility $\chi_{s,2}^{(2)}$ of the Corpuscular Microspheres Nanospheres particles can be estimated in between $4.6 \cdot 10^{-5}\,$M and $9.1 \cdot 10^{-5}\,$M effective ionic strength, whereas the change in sign occurs in between $7.0 \cdot 10^{-5}\,$M to $1.3 \cdot 10^{-4}\,$M for the Creative Diagnostics particles. This comparison highlights that the flipping point of $\chi_{s,2}^{(2)}$ occurs in a similar ionic strength range for both shell thicknesses and confirms the results obtained above: as AR-SHS only probes a few monolayers at the surface, both surface potential and interfacial water orientation data are independent of the shell thickness. The slightly higher surface susceptibility values could be explained by minor variations in the surface structure of the colloids resulting from different synthetic procedures of the two suppliers. Additionally, the Creative Diagnostics particles display a higher amount of organic contaminants after two washing steps, as determined by elemental analysis (4.36% C, 2.24% H, and 1.5% N for Creative diagnostics vs 1.04% C, 0.31% H, and 0% N for Corpuscular Microspheres Nanospheres). The presence of a higher organic residue after two washing steps, possibly due to stabilizing surfactants, could explain the slight differences in interfacial water order observed for the two different batches.

8.5   AR-SHS patterns support evidence of inner-/outer-sphere adsorption (Ch. 5)

In general, the AR-SHS patterns are strongly dependent on the particle size and the ionic strength of the solution, [107, 113, 127] which can also be seen from equation 2.8 in section 2.3.1. The SHS intensity is proportional to the effective particle susceptibilities $\Gamma^{(2)}$ and $\Gamma^{(3)'}$ that contain form factors depending, amongst others, on the geometry of the particle [113, 127]. One of the geometrical form factors contained in the contribution, $(F_3(qR, \kappa R))$, is a function of the inverse Debye length. Therefore, it is influenced by the ionic strength and by how far the electrostatic field generated between the particle surface and the ions reaches into the solution for a given ionic strength range. For spherical particles up to 100 nm, one can calculate that the $F_3(qR, \kappa R)$ factor has a significant influence on the scattering patterns up to 1 mM ionic strength, which includes our investigated ionic strength range (0-600 μM). In this case, the AR-SHS intensity is mainly associated with the thickness of the shell of water molecules oriented by the electric field. A decrease in the AR-SHS signal can therefore be visualized as a scenario where the electrostatic field extends less deeply into the solution, which results in fewer water molecules that are oriented and probed by the AR-SHS scattering technique.

We can use this property to examine the AR-SHS patterns presented in Figure 5.1 in chapter 5. For Na^+ and Rb^+ on SiO_2, the SHS intensity drops by a factor of 2 between 0 and 10 μM. For Ca^{2+} on SiO_2, the SHS intensity drops by a factor 3 in the same interval. This result indicates that the probed shell of water molecules is smaller in the case of Ca^{2+} and that the electric field penetrates less deeply into the bulk solution. Such a situation would correspond to the presence of an outer-sphere layer around the particles, which starts to form at lower ionic strength for Ca^{2+} than for Na^+ and Rb^+ on SiO_2. For Ca^{2+} on TiO_2, the AR-SHS scattering patterns show a less drastic decrease in normalized SHS intensity at low ionic strength (0 to 10 μM) compared to SiO_2. The decrease in SHS intensity is more similar to the case of Na^+ and Rb^+ on TiO_2 in the same ionic strength interval. This result suggests that the overall probed shell of the aqueous environment around the TiO_2 particles is not reduced in the same way as for Ca^{2+} on SiO_2, supporting the idea of preferential inner-sphere adsorption of Ca^{2+} on TiO_2.

8.6 Molecular dynamics simulations at different salt concentrations (Ch. 5)

Table 8.13 – Ion adsorption partitioned as inner-sphere or outer-sphere complex or in diffuse layer at the quartz (101) surface by MD simulations for different concentrations and salts. The left column indicates the number of ion pairs introduced in the system and the corresponding bulk concentration in [M]. The rows in bold correspond to the values shown in Table 5.2 of chapter 5, where the number of NaCl, RbCl, or $CaCl_2$ ions added to the system was set to achieve a similar bulk ionic strength for all solutions (i.e., the ratio of bulk ionic concentrations of $CaCl_2$ and NaCl/RbCl was ~ 1:3). Error bars are shown in parenthesis.

<table>
<tr><td colspan="5" align="center">SiO₂</td></tr>
</table>

	#/bulk concentration [M]	inner-sphere [%]	outer-sphere [%]	diffuse layer [%]
Na^+	6/~0.09	22 (<1)	20 (1)	58 (<1)
Na^+	9/~0.13	23 (1)	19 (<1)	58 (1)
Na^+	**18/~ 0.28**	**20** (<1)	**20** (<1)	**60** (1)
Rb^+	6/~0.09	26 (<1)	18 (<1)	56 (<1)
Rb^+	9/~0.15	26 (1)	18 (<1)	56 (1)
Rb^+	**18/~ 0.28**	**25** (1)	**18** (<1)	**57** (1)
Ca^{2+}	**6/~ 0.09**	**4** (<1)	**20** (<1)	**76** (1)
Ca^{2+}	9/~0.14	2 (1)	21 (<1)	77 (1)
Ca^{2+}	18/~0.29	2 (1)	22 (<1)	76 (1)

Table 8.14 – Ion adsorption partitioned as inner-sphere or outer-sphere complex or in diffuse layer at the rutile (110) surface by MD simulations for different concentrations and salts. The left column indicates the number of ion pairs introduced in the system and the corresponding bulk concentration in [M]. The rows in bold correspond to the values shown in Table 5.4 of chapter 5, where the number of NaCl, RbCl, or $CaCl_2$ ions added to the system was set to achieve a similar bulk ionic strength for all solutions (i.e., the ratio of bulk ionic concentrations of $CaCl_2$ and NaCl/RbCl was ~ 1:3). Error bars are shown in parenthesis.

<table>
<tr><td colspan="5" align="center">TiO₂</td></tr>
</table>

	#/bulk concentration [M]	inner-sphere [%]	outer-sphere [%]	diffuse layer [%]
Na^+	6/~0.10	83 (3)	6 (<1)	11 (1)
Na^+	9/~0.16	82 (<1)	7 (<1)	11 (1)
Na^+	**18/~ 0.33**	**76** (1)	**7** (<1)	**17** (1)
Rb^+	6/~0.11	75 (2)	7 (1)	18 (1)
Rb^+	9/~0.19	73 (5)	7 (<1)	20 (2)
Rb^+	**18/~ 0.36**	**71** (<1)	**7** (<1)	**22** (<1)
Ca^{2+}	6/~0.08	99 (7)	1 (<1)	0 (2)
Ca^{2+}	**13/~ 0.12**	**97** (1)	**0** (<1)	**3** (<1)
Ca^{2+}	18/~0.31	93 (2)	0 (<1)	7 (<1)

8.7 Band bending at the semiconductor/liquid interface with and without illumination (Ch. 7)

The semiconductor TiO_2 is intrinsically n-doped due to oxygen vacancies in the material. If an n-doped semiconductor is in contact with an electrolyte under equilibrium conditions, the Fermi-level E_F of the semiconductor and the redox-level of the electrolyte E_{redox} will establish an equilibrium ($E_F = E_{redox}$). This causes the formation of a positively charged space charge layer (w_{scl}), as electrons from the semiconductor surface will be transferred to the electrolyte until the equilibrium is established. This leads to a bending of the energy bands of the semiconductor, as it is shown in Figure 8.6 A. The potential drop inside the semiconductor
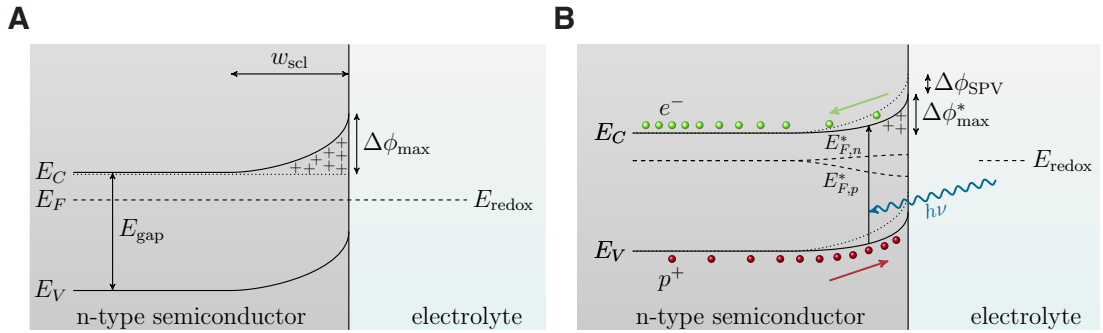

Figure 8.6 – Schematic illustration of the band bending of a n-doped semiconductor in contact with an electrolyte (A) under equilibrium conditions and (B) under illumination. E_V indicates the valence band, E_C the conduction band and E_{gap} the energy gap between the two. The space charge layer w_{scl} and the band bending potential $\Delta\Phi_{max}$ and their evolution with and without illumination are shown. $\Delta\Phi_{max}^*$ describes the band bending potential under non-equilibrium conditions. The Fermi-level E_F and the quasi-Fermi levels $E_{F,n}^*$ and $E_{F,p}^*$ of the semiconductor, as well as the redox-level E_{redox} of the electrolyte solution are displayed. $\Delta\Phi_{SPV}$ is the surface photovoltage. The band bending is reduced under illumination as a consequence of the generation of electron-hole pairs and quasi-Fermi levels under non-equilibrium conditions. See Refs. [212, 213, 237, 332, 343] for more details.

can be described by the Poisson-Boltzmann equation. The Debye length depends on the intrinsic donator density N_d of the semiconductor and can be written as follows:

$$L_D = \sqrt{\frac{\varepsilon_0 \varepsilon_r k_B T}{e^2 N_d}}. \tag{8.1}$$

In a case where the radius of the particle is in the size range of the space charge layer ($R \approx w_{scl}$) the maximum band bending $\Delta\Phi_{max}$ can be approximated as follows:

$$\Delta\Phi_{max} \approx \frac{k_B T}{6e} \left(\frac{R}{L_D} \right)^2. \tag{8.2}$$

133

The band bending will change under illumination due to the creation of electron-hole pairs (e^- and p^+) so that the electrons that are lifted to the conduction band screen the charges in the space charge layer w_{scl} (see Fig. 8.6 B) [332]. This is why we expect a reduction of the maximum band bending under illumination with respect to the maximum band bending under equilibrium condition ($\Delta\Phi^*_{max} < \Delta\Phi_{max}$). The band bending change can be expressed as $\Delta\Phi_{SPV} = \Delta\Phi_{max} - \Delta\Phi^*_{max}$. The higher N_d, the lower ε_r, and the larger the particle radius R, the higher is the maximum band bending $\Delta\Phi_{max}$ and the more probable it becomes that $\Delta\Phi_{SPV}$ can be resolved experimentally.

Bibliography

[1] Etacheri, V.; Di Valentin, C.; Schneider, J.; Bahnemann, D.; Pillai, S. C. Visible-light activation of TiO$_2$ photocatalysts: Advances in theory and experiments. *J. Photochem. Photobiol. C: Photochem. Rev.* **2015**, *25*, 1–29.

[2] Danish, M. S. S.; Bhattacharya, A.; Stepanova, D.; Mikhaylov, A.; Grilli, M. L.; Khosravy, M.; Senjyu, T. A Systematic Review of Metal Oxide Applications for Energy and Environmental Sustainability. *Metals* **2020**, *10*, 1604.

[3] Chavali, M. S.; Nikolova, M. P. Metal oxide nanoparticles and their applications in nanotechnology. *SN Appl. Sci.* **2019**, *1*, 607.

[4] Emeji, I. C.; Ama, O. M.; Aigbe, U. O.; Khoele, K.; Osifo, P. O.; Ray, S. S., *Nanostructured Metal-Oxide Electrode Materials for Water Purification; Properties and Synthesis of Metal Oxide Nanoparticles in Electrochemistry*; Ama, O. M., Ray, S. S., Eds.; Springer: Cham, 2020.

[5] Moma, J.; Baloyi, J., *Photocatalysts - Applications and Attributes, Modified Titanium Dioxide for Photocatalytic Applications*; Khan, S. B., Akhtar, K., Eds.; InTechOpen: 2018.

[6] Fujishima, A.; Honda, K. Electrochemical photolysis of water at a semiconductor electrode. *Nature* **1972**, *238*, 37–38.

[7] Hashimoto, K.; Irie, H.; Fujishima, A. TiO$_2$ Photocatalysis: A Historical Overview and Future Prospects. *Jpn. J. Appl. Phys.* **2005**, *44*, 8269–8285.

[8] Luttrell, T.; Halpegamage, S.; Tao, J.; Kramer, A.; Sutter, E.; Batzill, M. Why is anatase a better photocatalyst than rutile? - Model studies on epitaxial TiO$_2$ films. *Sci. Rep.* **2014**, *4*, 4043.

[9] Nazeeruddin, M. K.; Kay, A.; Rodicio, R.; Humphry-Baker, E.; Mueller, O.; Liska, N.; Vlachopoulos, N.; Grätzel, M. Conversion of light to electricity by cis-X2bis(2,2'-bipyridyl-4,4'-dicarboxylate)ruthenium(II) charge-transfer sensitizers (X=Cl-,Br-,I-,CN- and SCN-) on nanocrystalline titanium dioxide electrodes. *J. Am. Chem. Soc* **1993**, *115*, 6382–6390.

[10] Swierk, J. R.; Regan, K. P.; Jiang, J.; Brudvig, G. W.; Schmuttenmaer, C. A. Rutile TiO$_2$ as an Anode Material for Water-Splitting Dye-Sensitized Photoelectrochemical Cells. *ACS Energy Lett.* **2016**, *1*, 603–606.

[11] Sherman, B. D.; Bergkamp, J. J.; Brown, C. L.; Moore, A. L.; Gust, D.; Moore, T. A. A tandem dye-sensitized photoelectrochemical cell for light driven hydrogen production. *Energy Environ. Sci.* **2016**, *9*, 1812.

[12] Zhang, S.; Ye, H.; Hua, J.; Tian, H. Recent advances in dye-sensitized photoelectrochemical cells for water splitting. *J. Energy Chem.* **2019**, *1*, 100015.

[13] Ghosh, A. K.; Marushka, H. R. Photoelectrolysis of water in sunlight with sensitized semiconductor electrodes. *J. Electrochem. Soc.* **1977**, *124*, 1516–1522.

[14] Dozzi, M. V.; Selli, E. Doping TiO_2 with p-block elements: Effects on photocatalytic activity. *J. Photochem. Photobiol. C: Photochem. Rev.* **2013**, *14*, 13–28.

[15] Fadlallah, M. M. Magnetic, electronic, optical, and photocatalytic properties of nonmetal- and halogen-doped anatase TiO_2 nanotubes. *Physica E* **2017**, *89*, 50–56.

[16] Khlyustova, A.; Sirotkin, N.; Kusova, T.; Kraev, A.; Titov, V.; Agafonov, A. Doped TiO_2: the effect of doping elements on photocatalytic activity. *Mater. Adv.* **2020**, *1*, 1193–1201.

[17] Zhang, J.; Zhou, P.; Liu, J.; Yu, J. New understanding of the difference of photocatalytic activity among anatase, rutile and brookite TiO_2. *Phys. Chem. Chem. Phys.* **2014**, *16*, 20382–20386.

[18] Chalastara, K.; Guo, F.; Elouatik, S.; Demopoulos, G. P. Tunable Composition Aqueous-Synthesized Mixed-Phase TiO_2 Nanocrystals for Photo-Assisted Water Decontamination: Comparison of Anatase, Brookite and Rutile Photocatalysts. *Catalysts* **2020**, *10*, 407.

[19] Yamakata, A.; M., V. J. J. Curious behaviors of photogenerated electrons and holes at the defects on anatase, rutile, and brookite TiO_2 powders: A review. *J. Photochem. Photobiol. C: Photochem. Rev.* **2019**, *40*, 234–243.

[20] Xu, M.; Gao, Y.; Moreno, E. M.; Kunst, M.; Muhler, M.; Wang, Y.; Idriss, H.; Wöll, C. Photocatalytic Activity of Bulk TiO_2 Anatase and Rutile Single Crystals Using Infrared Absorption Spectroscopy. *Phys. Rev. Lett.* **2011**, *106*, 138302.

[21] Linsebigler, A. L.; Lu, G.; Yater Jr., J. T. Photocatalysis on TiO_2 Surfaces: Principles, Mechanisms, and Selected Results. *Chem. Rev.* **1995**, *3*, 735–758.

[22] Li, J.-G.; Ishigaki, T.; Sun, X. Anatase, Brookite, and Rutile Nanocrystals via Redox Reactions under Mild Hydrothermal Conditions: Phase-Selective Synthesis and Physicochemical Properties. *J. Phys. Chem. C* **2007**, *111*, 4969–4976.

[23] Kandiel, T. A.; Robben, L.; Alkaim, A.; Bahnemann, D. Brookite versus anatase TiO_2 photocatalysts: phase transformations and photocatalytic activities. *Photochem. Photobiol. Sci.* **2013**, *12*, 602–609.

[24] Li, Z.; Cong, S.; Xu, Y. Brookite vs anatase TiO_2 in the Photocatalytic Activity for Organic Degradation in Water. *ACS Catal.* **2014**, *4*, 3273–3280.

[25] Fu, F.; Zhang, Y.; Zhang, Y.; Chen, Y. Synthesis of Mn-doped and anatase/rutile mixed-phase TiO_2 nanofibers for high photoactivity performance. *Catal. Sci. Technol.* **2021**, *11*, 4181–4195.

[26] Hurum, D. C.; Agrios, A. G.; Gray, K. A.; Rajh, T.; Thurnauer, M. C. Explaining the Enhanced Photocatalytic Activity of Degussa P25 Mixed-Phase TiO_2 Using EPR. *J. Phys. Chem. B* **2003**, *107*, 4545–4549.

[27] Lei, J.; Li, H.; Zhang, J.; Anpo, M., *Low-Dimensional and Nanostructured Materials and Devices; Mixed-Phase TiO_2 Nanomaterials as Efficient Photocatalysts*; Ünlü, H., Horing, N. J. M., Dabrowski, J., Eds.; Springer: Cham, 2016.

[28] Ohno, T.; Sarukawa, K.; Tokieda, K.; Matsumura, M. Morphology of a TiO_2 Photocatalyst (Degussa, P-25) Consisting of Anatase and Rutile Crystalline Phases. *J. Catal.* **2001**, *203*, 82–86.

[29] Al-Ataffi, K.; Nattestad, A.; Wu, Q.; Ide, Y.; Yamauchi, Y.; Dou, S. X.; Kim, J. H. The effect of amorphous TiO_2 in P25 on dye-sensitized solar cell performance. *Chem. Commun.* **2018**, *54*, 381–384.

[30] Thiele, E. W. Relation between Catalytic Activity and Size of Particle. *Ind. Eng. Chem.* **1939**, *31*, 916–920.

[31] Lin, C.; Compton, R. G. Size Effects in Nanoparticle Catalysis at Nanoparticle Modified Electrodes: The Interplay of Diffusion and Chemical Reactions. *J. Phys. Chem. C* **2017**, *121*, 2521–2528.

[32] Cuenya, B. R. Synthesis and catalytic properties of metal nanoparticles: Size, shape, support, composition, and oxidation state effects. *J. Phys. Chem. C* **2010**, *518*, 3127–3150.

[33] Cao, S.; Tao, F.; Tang, y.; Li, Y.; Yu, J. Size- and shape-dependent catalytic performances of oxidation and reduction reactions on nanocatalysts. *Chem. Soc. Rev.* **2016**, *45*, 4747–4765.

[34] Grassian, V. H. When Size Really Matters: Size-Dependent Properties and Surface Chemistry of Metal and Metal Oxide Nanoparticles in Gas and Liquid Phase Environments. *J. Phys. Chem. C* **2008**, *112*, 18303–18313.

[35] Liu, Y.; Le Formal, F.; Boudoire, F.; Guijarro, N. Hematite Photoanodes for Solar Water Splitting: A Detailed Spectroelectrochemical Analysis on the pH-Dependent Performance. *ACS Appl. Energy Mater.* **2019**, *2*, 6825–6833.

[36] Shinangawa, T.; Takanabe, K. Towards Versatile and Sustainable Hydrogen Production through Electrocatalytic Water Splitting: Electrolyte Engineering. *ChemSusChem* **2017**, *10*, 1318–1336.

[37] Guijarro, N.; Prévot, M. S.; Silvula, K. Surface modification of semiconductor photoelectrodes. *Phys. Chem. Chem. Phys.* **2015**, *17*, 15655–15674.

[38] Iandolo, B.; Hellman, A. The Role of Surface States in the Oxygen Evolution Reaction on Hematite. *Angew. Chem. Int. Ed.* **2014**, *53*, 13404–13408.

[39] Ambrosio, F.; Wiktor, J.; Pasquarello, A. pH-Dependent Catalytic Reaction Pathway for Water Splitting at the $BiVO_4$-Water Interface from the Band Alignment. *ACS Energy Lett.* **2018**, *3*, 829–834.

Bibliography

[40] Koper, M. T. M. Theory of multiple proton-electron transfer reactions and its implications for electrocatalysis. *Chem. Sci.* **2013**, *4*, 2710–2723.

[41] Gonella, G.; Backus, E. H. G.; Nagata, Y.; Bonthuis, D. J.; Loche, P.; Schlaich, A.; Netz, R. R.; Kühnle, A.; McCrum, I. T.; Koper, M. T. M.; Wolf, M.; Winter, B.; Meijer, G.; Campen, R. K.; Bonn, M. Water at charged interfaces. *Nat. Rev. Chem.* **2021**, *5*, 1–20.

[42] Sridevi, D.; RamyaDevi, K. T.; Narmadha, J.; Sundaravadivel, E. pH dependent synthesis of TiO_2 nanoparticles exerts its effect on bacterial growth inhibition and osteoblasts proliferation. *AIP Advances* **2020**, *10*, 095119.

[43] Ahmed, S.; Rasul, M. G.; Martens, W. N.; Brown, R.; Hashib, M. A. Heterogeneous photocatalytic degradation of phenols in wastewater: A review on current status and developments. *Desalination* **2010**, *261*, 3–18.

[44] Haroune, L.; Salaun, M.; Ménard, A.; Legault, C. Y.; Bellenger, J.-P. Photocatalytic degradation of carbamazepine and three derivatives using TiO_2 and ZnO: Effect of pH, ionic strength, and natural organic matter. *Sci. Total Environ.* **2014**, *475*, 16–22.

[45] Helmholtz, H. Ueber einige Gesetze der Vertheilung elektrischer Ströme in körperlichen Leitern mit Anwendung auf die thierisch-elektrischen Versuche. *Ann. Phys.* **1853**, *165*, 211–233.

[46] Scott, K., *Sustainable and Green Electrochemical Science and Technology*; Wiley: Hoboken, NJ, 2017.

[47] Gouy, M. Sur la constitution de la charge électrique à la surface d'un électrolyte. *J. Phys. Theor. Appl.* **1910**, *9*, 457–468.

[48] Chapman, D. L. LI. A contribution to the theory of electrocapillarity. *Lond. Edinb. Dubl. Phil. Mag.* **1913**, *25*, 475–481.

[49] Srinivasan, S. *Fuel Cells: From Fundamentals to Applications*, Srinivasan, S., Ed.; Springer US: Boston, MA, 2006.

[50] Schmickler, W.; Santos, E., *Interfacial Electrochemistry*, 2nd ed.; Springer: Berlin, Heidelberg, 2010.

[51] Khademi, M.; Barz, D. P. J. Structure of the Electrical Double Layer Revisited: Electrode Capacitance in Aqueous Solutions. *Langmuir* **2020**, *36*, 4250–4260.

[52] Hunter, R. J., *Foundations of Colloid Science*, 2nd ed.; Oxford University Press: Oxford, 2000.

[53] Stern, O. Zur Theorie der Elektrolytischen Doppelschicht. *Z. Elektrochem. angew. phys. Chem.* **1924**, *30*, 508–516.

[54] Grahame, D. C. The Electrical Double Layer and the Theory of Electrocapillarity. *Chem. Rev.* **1947**, *41*, 441–501.

[55] Bockris, J. O.; Devanathan, M. A. V.; Müller, K. On the structure of charged interfaces. *Proc. Math. Phys. Eng.* **1963**, *274*, 55–79.

[56] Marcus, R. A. Chemical and Electrochemical Electron-Transfer Theory. *Ann. Rev. Phys. Chem.* **1964**, *15*, 155–196.

[57] *Fundamentals of Interface and Colloid Science*; Lyklema, J, Ed.; Academic Press: London, 2005; Vol. 5.

[58] Velikonja, A.; Gongadze, E.; Kralj-Iglič, V.; Iglič, A. Charge Dependent Capacitance of Stern Layer and Capacitance of Electrode/Electrolyte Interface. *Int. J. Electrochem. Sci.* **2014**, *9*, 5885–5894.

[59] Sonnefeld, J. Surface charge density on spherical silica particles in aqueous alkali chloride solutions. *Colloid Polym. Sci.* **1995**, *273*, 932–938.

[60] Sverjensky, D. A. Interpretation and prediction of triple-layer model capacitances and the structure of the oxide-electrolyte-water interface. *Geochim. Cosmochim. Acta* **2001**, *65*, 3643–3655.

[61] Chazalviel, J.-N., *Porous Silicon Science and Technology; The silicon/electrolyte interface*; Vial, J. C., Derrien, J., Eds.; Springer: Berlin, Heidelberg, 1995.

[62] Rashwan, M.; Rehl, B.; Sthoer, A.; Darlington, A. M.; Azam, M. S.; Zeng, H.; Liu, Q.; Tyrode, E.; Gibbs, J. M. Structure of the Silica/Divalent Electrolyte Interface: Molecular Insight into Charge Inversion with Increasing pH. *J. Phys. Chem. C* **2020**, *124*, 26973–26981.

[63] Rehl, B.; Gibbs, J. M. Role of Ions on the Surface-Bound Water Structure at the Silica/Water Interface: Identifying the Spectral Signature of Stability. *J. Phys. Chem. Lett.* **2021**, *12*, 2854–2864.

[64] Kroutil, O.; Chval, Z.; Skelton, A. A.; Předota, M. Computer Simulations of Quartz (101)-Water Interface over a Range of pH Values. *J. Phys. Chem. C* **2015**, *119*, 9274–9286.

[65] Griscom, D. L. The Electronic Structure Of SiO_2: A Review of Recent Spectroscopic and Theoretical Advances. *Journal of Non-Crystalline Solids* **1977**, *24*, 155–234.

[66] Shinde, P. S.; Suryawanshi, P. S.; Patil, K. K.; Belekar, V.; Sankpal, S. A.; Delekar, S. D.; Jadhav, S. A. A Brief Overview of Recent Progress in Porous Silica as Catalyst Supports. *J. Compos. Sci.* **2021**, *5*, 75.

[67] Panagiotopoulou, P.; Verykios, X. E. Metal-support interactions of Ru-based catalysts under conditions of CO and CO_2 hydrogenation. *Catalysis* **2020**, *32*, 1–23.

[68] Yang, F.; Zhao, H.; Wang, W.; Wang, L.; Zhang, L.; Liu, T.; Sheng, J.; Zhu, S.; He, D.; Lin, L.; He, J.; Wang, R.; Li, Y. Atomic origins of the strong metal-support interaction in silica supported catalysts. *Chem. Sci.* **2021**, *12*, 12651–12660.

[69] Zaera, F. Probing Liquid/Solid Interfaces at the Molecular Level. *Chem. Rev.* **2012**, *112*, 2920–2986.

[70] Zaera, F. Surface chemistry at the liquid/solid interface. *Surf. Sci.* **2011**, *605*, 1141–1145.

Bibliography

[71] Hiemenz, P. C.; Rajagopalan, R., *Principles of colloid and surface chemistry*, 3rd ed.; Marcel Dekker: New York, 1997.

[72] Hunter, R. J., *Zeta potential in colloid science. Principles and applications*; Academic Press: London, 1981.

[73] Lützenkirchen, J.; Preočanin, T.; Kovačević, D.; Tomišić, V.; Lövgren, L.; Kallay, N. Potentiometric Titrations as a Tool for Surface Charge Determination. *Croat. Chem. Acta* **2012**, *85*, 391–417.

[74] Holmberg, J. P.; Ahlberg, E.; Bergenholtz, J.; Hassellöv, M.; Abbas, Z. Surface charge and interfacial potential of titanium dioxide nanoparticles: experimental and theoretical investigations. *J. Colloid Interface Sci.* **2013**, *407*, 168–176.

[75] Machesky, M. L.; Wesolowski, D. J.; Palmer, D. A.; Ichiro-Hayashi, K. Potentiometric Titrations of Rutile Suspensions to 250°C. *J. Colloid Interface Sci.* **1998**, *200*, 298–309.

[76] Akratopulu, K. C.; Kordulis, C.; Lycourghiotis, A. Effect of temperature on the point of zero charge and surface charge of TiO_2. *J. Chem. Soc.,Faraday Trans.* **1990**, *86*, 3437.

[77] Yates, D. E. The structure of the oxide/aqueous electrolyte interface., Ph.D. Thesis, Faculty of Science, Chemistry, University of Melbourne, 1975.

[78] Kobayashi, M.; Juillerat, F.; Galletto, P.; Bowen, P.; Borkovec, M. Aggregation and Charging of Colloidal Silica Particles: Effect of Particle Size. *Langmuir* **2005**, *21*, 5761–5769.

[79] Pyman, M. a. F.; Bowden, J. W.; Posner, A. M. The movement of titration curves in the presence of specific adsorption. *Soil Res.* **1979**, *17*, 191–195.

[80] Sonnefeld, J. On the influence of background electrolyte concentration on the position of the isoelectric point and the point of zero charge. *Colloids Surf. A Physicochem. Eng.* **2001**, *190*, 179–183.

[81] Lyklema, J. Points of zero charge in the presence of specific adsorption. *J. Colloid Interface Sci.* **1984**, *99*, 109–117.

[82] Nonnenmacher, M.; O'Boyle, M. P.; Wickramasinghe, H. K. Kelvin probe force microscopy. *Appl. Phys. Lett.* **1991**, *58*, 2921–2923.

[83] Fujihira, M. Kelvin Probe Force Microscopy of Molecular Surfaces. *Annu. Rev. Mater. Sci.* **1999**, *29*, 353–380.

[84] Melitz, W.; Shen, J.; Kummel, A. C.; Lee, S. Kelvin probe force microscopy and its application. *Surface Science Reports* **2011**, *66*, 1–27.

[85] Strelcov, E.; Arble, C.; Guo, H.; Hoskins, B. D.; Yulaev, A.; Vlassiouk, I. V.; Zhitenev, N. B.; Tselev, A.; Kolmakov, A. Nanoscale Mapping of the Double Layer Potential at the Graphene-Electrolyte Interface. *Nano Lett.* **2020**, *20*, 1336–1344.

[86] Umeda, K.-i.; Kobayashi, K.; Oyabu, N.; Hirata, Y.; Matsushige, K.; Yamada, H. Practical aspects of Kelvin-probe force microscopy at solid/liquid interfaces in various liquid media. *J. Appl. Phys* **2014**, *116*, 134307.

[87] Collins, L.; Jesse, S.; Kilpatrick, J. I.; Tselev, A.; Okatan, M. B.; Kalinin, S. V.; Rodriguez, B. J. Kelvin probe force microscopy in liquid using electrochemical force microscopy. *Beilstein J. Nanotechnol.* **2015**, *6*, 201–214.

[88] Collins, L.; Jesse, S.; Kilpatrick, J. I.; Tselev, A.; Varenyk, O.; Okatan, M. B.; Weber, S. A. L.; Kumar, A.; Balke, N.; Kalinin, S. V.; Rodriguez, B. J. Probing charge screening dynamics and electrochemical processes at the solid-liquid interface with electrochemical force microscopy. *Nat. Commun* **2014**, *5*, 3871.

[89] Bazant, M. Z.; Thornton, K.; Ajdari, A. Diffuse-charge dynamics in electrochemical systems. *Phys. Rev. E* **2004**, *70*, 021506.

[90] Collins, L.; Kilpatrick, J. I.; Kalinin, S. V.; Rodriguez, B. J. Towards nanoscale electrical measurements in liquid by advanced KPFM techniques: a review. *Rep. Prog. Phys.* **2018**, *81*, 086101.

[91] Ducker, W. A.; Senden, T. J.; Pashley, R. M. Direct measurement of colloidal forces using an atomic force microscope. *Nature* **1991**, *353*, 239–241.

[92] Montes Ruiz-Cabello, F. J.; Trefalt, G.; Oncsik, T.; Szilagyi, I.; Maroni, P.; Borkovec, M. Interaction Forces and Aggregation Rates of Colloidal Latex Particles in the Presence of Monovalent Counterions. *J. Phys. Chem. B* **2015**, *119*, 8184–8193.

[93] Dobryden, I.; Mensi, E.; Holmgren, A.; Almqvist, N. Surface Forces between Nanomagnetite and Silica in Aqueous Ca^{2+} Solutions Studied with AFM Colloidal Probe Method. *Colloids Interfaces* **2020**, *4*, 41.

[94] Brown, M. A.; Abbas, Z.; Kleibert, A.; Green, R. G.; Goel, A.; May, S.; Squires, T. M. Determination of Surface Potential and Electrical Double-Layer Structure at the Aqueous Electrolyte-Nanoparticle Interface. *Phys. Rev. X* **2016**, *6*, 011007.

[95] Brown, M. A.; Goel, A.; Abbas, Z. Effect of electrolyte concentration on the Stern layer thickness at a charged interface. *Angew. Chem. Int. Ed.* **2016**, *55*, 3790–3794.

[96] Brown, M. A.; Beloqui Redondo, A.; Sterrer, M.; Winter, B.; Pacchioni, G.; Abbas, Z.; van Bokhoven, J. A. Measure of Surface Potential at the Aqueous–Oxide Nanoparticle Interface by XPS from a Liquid Microjet. *Nano Lett.* **2013**, *13*, 5403–5407.

[97] Brown, M. A.; Jordan, I.; Beloqui Redondo, A.; Kleibert, A.; Wörner, H. J.; van Bokhoven, J. A. In situ photoelectron spectroscopy at the liquid/nanoparticle interface. *Surf. Sci.* **2013**, *610*, 1–6.

[98] Gmür, T. A.; Goel, A.; Brown, M. A. Quantifying Specific Ion Effects on the Surface Potential and Charge Density at Silica Nanoparticle-Aqueous Electrolyte Interfaces. *J. Phys. Chem. C* **2016**, *120*, 16617–16625.

[99] Söderström, J.; Ottosson, N.; Pokapanich, W.; Öhrwall, G.; Björneholm, O. Functionalized nanoparticles in aqueous surroundings probed by X-ray photoelectron spectroscopy. *J. Electron Spectrosc. Relat. Phenom.* **2011**, *184*, 375–378.

[100] Shen, Y. R Surfaces probed by nonlinear optics. *Surf. Sci.* **1994**, *299-300*, 551–562.

Bibliography

[101]   Shen, Y. R. Surface properties probed by second-harmonic and sum-frequency generation. *Nature* **1989**, *337*, 519–525.

[102]   Wang, C. Second-harmonic generation of light at the boudary of an isotropic medium. *Phys. Rev.* **1969**, *178*, 1457–1461.

[103]   Boyd, R., *Nonlinear Optics*, 3rd ed.; Academic Press, Elsevier Science: Amsterdam, 2008.

[104]   Bloembergen, N., *Nonlinear optics*; World Scientific: Singapore, 1964.

[105]   Bain, C. D. Sum-frequency Vibrational Spectroscopy of the Solid/Liquid Interface. *J. Chem. Soc. Faraday Trans.* **1995**, *91*, 1281–1296.

[106]   Backus, E. H. G.; Schaefer, J.; Bonn, M. Probing the Mineral-Water Interface with Nonlinear Optical Spectroscopy. *Angew. Chem. Int. Ed.* **2021**, *60*, 10482–10501.

[107]   Roke, S.; Gonella, G. Nonlinear light scattering and spectroscopy of particles and droplets in liquids. *Annu. Rev. Phys. Chem.* **2012**, *63*, 353–378.

[108]   Wang, H.-F.; Velarde, L.; Gan, W.; Fu, L. Quantitative Sum-Frequency Generation Vibrational Spectroscopy of Molecular Surfaces and Interfaces: Lineshape, Polarization, and Orientation. *Annu. Rev. Phys. Chem.* **2015**, *66*, 189–216.

[109]   Raschke, M. B.; Shen, Y. R. Nonlinear optical spectroscopy of solid interfaces. *Curr. Opin. Solid State Mater. Sci.* **2004**, *8*, 343–352.

[110]   Eisenthal, K. B. Second Harmonic Spectroscopy of Aqueous Nano- and Microparticle Interfaces. *Chem. Rev.* **2006**, *106*, 1462–1477.

[111]   Macias-Romero, C.; Nahalka, I.; Okur, H. I.; Roke, S. Optical imaging of surface chemistry and dynamics in confinement. *Science* **2017**, *357*, 784–788.

[112]   Zoumi, A.; Yeh, A.; Tromberg, J. Imaging cells and extracellular matrix in vivo by using second-harmonic generation and two-photon excited fluorescence. *Proc. Natl. Acad. Sci.* **2002**, *99*, 11014–11019.

[113]   Gonella, G.; Lütgebaucks, C.; de Beer, A. G. F.; Roke, S. Second Harmonic and Sum-Frequency Generation from Aqueous Interfaces is Modulated by Interference. *J. Phys. Chem. C* **2016**, *120*, 9165–9173.

[114]   Lütgebaucks, C.; Gonella, G.; Roke, S. Optical label-free and model-free probe of the surface potential of nanoscale and microscopic objects in aqueous solution. *Phys. Rev. B* **2016**, *94*, 195410.

[115]   Schürer, B.; Wunderlich, S.; Sauerbeck, C.; Peschel, U.; Peukert, W. Probing colloidal interfaces by angle-resolved second harmonic light scattering. *Phys. Rev. B* **2010**, *82*, 241404.

[116]   Gomopoulos, N.; Lütgebaucks, C.; Sun, Q.; Macias-Romero, C.; Roke, S. Label-free second harmonic and hyper Rayleigh scattering with high efficiency. *Opt. Express* **2013**, *21*, 815–821.

[117] Wang, H.; Yan, E. C. Y.; Borguet, E.; Eisenthal, K. B. Second harmonic generation from the surface of centrosymmetric particles in bulk solution. *Chem. Phys. Lett.* **1996**, *259*, 15–20.

[118] Liu, Y.; Dadap, J. I.; Zimdars, D.; Eisenthal, K. B. Study of Interfacial Charge-Transfer Complex on TiO$_2$ Particles in Aqueous Suspension by Second-Harmonic Generation. *J. Phys. Chem. B* **1999**, *103*, 2480–2486.

[119] Yang, N.; Angerer, W. E.; Yodh, A. G. Angle-resolved second-harmonic light scattering from colloidal particles. *Phys. Rev. Lett.* **2001**, *87*, 103902.

[120] Dadap, J. I.; de Aguiar, H. B.; Roke, S. Nonlinear light scattering from clusters and single particles. *J. Chem. Phys.* **2009**, *130*, 214710.

[121] De Beer, A. G. F.; Roke, S.; Dadap, J. I. Theory of optical second-harmonic and sum-frequency scattering from arbitrarily shaped particles. *J. Opt. Soc. Am. B* **2011**, *28*, 1374–1384.

[122] Boutou, V.; Favre, C.; Woeste, L.; Wolf, J.-P. Measuring the electric charge in cloud droplets by use of second-harmonic generation. *Opt. Lett.* **2005**, *30*, 759–761.

[123] Jen, S.-H.; Dai, H.-L. Probing Molecules Adsorbed at the Surface of Nanometer Colloidal Particles by Optical Second-Harmonic Generation. *J. Phys. Chem. B* **2006**, *110*, 23000–23003.

[124] Jen, S.-H.; Gonella, G.; Dai, H.-L. The Effect of Particle Size in Second Harmonic Generation from the Surface of Spherical Colloidal Particles. I: Experimental Observations. *J. Phys. Chem. A* **2009**, *113*, 4758–4762.

[125] Martorell, J.; Vilaseca, R. Scattering of second-harmonic light from small spherical particles ordered in a crystalline lattice. *Phys. Rev. A* **1997**, *55*, 4520–4525.

[126] Roke, S.; Roeterdink, W. G.; Wijnhoven, J. E.G. J.; Petukhov, A. V.; Kleyn, A. W.; Bonn, M. Vibrational Sum Frequency Scattering from a Submicron Suspension. *Phys. Rev. Lett.* **2003**, *91*, DOI: 10.1103/PhysRevLett.91.258302.

[127] Roke, S.; Bonn, M.; Petukhov, A. V. Nonlinear optical scattering: the concept of the effective susceptibility. *Phys. Rev. B* **2004**, *70*, 115106.

[128] Brudny, V.; Mendoza, B. S.; Mochan, W. L. Second-harmonic generation from spherical particles. *Phys. Rev. B* **2000**, *62*, 11152.

[129] De Beer, A. G. F.; Roke, S. Sum frequency generation scattering from the interface of an isotropic particle: Geometrical and chiral effects. *Phys. Rev. B* **2007**, *75*, 245438.

[130] Dadap, J. I.; Shan, J.; Heinz, T. F. Theory of optical second-harmonic generation from a sphere of centrosymmetric material: small-particle limit. *J. Opt. Soc. Am. B* **2004**, *21*, 1328–1347.

[131] Dadap, J. I.; Shan, J.; Eisenthal, K. B.; Heinz, T. F. Second-Harmonic Rayleigh Scattering from a Sphere of Centrosymmetric Material. *Phys. Rev. Lett.* **1999**, *83*, 4045–4048.

Bibliography

[132]   Agarwal, G. S.; O'Neil, S. V. Effect of hydrodynamic dispersion of the metal on surface plasmons and surface-enhanced phenomena in spherical geometries. *Phys. Rev. B* **1983**, *28*, 487–493.

[133]   Dadap, J. I. Optical second-harmonic scattering from cylindrical particles. *Phys. Rev. B* **2008**, *78*, 205322.

[134]   Pavlyukh, Y.; Hübner, W. Nonlinear Mie scattering from spherical particles. *Phys. Rev. B* **2004**, *70*, 245434.

[135]   De Beer, A. G. F.; Roke, S. Nonlinear Mie theory for second-harmonic and sum-frequency scattering. *Phys. Rev. B* **2009**, *79*, 155420.

[136]   De Beer, A.; Kramer Campen, R.; Roke, S. Separating surface structure and surface charge with second-harmonic and sum-frequency scattering. *Phys. Rev. B* **2010**, *82*, 235431.

[137]   Ong, S.; Zhao, X.; Eisenthal, K. B. Polarization of Water Molecules at a Charged Interface: Second Harmonic Studies of the Silica/Water Interface. *Chem. Phys. Lett.* **1992**, *191*, 327–335.

[138]   Yan, E. C. Y.; Liu, Y.; Eisenthal, K. B. New Method for Determination of Surface Potential of Microscopic Particles by Second Harmonic Generation. *J. Phys. Chem. B* **1998**, *102*, 6331–6336.

[139]   Shan, J.; Dadap, J. I.; Stiopkin, I.; Reider, G. A.; Heinz, T. F. Experimental study of optical second-harmonic scattering from spherical nanoparticles. *Phys. Rev. A* **2006**, *73*, 023819.

[140]   Lütgebaucks, C.; Macias-Romero, C.; Roke, S. Characterization of the interface of binary mixed DOPC:DOPS liposomes in water: the impact of charge condensation. *J. Chem. Phys.* **2017**, *146*, 044701.

[141]   Chen, Y.; Roke et al., S. Zwitterionic and charged lipids form remarkably different structures on nanoscale oil droplets in aqueous solution. *Langmuir* **2018**, *34*, 1042–1050.

[142]   Sun, Q.; Xu, Y. Evaluation Intrinsic Photocatalytic Activities of Anatase and Rutile TiO_2 for Organic Degradation in Water. *J. Phys. Chem. C* **2010**, *114*, 18911–18918.

[143]   Suttiponparnit, K.; Biswas et al., P. Role of surface area, primary particle size, and crystal phase on titanium dioxide nanoparticle dispersion properties. *Nanoscale Res. Lett.* **2011**, *6*, 1–8.

[144]   Kosmulski, M. The significance of the difference in the point of zero charge between rutile and anatase. *Adv. Colloid Interface Sci.* **2002**, *99*, 255–264.

[145]   Lebrette, S.; Pagnoux, C.; Abelard, P. Stability of aqueous TiO_2 suspensions: influence of ethanol. *J. Colloid Inferface Sci.* **2004**, *280*, 400–408.

[146]   Barlow, S.; Marder, S. R. *Encyclopedia of Polymeric Nanomaterials*, Kobayashi, S., Müllen, K., Eds.; Springer: Berlin, Heidelberg, 2015.

[147]   Heinz, T. F.; Chen, C. K.; Ricard, D.; Shen, Y. R. Spectroscopy of Molecular Monolayers by Resonant Second-Harmonic Generation. *Phys. Rev. Lett.* **1982**, *48*, 478.

[148]   Ashkin, A.; Boyd, G.; Dziedzic, J. Resonant optical second harmonic generation and mixing. *IEEE J. Quantum Electron.* **1966**, *2*, 109–124.

[149]   De Beer, A. G. F.; Roke, S. Obtaining molecular orientation from second harmonic and sum frequency scattering experiments in water: Angular distribution and polarization dependence. *J. Chem. Phys.* **2010**, *132*, 234702.

[150]   Marchioro, A.; Bischoff, M.; Lütgebaucks, C.; Biriukov, D.; Předota, M.; Roke, S. Surface Characterization of Colloidal Silica Nanoparticles by Second Harmonic Scattering: Quantifying the Surface Potential and Interfacial Water Order. *J. Phys. Chem. C* **2019**, *123*, 20393–20404.

[151]   Bischoff, M.; Biriukov, D.; Předota, M.; Roke, S.; Marchioro, A. Surface Potential and Interfacial Water Order at the Amorphous TiO_2 Nanoparticle/Aqueous Interface. *J. Phys. Chem. C* **2020**, *124*, 10961–10974.

[152]   Bischoff, M.; Biriukov, D.; Předota, M.; Marchioro, A. Second Harmonic Scattering Reveals Ion-Specific Effects at the SiO_2 and TiO_2 Nanoparticle/Aqueous Interface. *J. Phys. Chem. C* **2021**, *125*, 25261–25274.

[153]   De Beer, A. G. F.; Roke, S. What interactions can distort the orientational distribution of interfacial water molecules as probed by second harmonic and sum frequency generation? *J. Chem. Phys.* **2016**, *145*, 044705.

[154]   Nihonyanagi, S.; Yamaguchi, S.; Tahara, T. Direct evidence for orientational flip-flop of water molecules at charged interfaces: A heterodyne-detected vibrational sum frequency generation study. *J. Chem. Phys.* **2009**, *130*, 204704.

[155]   Gubskaya, A. V.; Kusalik, P. G. The multipole polarizabilities and hyperpolarizabilities of the water molecule in liquid state: an ab initio study. *Mol. Phys.* **2001**, *99*, 1107–1120.

[156]   Hale, G. M.; Querry, M. R. Optical constants of water in the 200nm to 200μm wavelength region. *Appl. Opt.* **1973**, *12*, 555–563.

[157]   Martin, P Review of the filtered vacuum arc process and materials deposition. *Thin Solid Films* **2001**, *394*, 1–14.

[158]   Malitson, I. H. Interspecimen Comparison of the Refractive Index of Fused Silica. *J. Opt. Soc. Am.* **1965**, *55*, 1205–1209.

[159]   Austin, J.; Minelli, C.; Hamilton, D.; Wywijas, M.; Jankevics Jones, H. Nanoparticle number concentration measurements by multi-angle dynamic light scattering. *J. Nanopart. Res.* **2020**, *22*, 108.

[160]   Ohshima, H. A Simple Expression for Henry's Function for the Retardation Effect in Electrophoresis of Spherical Colloidal Particles. *J. Colloid Interface Sci.* **1994**, *168*, 269–271.

[161] Pullanchery, S.; Kulik, S.; Okur, H. I.; de Aguiar, H. B.; Roke, S. On the stability and necessary electrophoretic mobility of bare oil nanodroplets in water. *J. Chem. Phys.* **2020**, *152*, 241104.

[162] *Electrochemical dictionary*, 2nd ed.; Bard, A. J., Inzelt, G., Scholz, F., Eds.; Springer: Heidelberg, 2012.

[163] Lide, D. R., *Handbook of Chemistry and Physics*, 84th ed.; CRC Press: Boca Raton, 2004.

[164] *Colloidal Silica: Fundamentals and Applications*; Bergna, H. E., Roberts, W., Eds.; CRC Press: Boca Raton, 2005.

[165] *Electrochemical Methods: Fundamentals and Applications*; Bard, A. J., Faulkner, W. O., Eds.; Wiley: New York, 2000.

[166] Liu, S. H. Microscopically inhomogeneous nature of the Stern layer. *J. Electroanal. Chem. Interfacial Electrochem.* **1983**, *150*, 305–313.

[167] Halley, J. W.; Price, D. Quantum Theory of the Double Layer: Model Including Solvent Structure. *Phys. Rev. B: Condens. Matter Mater. Phys.* **1987**, *35*, 9095–9102.

[168] Weaver, M. J.; Wasileski, S. A. Influence of double-layer solvation on local versus macroscopic surface potentials on ordered platinum-group metals as sensed by the vibrational stark effect. *Langmuir* **2001**, *17*, 3039–3043.

[169] Wen, Y.-C.; Zha, S.; Liu, X.; Yang, S.; Guo, P.; Shi, G.; Fang, H.; Shen, Y. R.; Tian, C. Unveiling microscopic structures of charged water interfaces by surface-specific vibrational spectroscopy. *Phys. Rev. Lett.* **2016**, *116*, 016101.

[170] Lovering, K. A.; Bertram, A. K.; Chou, K. C. New Information on the Ion-Identity-Dependent Structure of Stern Layer Revealed by Sum Frequency Generation Vibrational Spectroscopy. *J. Phys. Chem. C* **2016**, *120*, 18099–18104.

[171] Lyklema, J. Molecular Interpretation of Electrokinetic Potentials. *Curr. Opin. Colloid Interface Sci.* **2010**, *15*, 125–130.

[172] Předota, M.; Machesky, M. L.; Wesolowski, D. J. Molecular Origins of the Zeta Potential. *Langmuir* **2016**, *32*, 10189–10198.

[173] Brkljača, Z.; Namjesnik, D.; Lützenkirchen, J.; Předota, M.; Preočănin, T. Quartz/Aqueous Electrolyte Solution Interface: Molecular Dynamic Simulation and Interfacial Potential Measurements. *J. Phys. Chem. C.* **2018**, *122*, 24025–24036.

[174] Scales, P. J.; Grieser, F.; Healy, T. W.; White, L. R.; Chan, D. Y. C. Electrokinetics of the Silica-Solution Interface: a Flat Plate Streaming Potential Study. *Langmuir* **1992**, *8*, 965–974.

[175] Jena, K. C.; Hore, D. K. Variation of Ionic Strength Reveals the Interfacial Water Structure at a Charged Mineral Surface. *J. Phys. Chem. C* **2009**, *113*, 15364–15372.

[176] Campen, R. K.; Pymer, A. K.; Nihonyanagi, S.; Borguet, E. Linking Surface Potential and Deprotonation in Nanoporous Silica: Second Harmonic Generation and Acid/Base Titration. *J. Phys. Chem. C* **2010**, *114*, 18465–18473.

[177]   Flores, S. C.; Kherb, J.; Konelick, N.; Chen, X.; Cremer, P. S. The Effects of Hofmeister Cations at Negatively Charged Hydrophilic Surfaces. *J. Phys. Chem. C* **2012**, *116*, 5730–5734.

[178]   Dewan, S.; Yeganeh, M. S.; Borguet, E. Experimental Correlation Between Interfacial Water Structure and Mineral Reactivity. *J. Phys. Chem. Lett.* **2013**, *4*, 1977–1982.

[179]   Covert, P. A.; Jena, K. C.; Hore, D. K. Throwing Salt Into the Mix: Altering Interfacial Water Structure by Electrolyte Addition. *J. Phys. Chem. Lett.* **2014**, *5*, 143–148.

[180]   Darlington, A. M.; Jarisz, T. A.; DeWalt-Kerian, E. L.; Roy, S.; Kim, S.; Azam, M. S.; Hore, D. K.; Gibbs, J. M. Separating the pH Dependent Behavior of Water in the Stern and Diffuse Layers with Varying Salt Concentration. *J. Phys. Chem. C* **2017**, *121*, 20229–20241.

[181]   DeWalt-Kerian, E. L.; Kim, S.; Azam, M. S.; Zeng, H.; Liu, Q.; Gibbs, J. M. pH-Dependent Inversion of Hofmeister Trends in the Water Structure of the Electrical Double Layer. *J. Phys. Chem. Lett.* **2017**, *8*, 2855–2861.

[182]   Boamah, M. D.; Ohno, P. E.; Geiger, F. M.; Eisenthal, K. B. Relative Permittivity in the Electrical Double Layer From Nonlinear Optics. *J. Chem. Phys.* **2018**, *148*, 222808.

[183]   Zhao, X.; Ong, S.; Eisenthal, K. B. Polarization of Water Molecules at a Charged Interface. Second Harmonic Studies of Charged Monolayers at the Air/Water Interface. *Chem. Phys. Lett.* **1993**, *202*, 513–520.

[184]   Zhao, X.; Ong, S.; Wang, H.; Eisenthal, K. B. New Method for Determination of Surface pKa Using Second Harmonic Generation. *Chem. Phys. Lett.* **1993**, *214*, 203–207.

[185]   Geiger, F. M. Second Harmonic Generation, Sum Frequency Generation, and $\chi^{(3)}$: Dissecting Environmental Interfaces with a Nonlinear Optical Swiss Army Knife. *Annu. Rev. Phys. Chem.* **2009**, *60*, 61–83.

[186]   Malin, J. N.; Holland, J. G.; Geiger, F. M. Free Energy Relationships in the Electric Double Layer and Alkali Earth Speciation. *J. Phys. Chem. C* **2009**, *113*, 17795–17802.

[187]   Azam, M. S.; Darlington, A.; Gibbs-Davis, J. M. The influence of concentration on specific ion effects at the silica/water interface. *J. Phys.: Condens. Matter* **2014**, *26*, 244107–244111.

[188]   Favaro, M.; Jeong, B.; Ross, P. N.; Yano, J.; Hussain, Z.; Liu, Z.; Crumlin, E. J. Unravelling the electrochemical double layer by direct probing of the solid/liquid interface. *Nat. Comm.* **2016**, *7*, 12695.

[189]   Leontyev, I.; Stuchebrukhov, A. Accounting for electronic polarization in non-polarizable force fields. *Phys. Chem. Chem. Phys.* **2011**, *13*, 2613–2626.

[190]   Biriukov, D.; Kroutil, O.; Předota, M. Modeling of solid-liquid interfaces using scaled charges: rutile (110) surfaces. *Phys. Chem. Chem. Phys.* **2018**, *20*, 23954–23966.

[191]   Kohagen, M.; Mason, P. E.; Jungwirth, P. Accounting for Electronic Polarization Effects in Aqueous Sodium Chloride via Molecular Dynamics Aided by Neutron Scattering. *J. Phys. Chem. B* **2016**, *120*, 1454–1460.

Bibliography

[192] Berendsen, H. J. C.; Grigera, J. R.; Straatsma, T. P. The missing term in effective pair potentials. *J. Phys. Chem.* **1987**, *91*, 6269–6271.

[193] Ohshima, H., *Theory of Colloid and Interfacial Electric Phenomena*; Interface Science and Technology, Vol. 12; Elsevier, Academic Press: Amsterdam, 2006.

[194] Abbas, Z.; Labbez, C.; Nordholm, S.; Ahlberg, E. Size-Dependent Surface Charging of Nanoparticles. *J. Phys. Chem. C* **2008**, *112*, 5715–5723.

[195] Hassanali, A. A.; J., S. S. Model for the Water-Amorphous Silica Interface: The Undissociated Surface. *J. Phys. Chem. B* **2007**, *111*, 11181–11193.

[196] Zhuravlev, L. T. Concentration of hydroxyl groups on the surface of amorphous silicas. *Langmuir* **1987**, *3*, 316–318.

[197] Kosmulski, M. Positive Electrokinetic Charge of Silica in the Presence of Chlorides. *J. Colloid Interface Sci.* **1998**, *208*, 543–545.

[198] Leroy, P.; N., D.; A., R.; M., B. Influence of Surface Conductivity on the Apparent Zeta Potential of Amorphous Silica Nanoparticles. *J. Colloid Interface Sci.* **2013**, *410*, 81–93.

[199] Bolt, G. H. Determination of the Charge Density of Silica Sols. *J. Phys. Chem.* **1957**, *61*, 1166–1169.

[200] Behrens, S. H.; Grier, D. G. The charge of glass and silica surfaces. *J. Chem. Phys.* **2001**, *115*, 6716.

[201] Yamanaka, J.; Hayashi, Y.; Ise, N.; Yamaguchi, T. Control of the surface charge density of colloidal silica by sodium hydroxide in salt-free and low-salt dispersions. *Phys. Rev. E: Stat. Phys., Plasmas, Fluids, Relat. Interdiscip. Top.* **1997**, *55*, 3028–3036.

[202] Dunstan, D. E. Temperature dependence of the electrokinetic properties of two disparate surfaces. *J. Colloid Interface Sci.* **1994**, *166*, 472–475.

[203] Darlington, A. M.; Gibbs, J. M. Bimodal or Trimodal? The Influence of Starting pH on Site Identity and Distribution at the Low Salt Aqueous/Silica Interface. *J. Phys. Chem. C* **2015**, *119*, 16560–16567.

[204] Brown, M. A.; Bossa, G. V.; May, S. Emergence of a Stern Layer From the Incorporation of Hydration Interactions Into the Gouy-Chapman Model of the Electrical Double Layer. *Langmuir* **2015**, *31*, 11477–11483.

[205] Sverjensky, D. A. Prediction of Surface Charge on Oxides in Salt Solutions: Revisions for 1:1 (M+L-) Electrolytes. *Geochim. Cosmochim. Acta* **2005**, *69*, 225–257.

[206] Sonnefeld, J. Determination of Surface Charge Density Constants for Spherical Silica Particles Using a Linear Transformation. *J. Colloid Interface Sci.* **1996**, *183*, 597–599.

[207] Barisik, M.; Atalay, S.; Beskok, A.; Qian, S. Size Dependent Surface Charge Properties of Silica Nanoparticles. *J. Phys. Chem. C* **2014**, *118*, 1836–1842.

[208] Shi, Y.-R.; Ye, M.-P.; Du, L.-C.; Weng, Y.-X. Experimental Determination of Particle Size-Dependent Surface Charge Density for Silica Nanospheres. *J. Phys. Chem. C* **2018**, *122*, 23764–23771.

[209] Vance, F. W.; Lemon, B. I.; Ekhoff, J. A.; Hupp, J. T. Interrogation of Nanoscale Silicon Dioxide/Water Interfaces via Hyper-Rayleigh Scattering. *J. Phys. Chem. B* **1998**, *102*, 1845–1848.

[210] Sulpizi, M.; Gaigeot, M.-P.; Sprik, M. The Silica-Water Interface: How the Silanols Determine the Surface Acidity and Modulate the Water Properties. *J. Chem. Theory. Comput.* **2012**, *8*, 1037–1047.

[211] Gongadze, E.; Petersen, S.; Beck, U.; van Rienen, U. Classical Models of the Interface Between an Electrode and an Electrolyte. *Proceedings of the COMSOL conference* **2009**.

[212] Memming, R., *Semiconductor Electrochemistry*, 2nd ed.; WILEY-VCH: Weinheim, 2015.

[213] Sharon, M., *An Introduction to the Physics and Electrochemistry of Semiconductors: Fundamentals and Applications*; Scrivener Publishing LLC, John Wiley & Sons, Inc.: Beverly, Hoboken, 2016.

[214] *Nanomaterial: Impacts on Cell Biology and Medicine*; Capco, D. G., Chen, Y., Eds.; Advances in Experimental Medicine and Biology; Springer: New York, 2014.

[215] *Application of Titanium Dioxide*; Janus, M., Ed.; InTech: Rijeka, 2017.

[216] Braun, J. H.; Baidins, A.; Marganski, R. E. TiO$_2$ pigment technology: a review. *Progress in Organic Coatings* **1992**, *20*, 105–138.

[217] Banerjee, A. N. The design, fabrication, and photocatalytic utility of nanostructured semiconductors: focus on TiO$_2$-based nanostructures. *Nanotechnol. Sci. Appl.* **2011**, *4*, 35–65.

[218] Fujishima, F TiO$_2$ photocatalysis fundamentals and applications. *A revolution in cleaning technology* **1999**, 14–21.

[219] *Application of Nanotechnology in Membranes for Water Treatment*, 1st ed.; Figoli, A., Hoinkis, J., Altinkaya, S. A., Bundschuh, J., Eds.; CRC Press: Boca Raton, 2017.

[220] Milošević, I.; Rtimi, S.; Jayaprakash, A.; van Driel, B.; Greenwood, B.; Aimable, A.; Senna, M.; Bowen, P. Synthesis and characterization of fluorinated anatase nanoparticles and subsequent N-doping for efficient visible light activated photocatalysis. *Colloids Surf. B: Biointerfaces* **2018**, *171*, 445–450.

[221] Náfrádi, B.; Náfrádi, G.; Martin-Hamka, C.; Forró, L.; Horváth, E. Superior Water Sheeting Effect on Photocatalytic Titania Nanowire Coated Glass. *Langmuir* **2017**, *33*, 9043–9049.

[222] *Application of titanium dioxide photocatalysis to construction materials: state-of-the-art report of the RILEM Technical Committee 194-TDP*; Ohama, Y., van Gemert, D., Eds.; RILEM state of the art reports; Springer: Dordrecht, 2011.

[223] *Photoelectrochemical hydrogen production*; van de Krol, R., Grätzel, M., Eds.; Electronic Materials: Science & Technology; Springer: New York, 2012.

[224] Bagotskiĭ, V. S.; Skundin, A. M.; Volfkovich, Y. V., *Electrochemical power sources: batteries, fuel cells, and supercapacitors*; John Wiley & Sons, Inc.: Hoboken, New Jersey, 2015.

Bibliography

[225] Ataka, K.-i.; Yotsuyanagi, T.; Osawa, M. Potential-Dependent Reorientation of Water Molecules at an Electrode/Electrolyte Interface Studied by Surface-Enhanced Infrared Absorption Spectroscopy. *J. Phys. Chem.* **1996**, *100*, 10664–10672.

[226] Bockris, J. O.; Khan, S. U. M., *Surface Electrochemistry: A Molecular Level Approach*; Springer Science & Business Media: Berlin, Heidelberg, 2013.

[227] Lange, E.; Miščenko, K. Zur Thermodynamik Der Ionensolvatation. *Ztg. für Phys. Chem. A* **1930**, *149*, 1–41.

[228] YazdanYar, A.; Aschauer, U.; Bowen, P. Interaction of biologically relevant ions and organic molecules with titanium oxide (rutile) surfaces: A review on molecular dynamics studies. *Colloids Surf. B: Biointerfaces* **2018**, *161*, 563–577.

[229] Gono, P.; Ambrosio, F.; Pasquarello, A. Effect of the Solvent on the Oxygen Evolution Reaction at the TiO_2–Water Interface. *J. Phys. Chem. C* **2019**, *123*, 18467–18474.

[230] Fedkin, M. V.; Zhou, X. Y.; Kubicki, J. D.; Bandura, A. V.; Lvov, S. N.; Machesky, M. L.; Wesolowski, D. J. High Temperature Microelectrophoresis Studies of the Rutile/Aqueous Solution Interface. *Langmuir* **2003**, *19*, 3797–3804.

[231] Makowski, M. J.; Galhenage, R. P.; Langford, J.; Hemminger, J. C. Liquid-Jet X-ray Photoelectron Spectra of TiO_2 Nanoparticles in an Aqueous Electrolyte Solution. *J. Phys. Chem. Lett.* **2016**, *7*, 1732–1735.

[232] Ali, H.; Seidel, R.; Bergmann, A.; Winter, B. Electronic structure of aqueous-phase anatase titanium dioxide nanoparticles probed by liquid jet photoelectron spectroscopy. *J. Mater. Chem. A* **2019**, *7*, 6665–6675.

[233] Zhang, Z.; Fenter, P.; Sturchio, N. C.; Bedzyk, M. J.; Machesky, M. L.; Wesolowski, D. J. Structure of rutile TiO_2 (110) in water and 1 molal Rb^+ at pH 12: Inter-relationship among surface charge, interfacial hydration structure, and substrate structural displacements. *Surf. Sci.* **2007**, *601*, 1129–1143.

[234] Tan, S.; Feng, H.; Zheng, Q.; Cui, X.; Zhao, J.; Luo, Y.; Yang, J.; Wang, B.; Hou, J. G. Interfacial Hydrogen-Bonding Dynamics in Surface-Facilitated Dehydrogenation.

[235] Zeta potential - An introduction in 30 minutes., 2015.

[236] Aschauer, U.; Burgos-Montes, O.; Moreno, R.; Bowen, P. Hamaker 2: A Toolkit for the Calculation of Particle Interactions and Suspension Stability and its Application to Mullite Synthesis by Colloidal Methods. *J. Dispers. Sci. Technol.* **2011**, *32*, 470–479.

[237] Beranek, R. (Photo)electrochemical Methods for the Determination of the Band Edge Positions of TiO_2 - Based Nanomaterials. *Adv. Phys. Chem.* **2011**, *2011*, 1–20.

[238] Alan, B. O.; Barisik, M.; Ozcelik, H. G. Roughness Effects on the Surface Charge Properties of Silica Nanoparticles. *J. Phys. Chem. C* **2020**, *124*, 7274–7286.

[239] Diebold, U. Perspective: A controversial benchmark system for water-oxide interfaces: H_2O/TiO_2 (110). *J. Chem. Phys.* **2017**, *147*, 040901.

[240] Diebold, U. The surface science of titanium dioxide. *Surf. Sci. Rep.* **2003**, *48*, 53–229.

[241] Bourikas, K.; Kordulis, C.; Lycourghiotis, A. Titanium Dioxide (Anatase and Rutile): Surface Chemistry, Liquid–Solid Interface Chemistry, and Scientific Synthesis of Supported Catalysts. *Chem. Rev.* **2014**, *114*, 9754–9823.

[242] Mueller, R.; Kammler, H. K.; Wegner, K.; Pratsinis, S. E. OH Surface Density of SiO_2 and TiO_2 by Thermogravimetric Analysis. *Langmuir* **2003**, *19*, 160–165.

[243] Karlsson, M.; Craven, C.; Dove, P. M.; Casey, W. H. Surface Charge Concentrations on Silica in Different 1.0 M Metal-Chloride Background Electrolytes and Implications for Dissolution Rates. *Aquat. Geochem.* **2001**, *7*, 13–32.

[244] Abendroth, R. P Behavior of a Pyrogenic Silica in Simple Electrolytes. *J. Colloid Interface Sci.* **1970**, *34*, 591–596.

[245] Kitamura, A.; Fujiwara, K.; Yamamoto, T.; Nishikawa, S.; Moriyama, H. Analysis of Adsorption Behavior of Cations onto Quartz Surface by Electrical Double-layer Model. *J. Nucl. Sci. Technol.* **1999**, *36*, 1167–1175.

[246] Tadros, T. F.; Lyklema, J. The electrical double layer on silica in the presence of bivalent counter-ions. *J Electroanal. Chem. Interfacial Electrochem.* **1969**, *22*, 1–7.

[247] Dove, P. M.; Craven, C. M. Surface charge density on silica in alkali and alkaline earth chloride electrolyte solutions. *Geochim. Cosmochim. Acta* **2005**, *69*, 4963–4970.

[248] Yates, D. E.; Healy, T. W. Titanium dioxide–electrolyte interface. Part 2. – Surface charge (titration) studies. *J. Chem. Soci. Faraday Trans. 1: Phys. Chem. Condens. Phases* **1980**, *76*, 9–18.

[249] Ridley, M.; Machesky, M.; Wesolowski, D.; Palmer, D. Calcium adsorption at the rutile-water interface: A potentiometric study in NaCl media to 250°C. *Geochim. Cosmochim. Acta* **1999**, *63*, 3087–3096.

[250] Ridley, M. K.; Hackley, V. A.; Machesky, M. L. Characterization and Surface-Reactivity of Nanocrystalline Anatase in Aqueous Solutions. *Langmuir* **2006**, *22*, 10972–10982.

[251] Machesky, M.; Wesolowski, D.; Rosenqvist, J.; Předota, M.; Vlcek, L.; Ridley, M.; Kohli, V.; Zhang, Z.; Fenter, P.; Cummings, P.; Lvov, S.; Fedkin, M.; Rodriguez-Santiago, V.; Kubicki, J.; Bandura, A. Comparison of Cation Adsorption by Isostructural Rutile and Cassiterite. *Langmuir* **2011**, *27*, 4585–4593.

[252] Wesolowski, D. J.; Machesky, M. L.; Ridley, M. K.; Palmer, D. A.; Zhang, Z.; Fenter, P. A.; Předota, M.; Cummings, P. T. Ion Adsorption on Metal Oxide Surfaces to Hydrothermal Conditions. *ECS Trans.* **2008**, *11*, 167–180.

[253] Jang, H. M.; Fuerstenau, D. W. The specific adsorption of alkaline-earth cations at the rutile/water interface. *Colloids Surf.* **1986**, *21*, 235–257.

[254] Franks, G. V. Zeta Potentials and Yield Stresses of Silica Suspensions in Concentrated Monovalent Electrolytes: Isoelectric Point Shift and Additional Attraction. *J. Colloid Interface Sci.* **2002**, *249*, 44–51.

[255] Kataoka, S.; Gurau, M. C.; Albertorio, F.; Holden, M. A.; Lim, S.-M.; Yang, R. D.; Cremer, P. S. Investigation of Water Structure at the TiO$_2$/Aqueous Interface. *Langmuir* **2004**, *20*, 1662–1666.

[256] Schaefer, J.; Backus, E. H. G.; Bonn, M. Evidence for auto-catalytic mineral dissolution from surface-specific vibrational spectroscopy. *Nat. Commun.* **2018**, *9*, 3316.

[257] Rehl, B.; Rashwan, M.; DeWalt-Kerian, E. L.; Jarisz, T. A.; Darlington, A. M.; Hore, D. K.; Gibbs, J. M. New Insights into $\chi^{(3)}$ Measurements: Comparing Nonresonant Second Harmonic Generation and Resonant Sum Frequency Generation at the Silica/Aqueous Electrolyte Interface. *J. Phys. Chem. C* **2019**, *123*, 10991–11000.

[258] Azam, M. S.; Weeraman, C. N.; Gibbs-Davis, J. M. Specific Cation Effects on the Bimodal Acid-Base Behavior of the Silica/Water Interface. *J. Phys. Chem. Lett.* **2012**, *3*, 1269–1274.

[259] Boamah, M. D.; Ohno, P. E.; Lozier, E.; Van Ardenne, J.; Geiger, F. M. Specifics about Specific Ion Adsorption from Heterodyne-Detected Second Harmonic Generation. *J. Phys. Chem. B* **2019**, *123*, 5848–5856.

[260] Biriukov, D.; Fibich, P.; Předota, M. Zeta Potential Determination from Molecular Simulations. *J. Phys. Chem. C* **2020**, *124*, 3159–3170.

[261] Bouhadja, M.; Skelton, A. A. Dynamical Properties of Water and Ions at the Quartz (101)-Water Interface at a Range of Solution Conditions: A Classical Molecular Dynamics Study. *J. Phys. Chem. C* **2018**, *122*, 1535–1546.

[262] Quezada, G. R.; Rozas, R. E.; Toledo, P. G. Molecular Dynamics Simulations of Quartz (101)-Water and Corundum (001)-Water Interfaces: Effect of Surface Charge and Ions on Cation Adsorption, Water Orientation, and Surface Charge Reversal. *J. Phys. Chem. C* **2017**, *121*, 25271–25282.

[263] Dewan, S.; Carnevale, V.; Bankura, A.; Eftekhari-Bafrooei, A.; Fiorin, G.; Klein, M. L.; Borguet, E. Structure of Water at Charged Interfaces: A Molecular Dynamics Study. *Langmuir* **2014**, *30*, 8056–8065.

[264] DelloStritto, M. J.; Kubicki, J. D.; Sofo, J. O. Effect of Ions on H-Bond Structure and Dynamics at the Quartz (101)–Water Interface. *Langmuir* **2016**, *32*, 11353–11365.

[265] Předota, M.; Zhang, Z.; Fenter, P.; Wesolowski, D. J.; Cummings, P. T. Electric Double Layer at the Rutile (110) Surface. 2. Adsorption of Ions from Molecular Dynamics and X-ray Experiments. *J. Phys. Chem. B* **2004**, *108*, 12061–12072.

[266] Zhang, Z. et al. Ion Adsorption at the Rutile-Water Interface: Linking Molecular and Macroscopic Properties. *Langmuir* **2004**, *20*, 4954–4969.

[267] Hiemstra, T.; Van Riemsdijk, W. H. On the relationship between charge distribution, surface hydration, and the structure of the interface of metal hydroxides. *J. Colloid Interface Sci.* **2006**, *301*, 1–18.

[268] Pfeiffer-Laplaud, M.; Gaigeot, M.-P. Electrolytes at the Hydroxylated (0001) α-Quartz/Water Interface: Location and Structural Effects on Interfacial Silanols by DFT-Based MD. *J. Phys. Chem. C* **2016**, *120*, 14034–14047.

[269] Pfeiffer-Laplaud, M.; Gaigeot, M.-P.; Sulpizi, M. pKa at Quartz/Electrolyte Interfaces. *J. Phys. Chem. Lett.* **2016**, *7*, 3229–3234.

[270] Martinek, T.; Duboué-Dijon, E.; Timr, S.; Mason, P. E.; Baxová, K.; Fischer, H. E.; Schmidt, B.; Pluhařová, E.; Jungwirth, P. Calcium ions in aqueous solutions: Accurate force field description aided by ab initio molecular dynamics and neutron scattering. *J. Chem. Phys.* **2018**, *148*, 222813.

[271] Ma, E.; Ohno, P. E.; Kim, J.; Liu, Y.; Lozier, E. H.; Miller, T. F.; Wang, H.-F.; Geiger, F. M. A New Imaginary Term in the Second-Order Nonlinear Susceptibility from Charged Interfaces. *J. Phys. Chem. Lett.* **2021**, *12*, 5649–5659.

[272] Diot, J. L.; Joseph, J.; Martin, J. R.; Clechet, P. pH dependence of the Si/SiO$_2$ interface state density for EOS systems: Quasi-static and AC conductance methods. *J. Electroanal. Chem. Interfacial Electrochem.* **1985**, *193*, 75–88.

[273] Siu, W.; Cobbold, R. Basic properties of the electrolyte–SiO$_2$–Si system: Physical and theoretical aspects. *IEEE Trans. on Electron Devices* **1979**, *26*, 1805–1815.

[274] Zdrali, E.; Chen, Y.; Okur, H. I.; Wilkins, D. M.; Roke, S. The Molecular Mechanism of Nanodroplet Stability. *ACS Nano* **2017**, *11*, 12111–12120.

[275] Cimas, A.; Tielens, F.; Sulpizi, M.; Gaigeot, M.-P.; Costa, D. The amorphous silica–liquid water interface studied by ab initio molecular dynamics (AIMD): local organization in global disorder. *J. Phys. Condens. Matter* **2014**, *26*, 244106.

[276] Tuladhar, A.; Dewan, S.; Pezzotti, S.; Brigiano, F. S.; Creazzo, F.; Gaigeot, M.-P.; Borguet, E. Ions Tune Interfacial Water Structure and Modulate Hydrophobic Interactions at Silica Surfaces. *J. Am. Chem. Soc.* **2020**, *142*, 6991–7000.

[277] Kubicki, J. D.; Sofo, J. O.; Skelton, A. A.; Bandura, A. V. A New Hypothesis for the Dissolution Mechanism of Silicates. *J. Phys. Chem. C* **2012**, *116*, 17479–17491.

[278] DelloStritto, M. J.; Kubicki, J.; Sofo, J. O. Density functional theory simulation of hydrogen-bonding structure and vibrational densities of states at the quartz (101)-water interface and its relation to dissolution as a function of solution pH and ionic strength. *J. Phys. Condens. Matter Inst. Phys. J.* **2014**, *26*, 244101.

[279] Marcus, Y. Ionic radii in aqueous solutions. *Chem. Rev.* **1988**, *88*, 1475–1498.

[280] Zeron, I. M.; Abascal, J. L. F.; Vega, C. A force field of Li$^+$, Na$^+$, K$^+$, Mg^{2+}, Ca^{2+}, Cl$^-$, and SO$_4^{2-}$ in aqueous solution based on the TIP4P/2005 water model and scaled charges for the ions. *J. Chem. Phys.* **2019**, *151*, 134504.

[281] Porus, M.; Labbez, C.; Maroni, P.; Borkovec, M. Adsorption of monovalent and divalent cations on planar water-silica interfaces studied by optical reflectivity and Monte Carlo simulations. *J. Chem. Phys.* **2011**, *135*, 064701.

[282] Marcus, Y. Thermodynamics of solvation of ions. Part 5. – Gibbs free energy of hydration at 298.15 K. *J. Chem. Soc., Faraday Trans.* **1991**, *87*, 2995–2999.

[283] Lee, Y.; Thirumalai, D.; Hyeon, C. Ultrasensitivity of Water Exchange Kinetics to the Size of Metal Ion. *J. Am. Chem. Soc.* **2017**, *139*, 12334–12337.

[284] Argyris, D.; Cole, D. R.; Striolo, A. Dynamic Behavior of Interfacial Water at the Silica Surface. *J. Phys. Chem. C* **2009**, *113*, 19591–19600.

[285] Asay, D. B.; Kim, S. H. Evolution of the Adsorbed Water Layer Structure on Silicon Oxide at Room Temperature. *J. Phys. Chem. B* **2005**, *109*, 16760–16763.

[286] Du, Q.; Freysz, E.; Shen, Y. R. Surface vibrational spectroscopic studies of hydrogen bonding and hydrophobicity. *Science* **1994**, *264*, 826–828.

[287] Ostroverkhov, V.; Waychunas, G. A.; Shen, Y. R. New Information on Water Interfacial Structure Revealed by Phase-Sensitive Surface Spectroscopy. *Phys. Rev. Lett.* **2005**, *94*, 046102.

[288] Du, Q.; Freysz, E.; Shen, Y. R. Vibrational spectra of water molecules at quartz/water interfaces. *Phys. Rev. Lett.* **1994**, *72*, 238–241.

[289] Shirai, K.; Sugimoto, T.; Watanabe, K.; Haruta, M.; Kurata, H.; Matsumoto, Y. Effect of Water Adsorption on Carrier Trapping Dynamics at the Surface of Anatase TiO_2 Nanoparticles. *Nano Lett.* **2016**, *16*, 1323–1327.

[290] Hosseinpour, S.; Tang, F.; Wang, F.; Livingstone, R. A.; Schlegel, S. J.; Ohto, T.; Bonn, M.; Nagata, Y.; Backus, E. H. G. Chemisorbed and Physisorbed Water at the TiO_2/Water Interface. *J. Phys. Chem. Lett.* **2017**, *8*, 2195–2199.

[291] Soria, F. A.; Valentin, C. D. Reactive molecular dynamics simulations of hydration shells surrounding spherical TiO_2 nanoparticles: implications for proton-transfer reactions. *Nanoscale* **2021**, *13*, 4151–4166.

[292] Zhou, G.; Liu, C.; Huang, L. Molecular Dynamics Simulation of First-Adsorbed Water Layer at Titanium Dioxide Surfaces. *J. Chem. Eng. Data* **2018**, *63*, 2420–2429.

[293] Zhao, Z.; Li, Z.; Zou, Z. Structure and Properties of Water on the Anatase TiO_2 (101) Surface: From Single-Molecule Adsorption to Interface Formation. *J. Phys. Chem. C* **2012**, *116*, 11054–11061.

[294] Žerjav, G.; Pintar, A.; Ferentz, M.; Landau, M.; Haimovich, A.; Goldbourt, A.; Herskowitz, M. Effect of Surface Chemistry and Crystallographic Parameters of TiO_2 Anatase Nanocrystals on Photocatalytic Degradation of Bisphenol A. *Catalysts* **2019**, *9*, 447.

[295] Martra, G. Lewis acid and base sites at the surface of microcrystalline TiO_2 anatase: relationships between surface morphology and chemical behaviour. *Appl. Catal. A: Gen.* **2000**, *200*, 275–285.

[296] Schindler, P. W.; Gamsjäger, H. Acid-base reactions of the TiO_2 (Anatase) - water interface and the point of zero charge of TiO_2 suspensions. *Kolloid Z. Z. Polym.* **1972**, *250*, 759–763.

[297] Preočanin, T.; Kallay, N. Point of Zero Charge and Surface Charge Density of TiO_2 in Aqueous Electrolyte Solution as Obtained by Potentiometric Mass Titration. *Croat. Chem. Acta* **2006**, *79*, 95–106.

[298] Lyon, L. A.; Hupp, J. T. Energetics of the Nanocrystalline Titanium Dioxide/Aqueous Solution Interface: Approximate Conduction Band Edge Variations between $H_0 = -10$ and $H_- = +26$. *J. Phys. Chem. B* **1999**, *103*, 4623–4628.

[299] Hiemstra, T.; Venema, P.; Riemsdijk, W. H. V. Intrinsic Proton Affinity of Reactive Surface Groups of Metal (Hydr)oxides: The Bond Valence Principle. *J. Colloid Interface Sci.* **1996**, *184*, 680–692.

[300] Cheng, J.; Sprik, M. Acidity of the Aqueous Rutile TiO_2 (110) Surface from Density Functional Theory Based Molecular Dynamics. *J. Chem. Theory Comput.* **2010**, *6*, 880–889.

[301] Cheng, J.; Liu, X.; VandeVondele, J.; Sprik, M. Reductive Hydrogenation of the Aqueous Rutile TiO_2 (110) Surface. *Electrochim. Acta* **2015**, *179*, 658–667.

[302] Hoffmann, M. R.; Martin, S. T.; Choi, W.; Bahnemann, D. W. Environmental Applications of Semiconductor Photocatalysis. *Chem. Rev.* **1995**, *95*, 69–96.

[303] Kim, N. Y.; Lee, H. K.; Moon, J. T.; Joo, J. B. Synthesis of Spherical TiO_2 Particles with Disordered Rutile Surface for Photocatalytic Hydrogen Production. *Catalysts* **2019**, *9*, 491.

[304] Aimable, A.; Bowen, P. Nanopowder metrology and nanoparticle size measurement - Towards the development and testing of protocols. *J. Dispers. Sci. Technol.* **2010**, *4*, 157–166.

[305] Bowen, P. Particle Size Distribution Measurement from Millimeters to Nanometers and from Rods to Platelets. *J. Dispers. Sci. Technol.* **2002**, *23*, 631–662.

[306] Herrmann, M.; Boehm, H. Über die Chemie der Oberfläche des Titandioxids. II. Saure Hydroxylgruppen auf der Oberfläche. *Z. Anorg. Allg. Chem* **1969**, *368*, 73–86.

[307] Barringer, E. A.; Bowen, H. K. High-purity, monodisperse TiO_2 powders by hydrolysis of titanium tetraethoxide. 1. Synthesis and physical properties. *Langmuir* **1985**, *1*, 414–420.

[308] James, R. O.; Parks, G. A. *Surface and Colloid Science*, Matijević, E., Ed.; Springer US: Boston, MA, 1982.

[309] Wehrli, B. Vanadium in der Hydrosphäre: Oberflächenkomplexe und Oxidationskinetik., Ph.D. Thesis, ETH Zürich, 1987.

[310] Kormann, C.; Bahnemann, D. W.; Hoffmann, M. R. Photolysis of Chloroform and Other Organic Molecules in Aqueous TiO_2 suspensions. *Environ. Sci. Technol.* **1991**, *25*, 494–500.

[311] Noh, J. S.; Schwarz, J. A. Estimation of the point of zero charge of simple oxides by mass titration. *J. Colloid Interface Sci.* **1989**, *130*, 157–164.

[312]   Kormann, C.; Bahnemann, D. W.; Hoffmann, M. R. Preparation and characterization of quantum-size titanium dioxide. *J. Phys. Chem.* **1988**, *92*, 5196–5201.

[313]   Kosmulski, M., *Surface Charging and Points of Zero Charge*; CRC Press: Boca Raton, 2009.

[314]   Reijenga, J.; van Hoof, A.; van Loon, A.; Teunissen, B. Development of Methods for the Determination of pKa Values. *Anal. Chem. Insights* **2013**, *8*, 53–71.

[315]   Ma, J.; S., M.; Bronsther, C.; Gao, Z.; Eisenthal, K. B. Second harmonic study of acid-base equilibrium at gold nanoparticle/aqueous interface. *Chem. Phys. Lett.* **2017**, *683*, 166–171.

[316]   Eisenthal, K. B. Equilibrium and Dynamic Processes at Interfaces by Second Harmonic and Sum Frequency Generation. *Annu. Rev. Phys. Chem.* **1992**, *43*, 627–661.

[317]   Gibbs-Davis, J. M.; Kruk, J. J.; Konek Christopher, T.; Scheidt, K. A.; Geiger, F. M. Jammed Acid-Base Reactions at Interfaces. *J. Am. Chem. Soc.* **2008**, *130*, 15444–15447.

[318]   Azam, M. S.; Weeraman, C. N.; Gibbs-Davis, J. M. Halide-Induced Cooperative Acid-Base Behavior at a Negatively Charged Interface. *J. Phys. Chem. C* **2013**, *117*, 8840–8850.

[319]   Dalstein, L.; Potapova, E.; Tyrode, E. The elusive silica/water interface: isolated silanols under water as revealed by vibrational sum frequency spectroscopy. *Phys. Chem. Chem. Phys.* **2017**, *19*, 10343–10349.

[320]   Cai, C.; Azam, M. S.; Hore, D. K. Determining the Surface Potential of Charged Aqueous Interfaces Using Nonlinear Optical Methods. *J. Phys. Chem. C* **2021**, *125*, 25307–25315.

[321]   Henderson, M. A. A surface science perspective on TiO_2 photocatalysis. *Surf. Sci. Rep.* **2011**, *66*, 185–297.

[322]   Lindström, H.; Södergren, S.; Solbrand, A.; Rensmo, H.; Hjelm, J.; Hagfeldt, A.; Lindquist, S.-E. Li^+ Ion Insertion in TiO_2 (Anatase). 2. Voltammetry on Nanoporous Films. *J. Phys. Chem. B* **1997**, *101*, 7717–7722.

[323]   Södergren, S.; Siegbahn, H.; Rensmo, H.; Lindström, H.; Hagfeldt, A.; Lindquist, S.-E. Lithium Intercalation in Nanoporous Anatase TiO_2 Studied with XPS. *J. Phys. Chem. B* **1997**, *101*, 3087–3090.

[324]   Hagfeldt, A.; Vlachopoulos, N.; Grätzel, M. Fast Electrochromic Switching with Nanocrystalline Oxide Semiconductor Films. *J. Electrochem. Soc.* **1994**, *141*, 82–84.

[325]   Dahlman, C. J.; Heo, S.; Zhang, Y.; Reimnitz, L. C.; He, D.; Tang, M.; Milliron, D. J. Dynamics of Lithium Insertion in Electrochromic Titanium Dioxide Nanocrystal Ensembles. *J. Am. Chem. Soc.* **2021**, *143*, 8278–8294.

[326]   Yuwono, J. A.; Burr, P.; Galvin, C.; Lennon, A. Atomistic Insights into Lithium Storage Mechanisms in Anatase, Rutile, and Amorphous TiO_2 Electrodes. *ACS Appl. Mater. Interfaces* **2021**, *13*, 1791–1806.

[327] Scrosati, B.; Garche, J. Lithium batteries: Status, prospects and future. *J. Power Sources* **2010**, *195*, 2419–2430.

[328] Lee, D.-H.; Lee, B.-H.; Sinha, A. K.; Park, J.-H.; Kim, M.-S.; Park, J.; Shin, H.; Lee, K.-S.; Sung, Y.-E.; Hyeon, T. Engineering Titanium Dioxide Nanostructures for Enhanced Lithium-Ion Storage. *J. Am. Chem. Soc.* **2018**, *140*, 16676–16684.

[329] Aravindan, V.; Lee, Y.-S.; Yazami, R.; Madhavi, S. TiO$_2$ polymorphs in 'rocking-chair' Li-ion batteries. *Materials Today* **2015**, *18*, 345–351.

[330] Wu, S.; Weng, Z.; Liu, X.; Yeung, K. W. K.; Chu, P. K. Functionalized TiO$_2$ Based Nanomaterials for Biomedical Applications. *Adv. Funct. Mater.* **2014**, *24*, 5464–5481.

[331] Rashid, M. M.; Simončič, B.; Tomšič, B. Recent advances in TiO$_2$-functionalized textile surfaces. *Surf. Interfaces* **2021**, *22*, 100890.

[332] Kronik, L.; Shapira, Y. Surface photovoltage phenomena: theory, experiment, and applications. *Surf. Sci. Rep.* **1999**, *37*, 1–206.

[333] Shei, S.-C. Optical and Structural Properties of Titanium Dioxide Films from and Starting Materials Annealed at Various Temperatures. *Adv. Mater. Sci. Eng.* **2013**, *2013*, 545076.

[334] Demirörs, A. F.; Jannasch, A.; van Oostrum, P. D. J.; Schäffer, E.; Imhof, A.; van Blaaderen, A. Seeded Growth of Titania Colloids with Refractive Index Tunability and Fluorophore-Free Luminescence. *Langmuir* **2011**, *27*, 1626–1634.

[335] Chen, X.; Mao, S. S. Titanium Dioxide Nanomaterials: Synthesis, Properties, Modifications, and Applications. *Chem. Rev.* **2007**, *107*, 2891–2959.

[336] Zhang, H.; Banfield, J. F. Size Dependence of the Kinetic Rate Constant for Phase Transformation in TiO$_2$ Nanoparticles. *Chem. Mater.* **2005**, *17*, 3421–3425.

[337] Zhang, H.; Finnegan, M.; Banfield, J. F. Preparing Single-Phase Nanocrystalline Anatase from Amorphous Titania with Particle Sizes Tailored by Temperature. *Nano Lett.* **2001**, *1*, 81–85.

[338] Ota, M.; Dwijaya, B.; Hirota, Y.; Uchida, Y.; Tanaka, S.; Nishiyama, N. Synthesis of Amorphous TiO$_2$ Nanoparticles with a High Surface Area and Their Transformation to Li$_4$Ti$_5$O$_{12}$ Nanoparticles. *Chem. Lett.* **2016**, *45*, 1285–1287.

[339] Shin, H.; Jung, H. S.; Hong, K. S.; Lee, J.-K. Crystal phase evolution of TiO$_2$ nanoparticles with reaction time in acidic solutions studied via freeze-drying method. *J. Solid State Chem.* **2005**, *178*, 15–21.

[340] Wang, Y.; Ma, C.; Sun, X.; Li, H. Synthesis and characterization of amorphous TiO$_2$ with wormhole-like framework mesostructure. *J. Non-Cryst. Solids* **2003**, *319*, 109–116.

[341] Moon, J. T.; Lee, S. K.; Joo, J. B. Controllable one-pot synthesis of uniform colloidal TiO$_2$ particles in a mixed solvent solution for photocatalysis. *Beilstein J. Nanotechnol.* **2018**, *9*, 1715–1727.

Bibliography

[342] Poluboyarinov, A. S.; Chelpanov, V. I.; Lebedev, V. A.; Kozlov, D. A.; Khazova, K. M.; Volkov, D. S.; Kolesnik, I. V.; Garshev, A. V. Titanium Oxide Microspheres with Tunable Size and Phase Composition. *Materials* **2019**, *12*, 1472.

[343] Kronik, L.; Shapira, Y. Surface photovoltage spectroscopy of semiconductor structures: at the crossroads of physics, chemistry and electrical engineeing. *Surf. Interface Anal.* **2001**, *31*, 954–965.

List of Acronyms

AFM	atomic force microscopy
AR-SHS	angle-resolved second harmonic scattering
CC	constant capacitor
DL	diffuse layer
DLS	dynamic light scattering
ECC	electronic continuum correction
EDL	electrical double layer
EDX	energy dispersive X-ray analysis
ES	energy state
GC	Gouy-Chapman
GCS	Gouy-Chapman-Stern
GS	groundstate
HER	hydrogen evolution reaction
HRS	hyper-Rayleigh scattering
IEP	isoelectric point
IHP	inner Helmholtz plane
KPFM	Kelvin probe force microscopy
MADLS	multi-angle dynamic light scattering
MD	molecular dynamics
NIR	near-infrared
NLM	nonlinear Mie-theory
OER	oxygen evolution reaction
OHP	outer Helmholtz plane
P	parallel
PDI	polydispersity index
PEC	photoelectrochemical cell
PMT	photomultiplier tube
PZC	point of zero charge
RGD	Rayleigh-Gans-Debye
S	perpendicular
SFG	sum-frequency generation
SH	second harmonic
SHG	second harmonic generation
SHS	second harmonic scattering
TEM	transmission electron microscopy
UV	ultra-violet
VS	virtual state
XPS	X-ray photoelectron spectroscopy
XRD	X-ray diffraction

Curriculum Vitae

Personal data

Name	Marie Bischoff (née Mende)
Date and place of birth	13.12.1990 in Pirna, Germany
Citizenship	German

Education

2017 – 2022	**Ph.D. in Materials Science and Engineering**,
	École polytechnique fédérale de Lausanne (EPFL), Switzerland
	Laboratory for Fundamental BioPhotonics, Ambizione project
2013 – 2017	**M.Sc. in Physics**, Friedrich-Schiller-Universität Jena, Germany
	Master thesis in Ion Beam Physics:
	Ionenstrahlanalyse von BiVO$_4$-Einkristallen und BiVO$_4$-Dünnschichten
2013 – 2014	**Study abroad with Erasmus**, Université Joseph Fourier Grenoble, France
2010 – 2013	**B.Sc. in Physics**, Friedrich-Schiller-Universität Jena, Germany
	Bachelor thesis in Medical Physics:
	Einfluss der experimentellen Designfunktion funktioneller MRT-Aufnahmen
	bei segmentierter k-Raumaquisition
2001 – 2010	**Abitur** at Wigbertgymnasium Hünfeld, Germany
2007	**Exchange Student** at Lycée Joliot Curie Aubagne, France

Extracurricular activities

Fix the Leaky Pipeline (FLP) Peer-Mentoring Group
Career-building program for women in science
07/2021 - 07/2022   Peer-Mentoring Group Member

EPFL Photonics Chapter (EPC)
Association promoting Optics and Photonics on Campus
02/2018 - 02/2022   Committee Member - Treasurer - Vice-President - Senior Committee Member

Honours and Awards related to this thesis

07/05/2021   **2021 Chemistry Travel Award**
by Swiss Academy of Science (SCNAT) and Swiss Chemical Society (SCS) for
2022 Electrochemistry Gordon Research Conference and Seminar, Ventura, USA

12/11/2020   **IBI Lebowska Award** at virtual EPFL BioEngineering Day, Lausanne, Switzerland
for contribution to the general good of the institute

22/06/2020   **Best Student Presentation Award** at the virtual TSRC Workshop on
Interfacial Molecular and Electronic Structure and Dynamics, Telluride, USA

29/11/2019   **Best Poster Presentation Award** at EDMX Research day, Lausanne, Switzerland

13-19/09/2019   **Optical Society** (Optica, formerly OSA) **travel grant** for student leadership conference
and Frontiers in Optics and Laser Science, Washington DC, USA

06/09/2019   **Best Poster Presentation Award** as Runner-Up in the Session Physical Chemistry
at the SCS Fall Meeting, Zürich, Switzerland

Publications related to this thesis

- **Bischoff, M.**; Kim, N. Y.; Joo J. B.; Marchioro, A. Interfacial water orientation uncovers surface pK_as at the anatase TiO_2 Nanoparticle/Aqueous Interface. *in preparation*

- **Bischoff, M.**; Biriukov, D.; Předota, M.; Marchioro, A. Second Harmonic Scattering Reveals Ion-Specific Effects at the SiO_2 and TiO_2 Nanoparticle/Aqueous Interface. *J. Phys. Chem. C,* **2021**, *125*, 25261-25274

- **Bischoff, M.**; Biriukov, D.; Předota, M.; Roke, S.; Marchioro, A. Surface Potential and Interfacial Water Order at the Amorphous TiO_2 Nanoparticle/Aqueous Interface. *J. Phys. Chem. C,* **2020**, *124*, 10961-10974

- **Bischoff, M.**; Marchioro, A.; Roke, S. Probing Surface Properties of Colloidal Nanoparticles in Aqueous Environments by Second Harmonic Scattering. *Frontiers in Optics + Laser Science APS/DLS,* The Optical Society, **2019**, JW4A.119

- Marchioro, A.; **Bischoff, M.**; Lütgebaucks, C.; Biriukov, D.; Předota, M.; Roke, S. Surface Characterization of Colloidal Silica Nanoparticles by Second Harmonic Scattering: Quantifying the Surface Potential and Interfacial Water Order. *J. Phys. Chem. C,* **2019**, *123*, 20393-20404

Other publications

- Wendler, E.; **Bischoff, M.**; Schmidt, E.; Schrempel, F.; Ellmer, K.; Kanis, M.; van de Krol, R. Ion beam modification of single crystalline $BiVO_4$. *Nucl. Instrum. Methods Phys. Res. B: Beam Interact. Mater. At.,* **2017**, *409*, 133-137

Summer schools, national and international conferences

19/08/2018 - 23/08/2018	LightChECSS Summer School, Les Diablerets, Switzerland
07/09/2018	SCS Fall Meeting, Lausanne, Switzerland
06/11/2018	EDMX Reserach Day, Lausanne, Switzerland
10/12/2018	Photonics Day, Lausanne Switzerland
29/02/2019	Lacus Day, Lausanne, Switzerland
31/03/2019 - 05/04/2019	DPG Spring Meeting of Condensed Matter Section, Regensburg, Germany
03/06/2019 - 09/06/2019	GraFOx Summer School on Oxide Semiconductors for Smart Electronic Devices, Menaggio, Italy
06/09/2019	SCS Fall Meeting, Zürich, Switzerland
13/09/2019 - 19/09/2019	Student Leadership Conference and Frontiers in Optics and Laser Sciences, Washington DC USA (Travel Grant from Optica (formerly OSA))
04/11/2019 - 08/11/2019	nanoGe Fall Meeting, Berlin Germany
27/11/2019	BioEngineering Day, Lausanne Switzerland
29/11/2019	EDMX Research Day, Lausanne Switzerland
06/12/2019	Photonics Day, Neuchatel, Switzerland
01/06/2020 - 14/08/2010	Telluride Science Summer Lecture Series, online
15/06/2020 - 22/06/2020	Telluride Science and Research Center (TSRC) Workshop on Interfacial Molecular and Electronic Structure and Dynamics 2020, online
25/08/2020	SCS Fall Meeting, online
12/11/2020	BioEngineering Day, online
07/12/2020 - 09/12/2020	10th International Colloids Conference 2020, online
10/02/2021	EDMX Research Day, online
03/09/2021 - 10/09/2021	European Colloid and Interface Society Conference and Training Course, Athens, Greece
02/12/2021	Photonics Day, Lausanne, Switzerland
09/02/2022	EDMX Research Day, online

This thesis work was presented at all the above occasions in form of a poster or oral presentation. The most common titles of the contributions were:

- *Polarimetric angle-resolved second harmonic scattering of colloidal TiO_2 nanoparticles in aqueous environments*

- *Surface potential and interfacial water order at the amorphous TiO_2 nanoparticle/aqueous interface*

- *Ion-specific effects at the SiO_2 and TiO_2 nanoparticle/aqueous interface*

Acknowledgements

I would like to dedicate this section to those who have contributed to the success of this work.

First of all, I want to thank my supervisor Prof. Sylvie Roke and my co-supervisor Dr. Arianna Marchioro for entrusting me with this exciting PhD thesis project. I am very grateful to have had the opportunity to work in the Laboratory for fundamental BioPhotonics at EPFL, a dynamic and inspiring research environment. Thank you for all the time and effort you invested into my professional and personal growth. I really appreciate your dedicated scientific guidance and your kind support throughout my PhD journey.

Furthermore, I want to thank Prof. Steven Baldelli, Prof. Paul Bowen, and Prof. Julianne Gibbs for serving on my PhD defense committee. Thank you for taking the time to carefully read my thesis and for your valuable thoughts and comments. I would especially like to thank the president of the jury Prof. Frank Nüesch, who has assisted me and my research work from the start as a committee member of my annual research presentations together with Prof. Anders Hagfeldt. Thank you for the helpful and encouraging scientific discussions during the years of my thesis work.

Many thanks also go to my colleagues and former colleagues at LBP: Prof. Halil Okur, Prof. Eric Tyrode, Dr. Yixing Chen, Dr. Pierre-Marc Dansette, Dr. Jan Dedic, Dr. Marie Didier, Dr. Maksim Eremchev, Dr. Igor Nahálka, Dr. Saranya Pullanchery, Dr. Benjamin Rehl, Dr. Nikolay Smolentsev, Dr. Orly Tarun, Dr. Evangelia Zdrali, Dr. des. Sergey Kulik, Bingxin Chu, Mischa Flór, Seonwoo Lee, Jinhao Li, David Roesel, Nathan Roncerey, Tereza Schönfeldová and Li Zhang. I want to especially thank Dr. Claire Teulon and Dr. Nathan Dupertuis for their friendship and loyal support. I also want to express my gratitude to Rebecca Veselinov for her friendly help with the administrative work. It has been a pleasure to work with you all.

Moreover, I would like to thank our collaborators Prof. Milan Předota and Dr. Denys Biriukov (University of South Bohemia, České Budějovice, Czech Republic) for providing the molecular dynamics simulations presented in this work. Likewise, I would like to thank Prof. Ji Bong Joo and Na Yeon Kim (Konkuk University, Seoul, Korea) for preparing TiO_2 particles for us: amongst others the anatase TiO_2 particles investigated in Chapter 6. Thank you for the great collaboration and for all the fruitful scientific discussions.

Acknowledgements

Lausanne, March 2022   *Marie Bischoff*

166